DISSERTATION

ELUCIDATING STRUCTURE-PROPERTY-PERFORMANCE RELATIONSHIPS OF PLASMA MODIFIED TIN(IV) OXIDE NANOMATERIALS FOR ENHANCED GAS SENSING APPLICATIONS

Submitted by

Erin P. Stuckert

Department of Chemistry

In partial fulfillment of the requirements

For the Degree of Doctor of Philosophy

Colorado State University

Fort Collins, Colorado

Spring 2017

Doctoral Committee:

Advisor: Ellen R. Fisher

B George Barisas
Amy L. Prieto
Amber T. Krummel
Kaka Ma

ABSTRACT

ELUCIDATING STRUCTURE-PROPERTY-PERFORMANCE RELATIONSHIPS OF PLASMA MODIFIED TIN(IV) OXIDE NANOMATERIALS FOR ENHANCED GAS SENSING APPLICATIONS

This dissertation examines structure-property-performance relationships of plasma modified tin(IV) oxide (SnO_2) nanomaterials to successfully and efficiently create sensitive targeted gas sensors. Different project aspects include (1) materials characterization before and after plasma modification, (2) plasma diagnostics with and without a SnO_2 nanomaterial, (3) sensor performance testing, and ultimately (4) elucidation of gas-surface relationships during this project. The research presented herein focuses on a holistic approach to addressing current limitations in gas sensors to produce desired capabilities for a given sensing application.

Strategic application of an array of complementary imaging and diffraction techniques is critical to determine accurate structural information of nanomaterials, especially when also seeking to elucidate structure-property relationships and their effects on performance in specific applications such as gas sensors. In this work, SnO_2 nanowires and nanobrushes grown via chemical vapor deposition (CVD) displayed the same tetragonal SnO_2 structure as revealed via powder X-ray diffraction (PXRD) bulk crystallinity data. Additional characterization using a range of electron microscopy imaging and diffraction techniques, however, revealed important structure and morphology distinctions between the nanomaterials. Tailoring scanning transmission electron microscopy (STEM) modes and combining these data with transmission electron backscatter diffraction (t-EBSD) techniques afforded a more detailed view of the SnO_2

nanostructures. Indeed, upon deeper analysis of individual wires and brushes, we discovered that despite a similar bulk structure, wires and brushes grew with different crystal faces and lattice spacings. Had we not utilized multiple STEM diffraction modes in conjunction with t-EBSD, differences in orientation related to bristle density would have been overlooked. Thus, it is only through methodical combination of several analysis techniques that precise structural information can be reliably obtained.

To begin considering what additional features can affect gas sensing capabilities, we needed to understand the driving force behind SnO_2 sensors. SnO_2 operates widely as a gas sensor for a variety of molecules via a mechanism that relies on interactions with adsorbed oxygen. To enhance these interactions by increasing surface oxygen vacancies, commercial SnO_2 nanoparticles and CVD-grown SnO_2 nanowires were plasma modified by Ar/O_2 and $H_2O_{(v)}$ plasmas. Scanning electron microscopy (SEM) revealed changes in nanomaterial morphology between pre- and post-plasma treatment using H_2O plasma treatments but not when using Ar/O_2 plasmas. PXRD patterns of the bulk SnO_2 showed the Sn^{4+} is reduced by H_2O and not Ar/O_2 plasma treatments. X-ray photoelectron spectroscopy (XPS) indicated Ar/O_2 plasma treatment increases oxygen adsorption with increasing plasma power and treatment time, without changing Sn oxidation. With the lowest plasma powers and treatment times, however, H_2O plasma treatment results in nearly complete bulk Sn reduction. Although both plasma systems increased oxygen adsorption over the untreated (UT) materials, there were clear differences in the tin and oxygen species as well as morphological variations upon plasma treatment.

Given that H_2O plasma modification of SnO_2 nanomaterials resulted in reduction of Sn^{+4} to Sn^0, this phenomenon was further explored. To develop a deeper understanding of the mechanism for this behavior, gas-phase species were detected via optical emission spectroscopy

(OES) during H_2O plasma processing (nominally an oxidizing environment), both with and without SnO_2 substrates in the reactor. Gas-phase species were also detected in the reducing environment of H_2 plasmas, which provided a comparative system without oxygen. Sn* and OH* appear in the gas phase in both plasma systems when SnO_2 nanowire or nanoparticle substrates are present, indicative of SnO_2 etching. Furthermore, H_2 and H_2O plasmas reduced the Sn in both nanomaterial morphologies. Differences in H* and OH* emission intensities as a function of plasma parameters show that plasma species interact differently with the two SnO_2 morphologies. The H_2O plasma gas-phase studies found that under most plasma parameters the ratio of reducing to oxidizing gas-phase species was ≥1.

The final consideration in our holistic approach relied on sensor performance studies of SnO_2 nanomaterials. Resistance was recorded as a function temperature for UT, Ar/O_2 and H_2O plasma treated nanoparticles and nanowires exposed to air, carbon monoxide (CO), or benzene (C_6H_6). Resistance data were then used to calculate sensor response (R_{air}/R_{gas}) and sensitivity ($R_{air}/R_{gas} > 1$ or $R_{gas}/R_{air} > 1$). Specifically, Ar/O_2 and H_2O plasma modification increase CO and C_6H_6 sensitivity under certain conditions, but H_2O plasma was more successful at increasing sensitivity over a wider range of plasma parameters. In particular, certain H_2O plasma conditions resulted in increased sensitivity over the UT nanomaterials at 25 and 50 °C. Overall, H_2O plasma appears to be more effective at increasing sensitivity than Ar/O_2 plasma. Furthermore, although certain treatments and temperatures for nanoparticles had greater CO or C_6H_6 sensitivity than nanowires, nanowire sensitivity was less temperature dependent than nanoparticle sensitivity. Prior materials characterization data were combined with resistance data to elucidate specific structure-property-performance relationships for the different UT and plasma treated materials.

ACKNOWLEDGMENTS

Today would not have been possible without support from numerous individuals. Your encouragement and assistance over the years provided invaluable aid to my graduate success, and for that I am truly grateful. First, I would like to thank Dr. Ellen Fisher for her willingness to jump into a new area of research. Through my independent research and with her guidance I was able to take true ownership of my project and learn a variety of aspects necessary for project development, collaboration, and while details are important, to never forget the big picture. Furthermore, I would like to thank all present and past Fisher Group members for all of their input and support over the years of my graduate studies. Thank you for being willing to talk through my research problems and listen to and provide feedback when needed while also being ready to relax and have fun just as easily, whether it be an after work drink and appetizers, sushi game night, or rafting down the Poudre. Your collaborations over the years have shown me what a supportive team should be, and without your willingness to work together my graduate experience would not have been nearly as rewarding. I also want to give a big thank you to all of the CIF, shops, and admin staff that were always available when I needed help running instrumentation, fixing equipment in lab, or navigating the numerous dept and graduate school requirements. You all provide a great deal of support for faculty and students to aid and guide us through our graduate careers and do not always receive the thanks you are due. Finally, for my family and friends' support, listening to my research troubles and progress, and making sure that I kept a work-life balance to control stressful situations, I am forever grateful. Such times away from school and research allowed me to keep moving forward full throttle without becoming overwhelmed by the graduate experience, and for that I thank you all.

TABLE OF CONTENTS

LIST OF TABLES

LIST OF FIGURES

CHAPTER 1

INTRODUCTION

This chapter provides information on the premise behind the work detailed in this dissertation including motivations for complete understanding of the process of plasma modification of SnO_2 nanomaterials for gas sensing applications. Most notably, this chapter conveys the necessity of combining comprehensive materials characterization, plasma diagnostics, and sensor performance testing to efficiently relate material structure and properties, as well as gas-phase plasma species with sensor performance. This inclusive combination of analyses expedites progress toward selecting materials and plasma systems to create sensors for targeted gas detection applications. The chapter concludes with an overview of the research presented in the remainder of this dissertation.

1.1. Motivation and foundation of research

1.1.1. Need for sensitive and selective gas detection. The increasing amount of energy produced and consumed worldwide has caused excessive emission of toxic gaseous species, negatively impacting human health and well-being.[1-3] Nitrogen oxides, benzene, and formaldehyde are just a few examples of gases that can result in immediate and long-term health problems.[4] To monitor such toxic gases, a large body of research has focused on developing sensitive and selective gas sensors.[1-3] Nevertheless, there remains room for further improvement as commercially available sensors have significant limitations. For example, most lack the sensitivity to detect analytes at concentrations below relevant toxicity levels, and often require high operating temperatures (100-500 °C) to achieve the necessary sensitivity with sufficiently

rapid response (ms to s).[1-3] Such high operating temperatures limit the lifetime of many sensors (anywhere from a few months to a couple of years), because of the wear on the materials resulting from the power consumption required for temperature maintenance.[1-3] Additionally, the accuracy of many commercial sensors is affected by the presence of interfering species, which decrease selectivity. For example, co-adsorption of both CO and NO can occur on an oxidized SnO_2 surface, ultimately resulting in a less reliable sensitivity reading for either CO or NO.[5]

1.1.2. Promising sensor materials. An active area of sensor research from which many commercial sensors arise focuses on metal oxide (MO) materials. These materials have numerous assets for sensing applications, including their capabilities as semiconductors in electronics.[2, 6] Indeed, many semiconductor MO-based sensors utilize thin films to exploit their conductivity and surface-gas interactions by monitoring gases via changes in resistance resulting from interactions between gases and oxygen adsorbed to the material surfaces.[2, 6] In particular, SnO_2 has been used extensively because of tin's dual valency (i.e., Sn^{4+} and Sn^{2+}), which provides more diverse surface chemistry than monovalent MO. This allows for greater material tunability, often resulting in SnO_2 being a more sensitive and selective gas sensor than other MO.[7, 8,] Markedly, it is necessary to monitor the tin oxidation state, as sensitivity and selectivity of particular gases can drop drastically with increased tin reduction.[9] Although improved over other MO, unmodified SnO_2 in its simplest thin film variation has several limitations, most notably its low surface area available for interaction with gases. The SnO_2 sensing mechanism is driven by interactions with surface adsorbed oxygen, whereby adsorbing oxygen in ambient atmosphere creates a base resistance of the material. Deviations from this base resistance with addition of a target gas can determine material sensitivity toward the given target gas.[8, 10, 11]

Thus, maximizing surface area is critical to increasing oxygen adsorption and thereby gas-surface interactions leading to improved SnO_2 sensor sensitivity.

1.1.3. Improving on a longstanding material. Recent work on SnO_2 materials with greater surface area includes studies aimed at fabricating doped and composite SnO_2 thin films, nanoplates, nanoparticles, nanowires, and porous nanofoams.[12-16] Although doping SnO_2 with precious metals (i.e., Pd, Pt) can increase SnO_2 material sensitivity, dopants increase the cost of the sensors and have limited tunability.[17-20] Creating sensors from nanomaterials that produce more three dimensional (3D) networks can expand the available surface area for gas surface interactions while maintaining a connected network for measuring resistance changes in the presence of different gases. Furthermore, nanomaterial morphology can be fine-tuned to alter surface area.

Although these nano-structured materials increase sensitivity over SnO_2 thin films through increased gas-surface interactions, detection below known/reported gas toxicity levels has yet to be achieved for many sensors, especially at room temperature.[9, 21, 22] The higher temperatures (~300°C) required for most sensors to have sufficient sensitivity toward certain gases largely results from the different adsorbed oxygen species present on the SnO_2 surface at different temperatures. Specifically, at temperatures <150 °C, physisorbed O_2 is the primary surface species; <300 °C, the O_2^- anion is observed; <600 °C, surface oxygen primarily takes the form of O^-; and >600°C, O^{2-} is the primary surface species observed.[8, 10, 11] Given that gas-phase species (e.g., CO, NO) are more likely to interact with $O^-_{(ad)}$ or $O^{2-}_{(ad)}$, it is understandable to observe higher sensitivity at temperatures 300 °C to 600 °C.[8, 23, 24]

Aside from maximizing surface area and doping, an additional method of creating materials with increased surface-gas interactions entails surface modification to alter surface

chemistry, as well as morphology. Some potential methods of surface modification include dip coating, grafting, dopant addition, polymeric nanocomposites, and plasma treatment.[25-27] Although facile processes, dip coating and grafting are more effective at modifying entire polymer constructs than surfaces alone. Furthermore, these methodologies often have less precision of the resulting surface modification. Dopant addition and polymeric nanocomposites are fabrication-based modification techniques versus surface modification methods, that can address sensor limitations, but often with limited control. Plasma surface modification is the method most equipped to controllably tailor surface or bulk properties. Plasmas contain a variety of reactive (i.e., electrons, ions, radicals), neutral atomic, and molecular species which can be tuned by changing plasma parameters including applied power, system pressure, precursor gas type and flow rate, as well as substrate location with the plasma.[28] The wide range of species present within plasmas are capable of creating numerous potential reactions at surfaces. Thus, the expansive parameter space of plasmas allows for significant control over surface reactions, and thus, the modification process.[9, 22, 29] Furthermore, in many instances, can reproducibly and uniformly tune surface properties that is not always possible with alternative modification techniques (e.g., dopants).

1.1.4. Underutilized surface modification strategy for sensor materials. Plasma modification is often used as a tool in industrial and academic settings to fabricate or modify materials for a wide array of applications, including growing nanomaterials for use in the semiconductor industry, polymer surface functionalization for biomedical devices, and coatings for a variety of commercially available products among others.[30-32] For instance, water vapor, fluorocarbon-based precursors, as well as co-polymerization systems using allylamine and allylalcohol have been used to plasma modify polymer materials to control biological

interactions.[31, 33, 34] Additional plasmas ignited from precursor gases such as Ar/CH_4, Ar/Cl, and O_2 are routinely used for etching surfaces in the semiconductor industry.[35, 36] Although plasma surface modification is not a new methodology,[37-39] it is severely underutilized as a tool for sensor material modification. Indeed, it has only been in the last decade that interest has grown in plasma treatment of sensor materials including using Ar/O_2, H_2, O_2, and N_2 plasmas to modify SnO_2 materials with the main focus on Ar/O_2[9, 22, 40, 41] plasma surface modification.[9, 42-44] Ar/O_2 is an oxidizing plasma that creates surface oxygen vacancies in SnO_2 materials under certain plasma parameters, which increases oxygen adsorption and thus sensitivity in many cases. Although other plasmas have been used to functionalize SnO_2 surfaces, such as those listed above, the sensor field has not begun to approach the full utility of plasma modification. Furthermore, those that employ plasma treatments in sensor fabrication rarely report on plasma chemistry or plasma-surface interactions during the modification process. It is not uncommon to find studies that use plasmas merely as a tool to modify materials to achieve desired sensor performance. Such studies often lack understanding of how the plasma modification process is resulting in such properties.

1.1.5. Exploring plasma-surface interactions. Plasma diagnostic techniques are often used to determine plasma species densities, kinetics, energetics, and end-point detection in etching systems.[45-48] Diagnostic techniques include, but are not limited to, Langmuir probes, Broadband Absorption Spectroscopy, Laser Induced Fluorescence, and Optical Emission Spectroscopy.[49-52] OES is most commonly used for measurement of plasma species densities and determining plasma temperatures without disrupting the plasma. Using a technique that doesn't alter the plasma is particularly important when attempting to elucidate the effects of adding a substrate to a plasma system.

It is well-known that plasma treatment of materials can change material structure, chemistry, and morphology. Plasma diagnostic studies as a function of substrate presence and type, as well as plasma parameters, indicate that different materials within a plasma can also affect internal temperatures (i.e., rotational (T_R) and vibrational (T_V)) and electrical profiles of plasmas.[50, 53] Nui *et al.* used OES to analyze different NO-containing plasmas to determine the effect of a Co-ZSM-5 packed catalyst. Using the collected spectra, they were able to calculate $T_R(N_2)$ and $T_V(N_2)$, which showed an increase in $T_R(N_2)$ and a decrease in $T_V(N_2)$ with the addition of the catalyst.[54] Such changes in temperature indicate that the presence of a substrate in a plasma can alter plasma energetics. Ultimately, this can result in different plasma modification of the material than initially expected from plasma analysis without a substrate.

With the limited studies on plasma modification of SnO_2 nanomaterials there are no studies that observe the effect of the plasma on the materials as well as the effect of the material on the plasma bulk. To examine how SnO_2 nanomaterials interact with plasma systems, changes in plasma species densities and plasma temperatures can be determined using OES as a function of nanomaterial presence. Combining these data with materials characterization can then be utilized to gain knowledge of plasma modification mechanisms of different plasma systems and nanomaterials.

1.1.6. Bridging the gaps in an incomplete story for optimal sensor creation. More broadly, there is a lack of fundamental understanding regarding the relationships between sensor fabrication, modification, and performance testing. To make advancements toward choosing materials and plasma systems for sensitive targeted gas detection, it is necessary to 1) comprehensively characterize materials' structure and properties pre- and post- plasma treatment, 2) characterize the plasma during the surface modification process, and 3)

systematically test sensor performance. This experimental methodology provides the ability to relate a) material structure and properties, b) specific plasma species and parameters, and c) sensor performance. As studies begin to relate all of these features during sensor design, a comprehensive library can be formed to aid in effective selection of optimum conditions for generating sensitive and selective gas sensors. Thus, it is through this study on plasma modified SnO_2 nanomaterials that we have made progress toward addressing gaps in understanding the effects of material properties and plasma parameters on sensor performance.

1.2. Overview of Research

This dissertation explores the sensor development process from fabrication of the sensing materials, to comprehensive materials characterization, to gas-phase plasma diagnostic studies, to application-based sensor performance experiments. Through this process we gain understanding of how SnO_2 nanomaterials are modified under specific plasma conditions. This knowledge will allow us to design and fabricate more sensitive and selective gas sensors. Chapter 2 details methods and materials used for nanomaterial growth and fabrication procedures, plasma modification, diagnostic, and sensor performance testing conditions, in addition to instrumental and software parameters for all research presented in Chapters 3-7.

Results from a variety of materials characterization techniques presented in Chapter 3 provide substantial information on SnO_2 nanomaterial structure and properties, specifically for CVD-grown SnO_2 nanowires and nanobrushes. All materials were evaluated via SEM to discern morphology differences. Additionally, a variety of analytical tools were used to collect diffraction-based data on SnO_2 nanowires and nanobrushes with a large emphasis on understanding differences in structure of nanowires and nanobrushes grown via the same CVD

process under varied growth parameters. PXRD was used to determine bulk crystallinity of all materials, whereas high-resolution STEM (HR-STEM) and t-EBSD were used to determine growth facets and other structural aspects of nanowires and nanobrushes.

Given that SnO_2 functions as a gas sensor through resistance changes as a result of atmospheric gases interacting with surface adsorbed oxygen, we focused our initial modification studies on plasma precursors known for increasing oxygen vacancies. Specifically, Ar/O_2 was chosen both for this reason and for direct comparison to the literature.[9, 22] Chapter 4 describes the optimization process of using an Ar/O_2 plasma to achieve surface modification of SnO_2 nanowires and nanoparticles. Nanowires and nanoparticles were chosen for plasma modification studies because of their dramatic differences in morphology. Material analysis was completed pre-and post-plasma treatment including SEM for morphology, PXRD for bulk structure and XPS to analyze surface chemistry. We also chose another system known for increasing surface oxygen content, $H_2O_{(v)}$ plasmas.[55-58] Interestingly, we found H_2O plasma treatments had unexpected results; instead of oxidizing the SnO_2 nanowires and nanoparticles, Sn was reduced to such a degree that material morphology post-plasma modification was radically altered with very little lattice or surface-adsorbed oxygen remaining after treatment. The structure and surface data gained from these analyses are later explored in Chapter 6/7 to determine structure-property-performance relationships of SnO_2 sensors.

To determine why a typically oxidizing plasma system reduced the SnO_2 nanomaterials as described above, Chapter 5 describes OES experiments used to detect plasma species within the H_2O plasma system with and without SnO_2 nanomaterial substrates. Furthermore, because of the well-known reducing nature of a H_2 plasma,[59, 60] similar studies were completed for a H_2 plasma system for comparison to the H_2O plasma treatments. Through plasma diagnostic

techniques, we determined which plasma species were produced in a plasma under the treatment conditions used. We were thus able to identify when a H_2O plasma would oxidize or reduce SnO_2 nanomaterials as a result of the species present in the plasma. These studies also allowed us to calculate T_R and T_V as a result of plasma parameters and substrate presence.

To determine the efficacy of the unmodified and plasma modified SnO_2 nanomaterials in gas sensing applications, it was necessary to first design and build a gas sensing system and sensor fabrication methodology, which were then used to optimize data collection for testing sensor performance. Chapter 6 details this design optimization process in addition to the data analysis methodology ultimately chosen for evaluating sensor performance. Specific performance tests are described in Chapter 7 for UT SnO_2 nanowire and nanoparticle sensors, as well as for sensors produced from Ar/O_2 and H_2O plasma modified materials. All sensors were tested for sensitivity toward carbon monoxide and benzene through exposure to the gases over a range of temperatures between 25 and 300 °C. Temperature dependence on sensor response of the different UT, Ar/O_2 and H_2O plasma treated nanoparticles and nanowires are explored. Sensitivity is considered in conjunction with the corresponding materials properties to elucidate optimum materials properties, plasma conditions, and temperatures for maximum carbon monoxide and benzene sensitivity. In particular, specific plasma parameters and material properties that resulted in the greatest increase in sensitivity over the sensitivity of untreated materials at room temperature varied dramatically as a function of plasma power and precursor for the different target gases.

Chapter 8 provides a summary of this dissertation research and the broader impacts that the knowledge gained from these studies may have on the sensor field. Some additional avenues of preliminary study are also included for their impact on expanding our understanding of

structure-property-performance relationships of sensor materials. In particular, issues and future directions associated with sensitivity and selectivity are explored. Future directions and studies that build on the work presented within this dissertation are proposed to address remaining gaps and limitations of the sensor field.

REFERENCES

1. Batra, A. K.; Chilvery, A.; Guggilla, P.; Aggarwal, M.; Currie, J. R. Micro-and Nano-Structured Metal Oxides Based Chemical Sensors: An Overview. *J. Nanosci. Nanotechnol.* **2014**, *14* (2), 2065-2085.
2. Eranna, G.; Joshi, B.; Runthala, D.; Gupta, R. Oxide Materials for Development of Integrated Gas Sensors—A Comprehensive Review. *Crit. Rev. Solid State Mater. Sci.* **2004**, *29* (3-4), 111-188.
3. Fine, G. F.; Cavanagh, L. M.; Afonja, A.; Binions, R. Metal Oxide Semi-Conductor Gas Sensors in Environmental Monitoring. *Sensors.* **2010**, *10* (6), 5469-5502.
4. Wang, S.; Ang, H. M.; Tade, M. O. Volatile Organic Compounds in Indoor Environment and Photocatalytic Oxidation: State of the Art. *Environ. Intern.* **2007**, *33* 694-705.
5. Tamaki, J.; Nagaishi, M.; Teraoka, Y.; Miura, N.; Yamazoe, N.; Moriya, K.; Nakamura, Y. Adsorption Behavior of CO and Interfering Gases on SnO_2. *Surf. Sci.* **1989**, *221* (1), 183-196.
6. Korotcenkov, G. Metal Oxides for Solid-State Gas Sensors: What Determines Our Choice? *Mater. Sci. Eng., B.* **2007**, *139* (1), 1-23.
7. Batzill, M.; Diebold, U. The Surface and Materials Science of Tin Oxide. *Prog. Surf. Sci.* **2005**, *79* (2), 47-154.
8. Ruhland, B.; Becker, T.; Müller, G. Gas-Kinetic Interactions of Nitrous Oxides with SnO_2 Surfaces. *Sens. Actuators B.* **1998**, *50* (1), 85-94.
9. Pan, J.; Ganesan, R.; Shen, H.; Mathur, S. Plasma-Modified SnO_2 Nanowires for Enhanced Gas Sensing. *J. Phys. Chem. C.* **2010**, *114* (18), 8245-8250.
10. Bielański, A.; Najbar, M. Adsorption Species of Oxygen on the Surfaces of Transition Metal Oxides. *J. Catal.* **1972**, *25* (3), 398-406.
11. Suematsu, K.; Yuasa, M.; Kida, T.; Yamazoe, N.; Shimanoe, K. Determination of Oxygen Adsorption Species on SnO_2: Exact Analysis of Gas Sensing Properties Using a Sample Gas Pretreatment System. *J. Electrochem. Soc.* **2014**, *161* (6), B123-B128.
12. Bing, Y.; Zeng, Y.; Liu, C.; Qiao, L.; Zheng, W. Synthesis of Double-Shelled SnO_2 Nano-Polyhedra and Their Improved Gas Sensing Properties. *Nanoscale.* **2015**, *7* (7), 3276-3284.
13. Yuliarto, B.; Nugraha, N.; Epindonta, B.; Aditia, R.; Iqbal, M. Synthesis of SnO_2 Nanostructure Thin Film and its Prospective as Gas Sensors. *Adv. Mater. Res.* **2013**, *789* 189-192.
14. Rane, S.; Arbuj, S.; Rane, S.; Gosavi, S. Hydrogen Sensing Characteristics of Pt–SnO_2 Nano-Structured Composite Thin Films. *J. Mater. Sci.: Mater. Electron.* **2015**, *26* (6), 3707-3716.
15. Lee, K.-C.; Chiang, Y.-J.; Lin, Y.-C.; Pan, F.-M. Effects of PdO Decoration on the Sensing Behavior of SnO_2 Toward Carbon Monoxide. *Sens. Actuators B.* **2016**, *226* 457-464.
16. Zhang, C.; Wang, J.; Hu, R.; Qiao, Q.; Li, X. Synthesis and Gas Sensing Properties of Porous Hierarchical SnO_2 by Grapefruit Exocarp Biotemplate. *Sens. Actuators B.* **2016**, *222* 1134-1143.
17. Iizuka, K.; Kambara, M.; Yoshida, T. Highly Sensitive SnO_2 Porous Film Gas Sensors Fabricated by Plasma Spray Physical Vapor Deposition. *Sens. Actuators B.* **2012**, *173* 455-461.

18. Xiao, L.; Shu, S.; Liu, S. A Facile Synthesis of Pd-Doped SnO_2 Hollow Microcubes with Enhanced Sensing Performance. *Sens. Actuators B.* **2015**, *221* 120-126.
19. Singhal, A. V.; Chandra, K.; Agarwala, V. Doped Nano–Phase Tin Oxide Thin Films for Selective Gas Sensing. *Int. J. Nanotechnol.* **2015**, *12* (3-4), 248-262.
20. Labeau, M.; Gautheron, B.; Delabouglise, G.; Pena, J.; Ragel, V.; Varela, A.; Román, J.; Martinez, J.; González-Calbet, J.; Vallet-Regi, M. Synthesis, Structure and Gas Sensitivity Properties of Pure and Doped SnO_2. *Sens. Actuators B.* **1993**, *16* (1), 379-383.
21. Jeun, J.-H.; Kim, D.-H.; Hong, S.-H. Synthesis of Porous SnO_2 Foams on SiO_2/Si Substrate by Electrochemical Deposition and Their Gas Sensing Properties. *Sens. Actuators B.* **2012**, *161* (1), 784-790.
22. Mathur, S.; Ganesan, R.; Grobelsek, I.; Shen, H.; Ruegamer, T.; Barth, S. Plasma-Assisted Modulation of Morphology and Composition in Tin Oxide Nanostructures for Sensing Applications. *Adv. Eng. Mater.* **2007**, *9* (8), 658-663.
23. Kocemba, I.; Rynkowski, J. M. The Effect of Oxygen Adsorption on Catalytic Activity of SnO_2 in CO Oxidation. *Catal. Today.* **2011**, *169* (1), 192-199.
24. Nakata, S.; Kato, Y.; Kaneda, Y.; Yoshikawa, K. Rhythmic Chemical Reaction of CO on the Surface of a SnO_2 Gas Sensor. *Appl. Surf. Sci.* **1996**, *103* (4), 369-376.
25. Yusoff, M. F. M.; Kadir, M. R. A.; Iqbal, N.; Hassan, M. A.; Hussain, R. Dipcoating of Poly (ε-Caprolactone)/Hydroxyapatite Composite Coating on Ti6Al4V for Enhanced Corrosion Protection. *Surf. Coat. Technol.* **2014**, *245* 102-107.
26. Li, Q.; Imbrogno, J.; Belfort, G.; Wang, X. L. Making Polymeric Membranes Antifouling Via "Grafting from" Polymerization of Zwitterions. *J. Appl. Polym. Sci.* **2015**, *132* (21).
27. Zhang, Z.; Zhai, S.; Wang, M.; He, L.; Peng, D.; Liu, S.; Yang, Y.; Fang, S.; Zhang, H. Electrochemical Sensor Based on a Polyaniline-modified SnO_2 Nanocomposite for Detecting Ethephon. *Anal. Methods.* **2015**, *7* (11), 4725-4733.
28. Graves, D.; Kushner, M. In *Low Temperature Plasma Science: Not Only the Fourth State of Matter but All of Them. Report of the Department of Energy Office of Fusion Energy Sciences*, Workshop on Low Temperature Plasmas, Los Angeles, CA, USA, 2008.
29. Chaturvedi, A.; Mishra, V. N.; Dwivedi, R.; Srivastava, S. K. Selectivity and Sensitivity Studies on Plasma Treated Thick Film Tin Oxide Gas Sensors. *Microelectron. J.* **2000**, *31* (4), 283-290.
30. Donato, N.; Neri, G. Plasma Technologies in the Synthesis and Treatment of Nanostructured Metal Oxide Semiconductors for Gas Sensing: A Short Review. *Nanosci. Nanotechnol. Lett.* **2012**, *4* (3), 211-227.
31. Hawker, M. J.; Pegalajar-Jurado, A.; Fisher, E. R. Conformal Encapsulation of Three-Dimensional, Bioresorbable Polymeric Scaffolds Using Plasma-Enhanced Chemical Vapor Deposition. *Langmuir.* **2014**, *30* (41), 12328-12336.
32. Zaldivar, R.; Nokes, J.; Adams, P.; Hammoud, K.; Kim, H. Surface Functionalization Without Lattice Degradation of Highly Crystalline Nanoscaled Carbon Materials Using a Carbon Monoxide Atmospheric Plasma Treatment. *Carbon.* **2012**, *50* (8), 2966-2975.
33. d'Agostino, R. Process Control and Plasma Modification of Polymers. *J. Photopolym. Sci. Technol.* **2005**, *18* (2), 245-249.
34. Pegalajar-Jurado, A.; Mann, M. N.; Maynard, M. R.; Fisher, E. R. Hydrophilic Modification of Polysulfone Ultrafiltration Membranes by Low Temperature Water Vapor Plasma Treatment to Enhance Performance. *Plasma Process. Polym.* **2015**, *13* 598-610.

35. Economou, D. J. Pulsed Plasma Etching for Semiconductor Manufacturing. *J. Phys. D: Appl. Phys.* **2014**, *47* (30), 303001.
36. Abe, H.; Yoneda, M.; Fujiwara, N. Developments of Plasma Etching Technology for Fabricating Semiconductor Devices. *Jpn. J. Appl. Phys.* **2008**, *47* (3R), 1435.
37. Gilman, A.; Zakharova, T.; Volkov, S.; Kolotyrkin, V.; Grigoreva, G.; Sakodynskii, K.; Tunitskii, N. Modification of the Surface of Porous Polymeric Sorbents in a Glow-Discharge Plasma. *Zh. Fiz. Khim.* **1979**, *53* (10), 2621-2624.
38. Wertheimer, M.; Schreiber, H. Surface Property Modification of Aromatic Polyamides by Microwave Plasmas. *J. Appl. Polym. Sci.* **1981**, *26* (6), 2087-2096.
39. Tiller, H.; Demme, U. Studies on Influence of Plasma Modification of SiO_2 Surfaces on Reaction-Kinetics in Low-Pressure Plasma. *Z. Phys. Chem.* **1972**, *251* (3-4), 137-144.
40. Comini, E.; Sberveglieri, G. Metal Oxide Nanowires as Chemical Sensors. *Mater. Today.* **2010**, *13* (7-8), 28-36.
41. Kim, H. W.; Choi, S. W.; Katoch, A.; Kim, S. S. Enhanced Sensing Performances of Networked SnO_2 Nanowires by Surface Modification with Atmospheric Pressure Ar-O_2 Plasma. *Sens. Actuators B.* **2013**, *177* 654-658.
42. Srivastava, R.; Dwivedi, R.; Srivastava, S. K. Development of High Sensitivity Tin Oxide Based Sensors for Gas/Odour Detection at Room Temperature. *Sens. Actuators B.* **1998**, *50* 175-180.
43. Srivastava, R.; Dwivedi, R.; Srivastava, S. Effect of Oxygen, Nitrogen and Hydrogen Plasma Processing on Palladium Doped Tin Oxide Thick Film Gas Sensors. *Phys. Semicond. Devices, Proc. Int. Workshop.* **1998**, 526-528.
44. Srivastava, R.; Dwivedi, R.; Srivastava, S. K. Effect of Oxygen and Hydrogen Plasma Treatment on the Room Temperature Sensitivity of SnO_2 Gas Sensors. *Microelectron. J.* **1998**, *29* (11), 833-838.
45. Trevino, K. J.; Fisher, E. R. Detection Limits and Decomposition Mechanisms for Organic Contaminants in Water Using Optical Emission Spectroscopy. *Plasma Process. Polym.* **2009**, *6* (3), 180-189.
46. Rahman, M. M.; Khan, S. B.; Marwani, H. M.; Asiri, A. M. A SnO_2-Sb_2O_3 Nanocomposite for Selective Adsorption of Lead Ions from Water Samples Prior to Their Determination by ICP-OES. *Microchim. Acta.* **2015**, *182* (3-4), 579-588.
47. Sarani, A.; Nikiforov, A. Y.; Leys, C. Atmospheric Pressure Plasma Jet in Ar and Ar/H_2O Mixtures: Optical Emission Spectroscopy and Temperature Measurements. *Phys. Plasmas.* **2010**, *17* (6), 063504.
48. Donnelly, V. Plasma Electron Temperatures and Electron Energy Distributions Measured by Trace Rare Gases Optical Emission Spectroscopy. *J. Phys. D: Appl. Phys.* **2004**, *37* (19), R217-R236.
49. Miakonkikh, A. V.; Rudenko, K. V. In *Application of Langmuir Probe Technique in Depositing Plasmas for Monitoring of Etch Process Robustness and for End-Point Detection*, International Conference on Micro-and Nano-Electronics 2009, International Society for Optics and Photonics: 2009; pp 75210A-75210A-9.
50. Morgan, M. M.; Cuddy, M. F.; Fisher, E. R. Gas-Phase Chemistry in Inductively Coupled Plasmas for NO Removal from Mixed Gas Systems. *J. Phys. Chem. A.* **2010**, *114* (4), 1722-1733.
51. Bruggeman, P.; Iza, F.; Guns, P.; Lauwers, D.; Kong, M. G.; Gonzalvo, Y. A.; Leys, C.; Schram, D. C. Electronic Quenching of OH (A) by Water in Atmospheric Pressure

Plasmas and its Influence on the Gas Temperature Determination by OH (A–X) Emission. *Plasma Sources Sci. Technol.* **2009**, *19* (1), 015016.
52. Bruggeman, P.; Cunge, G.; Sadeghi, N. Absolute OH Density Measurements by Broadband UV Absorption in Diffuse Atmospheric-Pressure He-H_2O RF Glow Discharges. *Plasma Sources Sci. Technol.* **2012**, *21* (3), 035019.
53. Guyon, C.; Cavadias, S.; Mabille, I.; Moscosa-Santillan, M.; Amouroux, J. Recombination of Oxygen Atomic Excited States Produced by Non-Equilibrium RF Plasma on Different Semiconductor Materials: Catalytic Phenomena and Modelling. *Catal. Today.* **2004**, *89* (1), 159-167.
54. Niu, J.; Peng, B.; Yang, Q.; Cong, Y.; Liu, D.; Fan, H. Spectroscopic Diagnostics of Plasma-Assisted Catalytic Systems for NO Removal from $NO/N_2/O_2/C_2H_4$ Mixtures. *Catal. Today.* **2013**, *211* 58-65.
55. Tarlov, M. J.; Evans, J. F. Surface Characterization of Radio Frequency Water Plasma Treated and Annealed Polycrystalline Tin Oxide Thin Films. *Chem. Mater.* **1990**, *2* (1), 49-60.
56. Tarlov, M. J.; Evans, J. F.; Newman, J. G. Static SIMS and XPS Study of Water Plasma Exposed Tin Oxide Films *Appl. Surf. Sci.* **1993**, *64* (2), 115-125.
57. Lee, J. H.; Park, J. W.; Lee, H. B. Cell Adhesion and Growth on Polymer Surfaces with Hydroxyl Groups Prepared by Water Vapour Plasma Treatment. *Biomaterials.* **1991**, *12* (5), 443-448.
58. Steen, M. L.; Hymas, L.; Havey, E. D.; Capps, N. E.; Castner, D. G.; Fisher, E. R. Low Temperature Plasma Treatment of Asymmetric Polysulfone Membranes for Permanent Hydrophilic Surface Modification. *J. Membr. Sci.* **2001**, *188* (1), 97-114.
59. Thomas III, J. H. X-Ray Photoelectron Spectroscopy Study of Hydrogen Plasma Interactions with a Tin Oxide Surface. *Appl. Phys. Lett.* **1983**, *42* (9), 794-796.
60. Bouchoule, A.; Ranson, P. Study of Volume and Surface Processes in Low Pressure Radio Frequency Plasma Reactors by Pulsed Excitation Methods. I. Hydrogen–Argon Plasma. *J. Vac. Sci. Technol., A.* **1991**, *9* (2), 317-326.

CHAPTER 2

EXPERIMENTAL METHODS

This chapter describes the materials, methods, and techniques necessary to complete this dissertation work. Many of these methods can be found in published work as reported in Ch.3-7 and are reported here with the consent of the respective publishers.[1, 2] The information is presented in sections to introduce how to fabricate SnO_2 nanomaterials (2.1), characterize the surface and materials properties (2.2), plasma modify materials (2.3), diagnose the gas-phase (2.4), and test the sensing performance of the modified and unmodified SnO_2 nanomaterials (2.5). Funding for this research was provided by the National Science Foundation (CHE-1152963).

2.1. Nanomaterial growth and fabrication

2.1.1. Chemical vapor deposition of nanowires and nanobrushes. All SnO_2 materials were grown or supported on zirconia (ZrO_2) wafers (50 nm ZrO_2 on n-type 100 Si wafer, BioStar). Note that ZrO_2 was used in place of SiO_2 or Al_2O_3 as it can also withstand the elevated temperatures often necessary for sensing. Additionally, with a higher electrical resistivity and dielectric constant, ZrO_2 may allow for observing smaller changes in resistance and thus contribute to developing a more sensitive gas sensor. ZrO_2 wafers were sputter coated with 5 nm Au (Denton Vacuum Desk II 100 mTorr, 30 mAmps, sputtered 16 s) and annealed in a Thermolyne 1300 furnace at 700 °C for 60 min to create Au nanoparticles. The CVD reactor was designed in house, based on a standard hot-wall CVD reactor system, Figure 2.1.[3] The ZrO_2 wafers with Au nanoparticles were placed in the center of the first heated region in the CVD

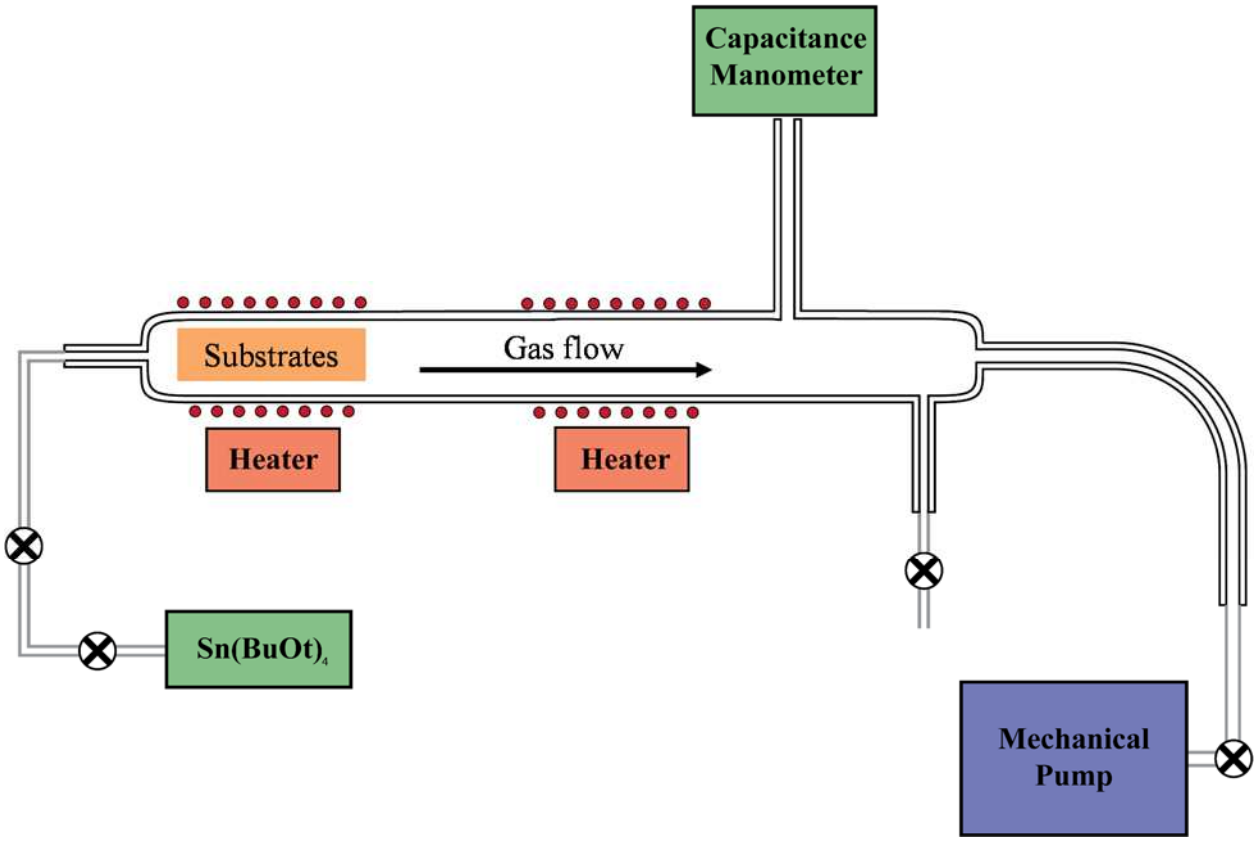

Figure 2.1. Schematic diagram of the hot-wall CVD reactor containing two heating regions where temperature is measured by a K-type thermocouple. Substrates were placed in the heated region nearest the $Sn(BuOt)_4$ precursor and the system kept under vacuum.

reactor nearest the precursor inlet (the second heater was not used for these studies). The precursor, tin (IV) tert-butoxide ($Sn(O^tBu)_4$) ≥99.99% trace metals basis (Aldrich) used as received, was contained in a Schlenk flask with molecular sieves and heated to 45-55 °C to increase vapor pressure. Precursor flow resulted in a constant pressure of ~200 mTorr. The substrate region was heated to 700 °C for nanowires and 625-650 °C for nanobrushes with three wafers placed lengthwise, equally spaced, in the center of the heated region. For OES studies, a single elongated wafer was placed lengthwise in the heated region. Temperatures were controlled via a K-type thermocouple and proportional-integral-derivative (PID) temperature controller. To measure the temperature gradient in the reactor, the temperature in the center of the heated region was held at 700 °C and temperatures were recorded at ~1 cm increments across the heated range of the reactor. This yielded measurements of 510 °C, 675 °C, 700 °C, 715 °C, and 612 °C, as a function of distance from the gas inlet. The process to achieve nanowire growth involved evacuating the reactor to base pressure while heating to the desired temperature over 30 min; heating the substrates and exposing them to the precursor for 20-45 min; stopping the flow of precursor and pumping it out of the system while the substrates were heated for an additional 10 min; and cooling the substrates under vacuum for 15 min.

2.1.2. Nanoparticle preparation. Commercial SnO_2 nanoparticles (<100nm, Aldrich) were suspended in methanol to either create a paste which was spread over ZrO_2 wafers or as a solution that was spin coated over ZrO_2 wafers and left to dry overnight under ambient conditions. Spin-coating resulted in the most uniform nanoparticle surface compared to drop-casting and spreading a paste as slight variations in the thickness of the supported nanoparticles resulted in large variations in surface compositions after plasma treatment. Thus, this was the method employed for the majority of the data presented here.

2.1.3. Sensor fabrication. Hand assembled sensors were fabricated by attaching silver wire as electrodes (~1 cm in length, 0.25 mm diameter, 99% Sigma Aldrich) to the SnO_2 substrates described in the prior sections with enough silver conductive paste (Sigma Aldrich) to cover the end of the electrode (~1-2 mm in diameter) as indicated in the Figure 6.5 (Chapter 6). The paste was cured by heating the substrates at 120 °C for 1 hour in an alumina tray. Sensors were cooled to room temperature prior to use in performance tests.

2.2. Materials characterization and simulation methods and instrumentation

2.2.1. Scanning Electron Microscopy/Energy Dispersive X-ray Spectroscopy (EDS). SEM images were collected to observe the approximate size of Au nanoparticles after annealing, as well as UT and plasma treated SnO_2 nanoparticles, nanowires, and nanobrushes. All samples were analyzed with a JEOL JSM-6500F instrument, equipped with a field emission source. A 15 kV electron beam accelerating voltage at 10.0 mm working distance was used. SEM tandem EDS (30 kV accelerating voltage) with a 60 mm silicon drift detector (EDAX) was used to determine chemical composition to confirm deposition of SnO_2, regardless of the resulting morphology.

2.2.2. X-ray Photoelectron Spectroscopy. XPS was performed on SnO_2 nanoparticle, nanowire, and nanobrush samples prior to and after plasma treatment using a PHI-5800 ESCA system with an Al K_α monochromatic X-ray source with a 45° takeoff angle. High resolution spectra were collected in triplicate for gold (Au_{4f}), tin (Sn_{3d}), and oxygen (O_{1s}). Although the binding environments of tin and oxygen were of particular interest for observing changes from pre-plasma treatment to post-plasma treatment, gold spectra were collected to allow for charge correction by setting the Au $4f_{7/2}$ component to 84.0 eV.[4] As such, it was necessary to sputter-

coat nanoparticle samples with ~1 nm Au prior to analysis, as there was no gold used in their synthesis. An XPS control experiment of treated nanoparticles without the 1 nm Au coating showed no apparent differences in the spectra compared to those with the Au coating. Multipak v6.1A and CasaXPS v2.3.16 PR 1.6 were used to determine elemental compositions, and XPSPeak v4.1 and CasaXPS v2.3.16 PR 1.6 were used to analyze specific binding information for the Sn_{3d} and O_{1s} high resolution spectra. Oxygen peaks were fit with a Shirley background, whereas tin and gold peaks were fit with a Tougaard background.[5, 6] All Sn_{3d} peak fits were allowed to vary from 100% Gaussian fittings. Chemical identifications were determined through comparison with the literature in conjunction with PXRD patterns.[7-9]

2.2.3. Powder X-ray Diffraction. PXRD patterns were collected to determine average SnO_2 material crystallinity and as an additional method of determining the different tin species present in the SnO_2 samples before and after plasma treatment. Patterns were collected on a Scintag X-2 with a Cu K_α radiation source using a 2theta scan from 20° to 80° at intervals of 0.02° with scans of 1 step/sec. Patterns were acquired for UT nanoparticles on zero diffraction plates; UT nanoparticles, nanowires, and nanobrushes on ZrO_2; and treated nanoparticles and nanowires on ZrO_2. A pattern was also collected for ZrO_2 and ZrO_2 annealed with Au for aid in matching sample patterns with the International Centre for Diffraction Data (ICDD) pattern database. Pattern intensities were multiplied by 5 to increase peak signals for easier pattern characterization.

2.2.4. Transmission Electron Backscatter Diffraction and Transmission Electron Microscopy sample preparation. Specimens for t-EBSD and TEM were prepared by brushing the carbon side of a 200 mesh copper grid with a carbon film across the surface of a nanowire/nanobrush sample. Hundreds of wires or brushes were captured and adhered to the

carbon film through this process. A single tilt TEM holder was customized to easily transfer samples between the SEM and TEM microscopes. Nanowire and nanobrush samples were analyzed in the TEM using both the modified single tilt and double tilt holder (JEOL).

2.2.5. Transmission Electron Backscatter Diffraction. All samples were analyzed with a JEOL JSM-6500F, equipped with a field emission source and a Hikari camera (EDAX) with a 60 mm^2 octane silicon drift detector (EDAX). Transmission data were collected using a 20 kV electron beam accelerating voltage, with most patterns collected at 2x2 binning. The sample holder (described above) was placed perpendicularly into the sample stage, where the stage was tilted 65° above the horizontal. This positioned the sample 10 or 15 mm from the detector (held -5° from the horizontal) tilted at 25° above the horizontal. The length of wires and brushes were scanned, collecting diffraction patterns which were individually indexed to reveal the crystal structure for the entire wire or brush. t-EBSD data were collected and analyzed using EDAX Orientation Imaging Microscopy (OIM) data collection and analysis software (v7 2004).

2.2.6. TEM/STEM/HRTEM/STEM-Diffraction Imaging (STEM-DI). These studies used a JEOL-JEM-2100F with 200 kV accelerating voltage (emission = 150 μA), equipped with an ultra-high resolution objective lens pole piece and an Oxford Instruments X-MAX 80 Silicon Drift Detector. A double tilt holder was necessary for orienting a wire/brush to achieve orientation along a zone axis (ZA) for HRTEM imaging and STEM-DI diffraction. STEM-DI is a software attachment (Gatan) for the TEM which allows for customizable spatial resolution imaging in conjunction with the acquisition of the associated diffraction pattern. This process utilizes 4D microscopy where a 2D image is collected and used to detect a 2D diffraction pattern. STEM-DI collected for this study approached pseudo parallel illumination convergent beam electron diffraction (CBED) patterns where diffraction spot resolution approached 2 mrads

(verified in Digital Micrograph®). This resolution was achieved with a 10 μm condenser aperture combined with special optics to narrow the incidence beam thereby reducing the incidence angle, while utilizing a 10 cm camera length.

CBED patterns collected for fitting Kikuchi lines with EDAX t-EBSD software were collected via STEM-DI with a 30 μm condenser aperture which allowed for sampling 40-50 mrads of reciprocal space. This resulted in imaging off of the ZA, allowing for observation of multiple poles with Kikuchi lines present for fittings that had higher precision symmetry. STEM-HR selective area electron diffraction (STEM-HRSAED) and nano-beam electron diffraction (STEM-HRNBED) were collected using the 10 μm condenser aperture without finding the zone axis, using a point and shoot method of selecting a random spot to collect an image and diffraction pattern. Digital Micrograph® software v2-3 (Gatan inc.) were used for data analysis.

2.2.7. Crystal Maker® software (v9.2.7). Crystal Diffract v6.5.5 and Single Crystal v2.3.3 software were used for simulating SnO_2 nanowire and nanobrush structure and diffraction. A ball and stick model of SnO_2 (2104754 from database) was transformed to a single crystal diffraction pattern in Crystal Maker using lattice constants a = b = 0.474 nm and c = 0.319 nm. The pattern was then rotated roughly 10° to match the experimental diffraction pattern collected via STEM-DI. The original SnO_2 modelled structure was then expanded to create a lattice model.

2.3. Plasma reactor design.

2.3.1. General reactor design. SnO_2 nanomaterials were plasma treated in a glass tubular reactor with an inductively coupled radio frequency (rf) plasma generated by an

Advanced Energy MFX600 rf power supply operating at 13.56 MHz, previously described.[10-12] Substrates were placed in the center of the eight-turn nickel-plated copper coil region and the reactor was pumped to base pressure (5-10 mTorr) for ~10 min.

2.3.2. Selective plasma etching (increasing oxygen adsorption) Ar/O_2 and H_2O. For Ar/O_2 plasma treatments, the gas flow rates were 10 and 15 sccm (1:1), respectively, resulting in a steady-state total system pressure of 145 mTorr after 5 min of gas flow (no plasma). Nanomaterials were treated for 5 min with a 30, 60, 100, or 150 W continuous wave (CW) plasma as well as for 10 and 30 min with a 150 W CW plasma. After treatment, gas flow over the substrates was allowed for 5 min to limit reactions with the atmosphere upon removal from the reactor. The same total pressure, treatment times, and applied rf power (P) were used with H_2O plasmas.

2.3.3. H_2 and H_2O plasma modification for plasma diagnostic studies. SnO_2 nanowires and nanoparticles were plasma treated in the reactor described in Section 2.3.1. Substrates were placed lengthwise on a glass slide in the center of the eight-turn nickel-plated copper coil region parallel to/in line with the quartz window (Figure 2.2) and the reactor was evacuated to base pressure (5-10 mTorr) for ~10 min. H_2 gas (Airgas, 99.9%) or Millipore water vapor were introduced into the reactor using either a mass flow controller (MKS) or a side-arm flask via needle metering valve, respectively. Steady-state total system pressure was maintained at 80 mTorr with ~10% Ar by partial pressure after 5 min of gas flow (no plasma). Nanomaterials were treated for 5 min with CW plasmas at P = 30, 60, 100, or 150 W. Precursor gas flow over the substrate continued for 5 min after plasma treatment to limit reactions with the atmosphere upon removal from the reactor. Note, Ar/O_2, H_2O, and H_2 plasma treated nanoparticles and

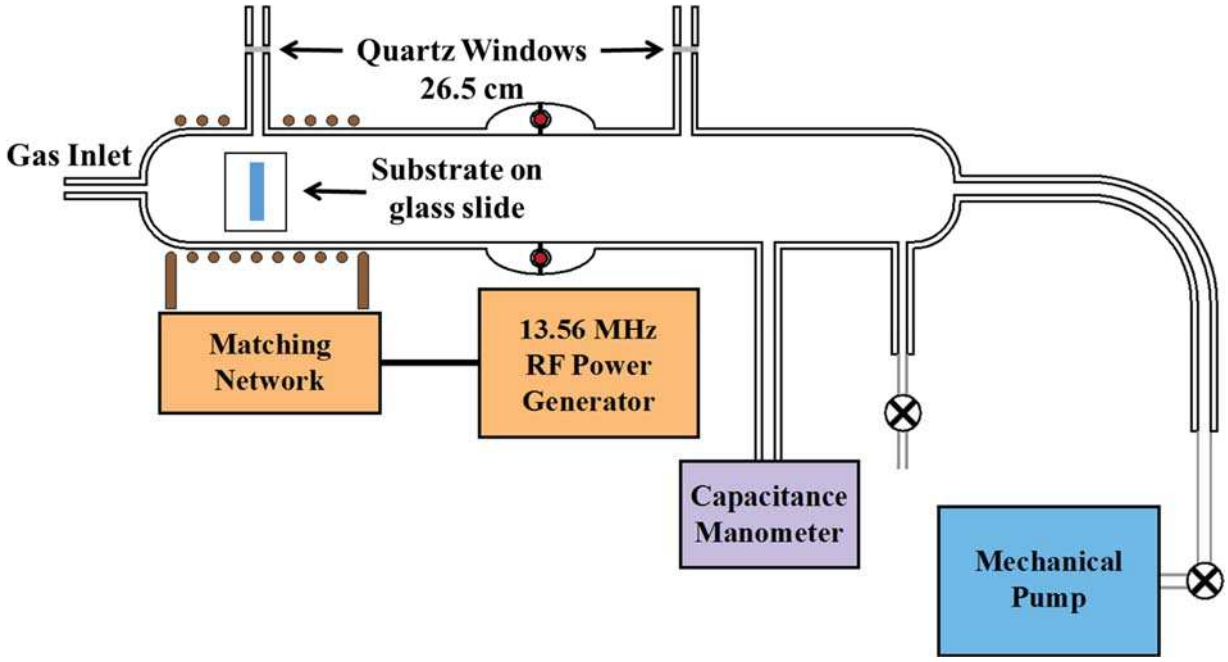

Figure 2.2. Schematic of an inductively coupled plasma reactor with quartz window in the center of the coil region and a second quartz window 26.5 cm downstream. Gas-phase species were detected at both quartz windows with substrates placed in the center of the coil parallel with the quartz window inlet to observe species downstream of the substrate.

nanowires will be described hereafter by the plasma precursor and NP (nanoparticles) or NW (nanowires); for example, Ar/O_2 plasma-treated nanoparticles would be Ar/O_2 NP.

2.4. Plasma diagnostic instrumentation and methods.

Emission spectra were collected for gas-phase H_2 and H_2O plasma species utilizing the same plasma modification conditions described in Section 2.3.3.[1] Two replaceable fused quartz windows were incorporated into the general reactor design for OES analysis, Figure 2.2. One window was placed on the inlet half of the reactor to collect cross-sectional emission signal in the center of the coil region and was aligned with substrate location. The second window was placed 26.5 cm downstream from the center of the coil (first quartz window) to evaluate the plasma afterglow. Unlike emission spectra collected in the coil, downstream spectra were only collected for P = 60 and 150 W treatments of nanoparticles to provide data at the low and high ends of the rf power range used here. Emission was collected via an Avantes AvaSpec-3648-USB2-RM multichannel spectrometer imaging onto a 10 μm entrance slit through a cable containing four optical fibers. Four fiber gratings and 3648-pixel charge-coupled array detectors allowed for detection over the wavelength range of 187-1016 nm with a 0.1 nm FWHM resolution. Spectra were collected with 50 ms integration time and 600 averages. Background/dark spectra were collected during the initial 5 min gas flow (e.g., before plasma ignition) and emission spectra were collected for the entire 5 min plasma treatment described in Section 2.3.3. Emission signals of interest arise from excited state atomic hydrogen (H*, 656 nm), hydrogen (H_2*, 601 nm), hydroxyl radical (OH*, 309 nm), atomic tin (Sn*, 243 nm), and argon (Ar*, 750 nm).[13-15] For species comparison, actinometric intensity ratios for excited state species were calculated, described throughout as I_H/I_{Ar}, I_{OH}/I_{Ar}, I_{Sn}/I_{Ar}, and I_{H2}/I_{Ar} where the

given ratios are proportional to excited state species densities or concentrations (described herein as [*gas species of interest*]).[16-18] Rotational temperatures for OH* radicals were calculated using LIFBASE software by fitting experimental emission spectra with simulated emission spectra of the OH(*A*-*X*) radical emission band from 306-325 nm.[19, 20] All rotational temperatures reported are based on these simulations where peak correlations are ≥0.9. Vibrational temperatures were calculated from vibrational populations and spectroscopic constants determined using LIFBASE.[21] Percent (relative) uncertainty was calculated from the standard deviation of 3 or more experimental trials. There is also uncertainty associated with the spectral fits themselves, namely 10% uncertainty with peak correlations ≥0.9 for all H_2O plasma fits and 15-30% uncertainty with peak correlations 0.7-0.85 for all H_2 plasma fits. Error was thus reported herein as the larger of the uncertainty values to indicate whether there was greater error dependence on experimental factors or spectral fits for temperatures under specific plasma conditions.

2.5. Gas sensing system and resistance measurements

A home-built gas sensing system was constructed to monitor and collect resistance data for testing gas sensor performance for a range of temperatures and gases. The glass sensing chamber was designed with a gas inlet and outlet port, two Rodaviss® joints to easily remove the heater and substrate as needed. It also contains two ports with septa for replacing Cu lead wires when necessary. Collectively, these features create a sealed system for measuring resistance data. Figure 6.4 (Chapter 6) shows the gas sensing system, whereby gas flow through the system was maintained at 15 sccm by a flowmeter (Dwyer Instruments Inc., RMA series). Additional description and images of the gas sensing chamber and sensing system are provided in Chapter 6.

Substrate temperature (T_S) was controlled by placing the substrates on an ULTRAMIC Advanced Ceramic Heater, type K thermocouple, power terminal exit on face, 25 x 50 mm. A PID temperature control system was used to regulate heater temperature. National Instruments LabVIEW SignalExpress software 2014 v2.5.1 was used to control the Tektronix DMM4040/4050 Digital Multimeter and record resistance measurements of the sensors during gas flow. 2-wire resistance measurements were collected by the multimeter through Cu leads connected to the sensors' Ag electrodes. Resistance was recorded at 25 °C and at T_S = 50 to 300 °C, in 50 °C intervals. Resistance was measured by increasing T_S and then maintaining T_S for ~10 min. Upon reaching 300 °C, T_S was then decreased and maintained at each T_S for ~10 min returning back to 25 °C.

Representative raw resistance data collected during an individual sensing experiment are shown in Figure 6.6 (Chapter 6), where each step is labeled with the corresponding T_S at which the resistance data were collected. Note that step shape is different when increasing than when decreasing T_S, with a sharp drop in resistance indicating a more instantaneous response to increases in T_S and a more gradual drop in resistance showing a slower response to decreases in T_S. Resistance data collected at each T_S were averaged for each trial, with error propagated through three trials (3 different nanomaterial sensing devices) for all plasma treatments and materials explored. Resistance was measured for gas sensors individually in air (Airgas) as a background response in addition to target gases carbon monoxide (99.8 ppm, air balance, Matheson) and benzene (94.3 ppm, air balance, Matheson). Specifically, sensor response is described as resistance in air (R_{air}) divided by resistance in gas of interest (R_{gas}) or (i.e. R_{air}/R_{gas}) and is used for direct comparison of materials treated with the same plasma modification conditions. $R_{air}/R_{gas} > 1$ indicates a reducing gas-surface interaction and $R_{air}/R_{gas} < 1$ indicates an

oxidizing gas-surface interaction. Given changes in reducing/oxidizing interactions of gases with SnO_2 surfaces as a result of plasma modification and nanomaterial morphology, sensitivity values are reported as the largest of R_{air}/R_{gas} (reducing interaction) or R_{gas}/R_{air} (oxidizing interaction). All response (R_{air}/R_{gas}) data presented herein are plotted on a log-linear scale as a function of temperature and applied power. The sensing design process is elaborated on further in Chapter 6.

REFERENCES

1. Stuckert, E. P.; Fisher, E. R. Ar/O_2 and H_2O Plasma Surface Modification of SnO_2 Nanomaterials to Increase Surface Oxidation. *Sens. Actuators B.* **2015**, *208* 379-388.
2. Stuckert, E. P.; Geiss, R. H.; Miller, C. J.; Fisher, E. R. In-Depth View of the Structure and Growth of SnO_2 Nanowires and Nanobrushes. *ACS Appl. Mater. Interfaces.* **2016**, *8* (34), 22345-22353.
3. Hitchman, M. L.; Jensen, K. F. *Chemical Vapor Deposition: Principles and Applications*. Academic Press London: 1993; Vol. 21.
4. Hernandez-Ramirez, F.; Tarancon, A.; Casals, O.; Arbiol, J.; Romano-Rodriguez, A.; Morante, J. High Response and Stability in CO and Humidity Measures Using a Single SnO_2 Nanowire. *Sens. Actuators B.* **2007**, *121* (1), 3-17.
5. Tougaard, S.; Jansson, C. Comparison of Validity and Consistency of Methods for Quantitative XPS Peak Analysis. *Surf. Interface Anal.* **1993**, *20* (13), 1013-1046.
6. Reiche, R.; Oswald, S. Monitoring Interface Interactions by XPS at Nanometric Tin Oxides Supported on Al_2O_3 and Sb_2O_x. *J. Phys. Chem. B.* **2004**, *108* 9905-9913.
7. Korotcenkov, G. Metal Oxides for Solid-State Gas Sensors: What Determines Our Choice? *Mater. Sci. Eng., B.* **2007**, *139* (1), 1-23.
8. Jeun, J. H.; Kim, D. H.; Hong, S. E. Synthesis of Porous SnO_2 Foams on SiO_2/Si Substrate by Electrochemical Deposition and Their Gas Sensing Properties. *Sens. Actuators B.* **2012**, *161* (1), 784-790.
9. Pan, J.; Ganesan, R.; Shen, H.; Mathur, S. Plasma-Modified SnO_2 Nanowires for Enhanced Gas Sensing. *J. Phys. Chem. C.* **2010**, *114* (18), 8245-8250.
10. Bogart, G.; Dalleska, N.; Fisher, E. R. Plasma Enhanced Chemical Vapor Deposition of SiO_2 Using Novel Alkoxysilane Precursors. *J. Vac. Sci. Technol., A.* **1995**, *13* (2), 476-480.
11. Mackie, N. M.; Dalleska, N.; Castner, D. G.; Fisher, E. R. Comparison of Pulsed and Continuous-Wave Deposition of Thin Films from Saturated Fluorocarbon/H_2 Inductively Coupled RF Plasmas. *Chem. Mater.* **1997**, *9* (1), 349-362.
12. Tompkins, B. D.; Fisher, E. R. Plasma Synthesis of Hydrocarbon/Fluorocarbon Thin Films with Compositional Gradients. *Plasma Process. Polym.* **2013**, *10* (9), 779-791.
13. Cuddy, M. F.; Fisher, E. R. Investigation of the Roles of Gas-Phase CF_2 Molecules and F Atoms During Fluorocarbon Plasma Processing of Si and ZrO_2 Substrates. *J. Appl. Phys.* **2010**, *108* (3).
14. Cuddy, M. F.; Fisher, E. R. Contributions of CF and CF_2 Species to Fluorocarbon Film Composition and Properties for C_xF_y Plasma-Enhanced Chemical Vapor Deposition. *ACS Appl. Mater. Interfaces.* **2012**, *4* (3), 1733-1741.
15. Stillahn, J. M.; Jianming, Z.; Fisher, E. R. Surface Interactions of SO_2 and Passivation Chemistry During Etching of Si and SiO_2 in SF_6/O_2 Plasmas. *J. Vac. Sci. Technol., A.* **2011**, *29* (1).
16. Donnelly, V. Plasma Electron Temperatures and Electron Energy Distributions Measured by Trace Rare Gases Optical Emission Spectroscopy. *J. Phys. D: Appl. Phys.* **2004**, *37* (19), R217-R236.
17. Tompkins, B. D.; Dennison, J. M.; Fisher, E. R. H_2O Plasma Modification of Track-Etched Polymer Membranes for Increased Wettability and Improved Performance. *J. Membr. Sci.* **2013**, *428* 576-588.

18. Morgan, M. M.; Cuddy, M. F.; Fisher, E. R. Gas-Phase Chemistry in Inductively Coupled Plasmas for NO Removal from Mixed Gas Systems. *J. Phys. Chem. A.* **2010**, *114* (4), 1722-1733.
19. Stillahn, J. M.; Fisher, E. R. CN Surface Interactions and Temperature-Dependent Film Growth During Plasma Deposition of Amorphous, Hydrogenated Carbon Nitride. *J. Phys. Chem. C.* **2009**, *113* (5), 1963-1971.
20. Luque, J.; Crosley, D. *LIFBASE: Database and Spectral Simulation*, v2.1.1; SRI International Report MP 99-009: 1999.
21. Bruggeman, P.; Iza, F.; Guns, P.; Lauwers, D.; Kong, M. G.; Gonzalvo, Y. A.; Leys, C.; Schram, D. C. Electronic Quenching of OH (A) by Water in Atmospheric Pressure Plasmas and its Influence on the Gas Temperature Determination by OH (A–X) Emission. *Plasma Sources Sci. Technol.* **2009**, *19* (1), 015016.

CHAPTER 3

IN-DEPTH VIEW OF THE STRUCTURE AND GROWTH OF SnO_2 NANOWIRES AND NANOBRUSHES

This chapter is based on the published work under the same title in *ACS Applied Materials & Interfaces*, written by Erin P. Stuckert, Roy H. Geiss, Christopher J. Miller, and Ellen R. Fisher.[1] The publication text and figures are reproduced here with permission from [Stuckert, E. P.; Geiss, R. H.; Miller, C. J.; Fisher, E. R. In-Depth View of the Structure and Growth of SnO_2 Nanowires and Nanobrushes. *ACS Appl. Mater. Interfaces.* **2016**, *8* 22345-22353.] Copyright [2016] American Chemical Society. Materials were grown by Erin and Chris; data collected by Roy; data analyzed and manuscript written by Erin, Roy, and Ellen. This chapter discusses the structure and growth by which SnO_2 nanowires and nanobrushes are formed via CVD. This will be achieved by utilizing a range of sensitive materials characterization techniques to confirm crystal structure and growth directions. Additional complementary techniques are used to elucidate morphology and surface chemistry for SnO_2 nanowires and nanobrushes. These studies emphasize the necessity of using a wide range of diffraction techniques in conjunction with surface analyses to elucidate structural variations in nanomaterials with slight differences in morphology and surface area. Specifically, the impact that small structural variations may impart on a material's performance in a given application will be discussed. Funding for this research was provided by the National Science Foundation (CHE-1152963).

3.1. Introduction

3.1.1. Motivation for complementary and comprehensive structural analysis. In the past two decades, nanomaterials have transitioned from the laboratory to numerous state-of-the-art gas sensing devices as the search for highly sensitive and selective sensors continues, as described in Chapter 1.[2-5] These materials exist in different dimensions (i.e., 1D, 2D), including a variety of morphologies (particles, rods/wires, brushes, etc.) and resulting bulk and surface properties, which may be further altered through modification techniques such as doping or plasma treatment. Given the vast array of material and modification parameters available, there are numerous methods by which materials properties can be altered, and ultimately affect/control sensor performance. To optimize sensor performance, it is essential to understand the underlying material structure that results in the properties that control sensing. Specifically, by understanding the structure corresponding to different nanomaterial morphologies we can begin to tailor materials through growth and modification parameters to achieve the necessary properties for sensitive and selective gas sensors.

As such, a variety of imaging and diffraction techniques have been used to analyze nanomaterial structure; however, many studies only employ one or two tools to confirm general structure and morphology, potentially omitting important detailed structural information and/or reporting results based on unreliable data.[6-9] In particular, there is a deficiency in structural characterization of nanomaterials of different morphology grown via the same process.[10] By fully evaluating the structure of such materials, we can better understand the mechanism by which the same growth process can create such different morphologies, and thus varied materials properties, with only slight changes in growth parameters.

Many of the nanomaterials of interest for device development are inorganic oxides, as detailed in Chapter 1. Consequently, numerous studies have presented structural data for this class of nanomaterials. Few, however, have utilized the full capabilities of all of the techniques currently available.[11-14] For example, SEM, TEM, STEM, and t-EBSD include a variety of imaging and electron diffraction techniques that all provide useful structural information (e.g., degree of crystallinity, crystal structure, crystallographic orientation, and lattice spacing).[15, 16] Electron diffraction techniques in TEM include CBED, NBED, and SAED, along with the more recent addition of 4D diffraction imaging in STEM (STEM-DI).[17, 18] These techniques are capable of providing various pieces of structural information (space group, strain, impurities, etc.), which yield details pertaining to overall material structure.[19-21] Through compilation of each of these experimental techniques in addition to computer modeling, a more complete understanding of material structure, growth process, and resulting morphologies arises.

3.1.2. Structural analysis of SnO_2 nanomaterials. As our work has focused on growth and modification of SnO_2 nanomaterials for gas sensor applications, our primary interests lie in characterizing the structure, probing structure-property-performance relationships, and ultimately determining growth mechanisms of SnO_2 nanowires and nanobrushes synthesized via CVD. To our knowledge, there has yet to be a comparative structural study of two different morphologies with the same base material that utilizes extensive imaging and diffraction techniques in the context of the same study. Indeed, comparative studies of different SnO_2 nanomaterial morphologies are quite limited.[10, 22, 23] Here, we briefly describe three of the arguably most complete studies that characterized SnO_2 nanomaterials, namely the works of Wang *et al.*,[24] Lupan *et al.*,[25] and Kelgenbaeva *et al.*[26] Wang and coworkers synthesized SnO_2 nano-pins via microwave plasma-enhanced CVD (PECVD). Resulting materials were analyzed by XRD,

which showed the nano-pins have the tetragonal rutile SnO_2 structure (a = b = 4.738 Å, c = 3.188 Å).[24] TEM/SAED and field emission SEM revealed the conditions under which the nano-pin structure was formed, resulting in pin and pin head with a growth direction of [001]. Based on these results, the authors provided potential reactions and a schematic to represent a probable vapor-liquid-solid (VLS) growth mechanism, wherein $SnCl_2 \cdot 2H_2O$ dissociates and ionizes to allow SnO to mix with Au sites upon which Sn and SnO_2 ultimately form nano-pins.

Lupan and coworkers synthesized tetragonal SnO_2 microtubes, confirmed by XRD and SAED,[25] where the distance between the (001) and (110) planes was reported and the growth direction confirmed to be along the [110]. SEM and TEM revealed no defects or dislocations in the microtubes. These data were then used to determine a series of reactions to propose a growth mechanism for the microtubes synthesized from $SnCl_2 \cdot 2H_2O$ and NH_4OH. The authors found that it was the hydrothermal reaction, $[Sn(OH)_6]^{2-} \longrightarrow SnO_2 + 2H_2O + 2OH^-$, that determined SnO_2 microtube growth.

Kelgenbaeva *et al*. created an impulse plasma by submerging Sn electrodes in water to synthesize Sn nanoparticles which were then annealed to form SnO_2 nanoparticles.[26] Analysis of XRD data showed Sn to be tetragonal and oriented along [200] with no peaks referencing Sn oxide. Using the Scherrer formula, the Sn nanoparticles were estimated to be 15 nm. Application of the Rietveld refinement allowed determination of structural parameters including space group, a, c, volume, density, and goodness of fit in comparison to the ICDD. Additionally, TEM was used to analyze material morphology and structure. The same analysis techniques were applied to SnO_2 nanoparticles, confirming tetragonal tin dioxide. Although similar data were presented for SnO_2, the structure was not described to the same extent as the Sn structure.

Moreover, this study did not suggest a potential growth mechanism for the Sn or SnO_2 nanoparticles created by the impulse plasma synthesis process.

These three studies utilized multiple imaging and diffraction techniques to determine structure to a greater degree and suggested new components for growth mechanisms than prior studies.[27-29] Despite this advancement, the studies employed diffraction modes that are often less sensitive to slight structural changes and are thus, less precise in determining material structure.[30, 31] Additionally, we have found only a handful of studies that have exploited t-EBSD in conjunction with TEM diffraction for analysis of a nanomaterial, despite the observation that t-EBSD can afford a larger sample view than TEM.[12] Notably, Hu *et al.*[32] reported the analysis of a variety of Zr-Nb-Sn-Fe alloys using electron energy loss spectroscopy, CBED, and t-EBSD; the latter two of which, along with STEM analysis, indicated the formation of hexagonal ZrO.

3.1.3. Implications of understanding structure and growth of SnO_2 nanomaterials. This study is one example of the utility of combining t-EBSD with other imaging and diffraction data to provide a more complete understanding of material structure and growth. We believe that to deduce the most representative growth mechanism and detailed structural information to relate the resulting properties and sensor performance, it is critical to comprehensively characterize a given nanomaterial via the application of a variety of techniques; this work represents such a study of SnO_2 nanomaterials.

3.2. Results and Discussion

As noted above, the information required to obtain comprehensive structural data for SnO_2 nanowires and nanobrushes includes the following: morphology, crystallinity, lattice spacing, crystal defects, specimen thickness, unit cell, crystal system, point group, space group,

growth face, and crystal structure. It is also important to determine if any of these features are altered as a function of experimental parameters. A study that determines as many of these facets as possible through complementary techniques will provide the most accurate structure of a material. Thus, we employed a variety of different imaging and diffraction techniques that allowed greater insight into the structure of these different SnO_2 morphologies grown via the same CVD process. Thereby, these data will allow for further understanding of structure-property-performance relationships for gas sensing applications.

3.2.1. Comparing nanowire and nanobrush morphology and relative surface area. The first step in comparing different SnO_2 nanomaterials requires analyzing the material morphology as it directly affects structure and properties. In particular, differences in morphology features and surface area of two SnO_2 nanomaterials can indicate vastly different sensitivity and selectivity capabilities when utilized in gas sensing applications.[2, 33, 34] SEM micrographs in Figure 3.1 show that as-deposited wires (grown at ~700 °C) and brushes (grown at ~625-650 °C) create interconnected networks over the surface of ZrO_2 substrates, with magnified images providing greater detail on individual wires and brushes. Interestingly, wires have diameters of 10-50 nm and lengths of a few microns, whereas brushes are significantly larger. The typical brush stem is 100 nm in diameter with bristles growing off of the stem, resulting in the overall brush diameter being 200-300 nm with lengths of 10-50 μm. The larger surface area of the brushes relative to the wires suggest these materials could have greater sensitivity in gas sensing applications.[35-37] The SEM micrographs show a particle on the end of the wires, indicative of nanomaterials grown via the VLS method.[38-42] This well-established method relies on Au nanoparticle diameter controlling nanomaterial diameter and length being controlled by changing the time of substrate exposure to the precursor during the CVD process. As wires and brushes

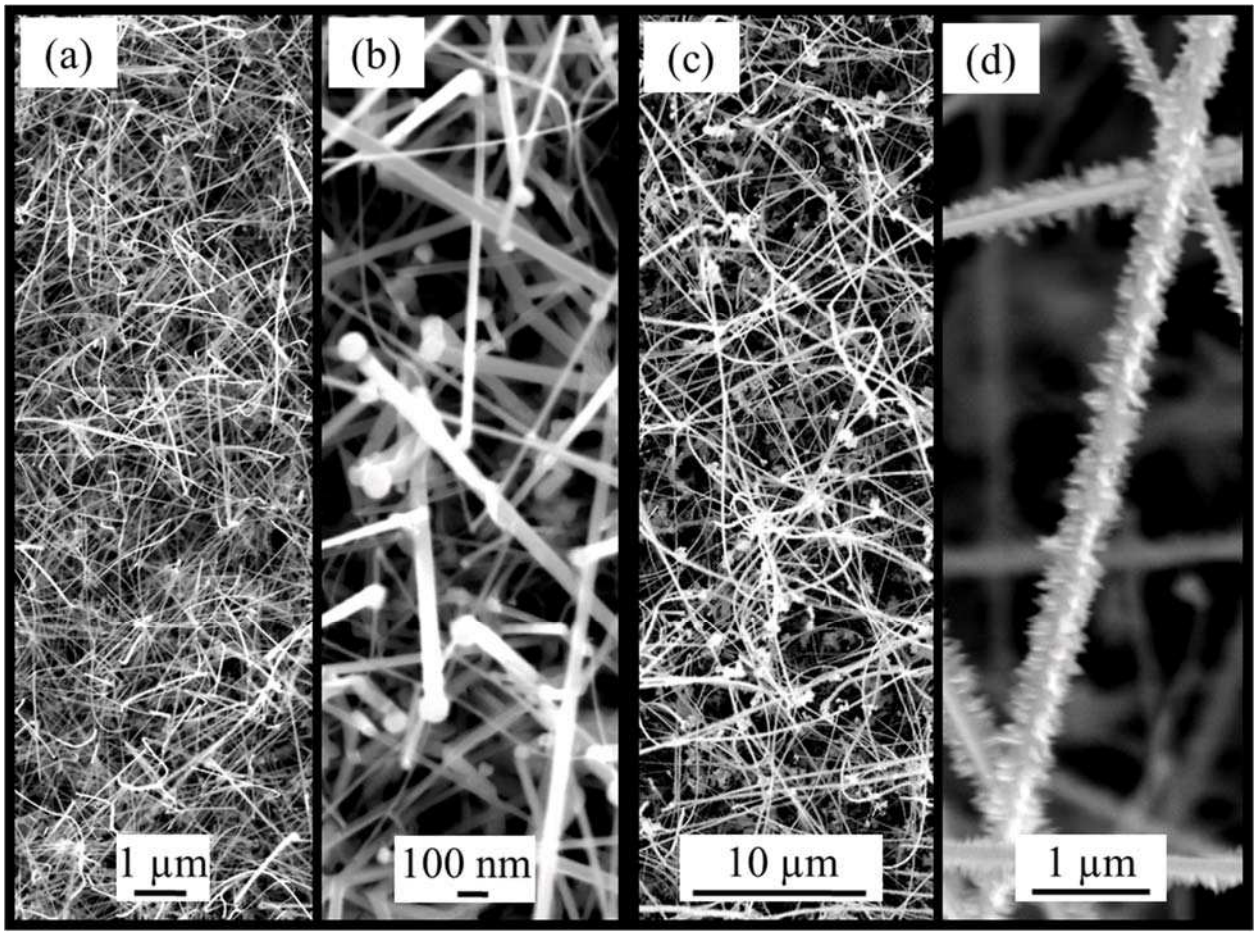

Figure 3.1. SEM images of CVD grown SnO_2 nanowires with magnification (a) 5,000X and (b) 30,000X; and nanobrushes with magnification (c) 1,700X and (d) 19,000X.

grow longer (i.e., over longer deposition times), they become more intertwined as the base can no longer support the growing wire or brush. Despite being intertwined, the wires and brushes maintain uniform diameters.

Information obtained from SEM data provides the foundation for developing insight into the growth for SnO_2 wires and brushes. We confirm that the precursor ($Sn(BuO^t)_4$) vaporizes under mild heating (45-55 °C), which allows it to react with liquefied Au particles in the CVD reactor once the eutectic temperature is reached.[43] As the Au-Sn-O mixture becomes saturated in the particle, SnO_2 begins to solidify and form the tin oxide nanomaterials shown in the SEM images, Figure 3.1. If the temperature of the Au-Sn-O mixture does not reach the eutectic temperature, however, variations in material morphology, structure, or a lack of growth entirely can result. This is likely the case for brush growth conditions, where an ill-defined end cap is observed instead of a uniform particle. The absence of Au particle caps in conjunction with the bristle structure and lower growth temperature of the brushes relative to that of the wires, confirm that the Au-Sn-O mixing is less efficient for brush growth than for wire growth. To determine if these morphological differences also resulted in structural differences (e.g., growth face, defects), however, further study using higher resolution imaging and diffraction was required.

3.2.2. Determining bulk or average nanomaterial crystallinity. Identification of bulk crystallinity was achieved using PXRD; patterns for SnO_2 nanowires (see Chapter 4 for additional characterization data) and nanobrushes are shown in Figure 3.2. The patterns consistently revealed the materials have the tetragonal SnO_2 structure. PXRD patterns, however, only reflect the average structure of the nanomaterials. To determine the details of wire and

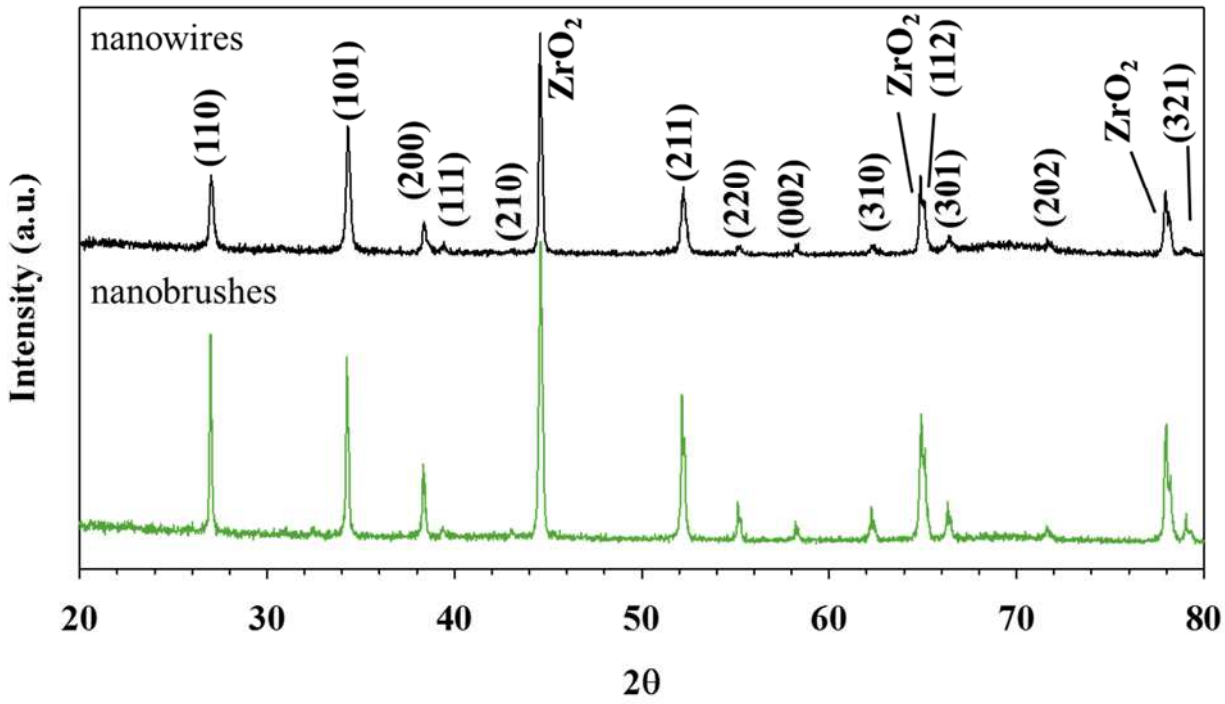

Figure 3.2. PXRD pattern of SnO_2 nanowires (top) and nanobrushes (bottom) on a ZrO_2 substrate with peaks labeled showing the tetragonal tin oxide structure and underlying ZrO_2.

brush imperfection and growth, we examined the crystalline properties of the individual wires and brushes using electron microscopy techniques including HRTEM, STEM-DI, and t-EBSD.

3.2.3. Using TEM to measure lattice spacings and determine zone axes. Initial HRTEM experiments used a single tilt holder to obtain lattice images from wires and brushes without any shifts in sample orientation–typically not oriented along a ZA, Figure 3.3 (representative images). Overall, the nanowires exhibit a growth direction wherein the crystal planes are parallel to the wire with lattice spacing of 2.4 Å, Figure 3.3 (b). The bristles on the brushes appear to be much lighter than the stem in the HRTEM image, Figure 3.3 (c), indicating they are likely thinner than the main brush stem. Interestingly, the growth plane remains the same from the main stem through the bristles, Figure 3.3 (d), with lattice spacing of 2.2 Å. The HRTEM images all show wires and brushes to be single crystal, devoid of defects. Although these images provide lattice spacings, determining growth direction of the wires and brushes is largely inconclusive using such images. Indeed, these images could even lead to false conclusions regarding growth direction because many possible orientations exist for any given lattice spacing.

To build upon the lattice spacing HRTEM images, we used a double tilt sample holder to orient individual wires and brushes to a ZA with only a few degrees of tilting around both the x- and y-axes. The alignment of a wire within a fraction of a degree along a ZA in the TEM is very time intensive, resulting in only a few wires and brushes being analyzed in this manner. Despite a limited sample population, structural results were consistent for wires and brushes for all samples analyzed in this HRTEM study. This is especially true as HRTEM images collected in a ZA orientation are crossed lattice images representative of the positions of columns of atoms in the sample. The wires had a <100> ZA and the brushes a <001> ZA as shown in the low-

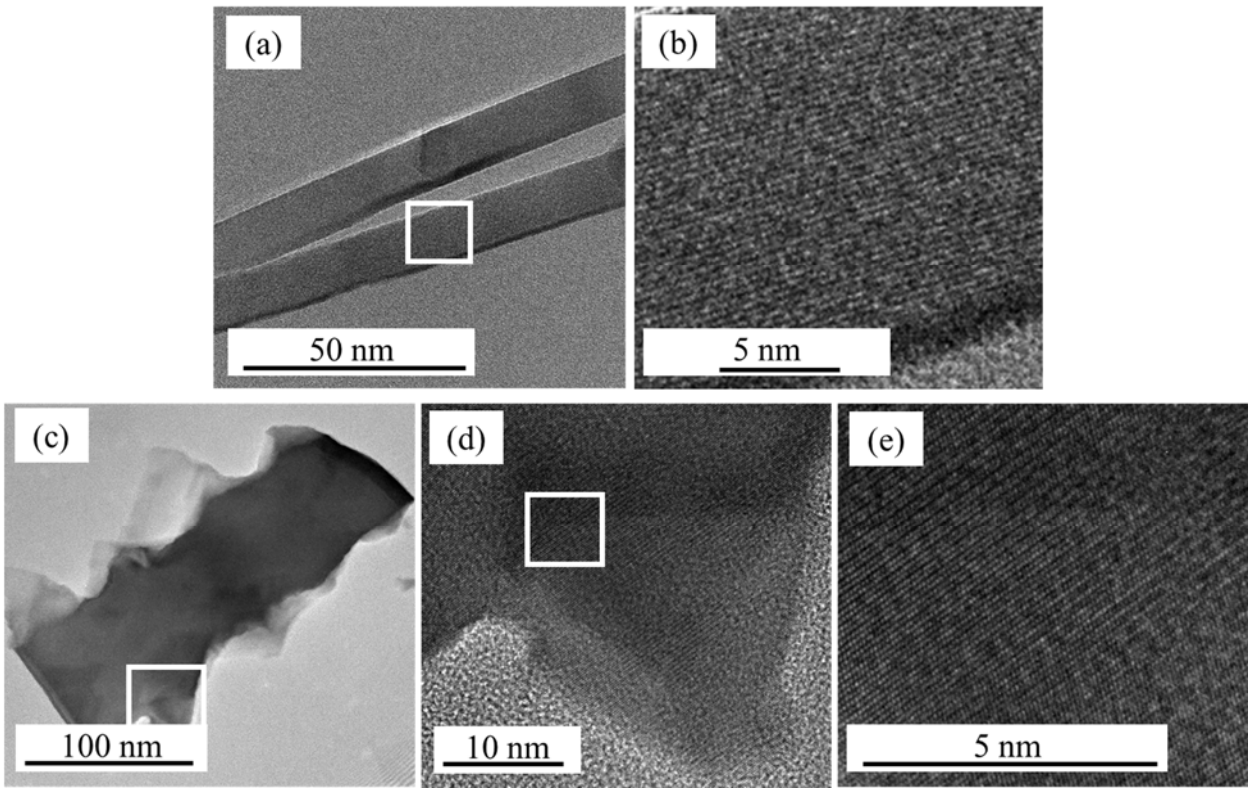

Figure 3.3. HRTEM images of lattice planes in SnO_2 nanowires (a, b) and nanobrushes (c-e), where (b) is a magnified image of the area highlighted in (a) and (d, e) are progressively magnified images of the areas highlighted by the boxes in (c) and (d), respectively.

magnification and high-resolution images in Figure 3.4. The different ZA for brushes compared to wires indicates the different morphologies grow with a different growth facet.

3.2.4. Customizing STEM diffraction and complementary simulations for determining nanowire and nanobrush growth faces. Further validation and identification of these growth faces came from employing a variety of TEM modes of diffraction that provided qualitative and quantitative information about material structure. Several studies have used TEM imaging and diffraction to determine lattice spacing and growth facets of SnO_2 nanomaterials, yet they do not report specific modes of diffraction used nor do they include analysis of greater structural detail the modes can provide.[27, 44-46] Here, we utilized STEM mode in TEM as it allows for collecting both imaging and diffraction data without needing to re-optimize the instrument and affords information on sub-nanometer regions. This concurrent information is unattainable using standard TEM mode but is essential for characterizing nanomaterials. Customizable STEM-DI, CBED, NBED, SAED, and t-EBSD were all used to provide structural detail on SnO_2 wires and brushes.

Traditionally, CBED provides quantitative data on specimen thickness, unit cell, crystal system, point group, and space group.[19, 47] Additionally, small changes in lattice parameter can be used to determine lattice strain and can also provide an indirect measure of material composition. We utilized a customizable form of STEM-DI that is essentially CBED with greater resolution near 2 mrads instead of the usual 10 mrads. STEM-DI data, Figure 3.5, were collected from the same wires and brushes used for HRTEM such that all STEM-DI data were collected in the ZA orientation. CrystalMaker and Single Crystal Diffraction software were used to simulate the orientation of the SnO_2 crystal that gave rise to the STEM-DI diffraction pattern and determined the growth direction along the wires to be the <201> and along the brushes to

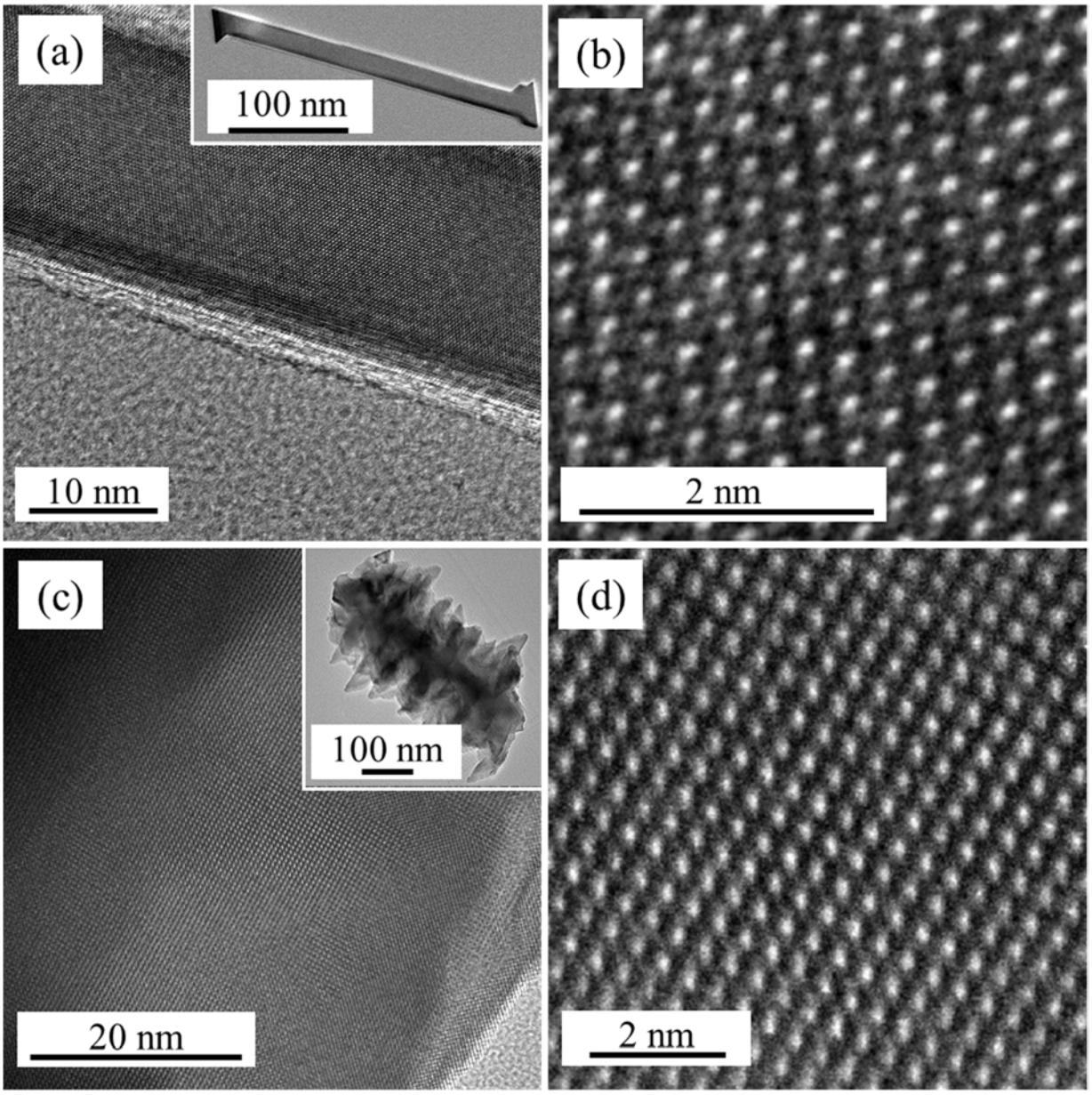

Figure 3.4. HRTEM crossed lattice images representative of atom columns in SnO_2 nanowires (a-b) and nanobrushes (c-d), where (a, c) show general morphology as insets and (b, d) are magnified images of (a, c) respectively.

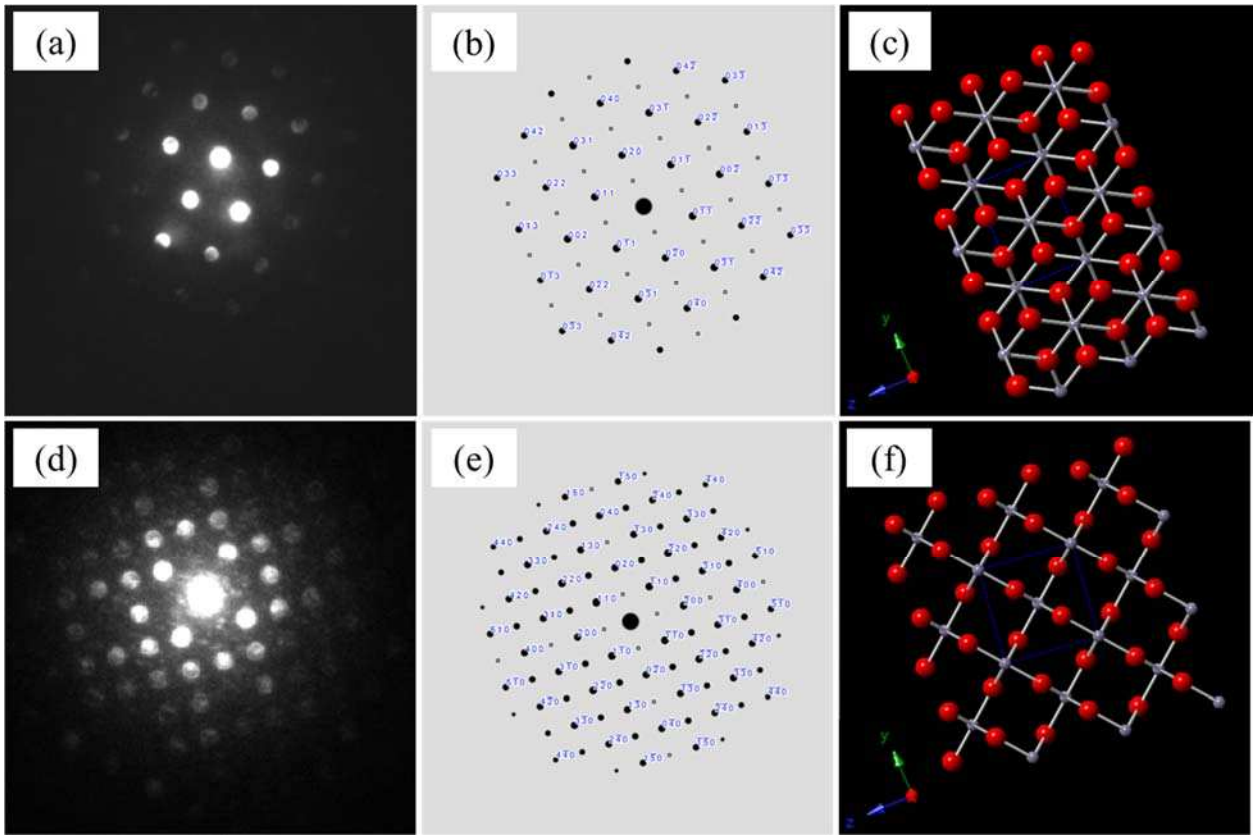

Figure 3.5. STEM-DI (CBED) diffraction patterns for SnO_2 (a) nanowires and (d) nanobrushes, with corresponding simulated diffraction patterns (b,e) and modeled structures (c, f) using Crystal Maker©.

the <010>. Further analysis of the diffraction patterns shows 6 Å and 4 Å spacing between spots in wire patterns and brush patterns, respectively. After optimizing the simulated pattern to match the experimental pattern, we also found a 32° rotation between the experimental HRTEM brush image and the resulting diffraction pattern. It is particularly noteworthy that the STEM-DI diffraction patterns had quasi-kinematical intensities even though the sample thickness is much greater than that supporting a kinematical approximation.[48] We believe that the diffraction patterns, Figure 3.5 (a, d), are quasi-kinematical as a result of the low convergence angle of the beam used for STEM-DI. The low angle results in minimal scattering instead of the typical dynamic scattering that would be expected of diffraction in a thicker sample using a larger convergence angle. These findings illustrate the benefits of using complimentary and tailored techniques in that our experimental design revealed hidden structural details in our nanomaterials and allowed for more direct comparison between experiment and simulation.

3.2.5. Expanding techniques for analyzing Kikuchi lines in STEM diffraction. Although not commonly utilized, CBED patterns may also be collected in a manner that allows for fitting Kikuchi lines. Studies that have presented CBED, as well as NBED and/or SAED patterns, rarely fit Kikuchi lines because it is a complex and time-intensive process.[6, 7, 9, 22, 47] We used EDAX software from t-EBSD to manually fit the Kikuchi lines in the brush CBED patterns, Figure 3.6, with and without indexing. The indexed patterns show a tetragonal structure, which remains in agreement with the results described above. Indexing Kikuchi lines in the higher resolution CBED patterns instead of those of t-EBSD patterns provides more accurate structural information as CBED is much more sensitive to changes in orientation (fractions of a mrad) than t-EBSD. Although there is limited knowledge on the reliability of the EDAX fits, we believe the results from this fitting method allow for direct comparison to other diffraction data, because the

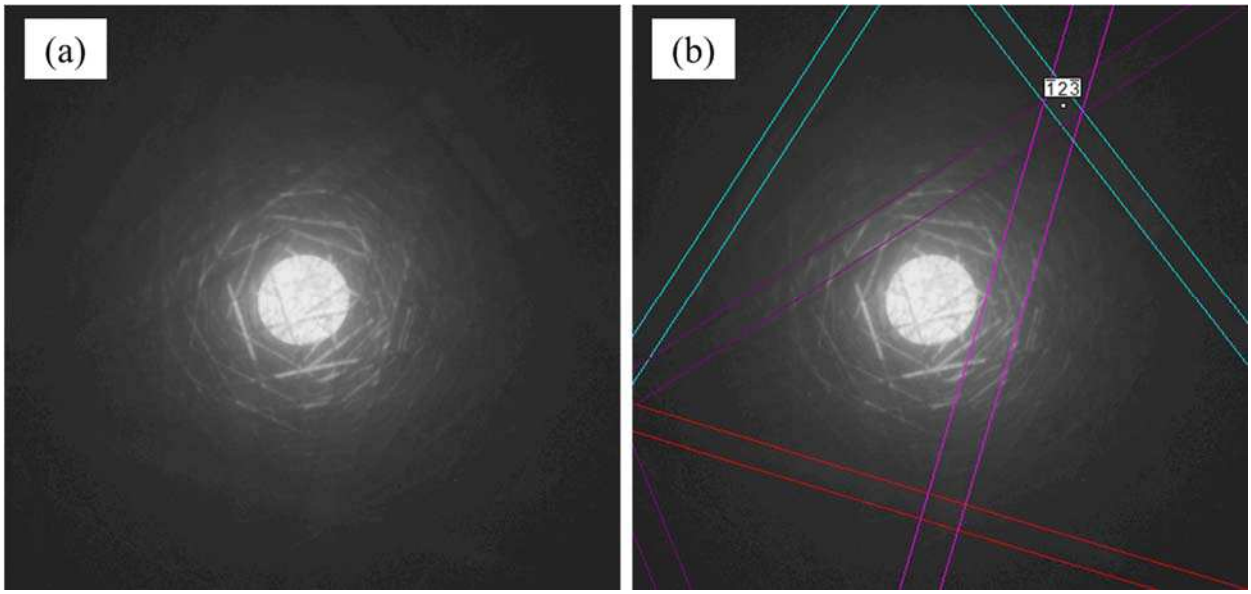

Figure 3.6. STEM-CBED pattern showing Kikuchi lines for nanobrushes (a) without indexing, and (b) with indexing using EDAX OIM analysis.

results of the EDAX fitting matched those of the simulations. Furthermore, fitting the Kikuchi lines can be more reliable than fitting spot patterns because CBED patterns showing Kikuchi lines also show the higher order laue zones that can be fit to reveal slight differences in orientation that may be lost in the context of spot patterns.

3.2.6. Complementary t-EBSD for reliably analyzing larger sample size. Although CBED data can provide greater detail than t-EBSD data, the latter is capable of analyzing a larger sample of wires or brushes more quickly than the tailored STEM-CBED collection methodology employed here allows.[49, 50] Furthermore, t-EBSD generates a color map displaying the sample orientation along three axes using an inverse pole figure (IPF) while simultaneously collecting diffraction patterns.[51, 52] Despite the exact axial orientations not being shown here, it is usually possible to approximate them from the IPF, especially given diffraction patterns can be collected simultaneously. Examples of typical t-EBSD data, with SEM images, colored orientation maps, IPFs, and cartoon simulations of the crystal orientation, are given in Figure 3.7 for a wire and two brush types. The most prevalent color in the maps and phase in the IPFs can be used to model the resulting tetragonal crystal structure for the wires and brushes, where a = b = 4.738 Å, c = 3.188 Å. These values are indicative of the rutile tetragonal SnO_2 structure for both morphologies. The resulting structures are supported by diffraction data collected simultaneously along each wire or brush.

Diffraction patterns collected at various points along wires and brushes were indexed, with a selection of representative patterns for wires and brushes shown in Figure 3.7 (d). t-EBSD patterns established wires and brushes are highly crystalline, with wires consistently indicating a <201> growth direction. In contrast, although most brushes had a <010> growth direction, some brush samples had a <722> growth direction. Closer inspection of the SEM

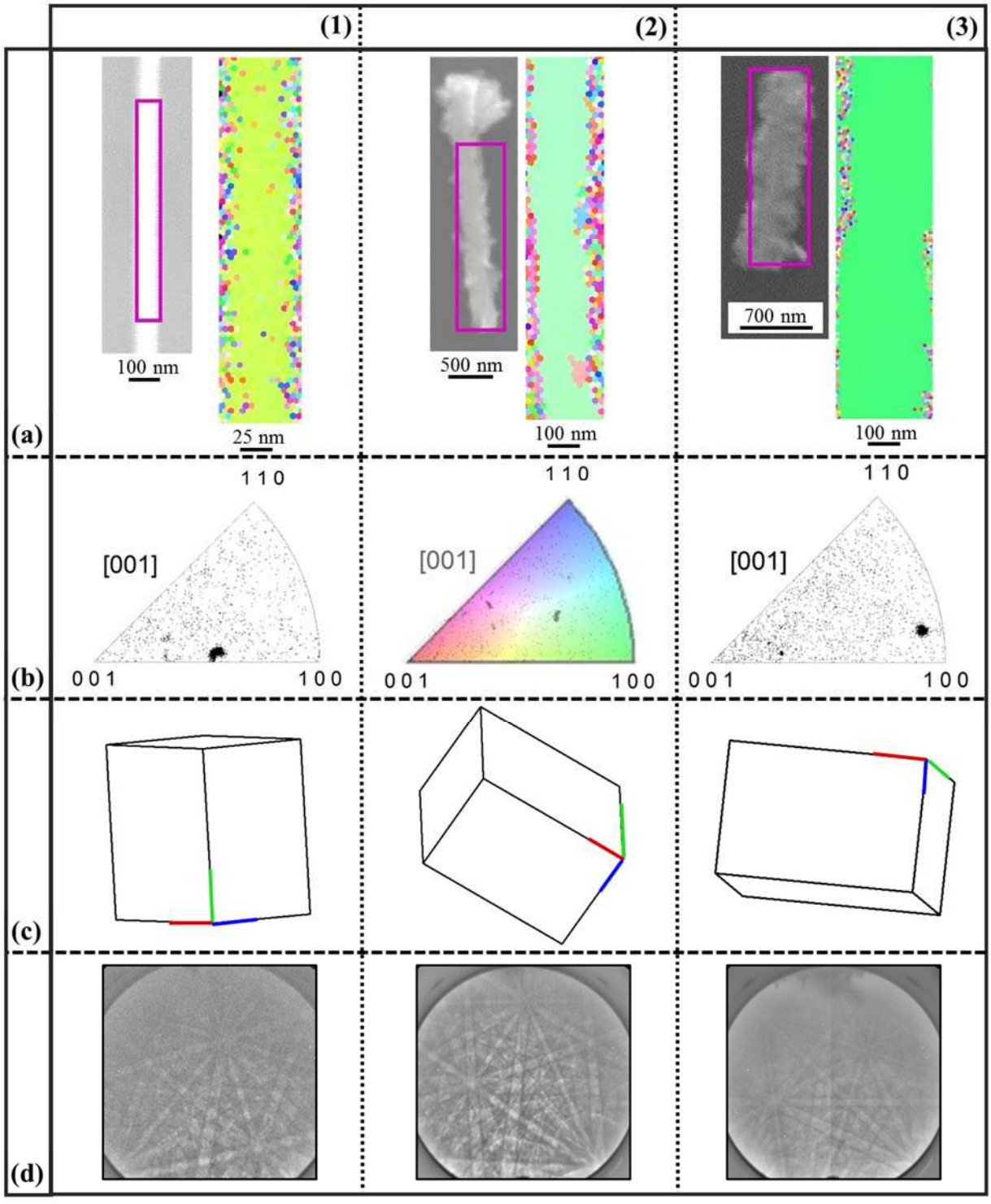

Figure 3.7. t-EBSD data for SnO_2 nanowires (1), low bristle density nanobrushes (2), and high bristle density nanobrushes (3). The data are as follows: (a) SEM images with scanned regions outlined and corresponding color maps; (b) IPFs with phase *probability*; (c) crystal shape determined from the t-EBSD analysis; and (d) diffraction patterns. The colored IPF overlaid in 2(b) is representative for the color maps on top.

images associated with the t-EBSD patterns revealed that deviations in brush growth direction were correlated with bristle density. Brushes with high bristle density, which were the type of brushes selected for study in the TEM, all had <010> growth directions as noted above, whereas those with low bristle density had a different growth direction, <722>, that more closely resembled the growth direction of the wires (<201>). The difference in structure between wires and brushes is also observed as facet rotation in the brush patterns relative to that of the wires. We believe this rotation in growth direction is a result of bristle density, which is controlled by growth temperature. As we have measured a temperature gradient in our reactor (see Section 2.1.1.), the different morphologies we obtained (including different bristle densities) are the result of substrates being placed in slightly different locations within the reactor. Given that at lower growth temperatures, the eutectic point of the Au-Sn-O mixture is less likely to be reached (affecting the Au-Sn-O mixing), growth at lower temperatures results in brushes and higher temperatures yield wires (as described above). The variation in bristle density demonstrates the importance of maintaining very specific temperatures should a certain morphology and/or crystal structure be desired. Notably, all of the t-EBSD data are consistent with the TEM and STEM-DI mapping information. More specifically, all data herein indicate the VLS synthesis method produces SnO_2 wires and brushes with high crystallinity in the rutile tetragonal structure, with lattice spacings and growth faces varying with morphology.

3.2.7. Potential for greater diffraction detail gained from additional STEM modes.

Additional STEM imaging and diffraction were collected in NBED and SAED modes, Figure 3.8 (a-d). These modes are not critical for evaluating the morphological and structural differences of our materials, as they provide limited additional information beyond what was attained through the previously discussed imaging and diffraction techniques. Both types of diffraction data can,

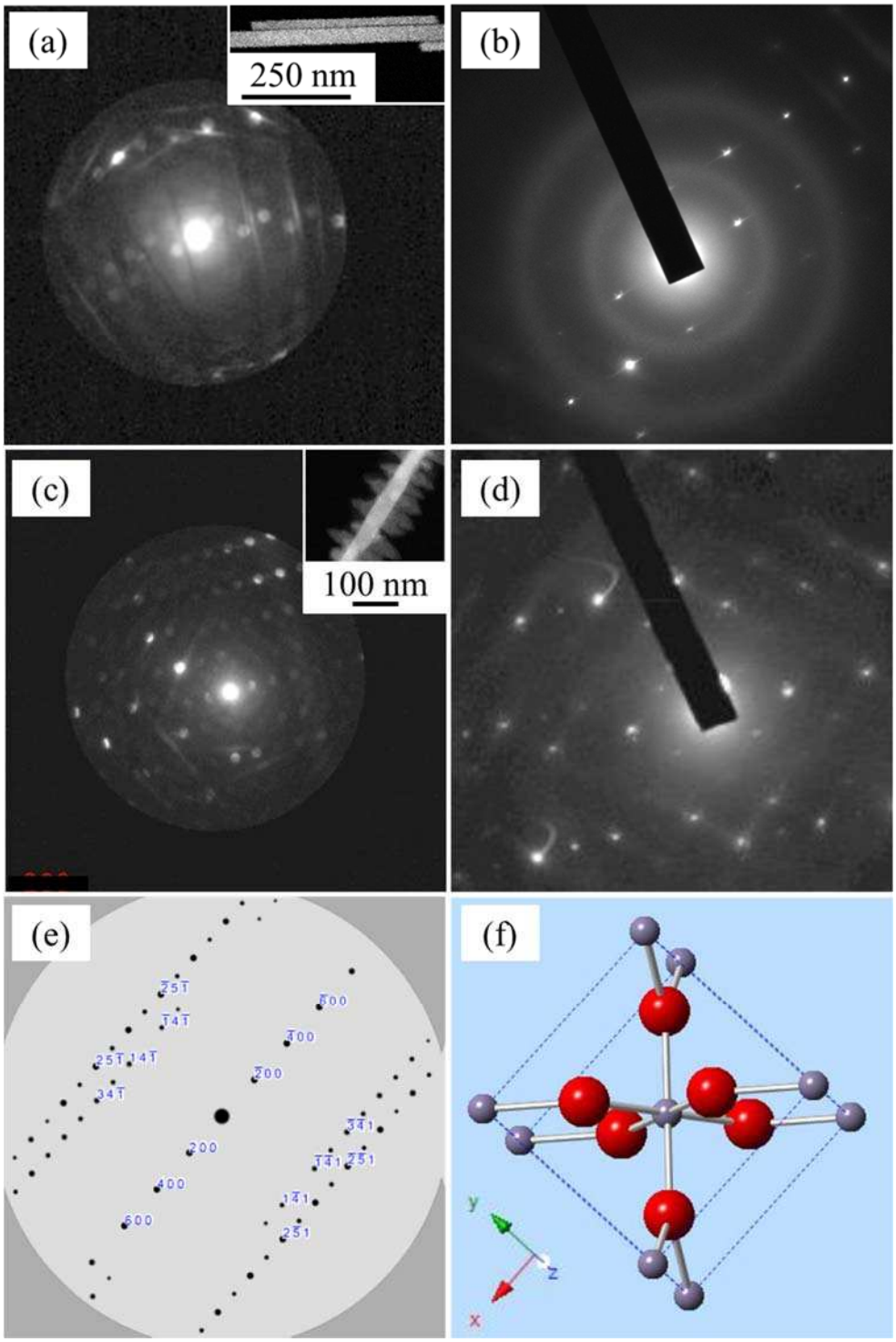

Figure 3.8. STEM imaging and diffraction for SnO_2 nanowires (a-b) and nanobrushes (c-f) derived from different techniques. STEM imaging (insets) in STEM-NBED patterns (a, c) and SAED patterns (b, d). Crystal Maker was used for simulating a diffraction pattern (e) to match the STEM-NBED pattern (c) and the corresponding simulated structure (f). The simulated pattern and structure have been rotated 32° to correct for the rotation between the brush NBED image and the experimental diffraction pattern.

however, provide insight into material structure—STEM-NBED spots can be monitored for position shifts to measure the strain in a material, whereas STEM-SAED is the classic method relating diffraction-contrast and specimen orientation in TEM images.[9, 22] The SAED patterns were collected off the ZA, providing minimal structural information, and so for greater detail, the samples were reanalyzed using CBED as described above. The NBED patterns do not show shifts in diffraction spots, indicating minimal to no strain in the wires and brushes. Further analysis of NBED data for brushes was completed through simulation by Crystal Maker, Figure 3.8 (e-f), where the SnO_2 tetragonal structure was simulated along the <001> ZA. The simulated pattern and corresponding structure were optimized to match the experimental NBED, producing simulated diffraction similar to experimental STEM-DI but with fewer points of diffraction. Those that were present in experimental and simulated NBED patterns match up with those observed in STEM-DI, in both plane and spacing. Unlike STEM-DI and CBED with a larger aperture, NBED and SAED less precisely determine the orientation of wires and brushes as a result of small changes in orientation often being lost in the spot patterns, which was further demonstrated by the NBED simulations. Additionally, when analyzing areas less than ~0.5 µm in diameter, it is critical to carefully interpret SAED patterns because the beam diameter is large relative to the crystalline feature dimensions. Additionally, SAED patterns have imprecise 2D crystallographic information as the Bragg conditions are relaxed for thin specimen and small grains within the specimen.[19, 20] Thus, it is important to carefully choose collection parameters to maximize pattern detail and assure accurate representation of the sample crystallinity (see Sections 2.2.4.-2.2.7. for more detail). Both NBED and SAED continue to support the high crystallinity and growth directions of the wires and brushes determined with our other analyses.

3.3. Summary and Conclusions

Through the comprehensive analysis created by the combined use of the techniques described in this work, we gained significant insight regarding the structure and growth of SnO_2 nanowire and nanobrush growth via CVD. Complementary PXRD, t-EBSD, and STEM-DI show both morphologies have a tetragonal rutile structure. SEM and HRTEM micrographs display SnO_2 nanowires grow out of Au nanoparticles and nanobrushes arise from ill-defined particles, indicating both materials' structures grow by the VLS method with different morphological features. t-EBSD and STEM (SAED, NBED, and customizable CBED) reveal that although wires and brushes have the same average SnO_2 structure, they have different zone axes (wires: <100>, brushes: <001>) and growth faces (wires: <201>, brushes: <010> and <722>) that were highly temperature-dependent. Slight structural variations all support the hypothesis that different growth temperatures result in preferential growth planes, thereby leading to the two broad categories of morphology (i.e., wires and brushes) and furthermore, that bristle density on nanobrushes can be controlled by only small variations in temperature. By using the collection of imaging and diffraction techniques described herein, we now have a more complete structural understanding of SnO_2 nanowires and nanobrushes.

3.3.1. Potential implications of structural variations on specific applications. As we deploy these nanomaterials in gas sensor devices, we can compare sensing capabilities with the structural information provided by this study to determine the optimum structural conditions for sensing under a given set of environmental conditions (i.e., detecting specific gases over specific temperature and relative humidity ranges). This optimization process becomes simpler when we also consider knowledge gained from additional characterization, such as SEM, PXRD, and XPS data described in Chapter 4 for UT and Ar/O_2 and $H_2O_{(v)}$ plasma-treated SnO_2 nanowires and

nanoparticles.[53] Specific performance testing for UT and Ar/O_2 and $H_2O_{(v)}$ plasma-treated SnO_2 nanoparticles and nanowires, Chapter 7, allows us to connect performance to the structural data described herein to better understand differences in sensing performance as a function of nanomaterial structure or as a function of plasma surface modification. Such structure-property-performance relationships will be further detailed in Chapters 7 and 8. Overall, the results presented in this chapter clearly demonstrate the benefits gained by using a broader range of analysis tools to create the most reliable understanding about a material's structure and growth.

REFERENCES

1. Stuckert, E. P.; Geiss, R. H.; Miller, C. J.; Fisher, E. R. In-Depth View of the Structure and Growth of SnO_2 Nanowires and Nanobrushes. *ACS Appl. Mater. Interfaces.* **2016**, *8* 22345-22353.
2. Donato, N.; Neri, G. Plasma Technologies in the Synthesis and Treatment of Nanostructured Metal Oxide Semiconductors for Gas Sensing: A Short Review. *Nanosci. Nanotechnol. Lett.* **2012**, *4* (3), 211-227.
3. Eranna, G.; Joshi, B. C.; Runthala, D. P.; Gupta, R. P. Oxide Materials for Development of Integrated Gas Sensors - A Comprehensive Review. *Crit. Rev. Solid State Mater. Sci.* **2004**, *29* 111-188.
4. Kwon, Y. J.; Kang, S. Y.; Wu, P.; Peng, Y.; Kim, S. S.; Kim, H. W. Selective Improvement of NO_2 Gas Sensing Behavior in SnO_2 Nanowires by Ion-Beam Irradiation. *ACS Appl. Mater. Interfaces.* **2016**, *8* (21), 13646-13658.
5. Maeng, S.; Kim, S. W.; Lee, D. H.; Moon, S. E.; Kim, K. C.; Maiti, A. SnO_2 Nanoslab as NO_2 Sensor: Identification of the NO_2 Sensing Mechanism on a SnO_2 Surface. *ACS Appl. Mater. Interfaces.* **2014**, *6* (1), 357-363.
6. Häusler, I.; Atkins, R.; Falmbigl, M.; Rudin, S. P.; Neumann, W.; Johnson, D. C. Insights from STEM and NBED Studies into the Local Structure and Growth Mechanism of Misfit Layered Compounds Prepared Using Modulated Reactants. *Z. Kristallogr.* **2015**, *230* (1), 45-54.
7. Li, J.; Lamberti, A.; Domenicucci, A.; Gignac, L.; Utomo, H.; Luo, Z.; Rovedo, N.; Fang, S.; Ng, H.; Holt, J. R. Channel Strain Characterization in Embedded SiGe by Nano-Beam Diffraction. *ECS Trans.* **2008**, *16* (10), 545-549.
8. Clement, L.; Cacho, F.; Pantel, R.; Rouviere, J.-L. Quantitative Evaluation of Process Induced Strain in MOS Transistors by Convergent Beam Electron Diffraction. *Micron.* **2009**, *40* (8), 886-893.
9. Uesugi, F.; Hokazono, A.; Takeno, S. Evaluation of Two-Dimensional Strain Distribution by STEM/NBD. *Ultramicroscopy.* **2011**, *111* (8), 995-998.
10. Qu, D.; Yan, P.; Chang, J.; Yan, D.; Liu, J.; Yue, G.; Zhuo, R.; Feng, H. Nanowires and Nanowire–Nanosheet Junctions of SnO_2 Nanostructures. *Mater. Lett.* **2007**, *61* (11), 2255-2258.
11. Neogy, S.; Savalia, R.; Tewari, R.; Srivastava, D.; Dey, G. Transmission Electron Microscopy of Nanomaterials. *Indian J. Pure Appl. Phys.* **2006**, *44* (2), 119-124.
12. Seyring, M.; Song, X.; Rettenmayr, M. Orientation and Phase Analysis of Nanoscale Grains Using Transmission Electron Microscopy. *Pract. Metallogr.* **2012**, *49* (10), 623-632.
13. Morkoç, H. Comprehensive Characterization of Hydride VPE Grown GaN Layers and Templates. *Mater. Sci. Eng., R.* **2001**, *33* (5), 135-207.
14. Chandra, R.; Taneja, P.; John, J.; Ayyub, P.; Dey, G.; Kulshreshtha, S. Synthesis and TEM Study of Nanoparticles and Nanocrystalline Thin Films of Silver by High Pressure Sputtering. *Nanostruct. Mater.* **1999**, *11* (8), 1171-1179.
15. Wang, Y.; Xia, H.; Lu, L.; Lin, J. Excellent Performance in Lithium-Ion Battery Anodes: Rational Synthesis of $Co(CO_3)_{0.5}(OH)0.11H_2O$ Nanobelt Array and Its Conversion into Mesoporous and Single-Crystal Co_3O_4. *ACS Nano.* **2010**, *4* (3), 1425-1432.

16. Tang, J.; Wang, C.-Y.; Hung, M.-H.; Jiang, X.; Chang, L.-T.; He, L.; Liu, P.-H.; Yang, H.-J.; Tuan, H.-Y.; Chen, L.-J. Ferromagnetic Germanide in Ge Nanowire Transistors for Spintronics Application. *ACS Nano.* **2012**, *6* (6), 5710-5717.
17. Mertens, J. C. E.; Kirubanandham, A.; Chawla, N. Electromigration Mechanisms in Sn-0.7Cu/Cu Couples by Four Dimensional (4D) X-ray Microtomography and Electron Backscatter Diffraction (EBSD). *Acta Mater.* **2016**, *102* 220-230.
18. Yurtsever, A.; Baskin, J. S.; Zewail, A. H. Entabled Nanoparticles: Discovery by Visualization in 4D Electron Microscopy. *Nano Lett.* **2012**, *12* 5027-5032.
19. Williams, D. B.; Carter, C. B. *The Transmission Electron Microscope*. Springer: US, 1996.
20. Williams, D. B.; Carter, C. B. Transmission Electron Microscopy: A Textbook for Materials Science. *Micron.* **1997**, *28* (1).
21. Cheng, C.; Liu, B.; Yang, H.; Zhou, W.; Sun, L.; Chen, R.; Yu, S. F.; Zhang, J.; Gong, H.; Sun, H. Hierarchical Assembly of ZnO Nanostructures on SnO_2 Backbone Nanowires: Low-Temperature Hydrothermal Preparation and Optical Properties. *ACS Nano.* **2009**, *3* (10), 3069-3076.
22. Béché, A.; Rouvière, J.; Barnes, J.; Cooper, D. Strain Measurement at the Nanoscale: Comparison Between Convergent Beam Electron Diffraction, Nano-Beam Electron Diffraction, High Resolution Imaging and Dark Field Electron Holography. *Ultramicroscopy.* **2013**, *131* 10-23.
23. Thanachayanont, C.; Yordsri, V.; Boothroyd, C. Microstructural Investigation and SnO Nanodefects in Spray-Pyrolyzed SnO_2 Thin Films. *Mater. Lett.* **2011**, *65* (17), 2610-2613.
24. Wang, C.-Y.; Chen, T.-W.; Lin, C.-C.; Hsieh, W.-J.; Chang, K.-L.; Shih, H. C. Synthesis, Characterization and Cathodoluminescence of Nanostructured SnO_2 Using Microwave Plasma Enhanced CVD. *J. Phys. D: Appl. Phys.* **2007**, *40* (9), 2787-2791.
25. Lupan, O.; Chow, L.; Chai, G.; Heinrich, H.; Park, S.; Schulte, A. Growth of Tetragonal SnO_2 Microcubes and Their Characterization. *J. Cryst. Growth.* **2008**, *311* (1), 152-155.
26. Kelgenbaeva, Z.; Omurzak, E.; Ihara, H.; Iwamoto, C.; Sulaimankulova, S.; Mashimo, T. Sn and SnO_2 Nanoparticles by Pulsed Plasma in Liquid: Synthesis, Characterization and Applications. *Phys. Status Solidi A.* **2015**, *212* (12), 2951-2957.
27. Liu, C.; Zu, X.; Wei, Q.; Wang, L. Fabrication and Characterization of Wire-Like SnO_2. *J. Phys. D: Appl. Phys.* **2006**, *39* (12), 2494-2497.
28. Li, Y.; Xu, G.; Zhu, Y.; Ma, X.; Cheng, H. SnO_2/In_2O_3 One-Dimensional Nano-Core–Shell Structures: Synthesis, Characterization and Photoluminescence Properties. *Solid State Commun.* **2007**, *142* (8), 441-444.
29. Zhou, H.; Li, Z.; Niu, X.; Xia, X.; Wei, Q. The Enhanced Gas-Sensing and Photocatalytic Performance of Hollow and Hollow Core–Shell SnO_2-Based Nanofibers Induced by the Kirkendall Effect. *Ceram. Int.* **2016**, *42* (1), 1817-1826.
30. Wilkinson, A. J. A New Method for Determining Small Misorientations from Electron Back Scatter Diffraction Patterns. *Scr. Mater.* **2001**, *44* 2379-2385.
31. Wilkinson, A. J.; Hirsch, P. B. Electron Diffraction Based Techniques in Scanning Electron Microscopy of Bulk Materials. *Micron.* **1997**, *28* (4), 279-308.
32. Hu, J.; Garner, A.; Ni, N.; Gholinia, A.; Nicholls, R. J.; Lozano-Perez, S.; Frankel, P.; Preuss, M.; Grovenor, C. R. Identifying Suboxide Grains at the Metal–Oxide Interface of

a Corroded Zr–1.0% Nb Alloy Using (S)TEM, Transmission-EBSD and EELS. *Micron.* **2015**, *69* 35-42.
33. Kim, H. W.; Choi, S.-W.; Katoch, A.; Kim, S. S. Enhanced Sensing Performances of Networked SnO_2 Nanowires by Surface Modification with Atmospheric Pressure Ar–O_2 Plasma. *Sens. Actuators B.* **2013**, *177* 654-658.
34. Mathur, S.; Ganesan, R.; Ruegamer, T.; Shen, H.; Barth, S. Plasma Assisted Modulation of Morphology and Composition in Tin Oxide Nanostructures for Sensing Applications. *Adv. Eng. Mater.* **2007**, *9* (8), 658-663.
35. Liu, Y.; Jiao, Y.; Zhang, Z.; Qu, F.; Umar, A.; Wu, X. Hierarchical SnO_2 Nanostructures Made of Intermingled Ultrathin Nanosheets for Environmental Remediation, Smart Gas Sensor, and Supercapacitor Applications. *ACS Appl. Mater. Interfaces.* **2014**, *6* (3), 2174-2184.
36. Guo, J.; Zhang, J.; Ju, D.; Xu, H.; Cao, B. Three-Dimensional SnO_2 Microstructures Assembled by Porous Nanosheets and Their Superior Performance for Gas Sensing. *Powder Technol.* **2013**, *250* 40-45.
37. Zhou, Q.; Chen, W.; Li, J.; Tang, C.; Zhang, H. Nanosheet-Assembled Flower-Like SnO_2 Hierarchical Structures with Enhanced Gas-Sensing Performance. *Mater. Lett.* **2015**, *161* 499-502.
38. Kumar, R. R.; Parmar, M.; Rao, K. N.; Rajanna, K.; Phani, A. Novel Low-Temperature Growth of SnO_2 Nanowires and Their Gas-Sensing Properties. *Scr. Mater.* **2013**, *68* (6), 408-411.
39. Bonu, V.; Das, A.; Prasad, A. K.; Krishna, N. G.; Dhara, S.; Tyagi, A. Influence of In-Plane and Bridging Oxygen Vacancies of SnO_2 Nanostructures on CH_4 Sensing at Low Operating Temperatures. *Appl. Phys. Lett.* **2014**, *105* (24), 243102.
40. Chen, Y.; Cui, X.; Zhang, K.; Pan, D.; Zhang, S.; Wang, B.; Hou, J. Bulk-Quantity Synthesis and Self-Catalytic VLS Growth of SnO_2 Nanowires by Lower-Temperature Evaporation. *Chem. Phys. Lett.* **2003**, *369* (1), 16-20.
41. Givargizov, E. Fundamental Aspects of VLS Growth. *J. Crystal Growth.* **1975**, *31* 20-30.
42. Golovin, A.; Davis, S.; Voorhees, P. Step-Flow Growth of a Nanowire in the Vapor-Liquid-Solid and Vapor-Solid-Solid Processes. *J. Appl. Phys.* **2008**, *104* (7), 074301.
43. Muller, R.; Hernandez-Ramirez, F.; Shen, H.; Du, H. C.; Mader, W.; Mathur, S. Influence of Precursor Chemistry on Morphology and Composition of CVD-Grown SnO_2 Nanowires. *Chem. Mat.* **2012**, *24* (21), 4028-4035.
44. Tripathi, A.; Shukla, R. Structural, Optical and Photoluminescence Study of Nanocrystalline SnO_2 Thin Films Deposited by Spray Pyrolysis. *Bull. Mater. Sci.* **2014**, *37* (3), 417-423.
45. Johari, A.; Srivastav, S.; Sharma, M.; Bhatnagar, M. C. Synthesis and Room-Temperature Ferromagnetism of Pure and Cu-Doped SnO_2 Nanowires Grown by Thermal Evaporation. *J. Magn. Magn. Mater.* **2014**, *362* 1-6.
46. Kamiuchi, N.; Muroyama, H.; Matsui, T.; Kikuchi, R.; Eguchi, K. Nano-Structural Changes of SnO_2-Supported Palladium Catalysts by Redox Treatments. *Appl. Catal. A.* **2010**, *379* (1), 148-154.
47. Tomokiyo, Y. Applications of Convergent Beam Electron Diffraction to Extract Quantitative Information in Materials Science. *J. Electron Microsc.* **1992**, *41* (6), 403-413.

48. Moeck, P. Structural Identification of Cubic Iron-Oxide Nanocrystal Mixtures: X-ray Powder Diffraction Versus Quasi-Kinematic Transmission Electron Microscopy. *Suppl. Proc. of TMS 137th Annual Meeting & Exhibition, Materials Processing and Properties.* **2008**, *1* pp. 25-32.
49. Keller, R.; Geiss, R. Transmission EBSD from 10 nm Domains in a Scanning Electron Microscope. *J. Microsc.* **2012**, *245* (3), 245-251.
50. Suzuki, S. Features of Transmission EBSD and Its Application. *JOM.* **2013**, *65* (9), 1254-1263.
51. Randle, V. Application of Electron Backscatter Diffraction to Grain Boundary Characterisation. *Internat. Mater. Rev.* **2004**, *49* (1), 1-11.
52. Gourgues-Lorenzon, A.-F. Application of Electron Backscatter Diffraction to the Study of Phase Transformations. *Internat. Mater. Rev.* **2007**, *52* (2), 65-128.
53. Stuckert, E. P.; Fisher, E. R. Ar/O_2 and H_2O Plasma Surface Modification of SnO_2 Nanomaterials to Increase Surface Oxidation. *Sens. Actuators B.* **2015**, *208* 379-388.

CHAPTER 4

Ar/O_2 AND $H_2O_{(v)}$ PLASMA SURFACE MODIFICATION OF SnO_2 NANOWIRES AND NANOPARTICLES TO INCREASE SURFACE OXIDATION

This chapter is based on published work under a similar title in *Sensors and Actuators B: Chemical* written by Erin P. Stuckert and Ellen R. Fisher.[1] The publication text, figures, and tables are reproduced here from *Sensors and Actuators B: Chemical* Volume 208, Erin P. Stuckert and Ellen R. Fisher, Ar/O_2 and H_2O Plasma Surface Modification of SnO_2 Nanomaterials to Increase Surface Oxidation, p. 379-388, 2015, with permission from Elsevier. This chapter discusses the effects of Ar/O_2 and $H_2O_{(v)}$ plasma modification of SnO_2 nanoparticles and nanowires observed via surface and bulk materials properties measurements pre- and post-plasma treatment. These plasma precursor systems were chosen as they are common oxidizing systems known for increasing surface oxidation and thereby enhancing sensor sensitivity. Different architectures are examined herein to determine if material morphology has an impact on the resulting plasma treatment. Materials properties resulting from plasma treatments are also placed in context of potential gas sensing applications. Funding for this research was provided by the National Science Foundation (CHE-1152963).

4.1. Introduction

4.1.1. Necessity for sensitive and selective gas sensors. Gas sensors have been used in homes, schools, and workplaces for decades to provide early warning of dangerous gases to human health and well-being. New material and technique research and development to improve sensitivity, selectivity, and other sensor features has spanned the same time period. Sensors have been fabricated from a wide range of materials (e.g., metal oxides, polymers, carbon nanotubes,

etc.) with varied properties (e.g., electrical, optical, acoustic, etc.).[2-5] Metal oxide semiconductors (MOS), specifically SnO_2, have risen to the forefront as some of the most promising sensor materials. Detectors have been created in many different forms from thin films to nanowires, often utilizing dopants (e.g., Pd, Pt) to further enhance sensor performance.[6-9] Despite efforts to improve sensitivity and selectivity of sensors operating at room temperature, limitations persist for many gas detectors. A method of material modification that can alter materials beyond altering surface area or including metal dopants is plasma modification. As described in Chapter 1, plasmas have an expansive parameter space, enabling us to maintain desirable bulk properties (i.e., conductivity) while tuning surface chemistry (i.e., functionalization) to achieve increased sensitivity and selectivity.

4.1.2. Plasma modification of sensor materials. Although plasmas are routinely used in the semiconductor industry, often for etching applications, it is only within the past decade that interest in plasma treatment of sensor materials has increased significantly.[10-12] In particular, Ar/O_2, H_2, O_2, and N_2 plasmas have been used to modify SnO_2 materials.[13, 14] Much work centers on Ar/O_2 plasma surface modification of SnO_2 nanomaterials for gas sensing.[14-17] Pan *et al.*[14] treated SnO_2 nanowires with Ar/O_2 plasmas (1:1, P = 10-80 W for 4 min), creating a sensor that showed increased sensitivity to ethanol gas. Tin reduction was observed on nanowire surfaces at the maximum P treatment leading to decreased sensitivity. Mathur *et al.*[17] also modified SnO_2 nanoplates with Ar/O_2 plasmas (3:1, P = 25-125 W for 3 min), where treated SnO_2 nanoplates showed similar increases in ethanol sensitivity relative to nanowires treated at low P. For higher power treatments, however, changes in morphology from nanoplates to nanoglobular particles were observed as a result of tin reduction throughout the nanoplates.

Although there are limited studies on alternative plasma modification systems, such as H_2, O_2, and N_2 plasmas, these systems exhibit a similar etching effect as Ar/O_2 plasma has on SnO_2.[13, 18] Such studies barely approach the utility of plasma surface modification, whereby the limited plasma parameters and materials explored leave room for further investigation and optimization of plasma surface modification strategies. H_2O vapor plasma is a nominally etching plasma containing oxygen that has not, to our knowledge, been used for treatment of SnO_2 nanomaterials. In a related study, however, Tarlov *et al.*[19, 20] examined the effect of using extremely low power H_2O plasmas (P = 1-5 W, 10-15 min) to remove surface carbon from SnO_2 films. Interestingly, they found that the H_2O plasma generally oxidized the surface of annealed SnO_2 films, converting Sn^{2+} to Sn^{4+} at the surface. In the same work, the authors demonstrated that annealing H_2O plasma treated SnO_2 films resulted in formation of oxygen vacancies and that Ar^+ bombardment of the SnO_2 film served to reduce the Sn at the surface. Tarlov *et al.* did not explore higher power plasmas, as their major goal with the H_2O plasma treatment was to remove adventitious carbon while still preserving the hydroxylated surface of the SnO_2 films.

4.1.3. Enhancing surface oxidation of SnO_2 nanomaterials. With the study described in this chapter, we sought to explore whether water plasma treatments would hydroxylate nanostructured SnO_2 materials similarly to the work of Tarlov *et al.* with thin films and if such treatments would provide an improved platform for ultimately creating more sensitive SnO_2 gas sensors. The H_2O plasma system is also a good comparison system for the Ar/O_2 plasma as it should add oxygen to the SnO_2 surface but may have milder etching/oxidizing behavior.[19-21] Thus, both SnO_2 nanoparticles and nanowires were plasma treated with Ar/O_2 and H_2O plasma systems to compare their effects on surface composition, morphology, and bulk crystallinity of SnO_2 materials with different morphologies and surface areas. Furthermore, to address the lack

of materials characterization often observed when plasmas are used to treat sensor materials, this study puts forth additional materials characterization pre- and post-plasma treatment that builds on the structural investigation in Chapter 3. The compilation of these studies aid in comprehensive materials analysis for understanding structure-property-performance relationships as these materials are deployed in sensing devices.

4.2. Results

4.2.1. Exploring untreated nanomaterial morphology. Initial morphology studies using SEM analysis provide information on relative sizes of SnO_2 nanoparticles, Figure 4.1 (a), and nanowires, Figure 4.1 (b-c), on ZrO_2 substrates. Note that additional SEM images can be found in Chapter 3, Figure 3.1 for further comparison. Nanoparticle diameters range from 10-50 nm with many on the smaller end of that range, and SnO_2 nanowires (the same as described in Chapter 3) have diameters ranging 10-50 nm averaging around 20 nm with lengths of several microns. Throughout the CVD process, color changes were observed on the substrate surface indicative of SnO_2 deposition. A detail of CVD growth not described in Chapter 3 is the color change observed throughout the deposition process. Figure 4.1 (d) shows the substrate color change from gold to green to blue-purple as a ZrO_2 wafer is sputtered and annealed with Au and undergoes SnO_2 nanowire growth. For comparison, a photograph of SnO_2 nanoparticles on a ZrO_2 wafer is also shown in Figure 4.1 (d).

4.2.2. Comparing structure and surface chemistry of nanowires and nanoparticles. As a material's gas sensing capabilities are largely dependent on both bulk and surface properties, UT nanoparticles and nanowires were analyzed for comparison with plasma treated nanomaterials. PXRD was used to analyze bulk crystallinity as resistance measurements for any sensing devices

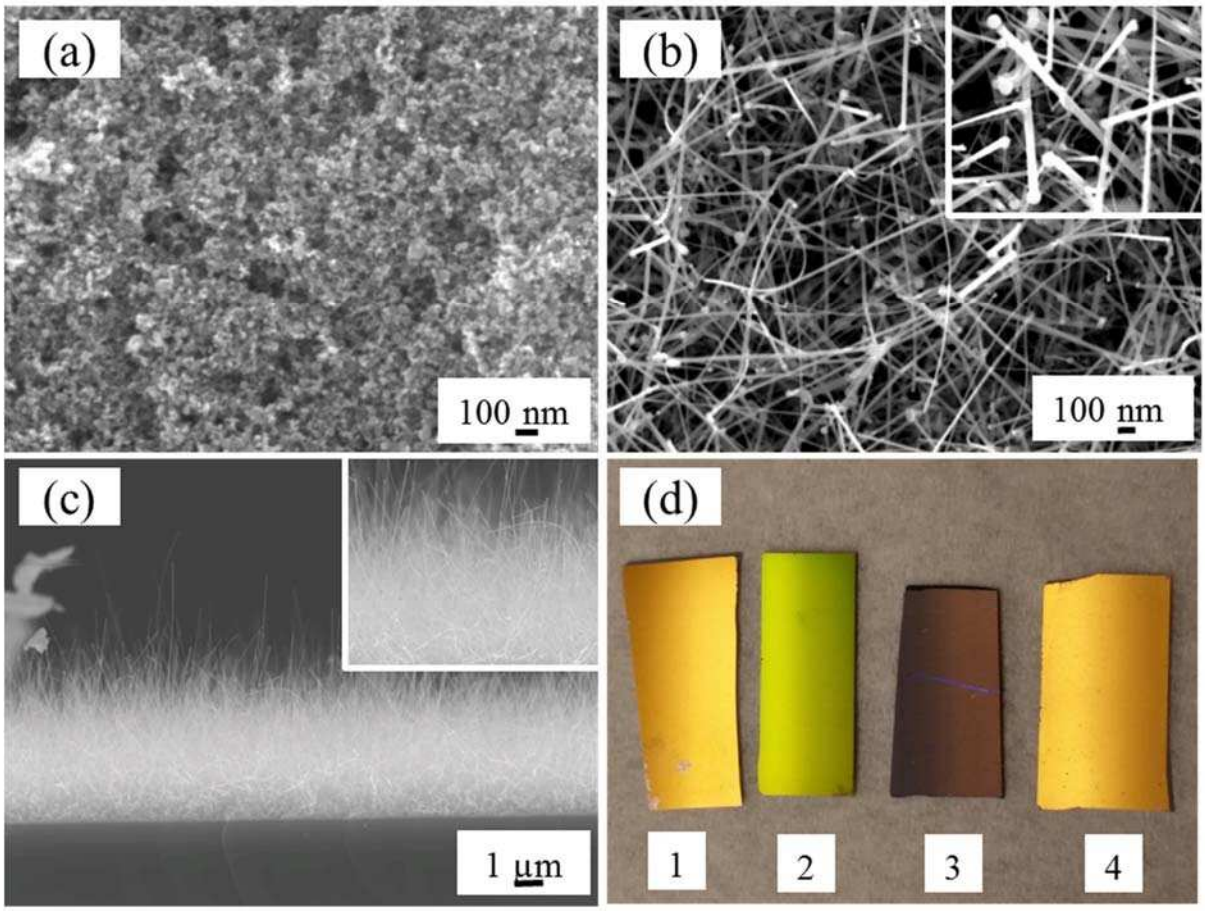

Figure 4.1. SEM images of (a) commercial SnO_2 nanoparticles; (b) SnO_2 CVD grown nanowires; and (c) a cross-section of SnO_2 nanowires, all on ZrO_2 substrates. Shown in panel (d) are photographs of a ZrO_2 substrate: (1) as-received, (2) sputtered with 5 nm Au and annealed for 60 min at 700 °C, (3) with CVD SnO_2 nanowires, and (4) covered with commercial SnO_2 nanoparticles. Insets show higher magnification images of the nanowires in (b) and (c).

created from these nanomaterials depend upon understanding the composition of the bulk material. PXRD patterns for a ZrO_2 substrate, SnO_2 nanoparticles on a zero diffraction plate, SnO_2 nanoparticles on ZrO_2, and SnO_2 nanowires (see Chapter 3 for additional characterization) on ZrO_2 can be seen in Figure 4.2. The patterns show both the SnO_2 nanoparticles and nanowires have a tetragonal SnO_2 structure where tin in the bulk of the material is in the Sn^{4+} oxidation state, consistent with nanowire structural analysis in Chapter 3. It is also important to understand the surface chemistry of our SnO_2 materials as it is the interactions of gases with the surface that drive the sensing mechanism of these devices. Gas-surface interactions are discussed further in Chapter 5 and 7. Figure 4.3 contains high resolution O_{1s} and Sn_{3d} XPS spectra for SnO_2 nanoparticles and nanowires. In particular, the main contribution to the O_{1s} spectra for both materials is that of oxygen bound to Sn^{4+} at 530.9 eV. A peak approximately 0.25 times as intense as the primary peak appears at 532.2 eV, indicating an additional binding environment assigned to oxygen adsorbed to the material surface.[22, 23] The Sn_{3d} spectra for both SnO_2 nanoparticles and nanowires show surface tin solely in the Sn^{4+} oxidation state, consistent with the bulk material.

4.2.3. Initial plasma modification treatments to increase surface oxygen. Ar/O_2 and H_2O plasma treated materials were also analyzed via XPS. The first experiments employed were designed to be directly comparable to literature studies.[16, 17, 24] Thus, we performed Ar/O_2 plasma treatments of SnO_2 nanoparticles and nanowires at P = 10, 20, 30, 40, 50, and 60 W for 4 min.[14, 17] Our XPS analyses of treated materials, however, revealed no changes in surface composition as all spectra showed no differences in comparison to UT nanomaterials. In addition, PXRD patterns showed no variation in the structure from the tetragonal structure of the

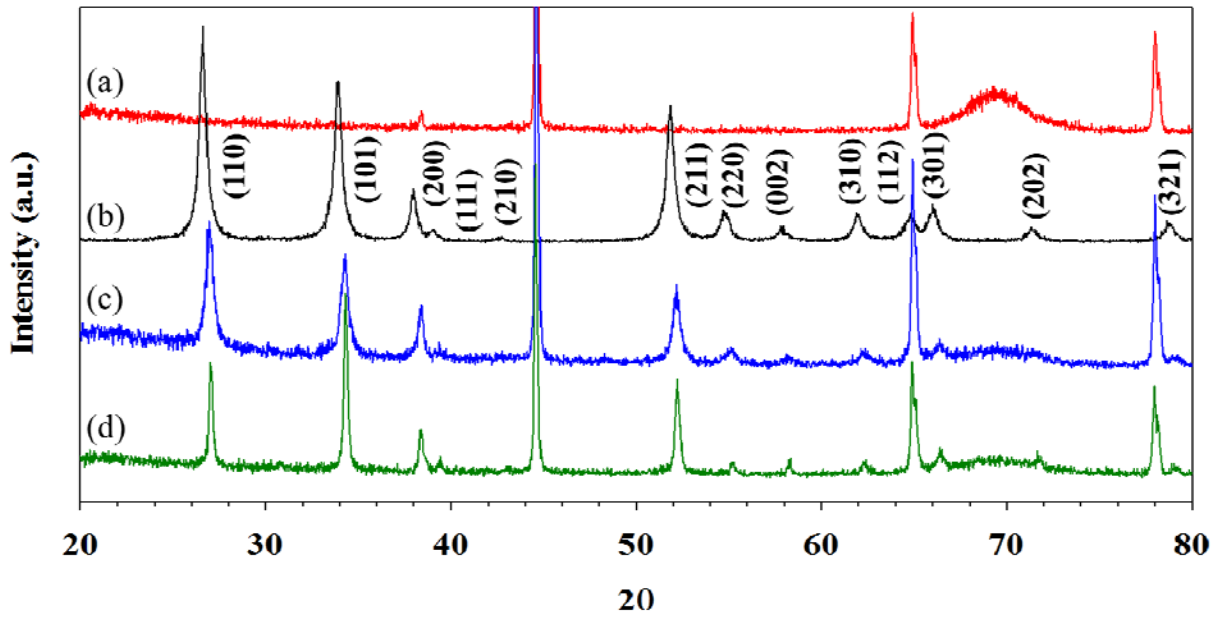

Figure 4.2. PXRD patterns for (a) ZrO_2 substrate; (b) SnO_2 nanoparticles on a zero diffraction plate; (c) SnO_2 nanoparticles on ZrO_2; and (d) SnO_2 nanowires on ZrO_2. The patterns show SnO_2 to be in the form of tetragonal SnO_2.

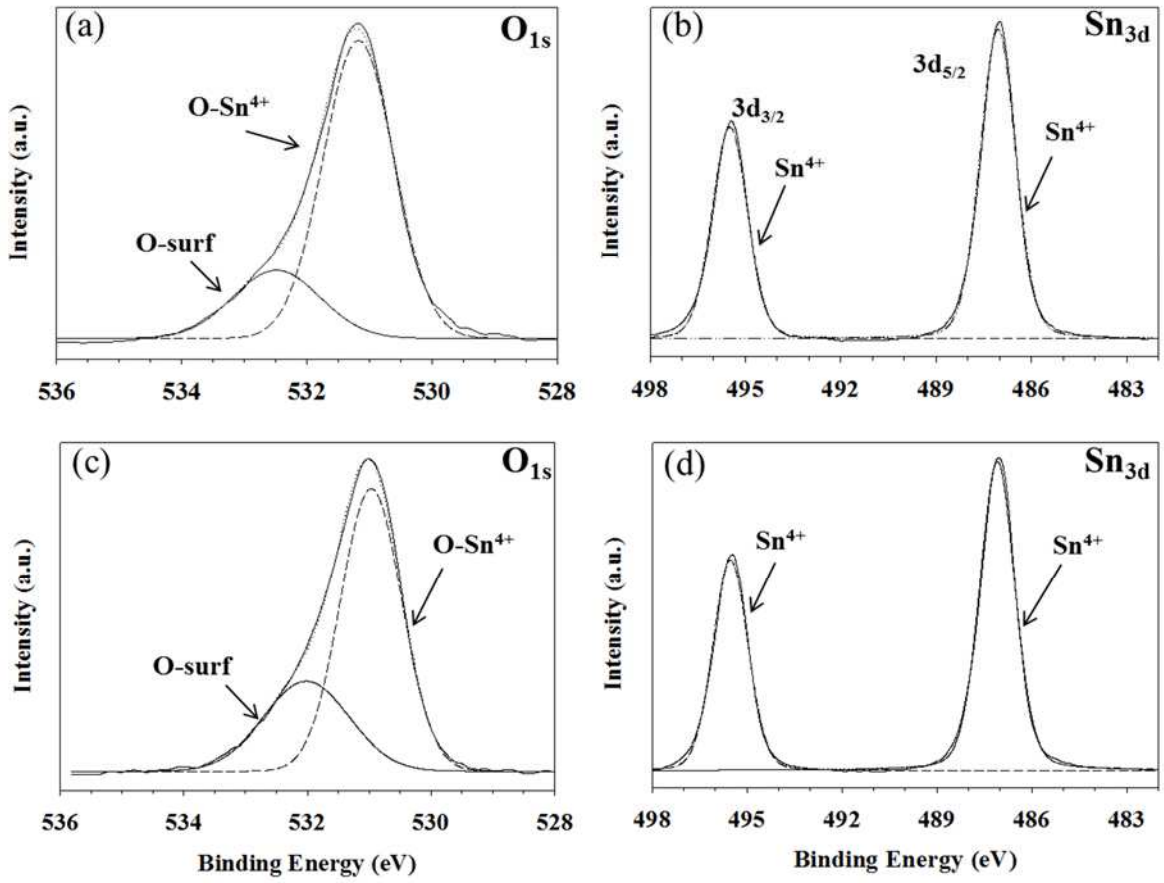

Figure 4.3. High resolution O_{1s} and Sn_{3d} XPS spectra of (a-b) commercial SnO_2 nanoparticles, and (c-d) CVD-grown SnO_2 nanowires.

UT SnO_2. These data suggested our plasma system under these conditions was not effective at significantly modifying the SnO_2 nanomaterials.

4.2.4. Optimizing Ar/O_2 and $H_2O_{(v)}$ plasma treatments for maximizing surface adsorbed oxygen. We therefore adjusted our plasma parameters to test increased applied powers and treatment times. Ultimately, we selected P = 150 W as the appropriate applied rf power to explore treatment times of 5, 10, and 30 min because it resulted in the highest etching and greatest oxygen adsorption. PXRD patterns collected post-plasma treatment for Ar/O_2 NP, Figure 4.4 (a), display virtually no change in the patterns from those of UT NP, Figure 4.2. Similarly, the patterns collected for Ar/O_2 NW, Figure 4.4 (b), show limited changes in crystallinity.

Although the bulk structure of the SnO_2 nanomaterials was not affected by the 150 W Ar/O_2 plasma treatment, the surface oxygen was altered, evidenced by XPS. Figure 4.5 shows high resolution O_{1s} and Sn_{3d} XPS spectra from plasma modified SnO_2 nanoparticles and nanowires. Regardless of treatment time, the 150 W Ar/O_2 plasma treatments did not change the Sn_{3d} binding environments for the NP and NW; thus the tin oxidation state remained unchanged. In contrast, the O_{1s} spectra show that adsorbed oxygen increases with treatment time for nanoparticles and nanowires as a result of the plasma creating oxygen vacancies within the SnO_2 lattice, as evidenced by the increase in the higher B.E. peak and the decrease in the peak at lower B.E. This trend can be seen in the XPS spectra for the NP treated at 30 min, but the most effective modification of those tested is the 30 min 150 W Ar/O_2 treatment of NW. This is supported by the chemisorbed oxygen O_{1s} peak at higher B.E. being approximately 1.5 times larger than the lower B.E. peak representative of lattice oxygen.

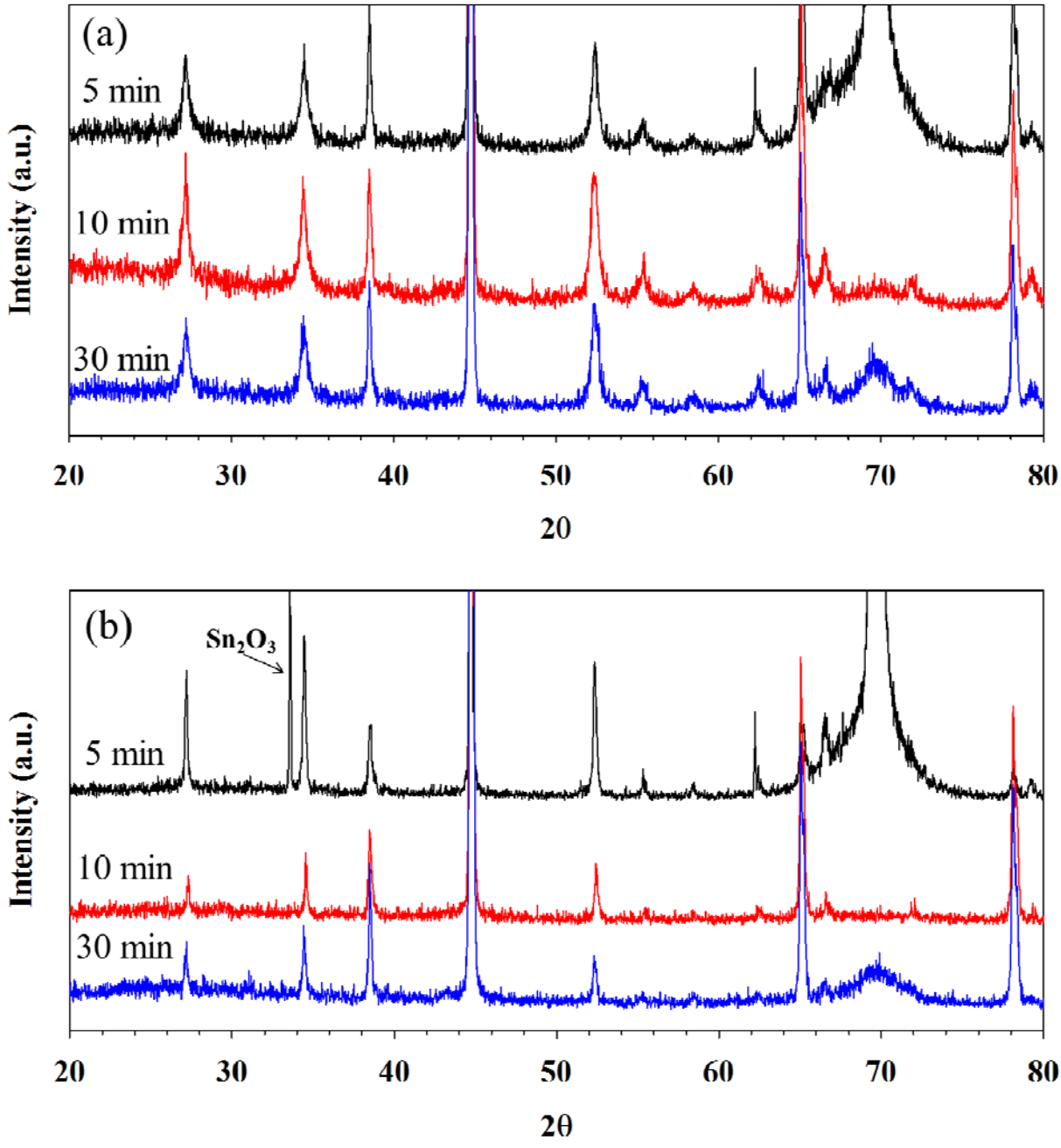

Figure 4.4. PXRD patterns for SnO_2 (a) nanoparticles and (b) nanowires treated in an Ar/O_2 plasma (145 mTorr, 150 W) for 5, 10, or 30 min. Some of the tetragonal SnO_2 facets are labeled in the patterns for reference, with the complete structure labelled in Figure 4.2.

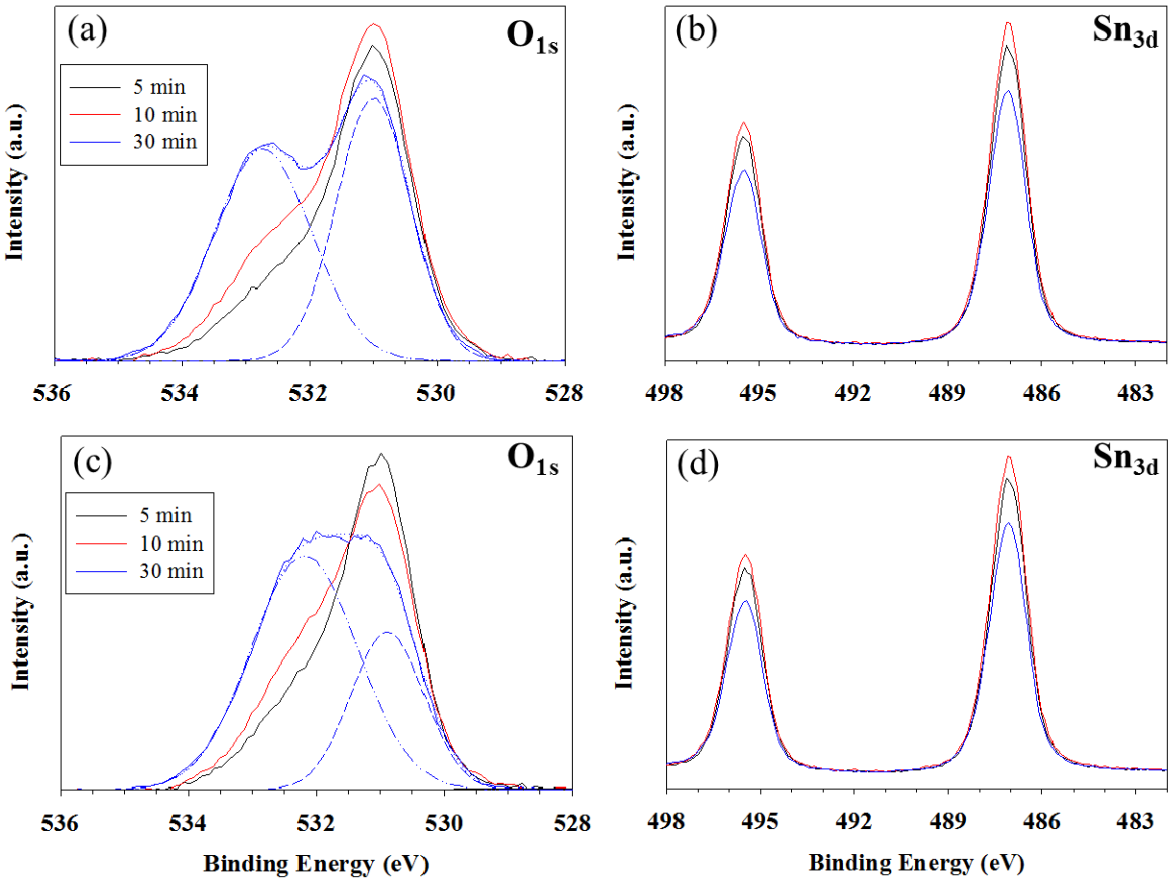

Figure 4.5. High resolution O_{1s} and Sn_{3d} XPS spectra of (a-b) SnO_2 nanoparticles, and (c-d) SnO_2 nanowires treated with an Ar/O_2 plasma (145 mTorr, 150 W) for 5, 10, or 30 min.

Despite these promising results, the Ar/O_2 system did not appear to provide the level of control over materials properties or plasma parameters that would be most desirable. We chose to explore an alternate system, $H_2O_{(v)}$ plasmas, which would likely provide different surface chemistries but would still be capable of increasing surface oxygen. As noted in Section 4.1.2., to our knowledge, H_2O plasmas have not been used for surface modification of SnO_2 nanomaterials. For direct comparison to the Ar/O_2 treatments, we used a 145 mTorr H_2O plasma. Effects of applied rf power on oxygen adsorption were explored by treating materials for 5 min at P = 30, 60, 100, and 150 W. XPS data collected post-H_2O plasma treatment showed increased oxygen adsorption at higher applied rf powers, Figure 4.6, similar to what was observed with the Ar/O_2 treatments but to a lesser extent. Whereas, Ar/O_2 plasma treatment resulted in a ratio of 1:1 for adsorbed oxygen to lattice oxygen, H_2O plasma treatment resulted in a ratio closer to 2:3. Notably, the 150 W H_2O plasma treatment appears to have a greater effect on oxygen adsorption with the NP than with the NW. Unexpectedly, given the increased oxygen adsorption, we also observed a reduction in Sn at higher P, Figure 4.6 (b, d). The Sn_{3d} spectra exhibit an additional binding environment at lower B.E. for both spin states (Sn^{4+} to Sn^0 ratio of approximately 3:2) with NW and NP displaying similar Sn reduction at P > 60 W.

To determine if Sn was reduced only at the surface or if Sn reduction occurred in the bulk material, PXRD patterns were collected for materials treated at 150 W where reduction was always observed, Figure 4.7. The nanoparticles showed several new peaks in the patterns, Figure 4.7 (a), representative of Sn in several reduced states (Sn^0, SnO, Sn_2O_3, Sn_3O_4) in addition to minimal presence of peaks for the initial tetragonal SnO_2 structure. 150 W H_2O NW PXRD patterns, Figure 4.7 (b), also contained peaks for reduced Sn phases. These patterns included

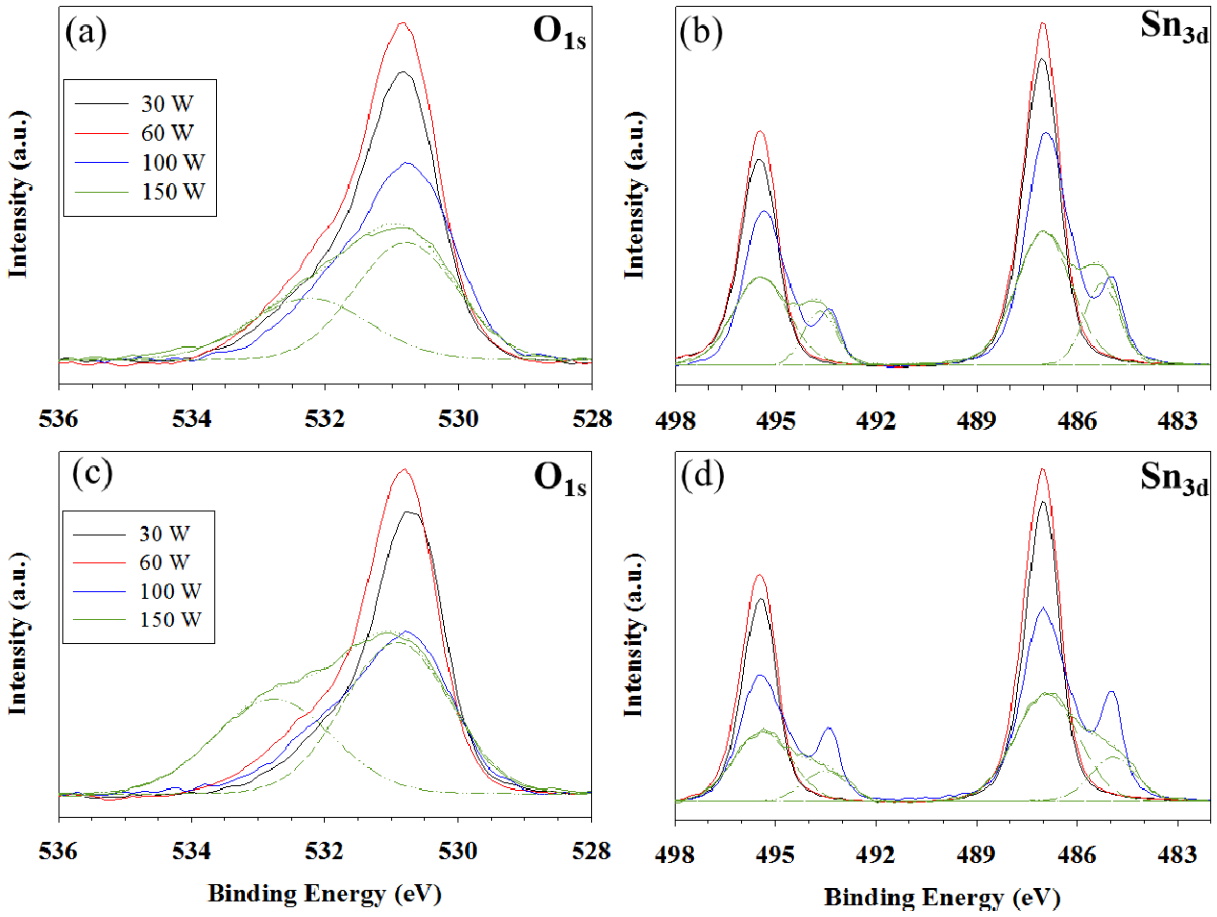

Figure 4.6. High resolution O_{1s} and Sn_{3d} XPS spectra of SnO_2 (a-b) nanoparticles and (c-d) nanowires treated with an H_2O plasma (145 mTorr, 5 min) at P = 30, 60, 100, or 150 W.

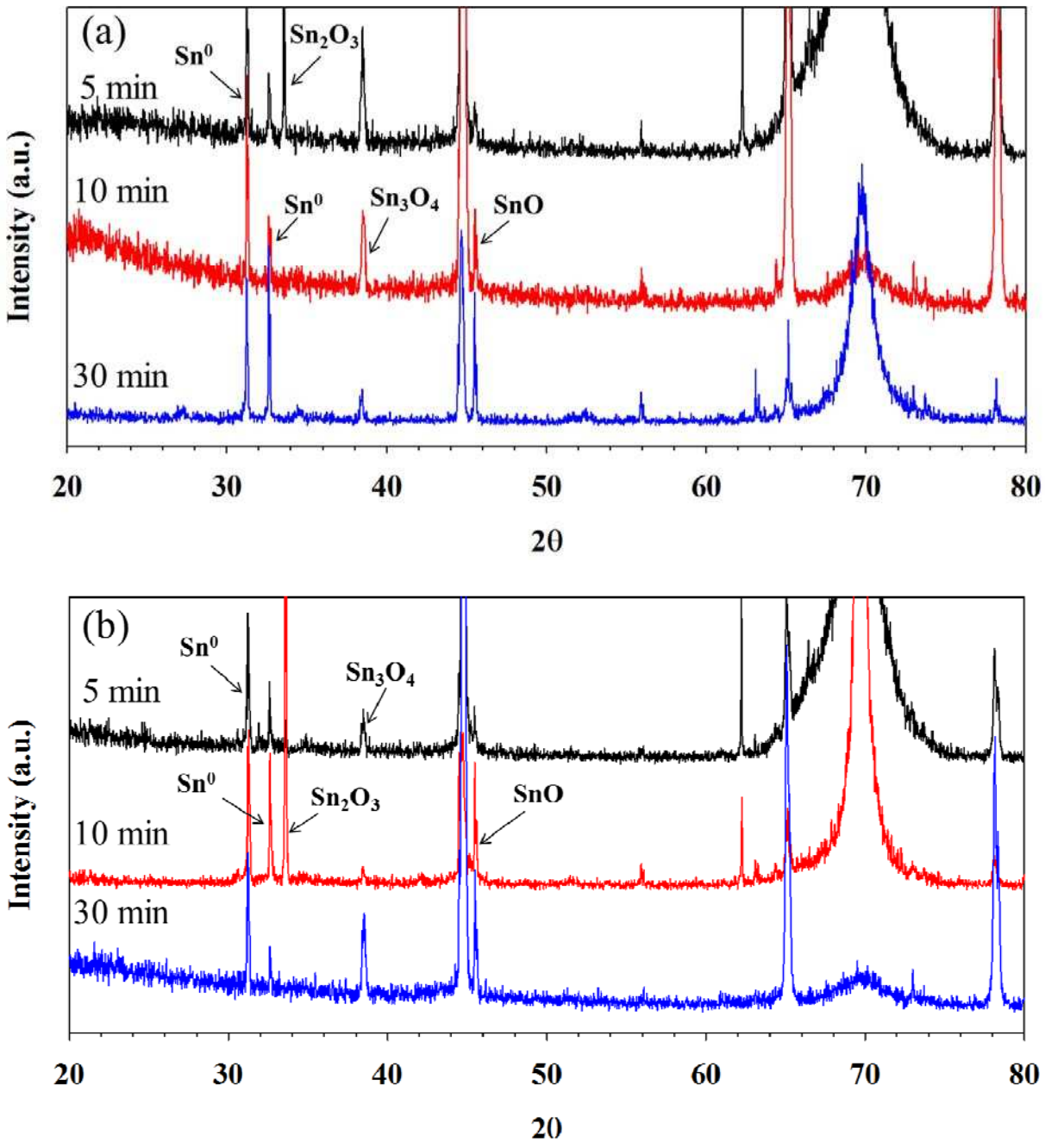

Figure 4.7. PXRD patterns for SnO_2 (a) nanoparticles and (b) nanowires, treated with an H_2O plasma (145 mTorr, 150 W) for 5, 10, or 30 min. Lines associated with various tin oxides are labeled; the complete pattern of tetragonal SnO_2 is labeled in Figure 4.2.

fewer peaks for tetragonal SnO_2 than those observed in the patterns for H_2O NP, which is discussed further below.

Sn reduction not only resulted in changing binding environments and additional tin oxidation states evidenced by XPS and PXRD, but morphological changes were also observed via SEM for H_2O NP and NW. Analyses suggest higher *P* and longer treatment time increase tin reduction, with decreasing mixtures of tin oxidation states being completely reduced to Sn^0. Figure 4.8 (a, c) show the reduction and agglomeration of SnO_2 nanoparticles into large Sn particles. As SnO_2 nanowires are reduced, they agglomerate into large Sn particles, Figure 4.8 (b, d), with nanowires on the exterior of the particles, Figure 4.8 (b). These chemical and morphological changes to the nanoparticles and nanowires also resulted in visual changes of the substrates, shown in the insets in Figure 4.8 (a-b), respectively. Such changes are discussed further below.

4.2.5. Expanded studies on $H_2O_{(v)}$ plasma system. As the 150 W 5 min H_2O plasma treatment displayed the greatest increase in oxygen adsorption for nanoparticles, Figure 4.6, this system was further explored by performing treatments at longer treatment times (10 and 30 min, Figure 4.9). The high resolution XPS oxygen binding environments for both nanowires and nanoparticles, Figure 4.9, display a trend of increasing oxygen adsorption with increasing treatment time. The increased treatment times studied do not, however, appreciably affect the amount of Sn reduction observed in the Sn_{3d} binding environment, likely due to the limitation of sampling depth associated with XPS.

Additional XPS data shown in Tables 4.1-4.3 provide compositional information on all untreated and plasma treated nanomaterials as well as ratios comparing different binding environments. These data show that the relative proportion of adsorbed to lattice oxygen is

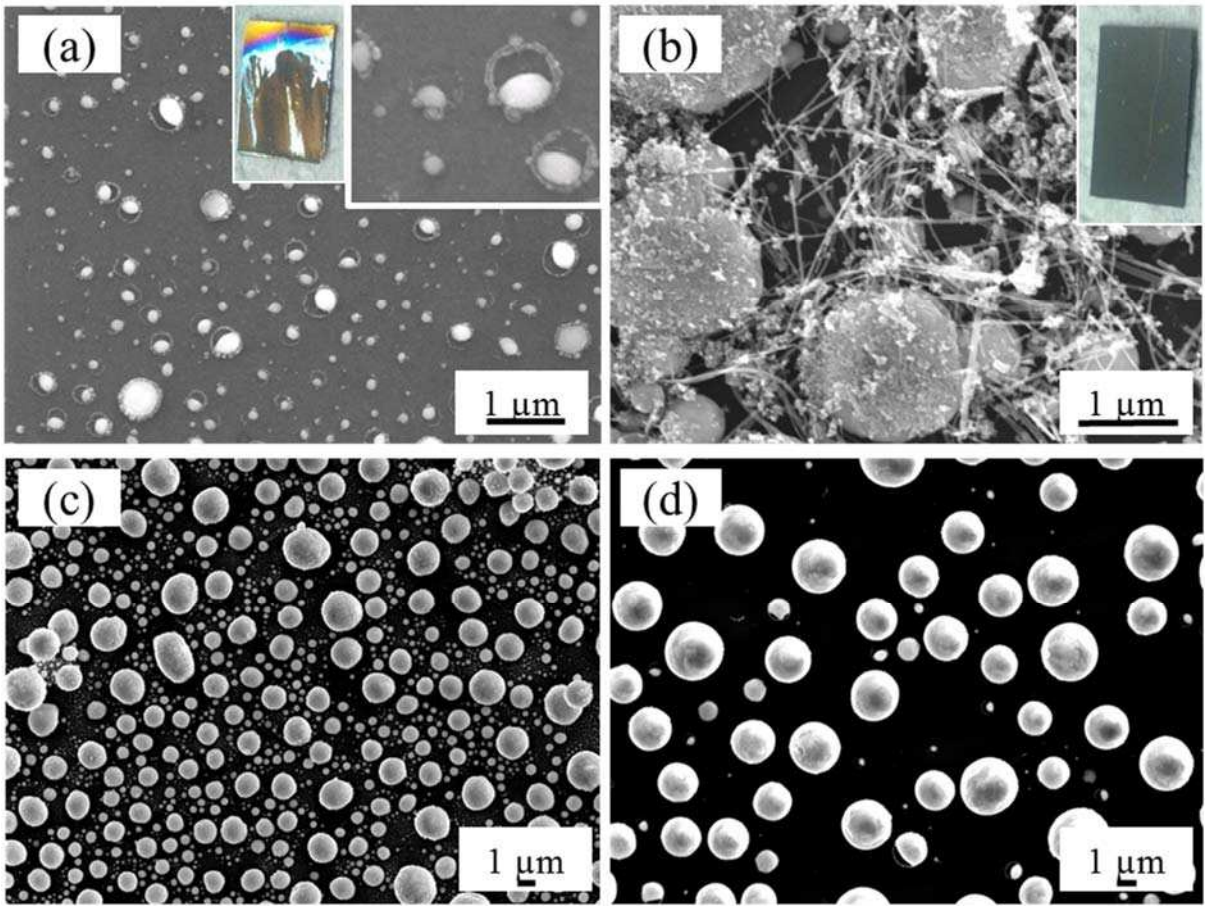

Figure 4.8. SEM images of (a,c) SnO_2 nanoparticles [mag 15,000X (inset 50,000X) and 19,000X, respectively] and (b,d) SnO_2 nanowires (mag 4,000X) treated with an H_2O plasma (145 mTorr 150 W, 5 min). Insets in (a) and (b) are photographs of the plasma treated nanoparticle and nanowire substrates, respectively.

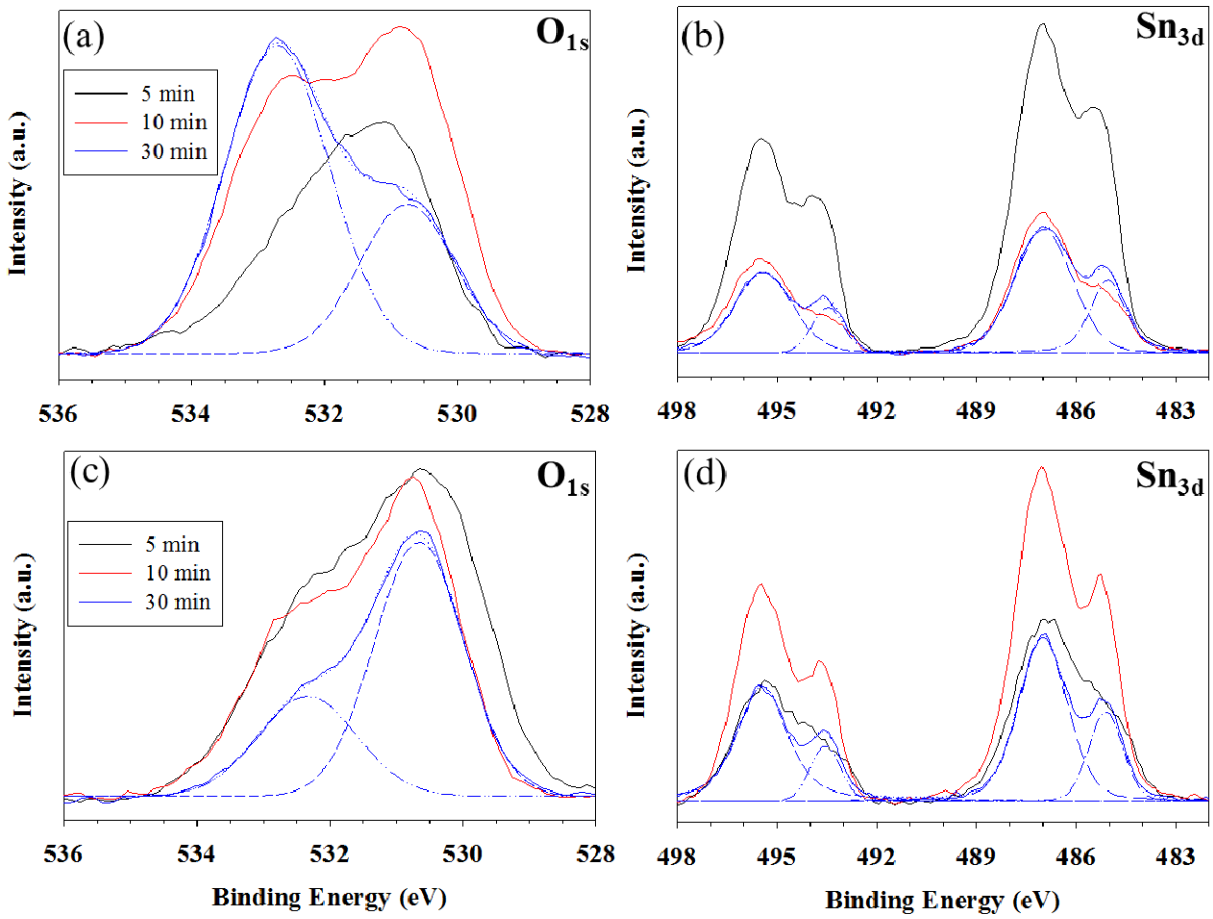

Figure 4.9. High resolution O_{1s} and Sn_{3d} XPS spectra of SnO_2 (a-b) nanoparticles; and (c-d) nanowires, treated with an H_2O plasma (145 mTorr, 150 W) for 5, 10, or 30 min.

Table 4.1. Elemental composition showing percent tin, oxygen, and carbon for UT, Ar/O_2, and H_2O NP and NW.

			Sn	%err	O	%err	C	%err
Untreated		nanoparticles	35.6	7.3	55.8	4.2	8.6	3.5
		nanowires	34.3	2.3	58.3	2.6	7.5	28.9
Ar/O_2	30 W 5 min	nanoparticles	28.7	7.5	55.5	22.1	15.9	87.5
		nanowires	34.1	4.4	57.3	4.9	8.6	50.4
	60 W 5 min	nanoparticles	33.1	8.1	61.1	13.0	5.7	142.5
		nanowires	36.9	10.9	59.4	6.0	3.7	19.5
	100 W 5 min	nanoparticles	27.7	6.9	68.6	2.6	3.7	38.1
		nanowires	34.2	7.9	59.7	8.2	6.0	38.1
	150 W 5 min	nanoparticles	33.2	15.7	63.3	9.7	3.5	30.1
		nanowires	36.4	4.7	59.2	3.5	4.4	12.7
	150 W 10 min	nanoparticles	31.7	8.6	63.5	3.4	4.8	14.6
		nanowires	34.6	6.5	62.4	4.6	2.9	39.8
	150 W 15 min	nanoparticles	28.5	9.9	67.2	2.6	4.3	25.9
		nanowires	27.5	17.1	69.7	7.1	2.8	25.0
H_2O	30 W 5 min	nanoparticles	27.5	4.9	65.7	4.6	6.8	25.1
		nanowires	33.8	6.2	60.6	5.4	5.6	94.8
	60 W 5 min	nanoparticles	31.0	3.6	66.2	0.7	2.8	25.0
		nanowires	33.5	6.9	64.3	2.2	2.2	49.8
	100 W 5 min	nanoparticles	41.6	1.6	54.4	2.1	4.0	23.6
		nanowires	41.9	10.1	46.5	16.2	11.6	101.0
	150 W 5 min	nanoparticles	27.3	9.9	42.7	16.7	30.1	17.9
		nanowires	7.6	50.7	29.5	116.4	62.8	60.7
	150 W 10 min	nanoparticles	11.5	7.2	73.8	5.6	14.7	25.6
		nanowires	14.6	22.3	57.1	33.9	28.3	73.2
	150 W 15 min	nanoparticles	14.6	2.9	75.0	3.1	10.5	19.5
		nanowires	8.9	12.1	47.7	24.2	43.4	27.9

Table 4.2. O/Sn ratios, percent Sn^{4+}, and percent reduced tin for UT, Ar/O_2, and H_2O NP and NW.

			O/Sn	%err	% Sn^{4+}	%err	% reduced Sn	%err
Untreated		nanoparticles	1.6	11.5	100.0	0.0	0.0	0.0
		nanowires	1.7	4.9	100.0	0.0	0.0	0.0
Ar/O_2	30 W 5 min	nanoparticles	1.9	29.6	100.0	0.0	0.0	0.0
		nanowires	1.7	9.3	100.0	0.0	0.0	0.0
	60 W 5 min	nanoparticles	1.8	21.1	100.0	0.0	0.0	0.0
		nanowires	1.6	16.9	100.0	0.0	0.0	0.0
	100 W 5 min	nanoparticles	2.5	9.6	100.0	0.0	0.0	0.0
		nanowires	1.7	16.1	100.0	0.0	0.0	0.0
	150 W 5 min	nanoparticles	1.9	25.4	100.0	0.0	0.0	0.0
		nanowires	1.6	8.2	100.0	0.0	0.0	0.0
	150 W 10 min	nanoparticles	2.0	12.0	100.0	0.0	0.0	0.0
		nanowires	1.8	11.1	100.0	0.0	0.0	0.0
	150 W 15 min	nanoparticles	2.4	12.5	100.0	0.0	0.0	0.0
		nanowires	2.5	24.1	100.0	0.0	0.0	0.0
H_2O	30 W 5 min	nanoparticles	2.4	9.5	100.0	0.0	0.0	0.0
		nanowires	1.8	11.6	100.0	0.0	0.0	0.0
	60 W 5 min	nanoparticles	2.1	4.3	100.0	0.0	0.0	0.0
		nanowires	1.9	9.1	100.0	0.0	0.0	0.0
	100 W 5 min	nanoparticles	1.3	3.7	83.6	26.0	16.4	31.7
		nanowires	1.1	26.2	76.4	32.0	23.6	24.8
	150 W 5 min	nanoparticles	1.6	26.6	73.9	37.3	26.1	45.6
		nanowires	3.9	167.1	71.7	85.8	28.3	66.0
	150 W 10 min	nanoparticles	6.4	12.8	82.2	48.9	17.8	67.8
		nanowires	3.9	56.2	71.4	61.8	28.6	48.7
	150 W 15 min	nanoparticles	5.1	5.9	73.8	28.8	26.2	29.2
		nanowires	5.3	36.3	74.7	32.3	25.3	23.6

Table 4.3. Percent lattice oxygen, adsorbed oxygen, and adsorbed oxygen to lattice oxygen ratios for UT, Ar/O_2, and H_2O NP and NW.

			% lattice O	%err	% adsorbed O	%err	adsorbed/ lattice	%err
Untreated		nanoparticles	74.4	30.3	25.6	32.3	0.3	31.8
		nanowires	71.6	5.8	28.4	8.9	0.4	8.0
Ar/O_2	30 W 5 min	nanoparticles	75.4	41.8	24.6	27.5	0.3	31.1
		nanowires	76.4	21.8	23.6	34.0	0.3	31.1
	60 W 5 min	nanoparticles	72.3	19.5	27.7	25.0	0.4	23.5
		nanowires	72.0	6.3	28.0	8.2	0.4	7.7
	100 W 5 min	nanoparticles	73.1	18.4	26.9	30.6	0.4	27.3
		nanowires	69.2	17.5	30.8	24.3	0.4	22.2
	150 W 5 min	nanoparticles	68.3	8.9	31.7	26.5	0.5	21.0
		nanowires	66.4	4.0	33.6	10.2	0.5	8.1
	150 W 10 min	nanoparticles	63.1	29.5	36.9	35.9	0.6	33.5
		nanowires	63.9	26.5	36.1	41.5	0.6	36.1
	150 W 15 min	nanoparticles	81.3	237.6	18.7	130.5	0.2	150.5
		nanowires	37.9	55.6	62.1	49.6	1.6	53.3
H_2O	30 W 5 min	nanoparticles	76.5	4.3	23.5	15.5	0.3	12.9
		nanowires	75.4	10.5	24.6	21.1	0.3	18.5
	60 W 5 min	nanoparticles	70.0	12.8	30.0	18.0	0.4	16.5
		nanowires	72.1	5.6	27.9	6.4	0.4	6.2
	100 W 5 min	nanoparticles	73.3	33.9	26.7	26.9	0.4	28.7
		nanowires	70.3	28.0	29.7	48.4	0.4	42.3
	150 W 5 min	nanoparticles	62.2	18.2	37.8	18.1	0.6	18.1
		nanowires	59.8	220.5	40.2	225.1	0.7	223.2
	150 W 10 min	nanoparticles	45.9	71.8	54.1	36.1	1.2	55.4
		nanowires	55.6	78.8	44.4	80.2	0.8	79.6
	150 W 15 min	nanoparticles	41.1	69.0	58.9	43.0	1.4	58.3
		nanowires	63.7	35.2	36.3	62.9	0.6	52.9

approximately 1:3 for UT materials. This ratio stays constant for Ar/O_2 plasma treatments with $P \leq 100$ W but increases to as high as 1.6:1 for nanowires treated at 150 W for 30 min. For the H_2O plasma treated materials, this ratio similarly rises to as high as 1.4:1 for nanowires treated at 150 W for 30 min. Table 4.2. shows the % Sn in a reduced state relative to that in the Sn^{+4} state. As noted above, the only samples that show contributions from reduced Sn are those treated in H_2O plasmas with $P \geq 100$ W.

Although the majority of the treated samples show small amounts of carbon in the XPS spectra, largely attributable to adventitious carbon, there is >10 % carbon in some of the Ar/O_2 plasma-treated materials. This likely arises from the creation of surface oxygen vacancies that allow not only for increased interactions with atmospheric oxygen but also with any carbon present near the treated samples. This is supported by the relatively large error associated with these measurements, which further suggests a non-uniform incorporation of carbon (often seen with plasma-treated materials).[25] For H_2O plasma treated samples, we also see high levels of carbon incorporation in the XPS spectra. Here, we attribute the carbon both to the increased availability of surface oxygen vacancies but also to the extreme morphology changes occurring with these plasma treatments. The changes in morphology upon tin reduction may leave an incomplete or non-uniform surface composition (as supported by EDS data, Figure 4.10., which suggest the microscale particles largely comprise tin, with very little oxygen). This is further evidenced by the relatively large error bars in these measurements, which indicate a non-uniform composition being sampled by the XPS.

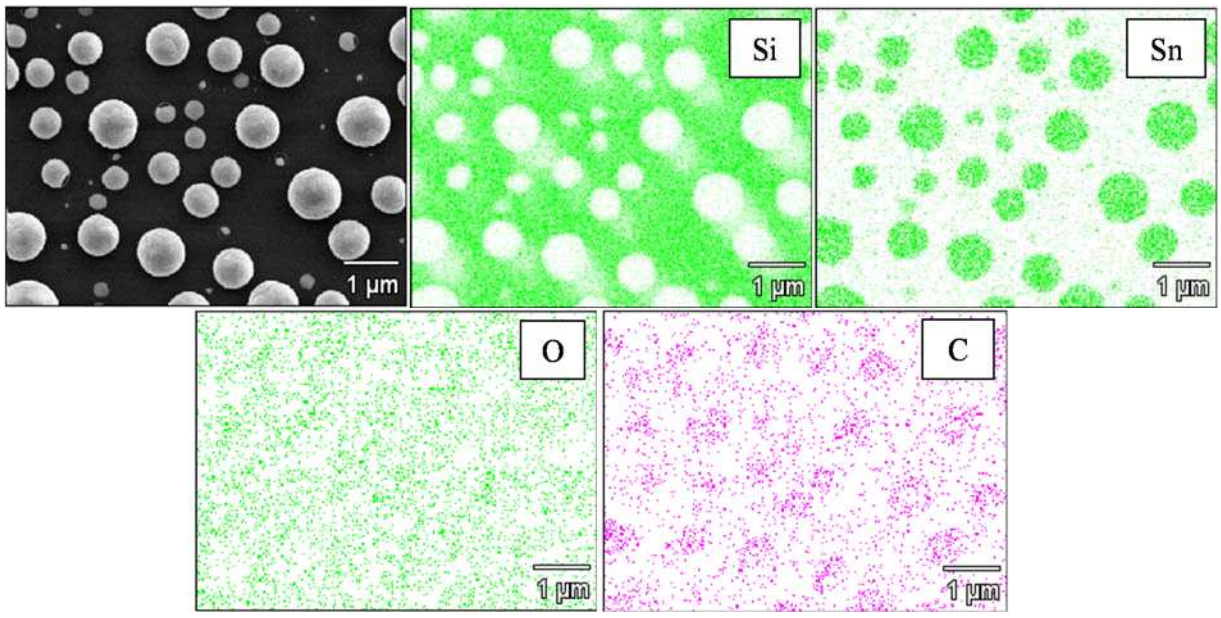

Figure 4.10. SEM image and corresponding EDS spectra of 150 W 30 min H_2O NW, Si, Sn, O, and C composition maps.

4.3. Discussion

4.3.1. Necessity for comprehensive materials characterization when plasma modifying materials. Scant literature exists on plasma surface modification of MO materials for gas sensing, specifically SnO_2, providing limited information on effects of such processes on materials properties and composition. Thus, this study was designed to focus on more comprehensive materials characterization and to explore the effects of different plasma systems on the chemical and morphological properties of SnO_2 nanomaterials. This is especially important because the bulk and surface properties of a sensing material are essential to a gas sensor's functionality, and controlling morphology is also critical for reproducibility of sensor fabrication processes.[16, 26] Moreover, it is also important to discern differences in the efficacy of plasma surface treatments that might arise from applying the treatment to different material morphologies. Additionally, SnO_2 materials tend to adsorb excess water in humid environments and, in some cases, adsorb more water than oxygen.[27-29] Thus, comparison between the two treatments, (one containing O_2 and one H_2O as the nominal oxidant) is also an interesting component of this current study. We have therefore characterized SnO_2 nanowires and nanoparticles to provide detailed chemical and morphological information about the two materials pre- and post-treatment.

4.3.2. Comparison of untreated SnO_2 nanowires and nanoparticles. Notably, the UT NP and NW have nearly identical PXRD patterns, Figure 4.2 (c-d), indicating similar crystal structures despite differences in morphology. Likewise, the XPS spectra for the two materials are very similar, Figure 4.3, indicating the surface chemistries are not substantially different prior to plasma treatment.

4.3.3. Understanding Ar/O_2 plasma systems and treatment of SnO_2 nanomaterials. The most intriguing results here are the morphological changes that occur upon H_2O plasma treatment. To understand how the different SnO_2 nanomaterials are altered by plasma modification it is necessary to first understand the mechanisms by which Ar/O_2 plasma systems can modify MO materials. Ar/O_2 plasmas etch SnO_2 surfaces by creating oxygen vacancies through activation of the surface with energetic Ar (and to a lesser extent, oxygen) species in the plasma, which also removes the activated surface oxygen.[30-32] Notably, several specific pathways are available for surface activation, most significantly heavy ion impact (Ar species), and chemical etching (oxygen species). Once oxygen vacancies are created, oxygen will preferentially adsorb to fill the vacancies on the SnO_2 surface. As our XPS data, Figure 4.5 and Table 4.1-4.3, show minimal changes after Ar/O_2 plasma treatment at lower P for both nanomaterials, it is likely that the surface is either insufficiently activated due to a limited amount of high energy Ar species, (Ar, Ar^*, or Ar^+) or the oxygen species are not capable of removing the activated oxygen.[30] Upon increasing the plasma power to $P \geq 100$ W, a sufficient amount of energetic plasma species are created to effectively etch SnO_2 surface oxygen. Thereby oxygen adsorption increases (as evidenced by the growth of the adsorbed oxygen peak in the XPS data) without altering the surface tin composition. Although we did not observe any tin reduction along with increased oxygen adsorption for the majority of Ar/O_2 treated materials, it is necessary to be aware that there is a transition point wherein the properties of SnO_2 become more characteristic of tin metal than the bulk MO.[14, 17]

Another intriguing aspect of the Ar/O_2 plasma treatment applied here is that we did not observe significant changes in the morphology of the nanomaterials, regardless of the plasma conditions. Although this agrees nicely with the work of Huang *et al.* who found that exposure

to an O_2 plasma (40 min) did not alter the morphology of SnO_2 nanocolumns,[33] it starkly contrasts with previous results from Mathur *et al.*[17] and Kim *et al.*[16] who found significant, albeit different, morphological changes occurred upon Ar/O_2 plasma treatment of SnO_2 nanomaterials. In particular, Mathur *et al.* found that their SnO_2 nanoplatelets, when treated with a 3:1 Ar/O_2 plasma (3 min, P = 25-125 W), were converted into elongated granular structures, even at the lowest applied powers. At the highest P, the structures became more globular and the formation of "pores" in the material was observed. They also witnessed that plasma treatment served to reduce Sn in the material to a range of sub-valent tin oxide species (Sn_3O_4, Sn_2O_3, SnO) that increased with plasma power. These changes were attributed to a combination of preferential oxygen etching and progressive reduction reactions upon plasma treatment. Indeed, the authors also noted that the relative amount of Sn^0 present in their materials was directly proportional to the plasma power as evidenced by their PXRD data. Given the relatively high concentration of Ar in their system, the resulting etching was not surprising.

Likewise, Kim *et al.*[16] found that exposure to a 1:1 Ar/O_2 atmospheric pressure plasma somewhat altered the morphology of their SnO_2 nanowires. Specifically, they found that nanowires exposed to the Ar/O_2 plasma grew nodules on the surface and the clusters of nodules grew proportionally with treatment time. Interestingly, no changes were observed in PXRD patterns of as grown and plasma treated nanowires, suggesting that plasma treatment altered nanowire morphology but not tin oxidation state. This suggests that particles bombarding the nanowire surface in this system were insufficient to appreciably etch or reduce SnO_2.

Although we did not observe any morphological changes to the nanomaterials under any Ar/O_2 plasma treatment parameters, we did observe small changes in bulk crystallinity. We clearly saw an increase in the surface oxygen at high powers and longer treatment times, Figure

4.5 and Table 4.1-4.3. In considering gas sensing applications, it is surface composition that allows for gas-surface interactions, whereas bulk crystallinity of the semiconductor contributes to charge flow through the material where changes in material resistance upon gas exposure tell information on sensitivity and selectivity. This change in resistance drives the gas sensing mechanism, which is why it is necessary to create large changes in resistance to maximize sensitivity. PXRD, Figure 4.4, showed negligible changes in the bulk crystallinity of SnO_2 nanoparticles after all Ar/O_2 plasma treatments. SnO_2 nanowires, however, showed minimal tin reduction. Although only the 5 min pattern displays an additional peak for Sn_2O_3, Figure 4.4 (b), additional peaks for Sn_2O_3 or other crystalline phases may be present in the nanowires that are simply not detected in all PXRD data as a result of the limitations of the technique and/or the orientation of the nanowire network.[34] Our results suggest the Ar/O_2 employed here does not appreciably etch or reduce the SnO_2 nanomaterials.

4.3.4. Understanding $H_2O_{(v)}$ plasma systems and treatment of SnO_2 nanomaterials. In contrast to the Ar/O_2 plasma treatments that resulted in only minor levels of tin reduction at high powers, H_2O plasma modification showed much greater tin reduction, irrespective of the applied rf power or treatment time. Furthermore, tin reduction occurs both on the surface and in the bulk material, as evidenced by XPS (Figure 4.6) and PXRD (Figure 4.7) data showing that the tin is almost completely reduced after H_2O treatment. In addition, extreme changes in morphology after H_2O plasma treatment were observed (Figure 4.8). Destruction of the initial crystalline structure resulted from extensive Sn reduction, allowing for Sn^0 to recombine and form relatively large particles, on the micrometer scale.

As with the Ar/O_2 system, it is instructive to consider possible mechanisms for how H_2O plasmas interact with surfaces. In particular, the reduction observed here may be the result of a

number of simultaneous effects occurring. First, the relatively high *P* in our plasmas likely led to significant ion bombardment of the surface. Previous work in our laboratory has shown that the average ion energy in Ar and Ar/CH_4 plasmas (with similar applied rf powers) in our laboratory is ~70-80 eV.[35] Thus, the plasma could potentially result in preferential sputtering as well as lattice disordering processes. Indeed, work in other groups has demonstrated that Ar/O_2 plasmas can preferentially remove specific elements from a range of metal oxides.[36-38] Second, the more delicate nanowires and nanoparticles could have been affected by increased substrate temperatures resulting from the higher applied rf powers. Although it is highly unlikely that our substrates are reaching these temperatures as previous work in our labs showed that T_S only rises to ~100 °C in 40 min,[39] the ambient heating of nanowires and nanoparticles has not previously been measured in our plasmas and may be reaching greater temperatures than we have previously reported for thin films. Notably, other researchers have found a size dependency of the melting points of Sn and SnO_2 particles.[40, 41]

Reduction and rearrangement were unexpected given that the literature shows H_2O plasma treatment generally has an oxidizing effect on SnO_2 thin films.[19, 20] In these previous studies, however, SnO_2 thin films were oxidized by low power (P = 1-5 W) H_2O plasmas, significantly lower than those used in our work; thus, Tarlov *et al.* could have observed a reducing effect with substantially increased plasma power due to subsequent heating or increased production of hydrogen atoms. Indeed, this is suggested as Tarlov *et al.*[19] observed a slight reduction of the near surface region when H_2O plasma treated SnO_2 thin films were annealed at relatively high temperatures (600 °C). Similar to the Ar/O_2 plasma system, this effect may manifest at lower T_S (which can result in mixed oxidation states[42]) in our studies, given the more delicate nature of the nanostructured materials. Nevertheless, H_2O plasmas do contain both

oxidizing (e.g., O, O*, OH) and reducing (e.g., H, H*, H_2) species and as such it is possible that our H_2O plasmas act more like H_2 plasmas than O_2 plasmas, the former of which are well known to reduce SnO_2 films.[43] The gas species present in H_2O plasmas resulting in Sn reduction are further examined in Chapter 5.

4.3.5. Implications in gas sensing applications. As a final note, reduction of SnO_2 thin films was previously reported to decrease conductivity,[44] suggesting that our Ar/O_2 plasma treated nanomaterials that still retain their semiconductor properties will show greater sensitivity and selectivity as gas sensors than H_2O plasma treated materials which are much more metallic in nature. As noted previously, having multiple valencies at the surface may enhance sensing properties, but extreme tin reduction may result in metallic behavior and suppress semiconducting capabilities that can be detrimental to sensing capabilities of the material.[14, 17] It was, therefore, important to closely monitor tin reduction via plasma treatment as we deployed these materials in gas sensor devices. The role of tin reduction on sensor sensitivity is explored in Chapter 7 where all Ar/O_2 and H_2O plasma treated nanomaterials are tested for sensor performance.

4.4. Summary

Through an increase in surface oxygen vacancies created via plasma treatments, our SnO_2 nanowires and nanoparticles exhibit increased oxygen adsorption, which can increase gas-surface interactions and ultimately affect sensor sensitivity. Thus, plasma modification is an effective method of surface modification for these materials. Notably, the 145 mTorr Ar/O_2 plasma (P = 150 W, 30 min) used here effectively etched lattice oxygen from SnO_2 nanowires and nanoparticles. This resulted in increased oxygen adsorption with both morphologies,

although greater oxygen adsorption was achieved with the nanowires. Interestingly, an alternative plasma treatment for oxygen etching, a similarly configured H_2O plasma also resulted in increased oxygen adsorption, but additionally resulted in the reduction of Sn. Significant morphological changes were also observed with H_2O plasma treatment, resulting in SnO_2 nanoparticles and nanowires being converted to large Sn particles. Thus, this plasma system may not be as effective for creating highly sensitive nanomaterials-based gas sensors.

REFERENCES

1. Stuckert, E. P.; Fisher, E. R. Ar/O_2 and H_2O Plasma Surface Modification of SnO_2 Nanomaterials to Increase Surface Oxidation. *Sens. Actuators B.* **2015**, *208* 379-388.
2. Liu, X.; Cheng, S.; Liu, H.; Hu, S.; Zhang, D.; Ning, H. A Survey on Gas Sensing Technology. *Sensors.* **2012**, *12* (7), 9635-9665.
3. Yamazoe, N. Toward Innovations of Gas Sensor Technology. *Sens. Actuators B.* **2005**, *108* (1), 2-14.
4. Patil, S. J.; Patil, A. V.; Dighavkar, C. G.; Thakare, K. S.; Borase, R. Y.; Nandre, S. J.; Deshpande, N. G.; Ahire, R. R. Semiconductor Metal Oxide Compounds Based Gas Sensors: A Literature Review. *Front. Mater. Sci.* **2015**, *9* (1), 14-37.
5. Moseley, P. Solid State Gas Sensors. *Meas. Sci. Technol.* **1997**, *8* (3), 223-237.
6. Eranna, G.; Joshi, B. C.; Runthala, D. P.; Gupta, R. P. Oxide Materials for Development of Integrated Gas Sensors - A Comprehensive Review. *Crit. Rev. Solid State Mater. Sci.* **2004**, *29* 111-188.
7. Labeau, M.; Gautheron, B.; Delabouglise, G.; Pena, J.; Ragel, V.; Varela, A.; Román, J.; Martinez, J.; González-Calbet, J.; Vallet-Regi, M. Synthesis, Structure and Gas Sensitivity Properties of Pure and Doped SnO_2. *Sens. Actuators B.* **1993**, *16* (1), 379-383.
8. Xiao, L.; Shu, S.; Liu, S. A Facile Synthesis of Pd-Doped SnO_2 Hollow Microcubes with Enhanced Sensing Performance. *Sens. Actuators B.* **2015**, *221* 120-126.
9. Singhal, A. V.; Chandra, K.; Agarwala, V. Doped Nano–Phase Tin Oxide Thin Films for Selective Gas Sensing. *Int. J. Nanotechnol.* **2015**, *12* (3-4), 248-262.
10. Bhardwaj, J. K.; Ashraf, H. In *Advanced Silicon Etching Using High-Density Plasmas*, Micromachining and Microfabrication, International Society for Optics and Photonics: 1995; pp 224-233.
11. Delsol, R.; Setton, M.; Vinet, F.; Valvin, P.; Blanc, R.; Berruyer, P.; Assous, M. Transformer Coupled Plasma Dielectric Etch for 0.25 μm Technologies. *Microelectron. Eng.* **2000**, *50* (1), 75-80.
12. Welch, C.; Goodyear, A.; Wahlbrink, T.; Lemme, M. C.; Mollenhauer, T. Silicon Etch Process Options for Micro-and Nanotechnology Using Inductively Coupled Plasmas. *Microelectron. Eng.* **2006**, *83* (4), 1170-1173.
13. Srivastava, R.; Dwivedi, R.; Srivastava, S. K. Development of High Sensitivity Tin Oxide Based Sensors for Gas/Odour Detection at Room Temperature. *Sens. Actuators B.* **1998**, *50* 175-180.
14. Pan, J.; Ganesan, R.; Shen, H.; Mathur, S. Plasma-Modified SnO_2 Nanowires for Enhanced Gas Sensing. *J. Phys. Chem. C.* **2010**, *114* (18), 8245-8250.
15. Comini, E.; Sberveglieri, G. Metal Oxide Nanowires as Chemical Sensors. *Mater. Today.* **2010**, *13* (7-8), 28-36.
16. Kim, H. W.; Choi, S. W.; Katoch, A.; Kim, S. S. Enhanced Sensing Performances of Networked SnO_2 Nanowires by Surface Modification with Atmospheric Pressure Ar-O_2 Plasma. *Sens. Actuators B.* **2013**, *177* 654-658.
17. Mathur, S.; Ganesan, R.; Grobelsek, I.; Shen, H.; Ruegamer, T.; Barth, S. Plasma-Assisted Modulation of Morphology and Composition in Tin Oxide Nanostructures for Sensing Applications. *Adv. Eng. Mater.* **2007**, *9* (8), 658-663.
18. Srivastava, R.; Dwivedi, R.; Srivastava, S. K. In *Effect of Oxygen, Nitrogen and Hydrogen Plasma Processing on Palladium Doped Tin Oxide Thick Film Gas Sensors*,

IX International Workshop on the Physics of Semiconductor Devices (IWPSD), Delhi, India, Dec 16-20; Spie-Int Soc Optical Engineering: Delhi, India, 1997; pp 526-528.
19. Tarlov, M. J.; Evans, J. F. Surface Characterization of Radio Frequency Water Plasma Treated and Annealed Polycrystalline Tin Oxide Thin Films. *Chem. Mater.* **1990**, *2* (1), 49-60.
20. Tarlov, M. J.; Evans, J. F.; Newman, J. G. Static SIMS and XPS Study of Water Plasma Exposed Tin Oxide Films. *Appl. Surf. Sci.* **1993**, *64* (2), 115-125.
21. Tompkins, B. D.; Dennison, J. M.; Fisher, E. R. Etching and Post-Treatment Surface Stability of Track-Etched Polycarbonate Membranes by Plasma Processing Using Various Related Oxidizing Plasma Systems. *Plasma Process. Polym.* **2014**, *11* 850-863.
22. Kwoka, M.; Ottaviano, L.; Passacantando, M.; Santucci, S.; Czempik, G.; Szuber, J. XPS Study of the Surface Chemistry of L-CVD SnO_2 Thin Films After Oxidation. *Thin Solid Films.* **2005**, *490* 36-42.
23. Szuber, J.; Czempik, G.; Larciprete, R.; Koziej, D.; Adamowicz, B. XPS Study of the L-CVD Deposited SnO_2 Thin Films Exposed to Oxygen and Hydrogen. *Thin Solid Films.* **2001**, *391* (2), 198-203.
24. Chaturvedi, A.; Mishra, V. N.; Dwivedi, R.; Srivastava, S. K. Selectivity and Sensitivity Studies on Plasma Treated Thick Film Tin Oxide Gas Sensors. *Microelectron. J.* **2000**, *31* (4), 283-290.
25. Kim, J. Y.; Kim, S. H.; Seo, H.; Kim, J.-H.; Jeon, H. Deposition and Plasma Measurements of Zr-Oxide Films with Low Impurity Concentrations by Remote PEALD. *Electrochem. Solid State Lett.* **2005**, *8* (3), G82-G84.
26. Ramgir, N.; Datta, N.; Kaur, M.; Kailasaganapathi, S.; Debnath, A. K.; Aswal, D. K.; Gupta, S. K. Metal Oxide Nanowires for Chemiresistive Gas Sensors: Issues, Challenges, and Prospects. *Colloids Surf., A.* **2013**, *439* 101-116.
27. McAleer, J. F.; Moseley, P. T.; Norris, J. O. W.; Williams, D. E. Tin Dioxide Gas Sensors. 1. Aspects of the Surface-Chemistry Revealed by Electrical Conductance Variations. *J. Chem. Soc., Faraday Trans.* **1987**, *83* 1323-1346.
28. Hernandez-Ramirez, F.; Tarancon, A.; Casals, O.; Arbiol, J.; Romano-Rodriguez, A.; Morante, J. R. High Response and Stability in CO and Humidity Measures Using a Single SnO_2 Nanowire. *Sens. Actuators B.* **2007**, *121* 3-17.
29. Yadav, B. C.; Sharma, P.; Khanna, P. K. Morphological and Humidity Sensing Characteristics of SnO_2-CuO_2, SnO_2-Fe_2O_3 and SnO_2-SbO_2 Nanocooxides. *Bull. Mater. Sci.* **2011**, *34* (4), 689-698.
30. Grill, A. *Cold Plasma in Materials Fabrication: From Fundamentals to Applications*. IEEE: New York, 1994.
31. Addonizio, M. L.; Antonaia, A. Enhanced Electrical Stability of LP-MOCVD-Deposited ZnO:B Layers by Means of Plasma Etching Treatment. *J. Phys. Chem. C.* **2013**, *117* 24268−24276.
32. Aronsson, B. O.; Lausmaa, J.; Kasemo, B. Glow Discharge Plasma Treatment for Surface Cleaning and Modification of Metallic Biomaterials. *J. Biomed. Mater. Res.* **1997**, *35* (1), 49-73.
33. Huang, H.; Lee, Y. C.; Chow, C. L.; Tan, O. K.; Tse, M. S.; Guo, J.; White, T. Plasma Treatment of SnO_2 Nanocolumn Arrays Deposited by Liquid Injection Plasma-Enhanced Chemical Vapor Deposition for Gas Sensors. *Sens. Actuators B.* **2009**, *138* 201-206.

34. Hammond, C.; Hammond, C. *Basics of Crystallography and Diffraction*. Oxford: 2001; Vol. 214.
35. Zhou, J.; Martin, I. T.; Ayers, R.; Adams, E.; Liu, D.; Fisher, E. R. Investigation of Inductively Coupled Ar and CH_4/Ar Plasmas and the Effect of Ion Energy on DLC Film Properties. *Plasma Sources Sci. Technol.* **2006**, *15* 714-726.
36. Liu, W.; Liu, Z.; Yan, F.; Tan, T.; Tian, H. Influence of O_2/Ar Flow Ratio on the Strucure and Optical Properties of Sputtered hafnium Dioxide Thin Films. *Surf. Coat. Technol.* **2010**, *205* 2120-2125.
37. Brown, N. M. D.; Liu, Z. H. The Etching of Natural Alpha-Recoil Tracks in Mica with an Argon RF-Plasma Discharge and Their Imaging via Atomic Force Microscopy. *Appl. Surf. Sci.* **1996**, *93* 89-100.
38. Stafford, L.; Lim, W. T.; Pearton, S. J.; Chicoine, M.; Gujrathi, S.; Schiettekatte, F.; Park, J.-S.; Song, J.-I.; Heo, Y.-W.; Lee, J.-H.; Kim, J.-J.; Kravchenko, I. I. Influence of the Film Properties on the Plasma Etching Dynamics of rf-Sputtered Indium Zinc Oxide Layers. *J. Vac. Sci. Technol., A.* **2010**, *25* 659-665.
39. Stillahn, J. M.; Fisher, E. R. CN Surface Interactions and Temperature-Dependent Film Growth During Plasma Deposition of Amorphous Hydrogenated Carbon Nitride. *J. Phys. Chem. C.* **2009**, *113* 1963-1971.
40. Jiang, H.; Moon, K.-S.; Hua, F.; Wong, C. P. In *Thermal Properties of Oxide Free Nano Non Noble Metal for Low Temperature Interconnect Technology*, Electronic Components and Technology Conference, IEEE: 2006; pp 1969-1973.
41. Bajaj, G.; Soni, R. K. Synthesis of Composite Gold/Tin-Oxide Nanoparticles by Nano-Soldering. *J. Nanopart. Res.* **2010**, *12* 2597-2603.
42. Batzill, M.; Diebold, U. The Surface and Materials Science of Tin Oxide. *Prog. Surf. Sci.* **2005**, *79* (2), 47-154.
43. Thomas, J. H. I. X-ray Photoelectron Spectroscopy Study of Hydrogen Plasma Interactions with a Tin Oxide Surface. *Appl. Phys. Lett.* **1983**, *42* (9), 794-796.
44. Shapira, Y. Electron Beam Induced Dissociation and Conductivity of SnO_2 Films. *J. Appl. Phys.* **1981**, *52* (9), 5696-5698.

CHAPTER 5

GAS-PHASE DIAGNOSTICS DURING H_2 AND H_2O PLASMA TREATMENT OF SnO_2 NANOMATERIALS: IMPLICATIONS FOR SURFACE MODIFICATION

This chapter is based on the work under a similar title submitted to *Journal of Vacuum Science & Technology B* by Erin P. Stuckert, Christopher J. Miller, and Ellen R. Fisher. The text, figures, and tables are reproduced here with data collected by Erin and Chris; data analyzed and manuscript written by Erin and Ellen. This chapter discusses the gas-phase species present under different plasma parameters with and without SnO_2 nanomaterials in H_2 and $H_2O_{(v)}$ plasmas. Comparing relative species densities as a result of these different plasma systems allows for determining the effect of the plasma on the nanomaterial and the nanomaterial on the plasma. Furthermore, understanding the plasma chemistry of these different plasma systems aids in elucidating why H_2O plasma (a nominally oxidizing system) would reduce SnO_2 nanomaterials. Funding for this research was provided by the National Science Foundation (CHE-1152963).

5.1. Introduction

5.1.1. Limited understanding of plasma-substrate interactions. Low-temperature inductively-coupled plasmas (LT-ICPs) are used for modifying a wide range of materials including polymeric constructs[1] and metal oxide nanomaterials,[2] for use in applications including biomedical devices,[3] textiles,[4] and gas sensors.[5] Choosing the appropriate plasma modification system, including relevant processing parameters, is essential when a material must have well-defined chemical and physical properties for a given application, such as nanomaterials for use as gas sensors. Often, researchers evaluate plasma modification parameter space through

characterization of the plasma treated nanomaterial.[6-9] This, however, only provides a fraction of the information needed to determine optimal plasma treatment conditions for a given application. To understand fundamental mechanisms of plasma surface modification it is necessary to understand the gas-phase chemistry with and without nanomaterial substrates. This allows for distinguishing the influence of the substrate on the plasma relative to the influence of the plasma on the substrate. Such an experimental approach can afford insight into how substrates can affect plasma chemistry and energetics, which provides a more complete understanding of plasma surface modification when combined with complementary surface characterization.

5.1.2. Examining the gas phase during plasma surface modification. OES is commonly used to detect excited state gas-phase species within LT-ICPs, as it allows for examination of plasma species without perturbing the plasma.[10] OES has also been used to monitor precursor decomposition,[11] detect adsorption/desorption of species from a substrate,[12] and determine which plasma processing conditions lead to nanomaterial growth,[13] among other applications.[14, 15] As measurements can be made in real time, OES can help elucidate reaction mechanisms through changes in species density. Species quantification (e.g., populations or concentrations) and characteristic plasma temperatures (e.g., T_R and T_V) can be determined by using an inert gas actinometer, such as Ar, thereby allowing for species comparison across plasma systems.[16] For example, Trevino, *et al.* used OES to explore different feed gases and determine detection limits of known water-contaminating species within plasma systems.[11] OES studies of plasmas ignited using three different feed gases [$H_2O_{(v)}$, methanol (CH_3OH), and methyl tert-butyl ether (MTBE)] revealed emission of disparate primary species in each plasma and led to proposed decomposition pathways of the plasma feed gases. This work increased understanding of $H_2O_{(v)}$,

CH_3OH, and MTBE plasmas, in addition to determining detection capabilities of OES for specific species considered to be water contaminants.

Trevino, *et al.* are not alone in using OES to examine plasmas in the absence of substrates; however, few explicitly use OES to monitor nanomaterial growth or interaction with plasma species.[17-21] To fully comprehend how materials are altered by and may influence plasma chemistry, it is necessary to monitor gas-phase species under various parameters with and without the material being modified. Some studies have explored surface characterization of plasma modified SnO_2 materials utilizing techniques such as XPS, TEM, and resistance measurements to determine the effect of plasma treatment on SnO_2 materials.[22-25] Each of these studies focuses solely on the post-modification characterization aspects of plasma processing. One report, however, addressed this gap in gas-phase detection of plasmas with substrates by examining recombination of oxygen atoms on n- and p-type semiconductors in low pressure rf plasmas.[26] Guyon, *et al*.'s work focused on observations of activation energies and recombination coefficients while altering surface chemistry. Although this study analyzed certain aspects of the plasma upon addition of a substrate, variations in plasma-species concentrations as a result of different nanomaterial substrates or as a result of detection location along the reactor were not measured. Ultimately, no works to date have directly incorporated OES analysis to understand plasma-surface interactions with SnO_2 nanomaterials. It is through the combination of such gas-phase diagnostics and materials characterization techniques that a comprehensive understanding of nanomaterial plasma surface modification can be achieved.

5.1.3. Detecting oxidative and reductive plasma species as a result of plasma parameters and presence of a substrate. With the current work presented herein, we make progress toward understanding plasma-surface interactions when modifying materials for a particular application.

Specifically, in prior work, we used $H_2O_{(v)}$ plasmas to surface modify SnO_2 nanowires and nanoparticles.[25] Although others[27, 28] had concluded H_2O plasma has an oxidizing effect on similar materials, we found H_2O plasmas actually reduced Sn^{+4} to Sn^0 in SnO_2 nanomaterials.[25] Thus, one goal of this work was to understand relative concentrations of species that were present in the gas phase with and without SnO_2 nanomaterials in the plasma systems as this could provide insight into surface modification mechanisms. To ascertain which species in H_2O plasma lead to reduction of tin in SnO_2 nanomaterials, we also treated SnO_2 nanomaterials with reducing H_2 plasmas to compare its effects with those of H_2O plasma, which contains both oxidizing (e.g., O, O*, OH*) and reducing (e.g., H, H*) species. Both plasma systems use ~10 % by pressure Ar as an actinometer to determine relative species densities.

5.2. Results and Discussion

5.2.1. Observing nanomaterial morphology before and after plasma treatment. SEM images of SnO_2 nanoparticles and nanowires, Figure 5.1, show the different morphologies and surface coverage for untreated, H_2 and H_2O plasma-treated nanomaterials. UT nanoparticles cover the ZrO_2 surface in a thin film with particle diameters ranging 10-50 nm, where most particles appear to fall closer to the lower end of this range.[25] Nanowires, grown via the VLS CVD mechanism,[29, 30] have an interconnected network covering the ZrO_2 surface. UT wires are a few microns in length with diameters ranging 10-50 nm, averaging around 20 nm; as discussed previously in Chapter 3 and 4, nanowire dimensions are dependent on Au nanoparticle dimensions and CVD parameters.[31] Overall, these images show significant differences in morphology and ZrO_2 coverage for the different UT SnO_2 nanomaterials.

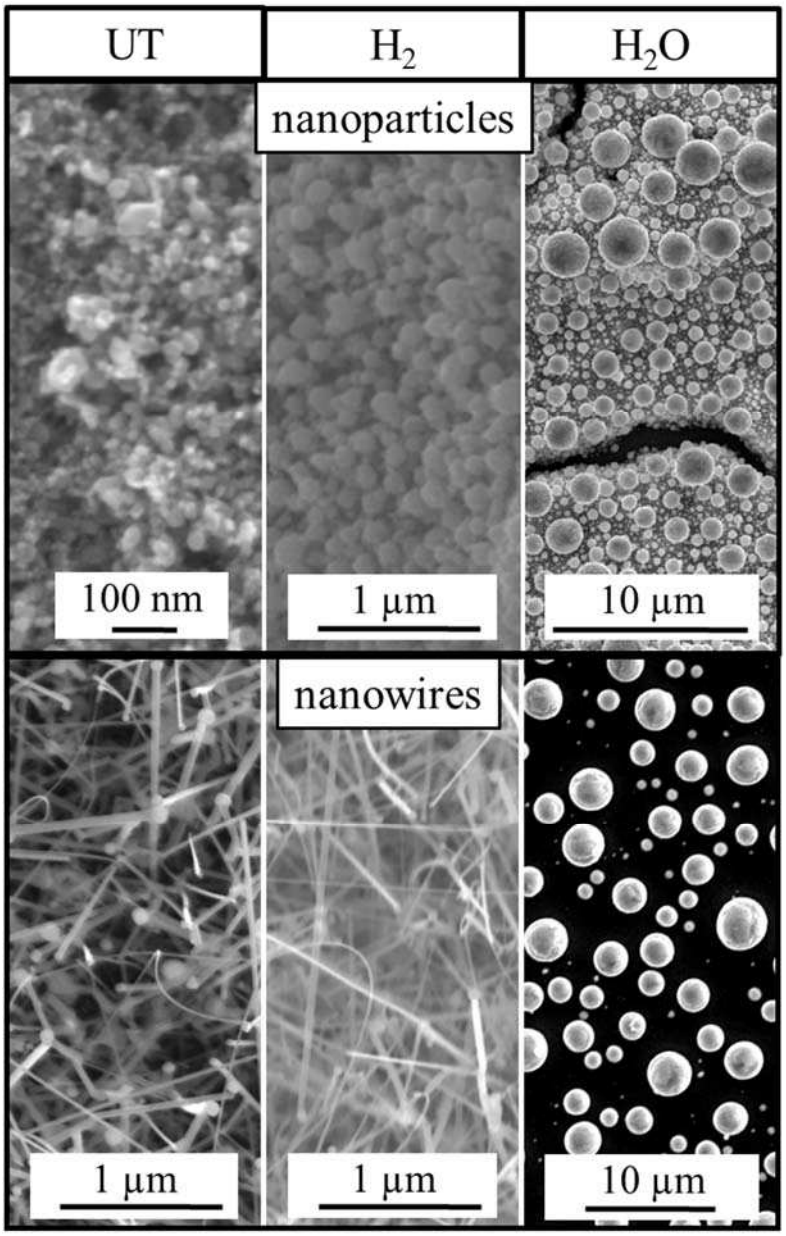

Figure 5.1. SEM images of SnO_2 nanoparticles (top) and nanowires (bottom) with untreated (left), H_2 plasma treated (middle), and H_2O plasma treated (right) (150 W, 80 mTorr, 5 min).

5.2.2. Determining changes in bulk structure and surface chemistry with plasma modification. As noted in Chapter 1 and Section 5.1, plasma treatment can effectively modify a range of materials, often with no change in substrate morphology or bulk structure. Here, we plasma treated the SnO_2 materials with H_2 for control and comparison to H_2O plasma treatments. Interestingly, tin reduction in the nanomaterials occurs upon H_2 plasma treatment confirmed by XPS shown in Figure 5.2. With H_2O plasma treated nanomaterials, this was verified by PXRD and XPS data shown in Chapter 4.[25] SEM images, Figure 5.1, show larger particles post-H_2 plasma treatment (diameters approaching 100 nm). Although the nanoparticles show slight changes in morphology after H_2 plasma modification, H_2 NW appear to have no structural changes, as the original wire dimensions are maintained post treatment. Notably, this is not the case after H_2O plasma treatment of either nanomaterial. Nanoparticles and nanowires form micron sized Sn aggregates [supported by EDS and XPS analyses (Chapter 4)],[25] whereby the discontinuous surface coverage leads to exposure of underlying zirconia. Although the images shown in Figure 5.1 are of materials treated in plasmas at the upper end of the power range evaluated here (150 W), our prior study in Chapter 4 showed that tin reduction and aggregation are observed to a lesser degree for P = 30-100 W H_2O plasmas.[25] Furthermore, materials characterization (e.g., SEM, XPS, PXRD)[25] showed different compositions and morphologies resulted from H_2O NP relative to H_2O NW. These data indicate that not only is the interaction of H_2O plasma with SnO_2 nanomaterials somewhat unexpected (i.e., a reductive rather than oxidative response), but it also varies with substrate morphology. These dramatic changes in morphology and composition can significantly affect the conductivity of plasma-treated materials for conductivity-dependent applications. Thus, further examination of plasma species

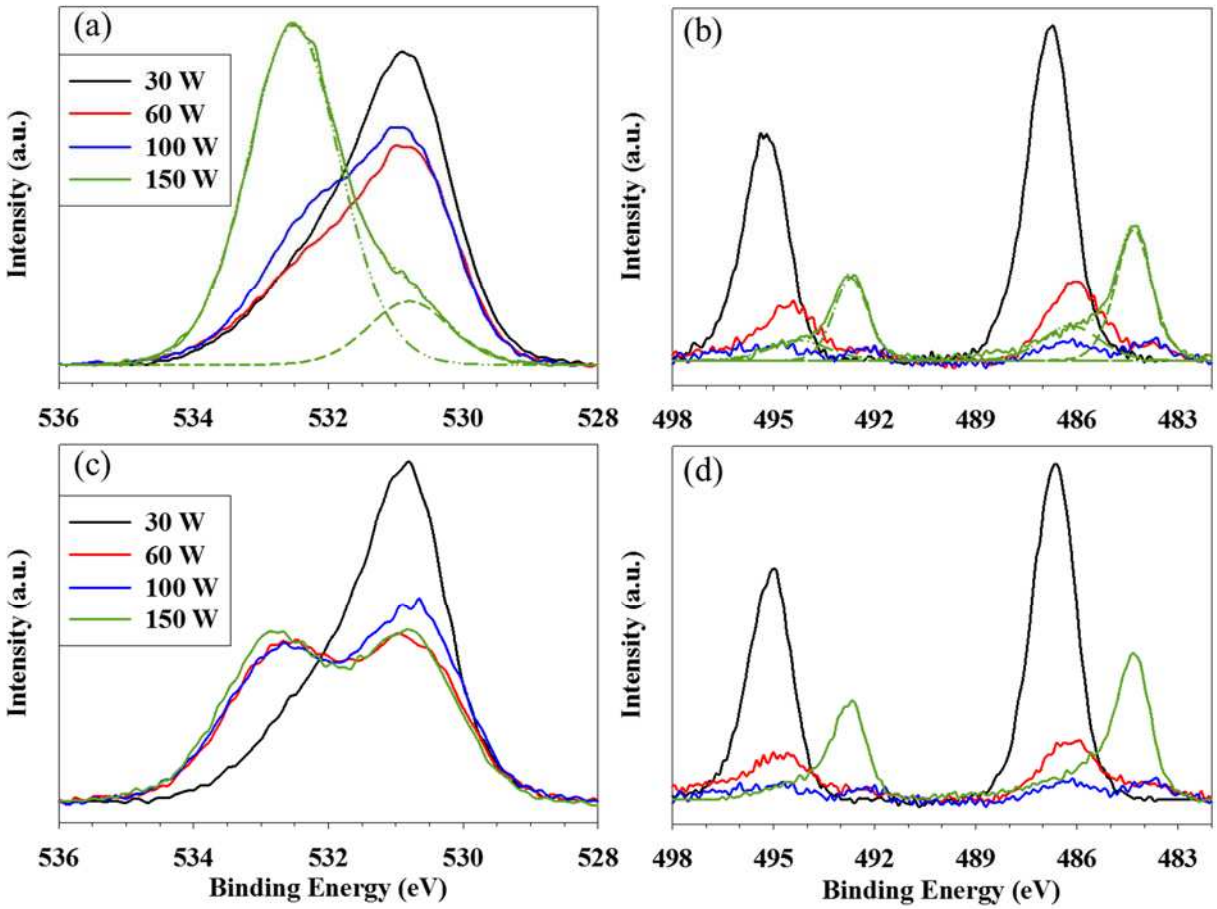

Figure 5.2. High resolution O_{1s} and Sn_{3d} XPS spectra of SnO_2 (a-b) nanoparticles and (c-d) nanowires treated with a H_2 plasma (80 mTorr, 5 min) at P = 30, 60, 100, or 150 W.

was needed to elucidate potential underlying causes controlling the extent of modification and corresponding materials properties and morphology.

5.2.3. Identification of plasma species. Initial gas-phase experiments focused on emission within the coil region of the reactor because our prior studies modified SnO_2 nanomaterials placed in the center of the plasma induction coil. For comparison, OES spectra were collected for both H_2 (our model reducing plasma system) and H_2O plasmas (the system previously used to modify SnO_2 nanomaterials) with no substrate in the plasma. OES spectra for H_2 plasmas, Figure 5.3, reveal emission arising only from hydrogen and argon species without a substrate present, where the H_α peak (656 nm) dominates the spectra. In H_2O plasmas, Figure 5.4, we witness emission from these species as well as oxygen-containing species, including OH radicals and O atoms, in the absence of a substrate. Regardless of the plasma precursor, addition of a nanomaterial to the plasma results in formation of OH* under all plasma powers. Although this finding is not surprising for H_2O plasmas because the precursor decomposition can easily lead to OH radical formation in the plasma,[11] OH* formation in H_2 plasmas is somewhat unexpected. Given that we do not measure OH* in the H_2 plasma when no substrate is present, OH* production is likely occurring through removal of oxygen from the SnO_2 nanomaterial. In addition to emission from OH*, we also observe formation of gas-phase Sn* atoms, Figure 5.3 (b), which must arise from interactions of plasma species with the SnO_2 nanomaterials. Specifically, Sn* is detected in H_2 plasmas at P = 100 and 150 W when treating nanomaterials. Detection of OH* and Sn* species clearly indicates H_2 plasmas behave as etching systems for SnO_2 nanomaterials, where the intensities of emission signals arising from Sn* and O*/OH* likely correlate to etching rates. These data indicate surface oxygen is selectively etched in H_2 plasmas at low P (only OH* observed), whereas at higher P, plasma species have sufficient

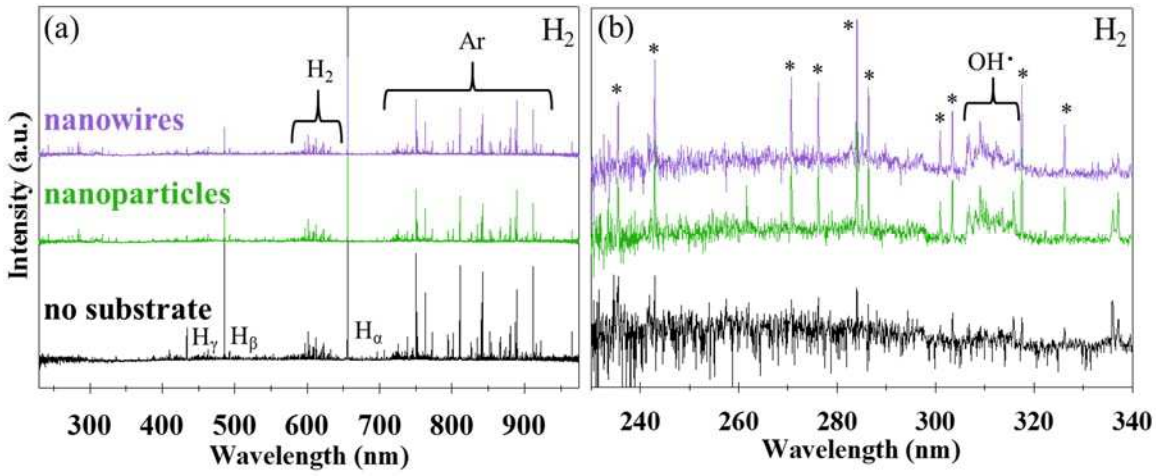

Figure 5.3. Raw OES spectra for the full spectral range (a) and a narrower range from 230-340 nm (b) for H_2 plasma treatments (150 W, 80 mTorr, 5 min) without a substrate, with SnO_2 nanoparticles, and with SnO_2 nanowires. Peaks are labeled with the corresponding species where * is used to label Sn peaks.

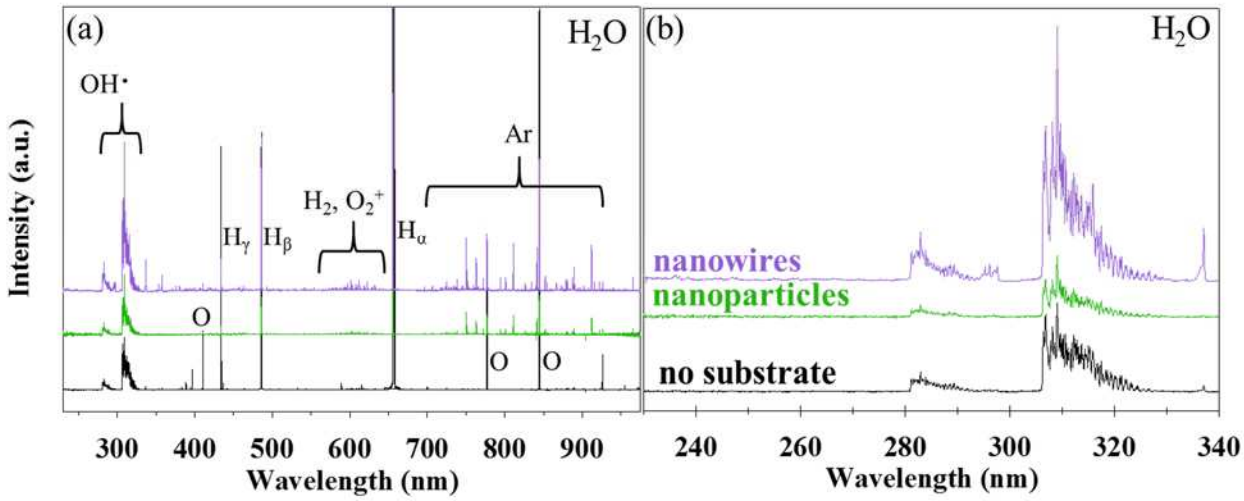

Figure 5.4. Raw OES spectra for the full spectral range (a) and a narrower range from 230-340 nm (b) for H_2O plasma treatments (150 W, 80 mTorr, 5 min) without a substrate, with SnO_2 nanoparticles, and with SnO_2 nanowires. Peaks are labeled with the corresponding species.

energy to remove both oxygen and tin (both OH* and Sn* observed). Nanomaterial morphology, or more specifically nanomaterial surface area, does not significantly affect etching in H_2 plasmas. Unfortunately, it is more difficult to determine if etching occurs during H_2O plasma treatment using OES spectra, because Sn is not detected in the gas phase and OH* is naturally formed in H_2O plasmas. Because of the gas-phase evidence of etching in H_2 plasmas we hypothesize that hydrogen plasma species (i.e., H*) in H_2 plasmas are more efficient at etching and/or are more energetic than those found in H_2O plasmas (at the same P).

5.2.4. The effect of substrate and plasma parameters on plasma temperatures. To gain further insight into the energetics of the two plasma systems we determined excited state T_R(OH) and T_V(OH) through simulation of spectral data, shown in Figure 5.5. Temperatures are calculated for OH because it is a species that changed more drastically than other species with different plasma parameters. Specifically, OH is always present in H_2O plasma, but is only observed in H_2 plasma in the presence of a SnO_2 substrate. Such changes in both the presence and intensity of gas-phase OH were further explored to determine if there were also differences in plasma temperatures for the given plasma parameters. Thus, within H_2 and H_2O plasmas OH is of particular interest as a diatomic species that can be modelled with LIFBASE software. Tables 5.1 and 5.2 provide the results of such simulations for a range of plasma parameter spaces. Under all conditions evaluated in H_2O plasmas, T_V(OH) ≈ 3600 K and T_R(OH) ≈ 2100 K with or without a substrate and regardless of substrate type. Some T_R(OH) and T_V(OH) values measured in H_2 plasmas appear to be within the same range as those calculated for H_2O plasma, whereas others appear to be greater than those in H_2O plasma. It is possible that all T_R(OH) and T_V(OH) values for H_2 and H_2O plasmas actually lie within the same range. Given the low OH emission peak intensity in the spectra for H_2 plasma, however, we are unable to achieve peak

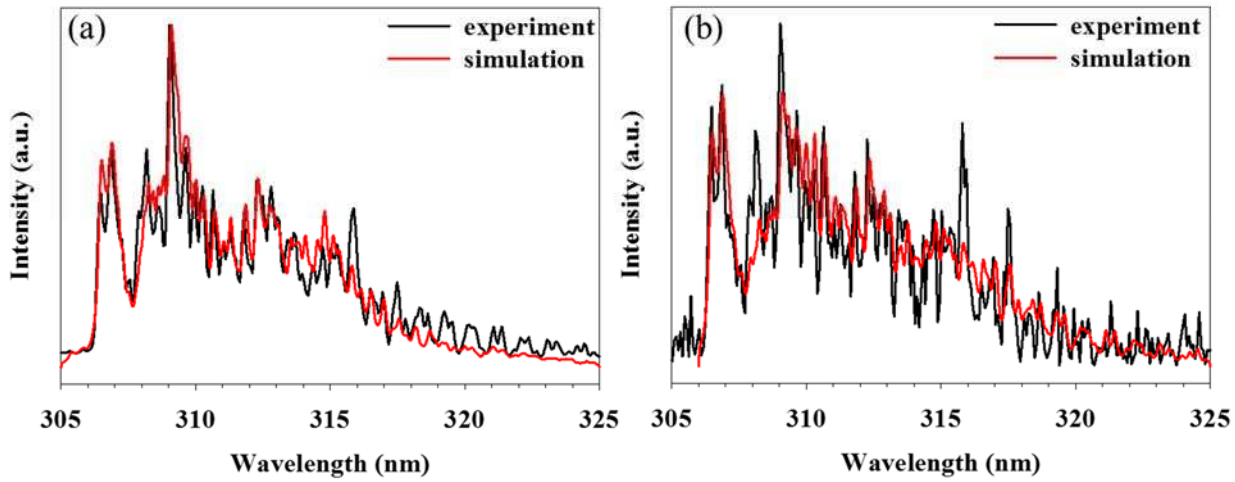

Figure 5.5. OH emission spectra fit with spectra simulated using LIFBASE for (a) H_2O/Ar plasma and (b) H_2/Ar plasma (150 W, 80 mTorr) with a nanowire substrate at the 4 min time point in a 5 min treatment.

Table 5.1. Rotational and vibrational temperatures for OH in the coil[a-b]

Precursor	Power (W)	Time Point (min)	T_R(OH) (K)			T_V(OH) (K)		
			no substrate	*particles*	*wires*	*no substrate*	*particles*	*wires*
H_2O/Ar	*30*	*0.5*	—	2130 (10)	2090 (10)	—	3610 (10)	3640 (10)
		4	2290 (20)	2150 (10)	2430 (20)	3540 (10)	3600 (10)	3670 (10)
	60	*4*	2550 (20)	2090 (10)	—	3510 (10)	3490 (10)	—
	100	*4*	2090 (30)	2120 (10)	—	3480 (10)	3480 (10)	—
	150	*0.5*	—	2280 (10)	2070 (10)	—	3560 (10)	3660 (10)
		4	1740 (30)	2040 (10)	2100 (10)	3460 (10)	3490 (10)	3650 (10)
H_2/Ar	*100*	*4*	—	2330 (20)	3220 (30)	—	3970 (30)	3740 (30)
	150	*0.5*	—	1800 (40)	3570 (30)	—	3930 (30)	3630 (30)
		4	—	3050 (20)	5400 (20)	—	4020 (20)	3450 (20)

[a]Time points were chosen for comparison during a 5 min total treatment time. [b]Errors denoted in parentheses are percent (relative) uncertainty calculated from standard deviation of the experimental trials or propagated through several trials arising from error associated with the calculated spectral fits, reporting whichever was largest.

Table 5.2. Rotational and vibrational temperatures for OH[a-c]

Power (W)	T_R(OH) (K)		T_V(OH) (K)	
	H_2O	H_2O/Ar	H_2O	H_2O/Ar
30	2740	2290 (20)	3740	3540
60	3410	2560	3760	3510
100	1900	2090 (30)	3750	3480
150	2100 (40)	1740 (30)	3780	3460

[a] Temperatures given are for plasma systems (no substrate). All temperatures were calculated at the 4 min time point in a 5 min treatment. [b]Errors denoted in parentheses are percent (relative) uncertainty calculated from standard deviation of the experimental trials. [c]For values that do not have an error reported in parentheses, the estimated error is 10% (relative) uncertainty propagated through several trials arising from error associated with the calculated spectral fits. [If error is reported as 10%, this indicates experimental reproducibility (standard deviation) or error was less than that inherent in the fits in LIFBASE software.]

correlations ≥0.9, which we were routinely able to do when fitting spectra from H_2O plasmas. The limited signal intensity is likely a result of two experimental factors: (1) emission being collected for a cross-section of the reactor instead of coaxially along the length of the reactor and (2) the small substrate surface area relative to the total volume of the plasma reactor. Overall, the higher OH signal intensity in H_2O plasmas allows for less variation from trial to trial.

T_R(OH) and T_V(OH) values have been measured in other plasma systems under various conditions. Some studies have used OES and LIFBASE to match experimental spectra with simulated spectra to determine rotational temperatures for excited state species, whereas others have used laser-induced fluorescence techniques to examine rotational temperatures of ground state species. T_R(OH) values reported for excited state and ground state OH in these reports range from 350-800 K with T_V(OH*) = 1550 - 6500 K.[14, 32-34] These results suggest that although our plasma systems have vibrational temperatures aligned with other plasma systems, the H_2O and H_2 plasmas examined in this work are rotationally hotter than previously observed. This may be a result of the plasma precursor and reactor systems being different than those utilized in other reported research. For example, Bruggeman and coworkers measured OH radicals in atmospheric pressure plasmas,[21, 32] which are much more likely to result in sufficient collisions to reduce rotational temperatures to roughly room temperature. In other studies, OH radicals were formed through the collision of O_2 with an organosiloxane;[33, 34] thus, the bimolecular collision formation mechanism could influence the internal temperature of reaction products. Similarly, in our system, the SnO_2 nanomaterials create yet another pathway (i.e., as opposed to unimolecular decomposition of H_2O) for formation of both ground state and excited state OH, again potentially influencing the internal temperatures of the OH radical.

5.2.5. Plasma species capable of etching SnO_2. Given the plasma temperatures calculated for the precursor systems, it is useful to consider which gas species have the potential to be etchants in both plasma systems. H* and Ar* are the most likely etchants as they are the most abundant species present within H_2 plasmas (other than H_2) and are also present in H_2O plasmas. Argon species (Ar, Ar^+, ArH^+) also have the potential to etch SnO_2 within either plasma system. Although we cannot rule out a small contribution from Ar^+ and ArH^+ ion-assisted etching, we do not believe this is a significant factor given the low ionization of our plasmas (ion species density << radical species density << neutral species density).[35] Furthermore, if Ar species were the primary etchants, we might anticipate detecting O* (g), even without a substrate in the plasma as etching of the SiO_2 reactor walls would likely also be occurring. Although the lattice energies of SiO_2 and SnO_2 are not the same (lattice energy of SiO_2 is ~1.2 times larger than the lattice energy of SnO_2 based on a basic calculation[36]), it seems plausible that some reactor wall etching would occur if Ar^+ or ArH^+ were significant etchants. Given that etching is observed in the absence of Ar in the feedgas, this leads to the conclusion that hydrogen atoms are likely the primary etchant in H_2 plasmas. A potential mechanism is shown in reactions 1-3, wherein • indicates a radical site formed on the nanomaterial surface.

$$H_2^* (g) \rightarrow 2\ H^* (g) \quad (1)$$

$$H^* (g) + SnO_2 (s) \rightarrow OH (g) + \bullet SnO (s) + e^- \quad (2a)$$

$$OH (g) + e^- \rightarrow OH^* (g) + e^- \quad (2b)$$

$$4H^* (g) + SnO_2 (s) \rightarrow Sn (g) + 2H_2O (g) \quad (3a)$$

$$Sn (g) + e^- \rightarrow Sn^* (g) + e^- \quad (3b)$$

A similar process likely occurs in H_2O plasmas with the source of H* being H_2O.

5.2.6. Examining relative species densities as a function of plasma parameters and presence of a substrate. Further spectral comparison explored how plasma parameters affect the intensity of specific gas species in both plasma systems and to elucidate further details about the H_2O plasma systems indiscernible from observing the raw spectra alone. Thus, we performed actinometric calculations to determine I_H/I_{Ar}, I_{OH}/I_{Ar}, I_{Sn}/I_{Ar}, and I_{H2}/I_{Ar} (i.e., relative species concentrations) for a range of *P* for both plasma precursor systems and nanomaterials. Measurements were made in two locations, the center of the coil region and 26.5 cm downstream from the coil. Given the experimental limitations of cross-sectional detection and small sample size, all I_{Sn}/I_{Ar} values measured in H_2 plasma were the same (Sn* was not detected above of the noise in H_2O plasma), within experimental error, regardless of substrate morphology. Similarly, I_{OH}/I_{Ar} values measured in H_2 plasmas were the same within error at all *P* for nanowires and nanoparticles. Figure 5.6 shows [OH*] remains relatively constant over the 5 min treatment for all H_2O plasma conditions when treating nanomaterials in the coil. H_2O plasmas with nanowire substrates generate higher [OH*] than plasmas containing nanoparticles, especially at lower *P*. Furthermore, H_2O plasma systems have the highest [OH*] at $P = 30$ W when treating nanoparticle substrates, whereas the greatest [OH*] occurs at $P = 60$ W when treating nanowires. These different *P* at which maximum [OH*] is observed indicate H_2O plasma species interact differently with SnO_2 nanoparticles than nanowires.

Another metric of interest to compare between the two plasma systems is [H*] measured in the coil, Figure 5.7. For H_2 plasmas, [H*] remains constant over the 5 min treatment time for treatment of nanoparticles and nanowires at all *P*. Both materials show the highest [H*] at 30 W, with [H*] for $P = 60$-150 W being essentially the same, regardless of *P*. The observation of higher [H*] at $P = 30$ W may indicate that H atoms are less likely to recombine at lower *P* than

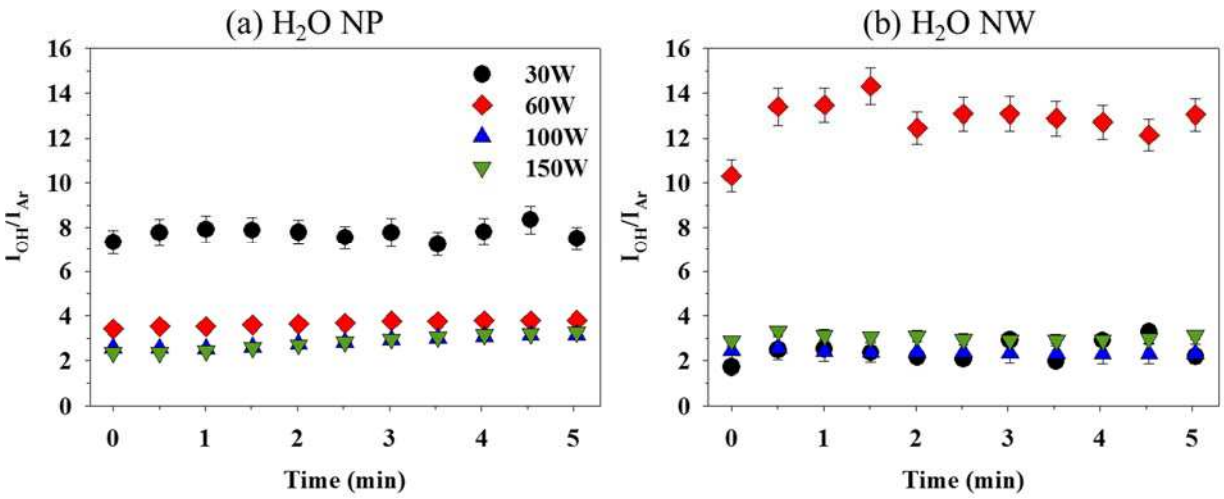

Figure 5.6. Relative OH* concentration as a function of time and *P* in H_2O plasma treatment of (a) SnO_2 nanoparticles and (b) SnO_2 nanowires, all at 80 mTorr total system pressure.

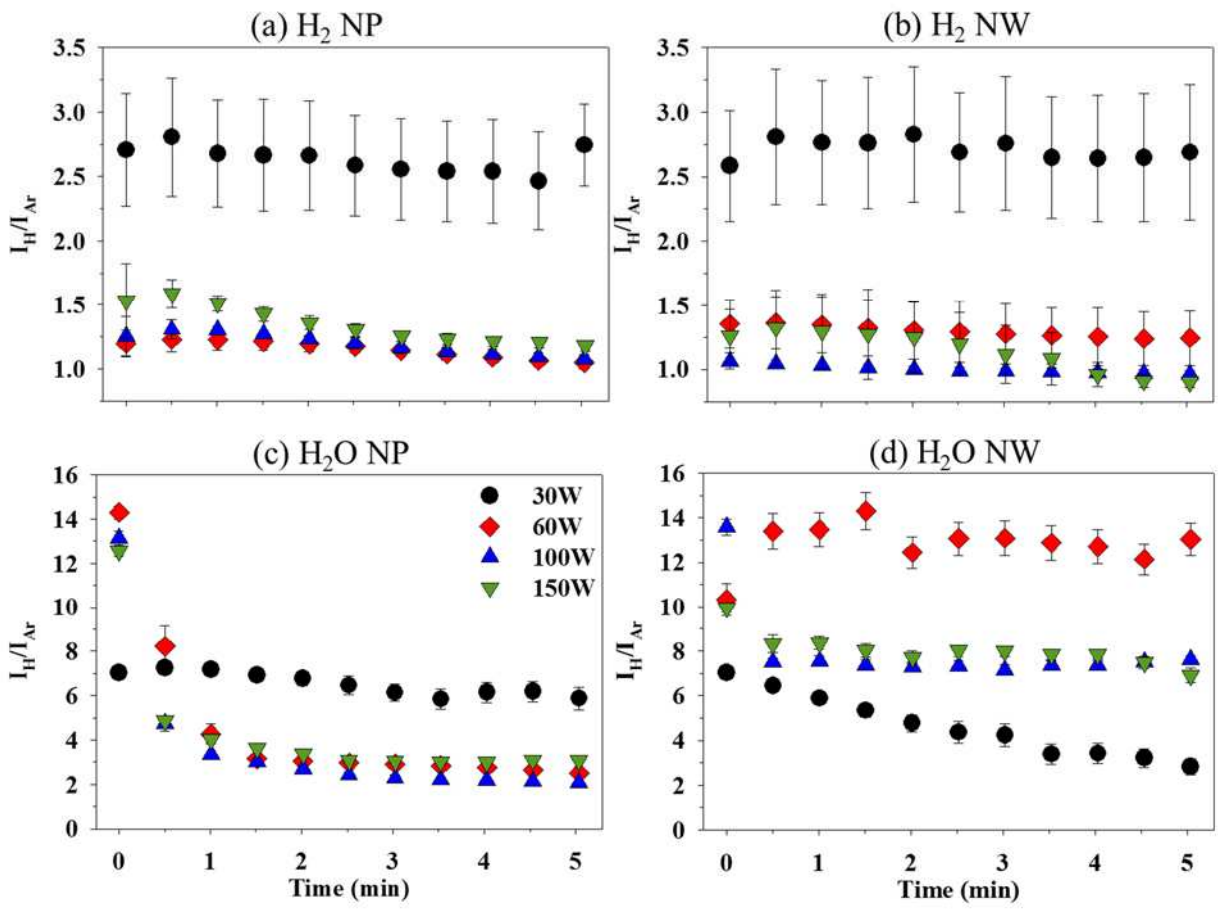

Figure 5.7. Relative H* concentration as a function of time and plasma power in H_2 plasma treating (a) SnO_2 nanoparticles and (b) SnO_2 nanowires and in H_2O plasma treating (c) SnO_2 nanoparticles and (d) SnO_2 nanowires, all at 80 mTorr total system pressure.

at $P \geq 60$ W in H_2 plasmas.[37, 38] Although higher [H_2*] (I_{H2}/I_{Ar} data shown in Figure 5.8) at $P = 30$ W is also observed, indicating low H_2 dissociation, these two trends may suggest that less H_2 dissociation occurs at 30 W than at higher powers, but once dissociation occurs, the H* is less likely to recombine. In contrast, [H*] changes dramatically in H_2O plasmas depending on the type of substrate being treated and as a function of time, Figure 5.7 (c-d). These [H*] variations, or lack thereof, are indicative of the increased likelihood of H atoms to react and form additional hydrogen species in the gas phase of H_2O plasmas as compared to H_2 plasmas.[37, 39, 40] Furthermore, observed decreases in [H*] suggest it reacts to form OH*, H_2*, and other hydrogen species (e.g., H^+*).

Under similar plasma parameters, [H*] ≥ [OH*] in both plasma systems, with higher [H*] and [OH*] on average measured in the H_2O plasma than in the H_2 plasma, Figures 5.6 and 5.7. Such results are consistent with the persistent source of hydrogen atoms in both systems. In H_2O plasmas, H* is less likely to recombine to form H_2* than it is in H_2 plasma (as indicated in Figure 5.8). Additionally, we detect higher [OH*] in H_2O plasmas than in H_2 plasmas as H_2O plasma can form OH* whether or not SnO_2 is present. Thus, with a SnO_2 nanomaterial substrate, H_2O plasmas have two oxygen sources: H_2O, which is continuously flowing, and the nanomaterial from which oxygen can be abstracted. In contrast, H_2 plasmas have only a single source of oxygen (the nanomaterial substrate). Formation of OH radicals, therefore, can occur continuously during H_2O plasma treatments, but the nanomaterial may serve as a limiting reagent in H_2 plasmas, especially if all surface oxygen is removed from the nanomaterial.

Interestingly, we detect more [H*] than [OH*], or at least equivalent concentrations, in H_2O plasmas. Specifically, [H*] ≈ [OH*] in H_2O plasmas with nanoparticles, but with nanowires, under the majority of P conditions (i.e., 100 and 150 W), [H*] ≥ [OH*]. These data

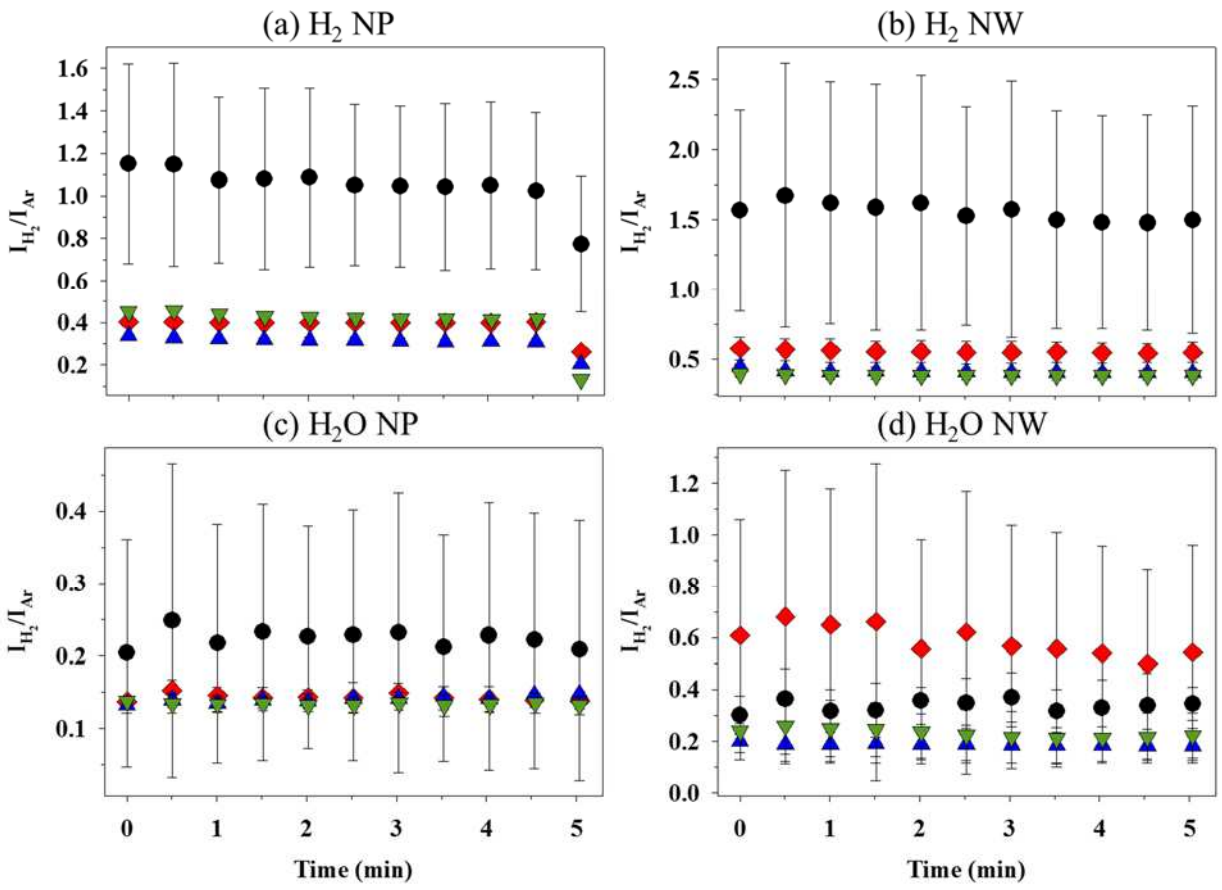

Figure 5.8. Relative H_2* concentration as a function of time and plasma power in H_2 plasma treating (a) SnO_2 nanoparticles and (b) SnO_2 nanowires and in H_2O plasma treating (c) SnO_2 nanoparticles and (d) SnO_2 nanowires, all at 80 mTorr total system pressure.

demonstrate that at lower *P*, the H_2O plasma tends to contain more oxidizing species (e.g., OH radicals), whereas at higher *P*, it contains more reducing species (e.g., H atoms). Furthermore, reducing species concentrations (i.e., H*) are significantly higher when treating nanowires in H_2O plasmas, than when treating nanoparticles. These differences in reducing species concentrations may contribute to the observed tin reduction and morphological changes in nanowires over a wider range of plasma parameters than found with nanoparticles.[25] Overall, the predominance of H* over OH*, the presence of Sn in the gas phase, and surface characterization data (SEM and XPS data presented in this study as well as our prior study (Chapter 4)[25]) collectively demonstrate that at high *P*, H_2O plasma treatments of SnO_2 nanomaterials remove nearly all lattice oxygen, leaving behind mainly Sn in an altered morphology with minimal adsorbed oxygen.[25] Thus, these data support the hypothesis that H_2O plasma conditions used to modify SnO_2 nanomaterials are more reducing than oxidizing in nature, making them very similar to H_2 plasmas.

5.2.7. Observing relative plasma species densities along the length of the reactor. To determine if the gas-phase trends observed in the coil region were the same in the plasma afterglow, we monitored gas-phase species 26.5 cm downstream for a subset of parameters (i.e., power and nanomaterial type), Figure 5.9. All [Sn*] detected downstream remained within error of [Sn*] measured in the coil (data not shown), indicating that Sn atoms removed from the substrate likely remain in the gas phase or react with the surface at the same rate they are being removed. Contrary to results for [Sn*], higher [OH*] was measured downstream compared to that measured in the coil for 60 and 150 W H_2 and H_2O plasmas in the presence of nanoparticles. Specifically, downstream [OH*] in H_2 plasmas are consistently three to four times greater than in the coil throughout the 5 min treatment, whereas those in H_2O plasmas are only ~0.8 to 1.2 times

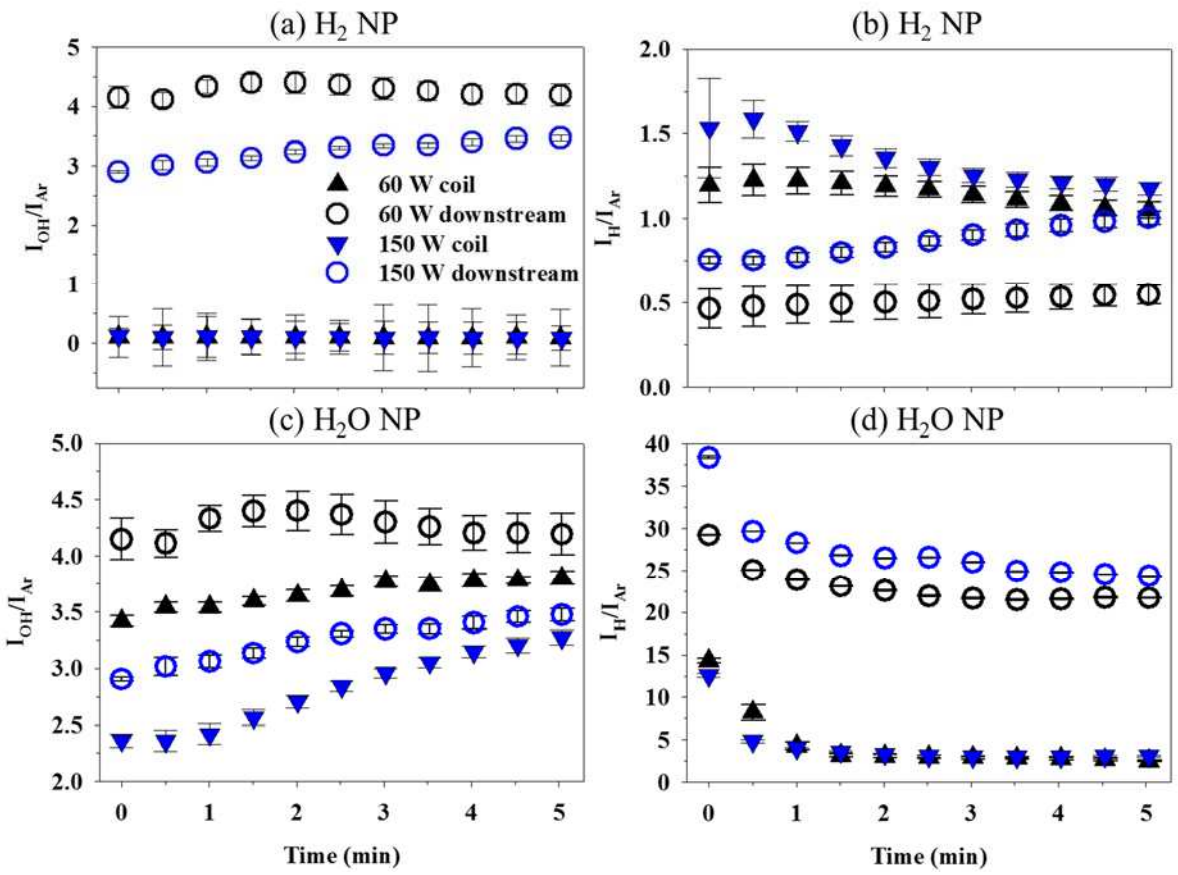

Figure 5.9. Relative OH* concentration in (a) H_2 plasma and (c) H_2O plasma and relative H* concentration in (b) H_2 plasma and (d) H_2O plasma as a function of time, power, and in the coil versus downstream for SnO_2 nanoparticles.

greater than in the coil. [OH*] downstream and in the coil remains relatively constant over the 5 min H_2 plasma treatment, but shows an increase over time in H_2O plasmas. Despite these differences, [OH*] ranges from 0-4 for all plasma parameters in both H_2 and H_2O plasma systems. Given greater [OH*] downstream than in the coil in H_2 plasma and minimal oxygen remaining in the nanomaterials post-treatment, it is probable that OH* forms in the coil, moves downstream, and is removed from the reactor with limited interactions with SnO_2.

Additional insight into the two plasma systems arises from comparing [H*] downstream and in the coil, Figure 5.9 (b, d). In H_2 plasmas with nanoparticles, [H*] in the coil region is approximately twice that measured downstream, as expected given the constant source of H_2 gas which can dissociate to form H* in the coil. Further downstream, H atoms can react with the SnO_2 surface to form OH*, or recombine to form H_2* as shown in the Figure 5.3 OES spectra. Moreover, [H*] remains constant over the 5 min treatment for 60 W, suggesting an equilibrium is reached between production and/or reaction of hydrogen in the coil and downstream. In 150 W H_2 plasmas with nanoparticles, however, [H*] in the coil decreases as downstream [H*] increases, converging at ~1 over the 5 min treatment. These concentration trends at 150 W indicate that over time, hydrogen is reacting to form new species and/or is not forming in the coil as quickly as it is forming/moving downstream.[37, 38] Although it is difficult to distinguish H_2* formed from the precursor gas versus H recombination, our data indicate [H*] ~1 in the coil, whereas [OH*] ~4 downstream from the coil, corroborating the possible reaction of O* and H* to form OH*. These trends are not observed in H_2O plasmas during treatment of nanoparticles, as [H*] is ~8 times higher downstream than in the coil. Additionally, [H*] remains relatively constant over the 5 min treatments. Notably, downstream [H*] in H_2O plasmas with nanoparticles is an order of magnitude larger than for H_2 plasmas, regardless of sampling

location. These differences between plasma systems suggest that once H* is formed in H_2O plasmas, it is more likely to either remain unreacted or form OH* after interacting with a nanomaterial surface than it is to recombine into H_2*, as observed in H_2 plasmas (Figures 5.3 and 5.4).[38]

Although the downstream experiments were only completed at P = 60 and 150 W and only for SnO_2 nanoparticles, we believe similar trends can be inferred for 30 and 100 W treatments. Likewise, the species concentrations measured downstream for H_2 and H_2O plasmas when treating nanoparticles will be similar when treating nanowires. This is feasible because the same etching process (i.e., etchants and the corresponding species being etched) occurs with both materials and only differs in its P dependence. As such, we expect any tin and oxygen etched from the nanowires to undergo similar reactions, and thus we anticipate detecting similar gas-phase species as those described above for H_2 and H_2O plasma treated nanoparticles.

5.3. Summary and Conclusions

Measurements of Sn*, OH*, and H* species in H_2 and H_2O plasmas clearly revealed the etching and reducing nature of H_2 and H_2O plasmas when interacting with SnO_2 nanomaterials. Specifically, the detection of both OH* and Sn* in the gas phase of H_2 plasmas provides direct evidence that H_2 plasmas, and by extension H_2O plasmas, etch SnO_2. Moreover, in conjunction with prior surface analysis data,[25] the gas-phase data presented here indicate H_2 plasmas reduce Sn as expected.[41] We also found greater [OH*] in H_2O plasmas when treating nanoparticles than when treating nanowires, further suggesting the materials are etched differently over the P range studied. These data support the hypothesis that H atoms react with SnO_2 nanomaterials in H_2 plasmas independent of morphology, whereas such reactions are substrate dependent in H_2O

plasmas. Downstream OES measurements show H atoms are more likely to recombine in H_2 plasmas than in H_2O plasmas. Notably, comparison of coil and downstream OES data indicates that under nearly all plasma conditions explored, equivalent or higher concentrations of reducing species are formed in H_2O plasmas when treating SnO_2 nanoparticles and nanowires. Thus, this study reveals that H_2O plasmas reduce SnO_2 nanoparticles and nanowires when reducing species, such as H atoms, exist in greater concentrations than oxidizing species (i.e., O*, OH*). Although this may seem an obvious conclusion, this is the first study to directly demonstrate the underlying chemistry leading to the outcome of Sn reduction in H_2O plasmas generally thought to be oxidizing in nature. Perhaps as important, these results indicate the concentrations of oxidizing and reducing species can be adjusted by changing *P* and sampling location within the reactor.

Further insight into the impact of nanomaterials on the gas phase in a plasma, and the corresponding SnO_2 nanomaterial modification mechanisms, could be gained through additional studies of plasma energetics and plasma-surface interactions.[42] Even without further study, however, these gas-phase diagnostics emphasize the necessity of comparing plasma gas-phase species with and without a substrate. Ultimately, these data provide critical information on plasma-surface interactions during materials modification that help elucidate how plasmas can be tuned to produce specific materials properties necessary for a chosen application.

REFERENCES

1. Oehrlein, G. S.; Phaneuf, R. J.; Graves, D. B. Plasma-Polymer Interactions: A Review of Progress in Understanding Polymer Resist Mask Durability During Plasma Etching for Nanoscale Fabrication. *J. Vac. Sci. Technol., B.* **2011**, *29* (1), 010801.
2. Gasparotto, A.; Barreca, D.; Bekermann, D.; Devi, A.; Fischer, R. A.; Maccato, C.; Tondello, E. Plasma Processing of Nanomaterials: Emerging Technologies for Sensing and Energy Applications. *J. Nanosci. Nanotechnol.* **2011**, *11* (9), 8206-8213.
3. Hawker, M. J.; Pegalajar-Jurado, A.; Fisher, E. R. Conformal Encapsulation of Three-Dimensional, Bioresorbable Polymeric Scaffolds Using Plasma-Enhanced Chemical Vapor Deposition. *Langmuir.* **2014**, *30* (41), 12328-12336.
4. Shahidi, S.; Ghoranneviss, M.; Moazzenchi, B. New Advances in Plasma Technology for Textile. *J. Fusion Energy.* **2014**, *33* (2), 97-102.
5. Patil, S. J.; Patil, A. V.; Dighavkar, C. G.; Thakare, K. S.; Borase, R. Y.; Nandre, S. J.; Deshpande, N. G.; Ahire, R. R. Semiconductor Metal Oxide Compounds Based Gas Sensors: A Literature Review. *Front. Mater. Sci.* **2015**, *9* (1), 14-37.
6. Zille, A.; Oliveira, F. R.; Souto, A. P. Plasma Treatment in Textile Industry. *Plasma Process. Polym.* **2015**, *12* (2), 98-131.
7. Cheruthazhekatt, S.; Černák, M.; Slavíček, P.; Havel, J. Gas Plasmas and Plasma Modified Materials in Medicine. *J. Appl. Biomed.* **2010**, *8* (2), 55-66.
8. Chien, H.-H.; Ma, K.-J.; Kuo, C.-H.; Huang, S.-W. Effects of Plasma Power and Reaction Gases on the Surface Properties of ePTFE Materials During a Plasma Modification Process. *Surf. Coat. Technol.* **2013**, *228* S477-S481.
9. Lota, G.; Tyczkowski, J.; Kapica, R.; Lota, K.; Frackowiak, E. Carbon Materials Modified by Plasma Treatment as Electrodes for Supercapacitors. *J. Power Sources.* **2010**, *195* (22), 7535-7539.
10. Stillahn, J. A.; Trevino, K. J.; Fisher, E. R. Plasma Diagnostics for Unraveling Process Chemistry. *Annu. Rev. Anal. Chem.* **2008**, *1* 261-291.
11. Trevino, K. J.; Fisher, E. R. Detection Limits and Decomposition Mechanisms for Organic Contaminants in Water Using Optical Emission Spectroscopy. *Plasma Process. Polym.* **2009**, *6* (3), 180-189.
12. Rahman, M. M.; Khan, S. B.; Marwani, H. M.; Asiri, A. M. A SnO_2-Sb_2O_3 Nanocomposite for Selective Adsorption of Lead Ions from Water Samples Prior to Their Determination by ICP-OES. *Microchim. Acta.* **2015**, *182* (3-4), 579-588.
13. Zheng, J.; Yang, R.; Xie, L.; Qu, J. L.; Liu, Y.; Li, X. G. Plasma-Assisted Approaches in Inorganic Nanostructure Fabrication. *Adv. Mater.* **2010**, *22* (13), 1451-1473.
14. Sarani, A.; Nikiforov, A. Y.; Leys, C. Atmospheric Pressure Plasma Jet in Ar and Ar/H_2O Mixtures: Optical Emission Spectroscopy and Temperature Measurements. *Phys. Plasmas.* **2010**, *17* (6), 063504.
15. Vassallo, E.; Cremona, A.; Ghezzi, F.; Ricci, D. Characterization by Optical Emission Spectroscopy of an Oxygen Plasma Used for Improving PET Wettability. *Vacuum.* **2010**, *84* (7), 902-906.
16. Donnelly, V. Plasma Electron Temperatures and Electron Energy Distributions Measured by Trace Rare Gases Optical Emission Spectroscopy. *J. Phys. D: Appl. Phys.* **2004**, *37* (19), R217-R236.

17. Cruden, B. A.; Meyyappan, M. Characterization of a Radio Frequency Carbon Nanotube Growth Plasma by Ultraviolet Absorption and Optical Emission Spectroscopy. *J. Appl. Phys.* **2005**, *97* (8), 084311.
18. Woo, Y. S.; Jeon, D. Y.; Han, I. T.; Lee, N. S.; Jung, J. E.; Kim, J. M. In Situ Diagnosis of Chemical Species for the Growth of Carbon Nanotubes in Microwave Plasma-Enhanced Chemical Vapor Deposition. *Diamond Relat. Mater.* **2002**, *11* (1), 59-66.
19. Caughman, J.; Baylor, L. R.; Guillorn, M. A.; Merkulov, V. I.; Lowndes, D. H.; Allard, L. Growth of Vertically Aligned Carbon Nanofibers by Low-Pressure Inductively Coupled Plasma-Enhanced Chemical Vapor Deposition. *Appl. Phys. Lett.* **2003**, *83* (6), 1207-1209.
20. Thomson, M.; Hodgkinson, J.; Sheel, D. Control of Zinc Oxide Surface Structure Using Combined Atmospheric Pressure-Based CVD Growth and Plasma Etching. *Surf. Coat. Technol.* **2013**, *230* 190-195.
21. Bruggeman, P.; Cunge, G.; Sadeghi, N. Absolute OH Density Measurements by Broadband UV Absorption in Diffuse Atmospheric-Pressure He-H_2O RF Glow Discharges. *Plasma Sources Sci. Technol.* **2012**, *21* (3), 035019.
22. Thomas, J. H. I. X-ray Photoelectron Spectroscopy Study of Hydrogen Plasma Interactions with a Tin Oxide Surface. *Appl. Phys. Lett.* **1983**, *42* (9), 794-796.
23. Jiang, J. C.; Lian, K.; Meletis, E. I. Influence of Oxygen Plasma Treatment on the Microstructure of SnO_x Thin Films. *Thin Solid Films.* **2002**, *411* (2), 203-210.
24. Srivastava, R.; Dwivedi, R.; Srivastava, S. K. Effect of Oxygen and Hydrogen Plasma Treatment on the Room Temperature Sensitivity of SnO_2 Gas Sensors. *Microelectron. J.* **1998**, *29* (11), 833-838.
25. Stuckert, E. P.; Fisher, E. R. Ar/O_2 and H_2O Plasma Surface Modification of SnO_2 Nanomaterials to Increase Surface Oxidation. *Sens. Actuators B.* **2015**, *208* 379-388.
26. Guyon, C.; Cavadias, S.; Mabille, I.; Moscosa-Santillan, M.; Amouroux, J. Recombination of Oxygen Atomic Excited States Produced by Non-Equilibrium RF Plasma on Different Semiconductor Materials: Catalytic Phenomena and Modelling. *Catal. Today.* **2004**, *89* (1), 159-167.
27. Tarlov, M. J.; Evans, J. F. Surface Characterization of Radio Frequency Water Plasma Treated and Annealed Polycrystalline Tin Oxide Thin Films. *Chem. Mater.* **1990**, *2* (1), 49-60.
28. Tarlov, M. J.; Evans, J. F.; Newman, J. G. Static SIMS and XPS Study of Water Plasma Exposed Tin Oxide Films. *Appl. Surf. Sci.* **1993**, *64* (2), 115-125.
29. Kumar, R. R.; Parmar, M.; Rao, K. N.; Rajanna, K.; Phani, A. Novel Low-Temperature Growth of SnO_2 Nanowires and Their Gas-Sensing Properties. *Scr. Mater.* **2013**, *68* (6), 408-411.
30. Golovin, A.; Davis, S.; Voorhees, P. Step-Flow Growth of a Nanowire in the Vapor-Liquid-Solid and Vapor-Solid-Solid Processes. *J. Appl. Phys.* **2008**, *104* (7), 074301.
31. Hitchman, M. L.; Jensen, K. F. *Chemical Vapor Deposition: Principles and Applications*. Academic Press London: 1993; Vol. 21.
32. Bruggeman, P.; Iza, F.; Guns, P.; Lauwers, D.; Kong, M. G.; Gonzalvo, Y. A.; Leys, C.; Schram, D. C. Electronic Quenching of OH (A) by Water in Atmospheric Pressure Plasmas and its Influence on the Gas Temperature Determination by OH (A–X) Emission. *Plasma Sources Sci. Technol.* **2009**, *19* (1), 015016.

33. Bogart, K.; Cushing, J.; Fisher, E. R. Effects of Plasma Processing Parameters on the Surface Reactivity of OH ($X^2\Pi$) in Tetraethoxysilane/O_2 Plasmas during Deposition of SiO_2. *J. Phys. Chem. B.* **1997**, *101* (48), 10016-10023.
34. Zhang, J.; Fisher, E. R. Surface Reactivity of OH Molecules During Deposition of SiO_2 from Siloxane-Based Plasmas. *J. Phys. Chem. B.* **2004**, *108* (28), 9821-9828.
35. Grill, A. *Cold plasma in materials fabrication*. IEEE Press, New York: 1994; Vol. 151.
36. Silberberg, M. S.; Duran, R.; Haas, C. G.; Norman, A. D. *Chemistry: The Molecular Nature of Matter and Change*. 6 ed.; McGraw-Hill Companies, Inc.: New York, 2012.
37. Thomas, L.; Jauberteau, J.; Jauberteau, I.; Aubreton, J.; Catherinot, A. Characterization of an Argon-Hydrogen Microwave Discharge Used as an Atomic Hydrogen Source. Effect of Hydrogen Dilution on the Atomic Hydrogen Production. *Plasma Chem. Plasma Process.* **1997**, *17* (2), 193-206.
38. Bouchoule, A.; Ranson, P. Study of Volume and Surface Processes in Low Pressure Radio Frequency Plasma Reactors by Pulsed Excitation Methods. I. Hydrogen–Argon Plasma. *J. Vac. Sci. Technol., A.* **1991**, *9* (2), 317-326.
39. Phillips, J.; Chen, C. K.; Mills, R. L. Evidence of Energetic Reactions Between Hydrogen and Oxygen Species in RF Generated H_2O Plasmas. *Int. J. Hydrogen Energy.* **2008**, *33* (10), 2419-2432.
40. Phelps, A. Collisions of H^+, H_2^+, H_3^+, ArH^+, H^-, H, and H_2 with Ar and of Ar^+ and ArH^+ with H_2 for Energies from 0.1 eV to 10 keV. *J. Phys. Chem. Ref. Data.* **1992**, *21* (4), 883-897.
41. Sabat, K.; Rajput, P.; Paramguru, R.; Bhoi, B.; Mishra, B. Reduction of Oxide Minerals by Hydrogen Plasma: An Overview. *Plasma Chem. Plasma Process.* **2014**, *34* (1), 1-23.
42. Blechle, J. M.; Cuddy, M. F.; Fisher, E. R. Effect of Ion Energies on the Surface Interactions of NO Formed in Nitrogen Oxide Plasma Systems. *J. Phys. Chem. A.* **2012**, *117* (6), 1204-1215.

CHAPTER 6

DESIGN AND OPTIMIZATION OF A GAS SENSING SYSTEM

This chapter describes the process of designing a gas sensor and gas sensing system for measuring resistance of a material when exposed to different gases. In particular, this system was designed for measuring the resistance of our SnO_2 nanomaterials. Details are provided for the necessary functions of both the sensor and sensing system. Additionally, the evolution of data analysis procedures is explained. Funding for this research was provided by the National Science Foundation (CHE-1152963).

6.1. Driving force behind metal oxide semiconductor (MOS) gas sensors.

MOS are often used for gas sensors given they are easy to fabricate and use, in addition to being capable of detecting both oxidizing and reducing gases. As described in Chapter 1, given their semiconductor nature, MOS sensors function based on changes in material resistance upon reactions between gases and surface adsorbed oxygen. As such it is necessary to have specific features in a gas sensing system to measure gas sensor performance.

6.2. Designing a resistance-based gas sensor and sensing system.

6.2.1. Desired features of gas sensors and a gas sensing system. Various sensing systems have been designed for examining sensor performance (i.e., sensitivity, response and recovery). It is, however, less common to find reports that explicitly describe system design or that provide sufficient detail on sensor fabrication to allow for system replication.[1-5] As such, we designed a method of sensor fabrication as well as a sensing system capable of meeting a

fundamental level of needs for performance tests of our materials. Specific features desired for the sensing system and chamber include:

For the sensing system

1. Multimeter and laptop with corresponding software for recording resistance
2. Gas line for air
3. Gas line for target gas
4. Sensing chamber to contain the sensor and gas
5. Flow meter for controlling gas flow
6. Pressure gauge
7. Exhaust line
8. Bubbler for visual of gas flow in case of pressures below pressure gauge
9. Back up chamber with venting for safety in case of leaks
10. Heater with temperature control/readout
11. Must be air tight for use with toxic gases

For the sensing chamber

1. Gas inlet and outlet
2. 2 re-sealable ports for connecting sensor electrodes to the multimeter
3. Sealable port for inserting a heater
4. Removable port for inserting and removing sensors
5. Sufficient volume to contain the heater with sensor, and movement of copper leads
6. Minimal volume for easier chamber evacuation
7. Withstand temperatures up to 300 °C

6.2.2. Designing a resistance-based gas sensing system. With the aid of the department glassblower, Mr. Michael Olsen, a glass sensor chamber (Figure 6.1 (a)) was designed and built with a volume of ~25 cm^3, similar to the volume of other systems reported in the literature.[6] A gas inlet and outlet port (½" Ultra Torr fittings) are on opposite sides of the main cylindrical part of the chamber near the bottom. Directly above the gas inlet port (in a downward facing triangle arrangement) are two ports with ¼" septa screw caps for inserting a single copper lead through each port. The copper leads were necessary to maintain a closed sensing system while measuring sensor resistance. Copper was used because of its high conductivity and relatively low reactivity in our gas environments; any potential variations resulting from gas interactions with copper should thus be minimal and constant given its use in all sensing experiments. The two septa ports are halfway up the height of the main chamber (~1.25"). A Rotaviss joint was used to easily open and reseal the system, necessary for inserting and removing sensors from the sensing chamber. Specifically, a 45/50 Rotaviss joint roughly the height of the main chamber is between the gas inlet and outlet ports, where the Rotaviss outlet port is a ¼" Ultra Torr port. A 25 mm x 50 mm Watlow Ultramic advanced ceramic heater with maximum temperature of 400 °C measured via a connected k-type thermocouple was chosen for its rapid response (see Figure 6.2 for specifications). The size of this heater allows for small movements of the sensor on the heater while connecting the electrodes to the copper wires such that the sensor does not easily fall off the heater. With the Rotaviss joint open and the heater wires disconnected, the wires were threaded through the outlet port such that when the Rotaviss joint is closed the heater will be inside of the center of the main chamber, Figure 6.1 (b). Copper wire was used to strengthen the wires from the heater to support it mid-air. Epoxy was used to enclose the system and secure the heater in the Rotaviss port.

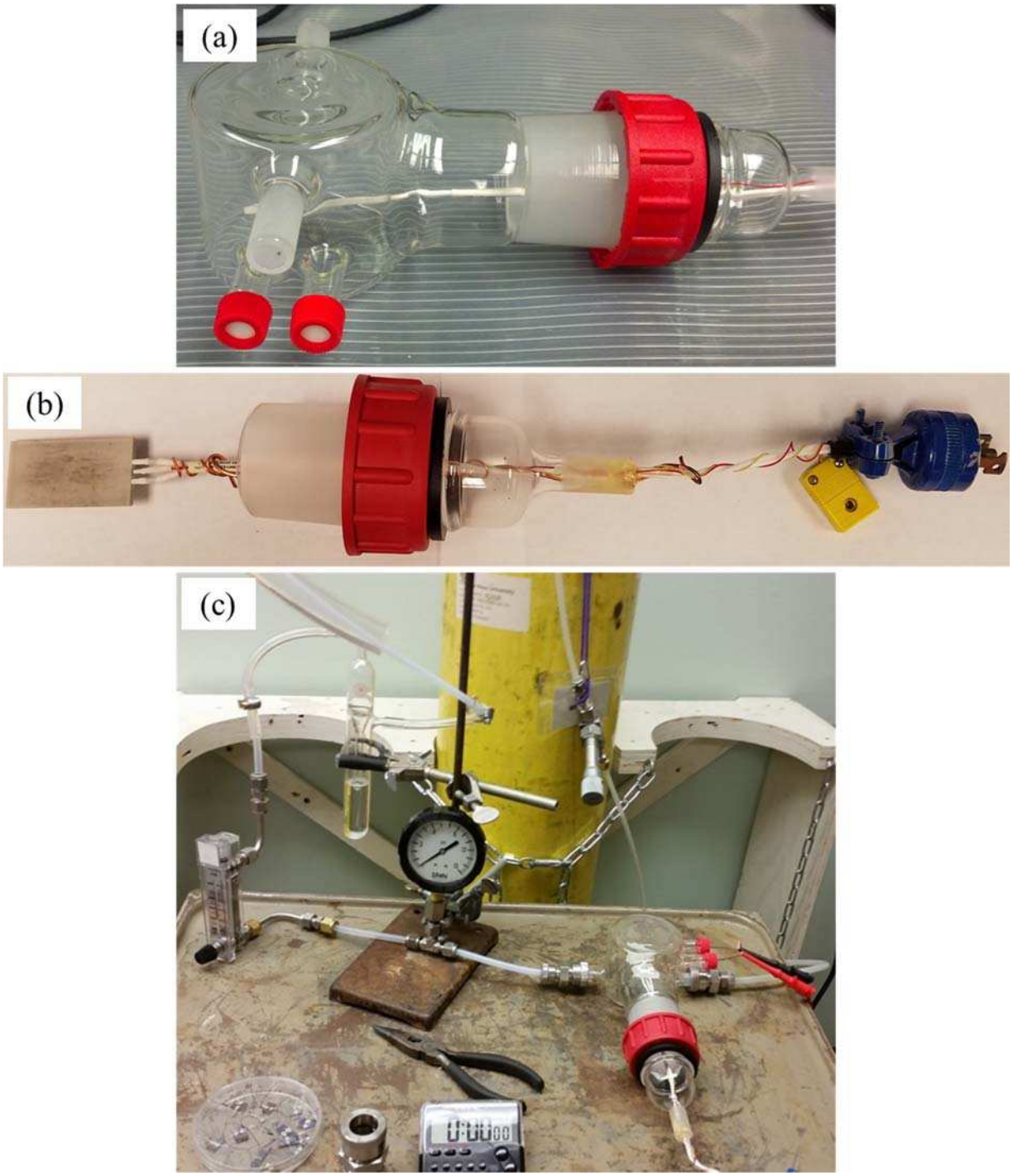

Figure 6.1. (a) Initial sensing chamber with ceramic heater inserted, (b) ceramic heater with wires glued into Rotaviss port, and (c) initial sensing system set-up.

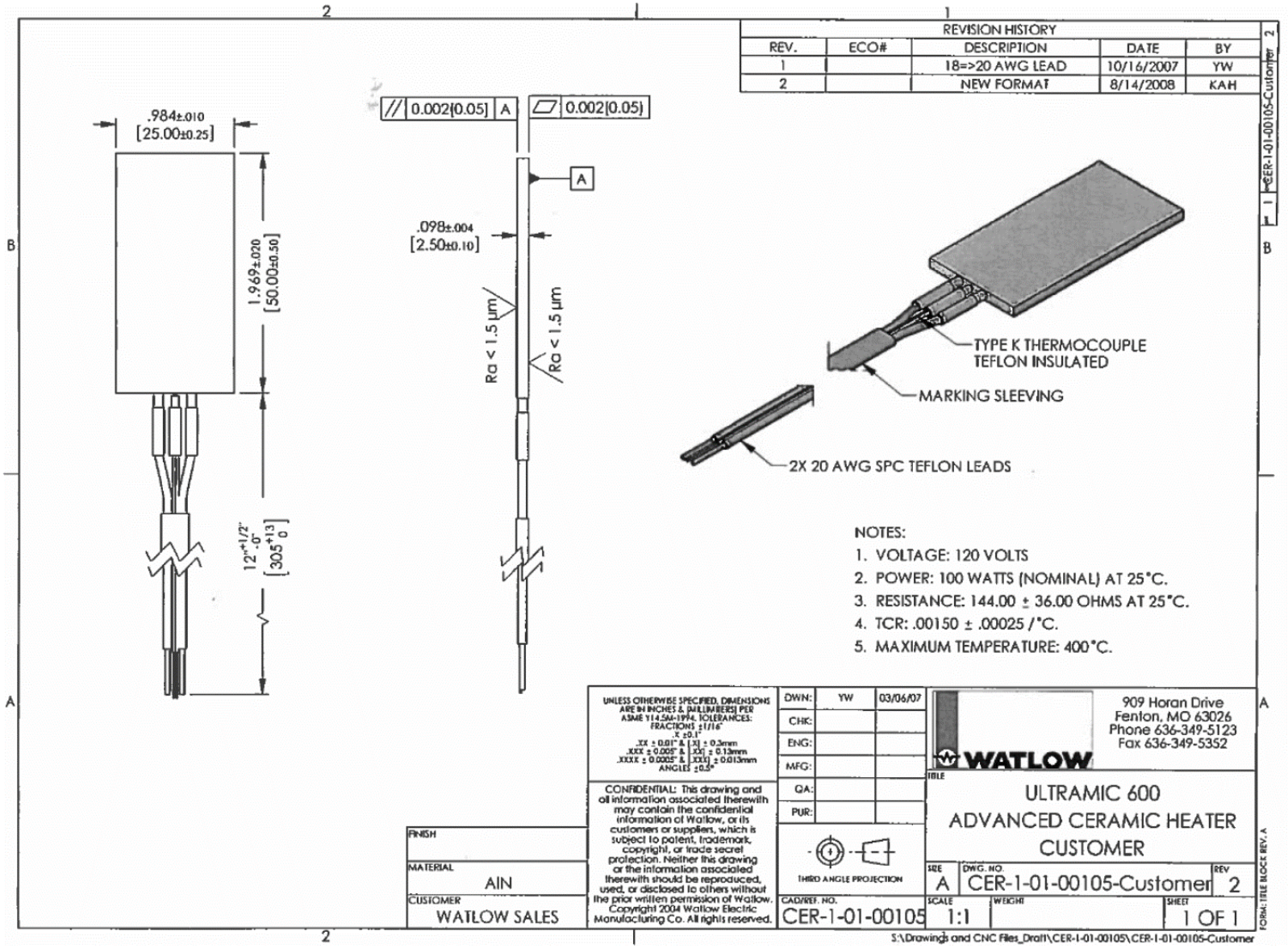

Figure 6.2. Watlow Ceramic Heater specifications.

Testing this initial sensing system, shown in Figure 6.1 (c), with the newly designed sensing chamber, revealed it was difficult to place sensors on the heater, insert both into the sensing chamber, and close the Rotaviss joint without the sensor falling off of the heater. As such, it was necessary to add an additional 45/50 Rotaviss joint on the top of the cylinder (Figure 6.3 (a)) for easier and more direct access to the heater when inserting and removing sensors from the sensing chamber. This top joint was created with a closed insert, unlike the side Rotaviss joint for the heater, to maintain a small volume (~25 cm^3) when adding the joint, see Figure 6.3 (b). Special hook/clamp leads were purchased for the multimeter, which helped to keep constant contact between the multimeter leads and the copper leads connected to the sensor, Figure 6.3 (c). When running initial sensor response studies and testing the heater capabilities, however, the heater would tend to droop enough such that contact between the electrodes and copper wires would change slightly. This shift in contact caused changes in resistance that would be potentially difficult to distinguish from resistance changes as a result of heating or gas-surface interactions. To eliminate potential shifts in heater location, a hollow ceramic cylinder ~1" tall was placed beneath the heater to provide consistent support of the heater and maintain constant contact between the electrodes and the copper wires, Figure 6.3 (d).

Extra safety containment for the sensing chamber was designed based on the principles of a functioning fume hood, whereby the exhaust line had sufficient pull to evacuate the inside of the safety containment. The walls are made of ½" thick plastic with holes drilled or cut out for the gas inlet and exhaust lines. The walls were attached by applying small amounts of dichloromethane along the edges to sufficiently melt the plastic while clamping the corners together. The walls were allowed to sit and dry for ~1 hour before removing the clamps. The

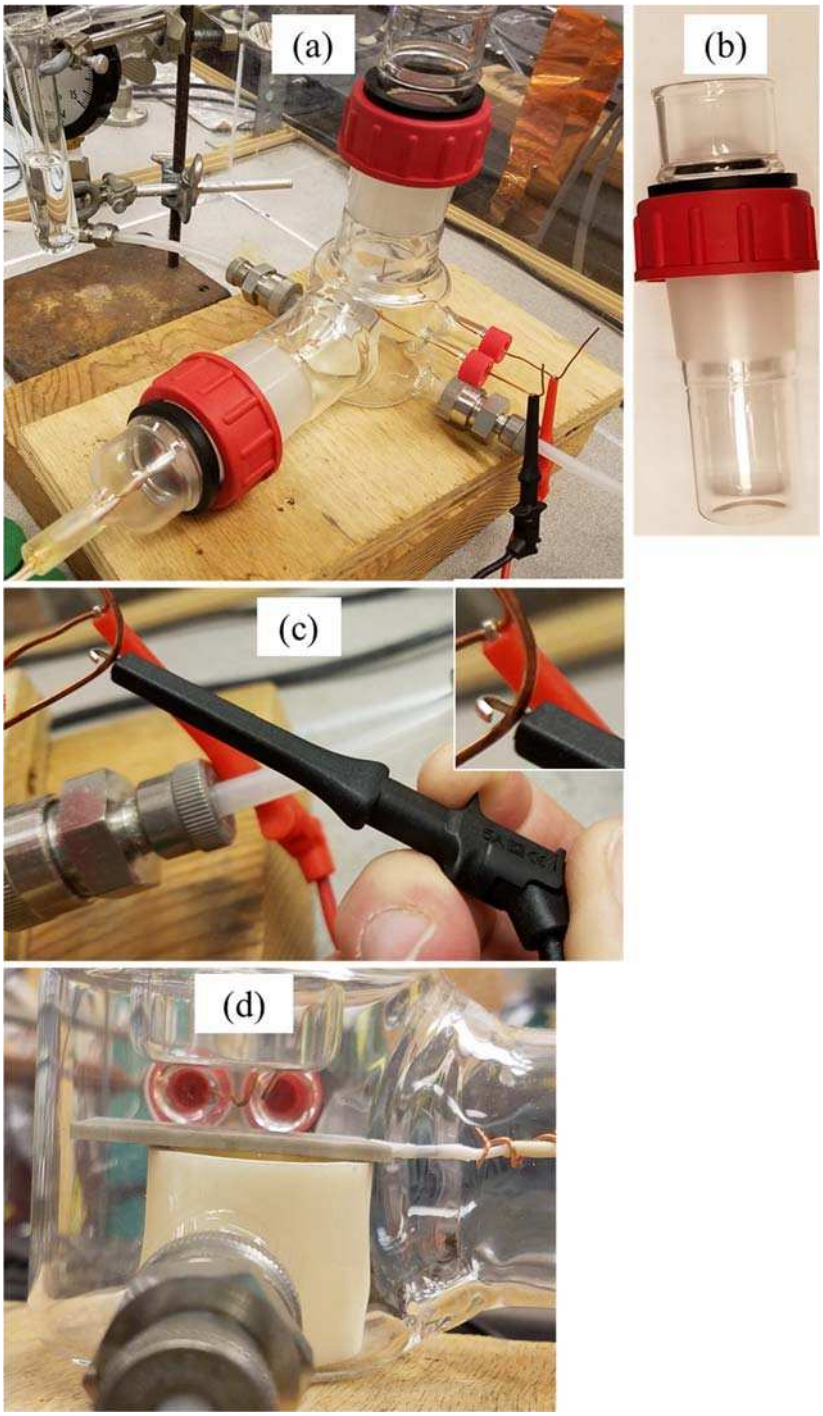

Figure 6.3. (a) Modified sensing chamber with additional Rotaviss joint as shown in (b), with multimeter clamp leads shown in (c) and (d) providing a close-up view of the heater sitting on a ceramic tube holding it in place across from the copper leads with the Rotaviss joint from above seating just above the copper leads.

completed containment and final sensing system are shown in Figure 6.4 (a), with a schematic to scale including dimensions in Figure 6.4 (b).

6.2.3. Sensor fabrication methodology for resistance measurements. Substrates chosen throughout the studies presented in this dissertation were approximately 1 x 1 cm^2, allowing sufficient surface area for completing necessary analyses and sensor fabrication while not using excessive amounts of materials. Silver conductive paste was used to attach ~1 cm long silver wires as electrodes to the substrate.[6-8] Silver was the chosen material for the paste and the wire as both are relatively inert and conductive but are more cost-efficient than alternatives such as Pt. The amount of conductive paste needed to securely attach wires to the substrates was found to be approximately the size of observed lead for a #2 pencil. This amount allowed for the wire end (~1-2 mm) to be completely encased in the paste and resulted in adequate surface area of paste in contact with the substrate surface after curing the paste for 1 hour at 120 °C. When less paste was used, electrodes tended to fall off of the substrate upon heating the sensor or applying slight pressure when connected to the copper lead. The silver wire was long enough to attach to the substrate and bend to maximize contact with a copper lead wire which was connected directly to the multimeter leads. The final sensor connected to the copper leads ready for testing performance is shown in Figure 6.5.

6.3. Sensor performance data analysis

To gain as much information as possible about changes in resistance as a function of temperature (T_S), as well as how a sensor will behave after being heated and cooled down, experiments were started at room temperature, with T_S gradually heated up to 300 °C and then gradually cooled back down to 25 °C. Representative raw resistance data collected during an

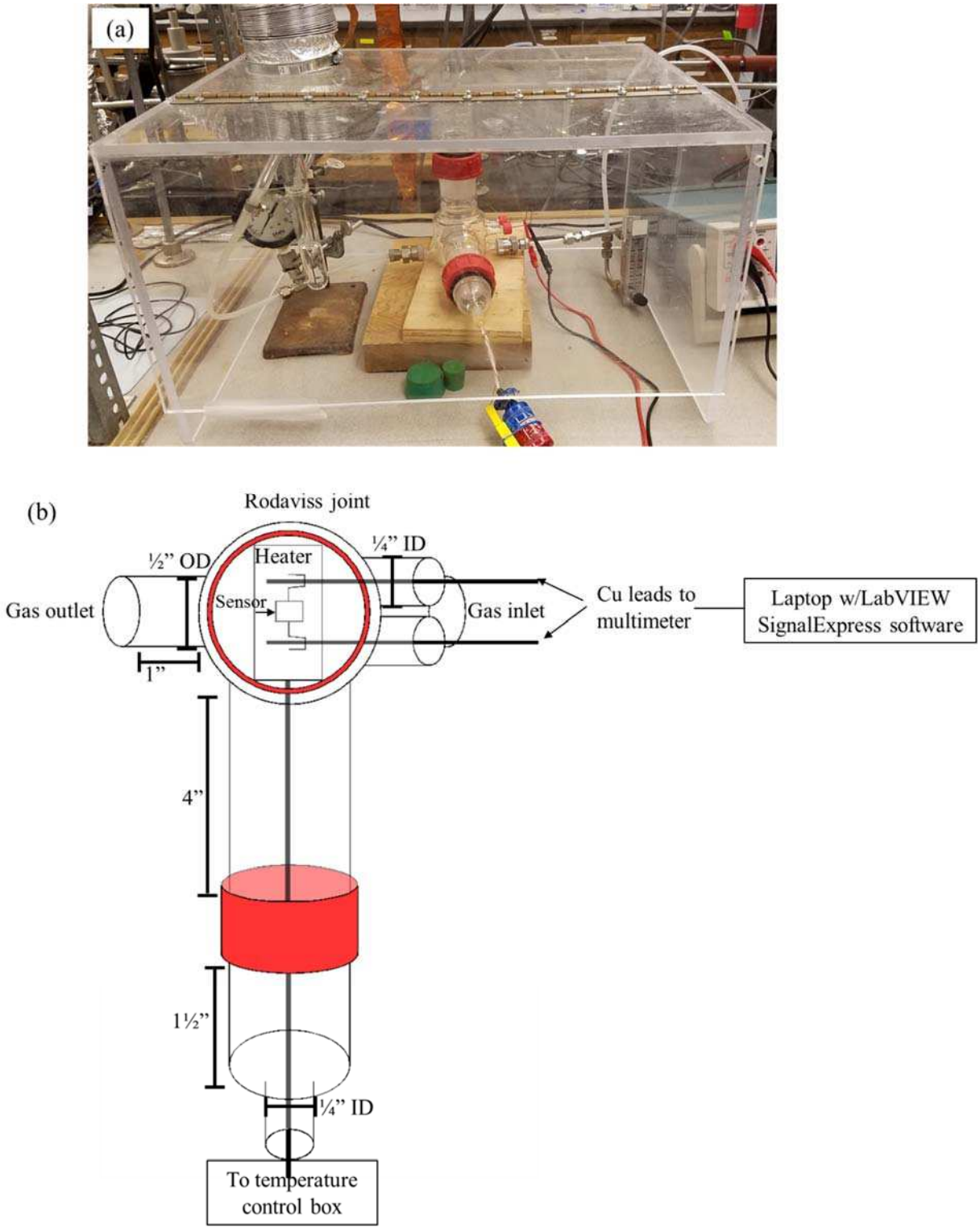

Figure 6.4. The final sensing system set-up and containment (a) and a schematic to scale with corresponding dimensions (b). (OD-outer diameter, ID-inner diameter)

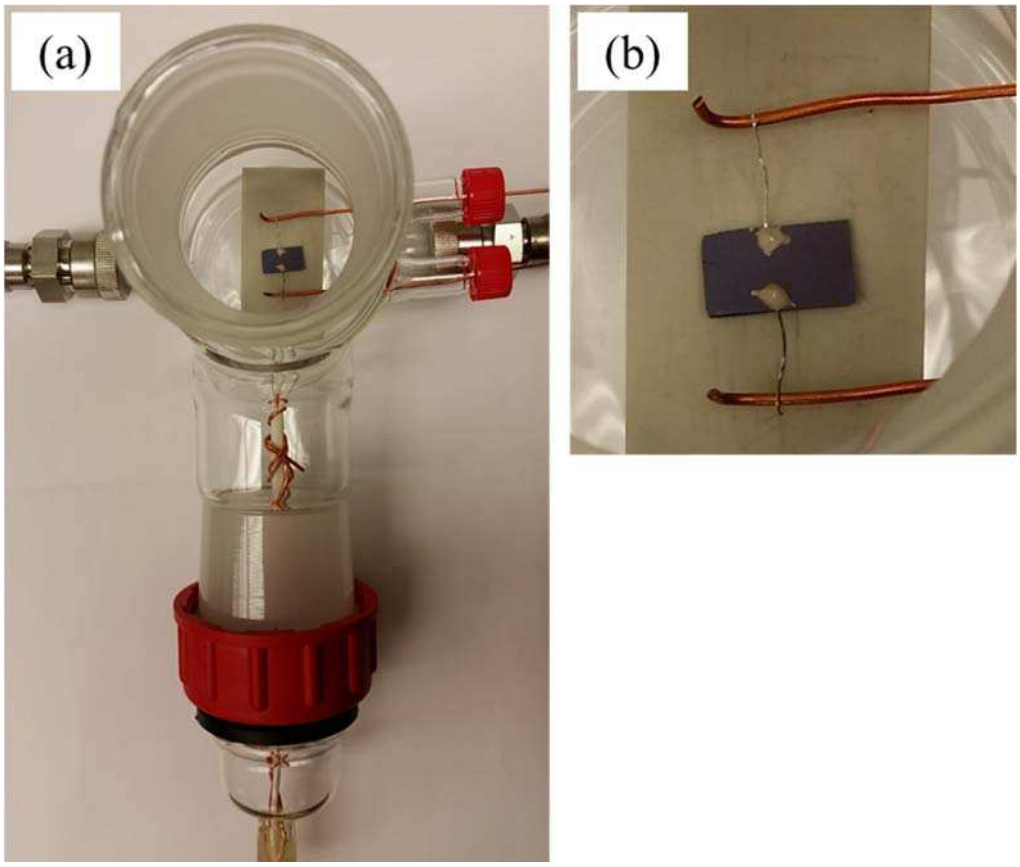

Figure 6.5. A top-down view of the sensor placement in the sensing chamber (a) with a close-up view of the sensor connected to the copper leads (b).

individual sensing experiment are shown in Figure 6.6, where each step is labeled with the corresponding T_S at which the resistance data were collected. This process should account for changes in oxygen species adsorbed on the sensor surface due to adsorption and desorption processes that occur at different temperatures. Collection times and iterations (as shown in the LabVIEW SignalExpress software) are recorded for each temperature step and upon reaching steady state resistance (≥10 min for total collection time at steady state resistance). Final approximate resistance for each temperature is recorded, such that these pieces of information can be used to locate the different temperature steps in the raw data during processing. By allowing the resistance to reach a steady state at each temperature, we can more accurately determine an average resistance value for elucidating sensitivity. Additional future modifications to the system will allow for the collection of response and recovery data over much shorter time frames (on the order of seconds instead of several minutes).

Resistance was recorded for UT materials and for plasma treated materials during exposure to air, CO, and C_6H_6, with a new sensor used for each individual test in a single gas sample. Upon collection of the resistance data using National Instruments LabVIEW SignalExpress software, the raw resistance data as a function of iteration are exported as Excel files. Three or more trials were completed for each set of parameters described in Chapters 3 and 7 for UT, Ar/O_2 and H_2O NP and NW. Each trial was then processed using the following procedure. Utilizing the data sort functions in Excel combined with the iteration and resistance recorded for each sensing trial, we sorted the data into resistance per each T_S step. The average resistance with standard deviation was calculated for each T_S step. Thus, each T_S has two different values for average resistance (representing both heating and cooling) with corresponding standard deviation except 300 °C. To account for not recording resistance twice

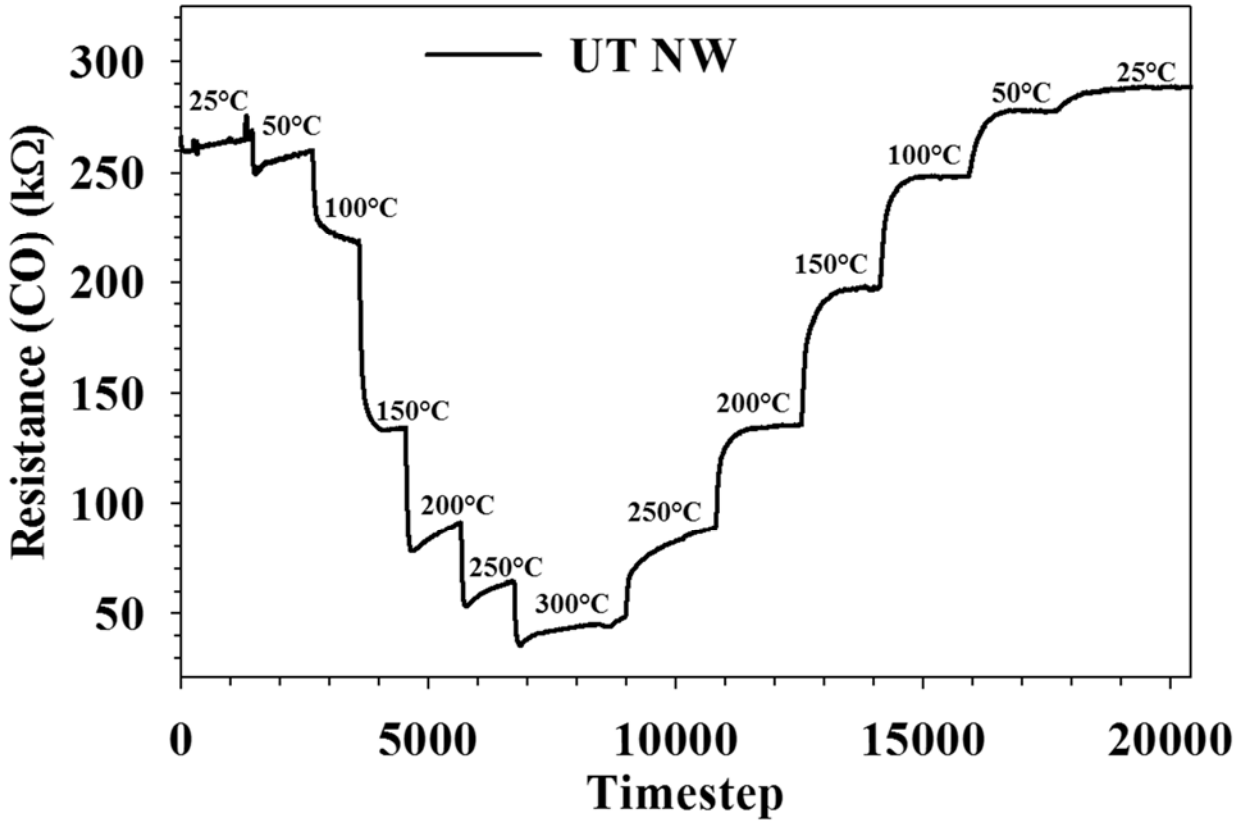

Figure 6.6. Representative raw resistance data for untreated SnO_2 nanowires exposed to 100 ppm CO where each step is labeled with the corresponding T_S at which the resistance data were collected.

for 300 °C, we collect resistance for twice as long (~20 min) to average the same number of iterations accounted for at all lower T_S. Upon analyzing all trials for a given set of material parameters, the average resistance values for each T_S were then averaged with error propagated across all trials for a final average resistance with error for each T_S. These final averages were used to calculate sensitivity toward CO and C_6H_6 for all material parameters and temperatures by calculating the ratio of the resistance in air (R_{air}) at a given T_S to the resistance in target gas (R_{gas}) for the same T_S (i.e., R_{air}/R_{gas}) or the reciprocal depending on whichever calculation resulted in a value >1. The reasoning behind using these two different ratios to describe sensitivity and specific sensing experiments are further discussed in Chapter 7.

6.4. Avenues of system/fabrication alterations for further performance testing.

To measure response and recovery times by exposing the sensor to short bursts of target gas, the system needs to be slightly altered to reproducibly turn gas flow on and off over an extended period of time. One potential approach to this problem lies with using mass flow controllers combined with LabVIEW programming to control the on/off time of gas flow into the system as was previously utilized in our lab to create gradient films.[9] This process can also be applied to vary concentrations of CO and C_6H_6 by using flow controllers to accurately introduce a mixture of air and either target gas to create concentrations <100 ppm. This process will allow for determining the sensitivity of the different UT and plasma treated nanomaterials toward different CO and C_6H_6 concentrations. Additional testing of mixed gas systems will require adding more gas lines with the potential for using mass flow controllers to tune the flow rates/percentages of different gaseous components. These more complex systems will allow for

determination of selectivity for the UT and plasma treated nanomaterial sensors beyond our current gases tested.

Alternative sensor fabrication techniques can also be considered. Different metals such as gold or platinum could be used for the electrodes and conductive paste to provide a comparison to the silver electrodes and paste. These comparisons could help to determine how much of a role the metal type has on sensor sensitivity.[10] Additionally, utilizing photolithography or different patterning processes to deposit sensor electrodes may result in a more reproducible sensor fabrication method than the one described herein. The addition of a micro heater with patterned electrodes could also eliminate some of the issues we had with maintaining a constant distance between sensor and heater or electrodes falling off the sensor as a result of too much pressure from the copper electrodes.[11-13]

The current gas sensing system set-up was designed to allow for a great deal of flexibility such that different features could be modified to add additional performance tests to our current studies. Furthermore, by trying different metals and methods of electrode attachment, we may be able to increase fabrication reproducibility from sensor to sensor. Some of these alterations to our sensing platform are already in progress, with others to be considered for future studies.

REFERENCES

1. Choi, U.-S.; Sakai, G.; Shimanoe, K.; Yamazoe, N. Sensing Properties of SnO_2–Co_3O_4 Composites to CO and H_2. *Sens. Actuators B.* **2004**, *98* (2), 166-173.
2. Prasad, R.; Gurlo, A.; Riedel, R.; Hübner, M.; Barsan, N.; Weimar, U. Microporous Ceramic Coated SnO_2 Sensors for Hydrogen and Carbon Monoxide Sensing in Harsh Reducing Conditions. *Sens. Actuators B.* **2010**, *149* (1), 105-109.
3. Lee, K.-C.; Chiang, Y.-J.; Lin, Y.-C.; Pan, F.-M. Effects of PdO Decoration on the Sensing Behavior of SnO_2 Toward Carbon Monoxide. *Sens. Actuators B.* **2016**, *226* 457-464.
4. Sun, P.; Cao, Y.; Liu, J.; Sun, Y.; Ma, J.; Lu, G. Dispersive SnO_2 Nanosheets: Hydrothermal Synthesis and Gas-Sensing Properties. *Sens. Actuators B.* **2011**, *156* (2), 779-783.
5. Baruwati, B.; Kumar, D. K.; Manorama, S. V. Hydrothermal Synthesis of Highly Crystalline ZnO Nanoparticles: A Competitive Sensor for LPG and EtOH. *Sens. Actuators B.* **2006**, *119* (2), 676-682.
6. Pan, J.; Ganesan, R.; Shen, H.; Mathur, S. Plasma-Modified SnO_2 Nanowires for Enhanced Gas Sensing. *J. Phys. Chem. C.* **2010**, *114* (18), 8245-8250.
7. Jang, D. M.; Jung, H.; Hoa, N. D.; Kim, D.; Hong, S.-K.; Kim, H. Tin Oxide-Carbon Nanotube Composite for NO_X Sensing. *J. Nanosci. Nanotechnol.* **2012**, *12* (2), 1425-1428.
8. Wu, J.; Zeng, D.; Tian, S.; Xu, K.; Li, D.; Xie, C. Competitive Influence of Surface Area and Mesopore Size on Gas-Sensing Properties of SnO_2 Hollow Fibers. *J. Mater. Sci.* **2015**, *50* (23), 7725-7734.
9. Tompkins, B. D.; Fisher, E. R. Plasma Synthesis of Hydrocarbon/Fluorocarbon Thin Films with Compositional Gradients. *Plasma Process. Polym.* **2013**, *10* (9), 779-791.
10. Saukko, S.; Lantto, V. Influence of Electrode Material on Properties of SnO_2-Based Gas Sensor. *Thin Solid Films.* **2003**, *436* (1), 137-140.
11. Barsan, N.; Weimar, U. Understanding the Fundamental Principles of Metal Oxide Based Gas Sensors; The Example of CO Sensing with SnO_2 Sensors in the Presence of Humidity. *J. Phys.: Condens. Matter.* **2003**, *15* (20), R813-R839.
12. Hwang, W.-J.; Shin, K.-S.; Roh, J.-H.; Lee, D.-S.; Choa, S.-H. Development of Micro-Heaters with Optimized Temperature Compensation Design for Gas Sensors. *Sensors.* **2011**, *11* (3), 2580-2591.
13. Wang, D.; Chen, Y.; Liu, Z.; Li, L.; Shi, C.; Qin, H.; Hu, J. CO_2-Sensing Properties and Mechanism of Nano-SnO_2 Thick-Film Sensor. *Sens. Actuators B.* **2016**, *227* 73-84.

CHAPTER 7

THE EFFECT OF Ar/O_2 AND $H_2O_{(v)}$ PLASMA TREATMENT OF SnO_2 NANOPARTICLES AND NANOWIRES ON CARBON MONOXIDE AND BENZENE DETECTION

This chapter is based on the work submitted to *ACS Applied Materials & Interfaces*, written by Erin P. Stuckert, Christopher J. Miller, and Ellen R. Fisher. The test, figures, and tables are reproduced here with data collected and analyzed by Erin and Chris; manuscript written by Erin and Ellen. This chapter details the sensor performance for devices fabricated from UT, Ar/O_2 and H_2O plasma treated SnO_2 nanoparticles and nanowires. Specifically, sensitivity toward 100 ppm carbon monoxide and 100 ppm benzene are examined at different temperatures ranging 25-300 °C. Prior materials and gas-phase data presented in Chapter 3-5 are used to examine structures and properties that may lead to the observed sensor performance. In particular, this chapter encompasses the aim of this project by tying together potential structure-property-performance relationships that were gradually built upon throughout this dissertation. Funding for this research was provided by the National Science Foundation (CHE-1152963).

7.1. Introduction

This study describes the sensing performance of untreated (UT) and plasma treated SnO_2 nanomaterials as an important component of our holistic approach to creating sensitive, targeted gas sensors. This work builds on our prior studies analyzing material structure and properties of SnO_2 nanomaterials before and after plasma modification.[1-3] It is particularly important to elucidate connections between these different features to understand structure-property-performance relationships essential to creating sensitive and selective sensors in a targeted and meaningful way. Therefore, this investigation focuses on sensor performance, drawing on earlier

characterization data to explain what materials chemistry and properties lead to specific sensor capabilities.

7.1.1. Methods for improving gas sensor capabilities. The need for sensitive and selective gas sensors arises from continued, often increasing, emission of toxic gases such as carbon monoxide, nitric oxides, benzene, and formaldehyde. Exposure to these gases causes adverse health effects necessitating the design of numerous gas sensors as early warning systems.[4-7] Despite this emphasis on reliable detection, many sensors have limited sensitivity and selectivity toward some gases;[8-10] others require elevated operating temperatures that limit sensor lifetime.[11-13] Notably, although gas sensors from a wide array of materials and morphologies (from polymers to metal-oxide-semiconductors (MOS) and from thin films to nanomaterials) have been used,[14-18] MOS nanomaterials are a current area of intense focus. Advantages of these materials in sensor applications include their cost efficiency over other options, such as precious metal doping (e.g., Pd, Pt),[19-21] and their effectiveness that arises from utilizing changes in metal oxidation state (and thereby charge transfer through the material) as a result of gas-surface interactions, to detect and differentiate gas species.[17, 22-26] SnO_2, in particular, is often used for its dual valency (Sn^{4+} and Sn^{2+}), which can aid in creating sensitive sensors.[27-29] Additionally, the increased surface area of nanomaterials over thin films allows for more oxygen to adsorb to the sensor surface, maximizing sensor sensitivity.[30-32]

Many studies continue to seek different dopant-MO pairings[19, 21, 33, 34] and alternative MOS nanomaterial morphologies/architectures to develop next generation gas sensors.[35, 36] Sensor material fabrication and surface modification utilizing plasmas, however, is an often underutilized approach to altering sensor materials in a focused manner. This methodology has an expansive parameter space that can be utilized to tune surface chemistry with a greater degree

of control than is sometimes possible with alternative wet chemical processes.[37, 38] Despite extensive use of plasma enhanced chemical vapor deposition (PECVD)[32, 39-41] or similar processes (i.e., plasma enhanced atomic layer deposition, PEALD)[42-44] for nanomaterial growth or fabrication, few studies have exploited plasma modification of sensing nanomaterials, and those that do mainly focus on O_2 or Ar/O_2 plasma treatment.[45-50] A few studies on alternative plasma precursors such as H_2, N_2, H_2O, and halogen-based have been reported,[28, 51-54] indicating SnO_2 nanowires with enhanced sensing capabilities can be further improved with respect to sensitivity and selectivity via plasma treatment.

Kim *et al.*[50] and Pan *et al.*[48] both treated SnO_2 nanowires with Ar/O_2 plasmas, but had differing results because the former study used an atmospheric pressure plasma, whereas the latter employed a low pressure rf plasma. Kim *et al.* found longer treatment times resulted in clusters of small particles or monolithic structures encasing individual nanowires of the interconnected nanowire network, but the bulk SnO_2 structure was maintained. Furthermore, with longer plasma treatment, SnO_2 nanowires showed greater changes in resistance, or higher sensitivity, than UT nanowires upon exposure to NO_2. Response and recovery times also increased with plasma treatment times. In contrast, Pan *et al.* changed the applied rf power (P = 10-80 W) while holding treatment time constant at 4 min. Similar to Kim *et al.*, Pan *et al.* observed changes in morphology as a result of plasma treatment; at higher P, an amorphous layer formed around the crystalline SnO_2 nanowire core. They also observed Sn reduction at $P \geq 40$ W, such that the amorphous overlayer became Sn particles, with an accompanying decrease in sensitivity toward ethanol gas. Despite decreased sensitivity observed with certain plasma parameters in these two studies, each demonstrated plasma treating SnO_2 nanowires can enhance sensor sensitivity.

7.1.2. Plasma-modified SnO_2 nanomaterials and sensor performance. Our initial studies of plasma surface modification of SnO_2 sensor materials employed Ar/O_2 and $H_2O_{(v)}$ plasmas.[1] The first of these was chosen for direct comparison to the literature; moreover, Ar/O_2 plasmas etch SnO_2 to create surface oxygen vacancies, thereby enhancing gas-surface interactions while maintaining the bulk SnO_2 structure.[1, 48, 49] These studies of Ar/O_2 plasma treatment of SnO_2 materials revealed increases in adsorbed oxygen under some treatment conditions, specifically at $P \geq 100$ W, without any changes to tin oxidation or morphology. The second plasma treatment system was chosen as an alternative, nominally oxidizing plasma system. H_2O plasma treatment resulted in increased oxygen adsorption to a lesser degree than Ar/O_2 treatment. Additionally, H_2O treatment resulted in Sn reduction that increased with higher P, leading to morphological changes not observed with Ar/O_2 plasma treatment.

The two plasma systems resulted in different material chemistry and morphology changes, which were further varied as a function of initial nanomaterial morphology.[1] Here, to determine which nanomaterial and plasma modification parameters were most effective at enhancing sensor performance, resistance was measured as a function of temperature for all UT and plasma treated nanomaterials as they were exposed to air, carbon monoxide, or benzene. CO sensitivity was determined for comparison with numerous literature studies,[55-59] whereas C_6H_6 sensitivity was examined to increase our understanding of sensor activity beyond the current, limited knowledge of SnO_2 nanomaterial-based sensors for benzene detection.[26, 60-63] Sensor performance data were evaluated in relation to both oxygen adsorption chemistry as a function of substrate temperature (T_S) and to specific materials characterization data published previously.[1, 2]

7.2. Results

7.2.1. Sensor response to CO and C_6H_6. Figure 7.1 shows sensor response (R_{air}/R_{gas}) to the target gases CO and C_6H_6 as a function of T_S for all UT and Ar/O_2 plasma-treated nanoparticle and nanowire sensors. Notably, sensor response to the two gases displays varying degrees of temperature dependence. In general, UT and Ar/O_2 NP sensors (Figure 7.1 (a, c)), exhibit relatively constant CO and C_6H_6 response for $T_S \leq 150$ °C. Sensor response at $T_S \geq 200$ °C, however, tends to increase with temperature. Indeed, 150 W Ar/O_2 NP sensors had the greatest temperature dependence, changing from a sensor response of ~3 at room temperature to ~100 at 300 °C, regardless of target gas. In contrast, sensor response is less temperature dependent for UT and Ar/O_2 NW sensors (Figure 7.1 (b, d)), than for UT and Ar/O_2 NP sensors, regardless of target gas, as evidenced by the smaller changes in sensor response of NW sensors as a function of temperature.

Figure 7.2 displays responses for UT and H_2O plasma treated nanoparticle and nanowire sensors to CO and C_6H_6. Generally, none of the plots in Figure 7.2 exhibit dramatic temperature dependence, with the possible exception of low power treatments of nanoparticles (Figure 7.2 (a)). With CO as the target gas, H_2O NW sensor response is less temperature dependent than that of H_2O NP sensors, as evidenced by smaller changes in response of NW sensors as a function of T_S. Indeed, H_2O NW sensors have a relatively constant CO response from T_S = 100-300 °C, Figure 7.2 (b), that is also independent of treatment conditions (i.e., applied rf power). A similar lack of T_S and P dependence is also observed for H_2O NP sensor response to C_6H_6 (Figure 7.2 (c)). Although H_2O NW sensor response to C_6H_6 also displays little to no temperature dependence (Figure 7.2 (d)), the actual response ratios appear somewhat dependent on P.

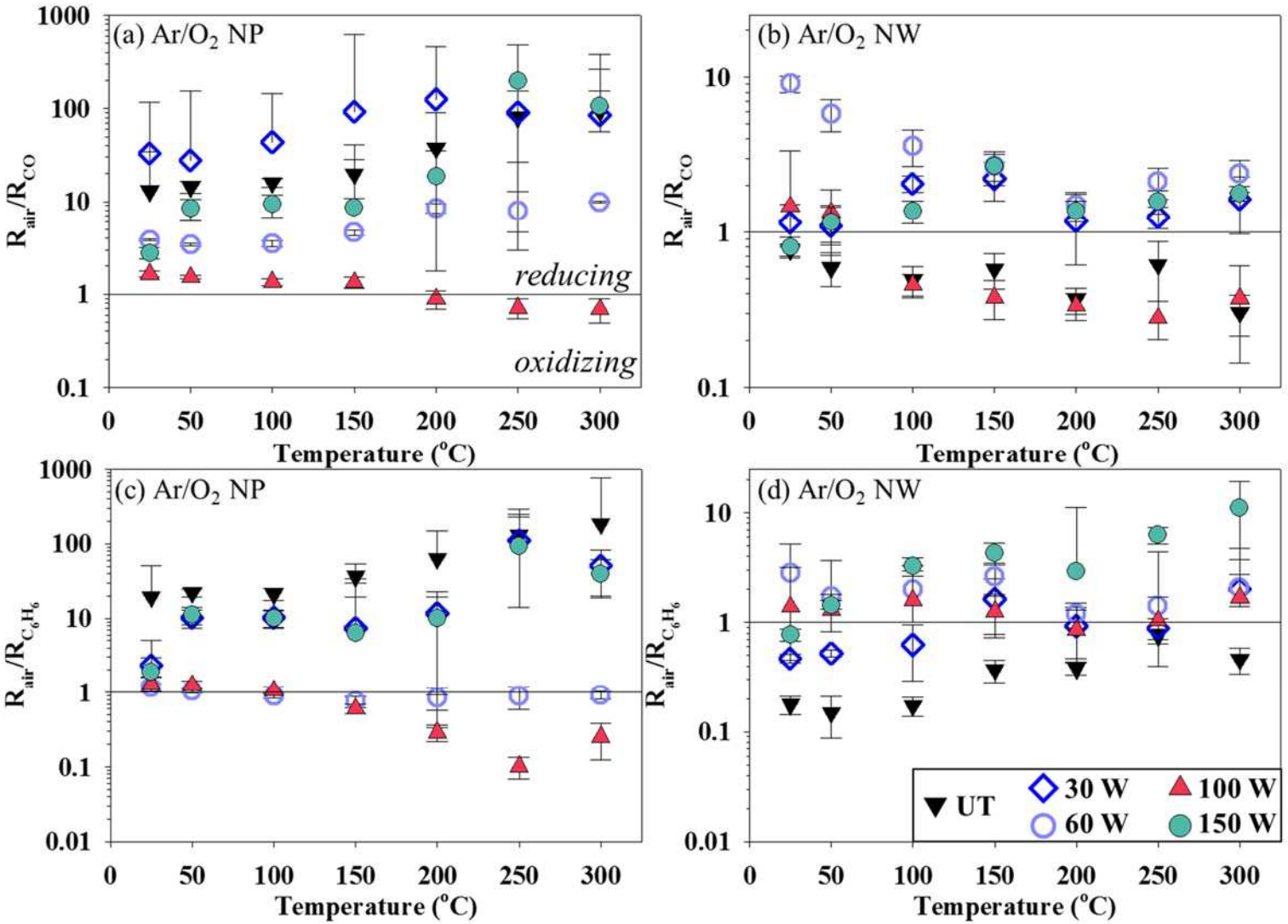

Figure 7.1. Gas sensor response R_{air}/R_{CO} for Ar/O_2 NP (a) and Ar/O_2 NW (b) and R_{air}/R_{C6H6} for Ar/O_2 NP (c) and Ar/O_2 NW (d) as a function of T_S and P. The horizontal line at 1 separates reducing interactions ($R_{air}/R_{gas} > 1$) from oxidizing interactions ($R_{air}/R_{gas} < 1$). Negative error not shown on plots are equivalent to positive error plotted.

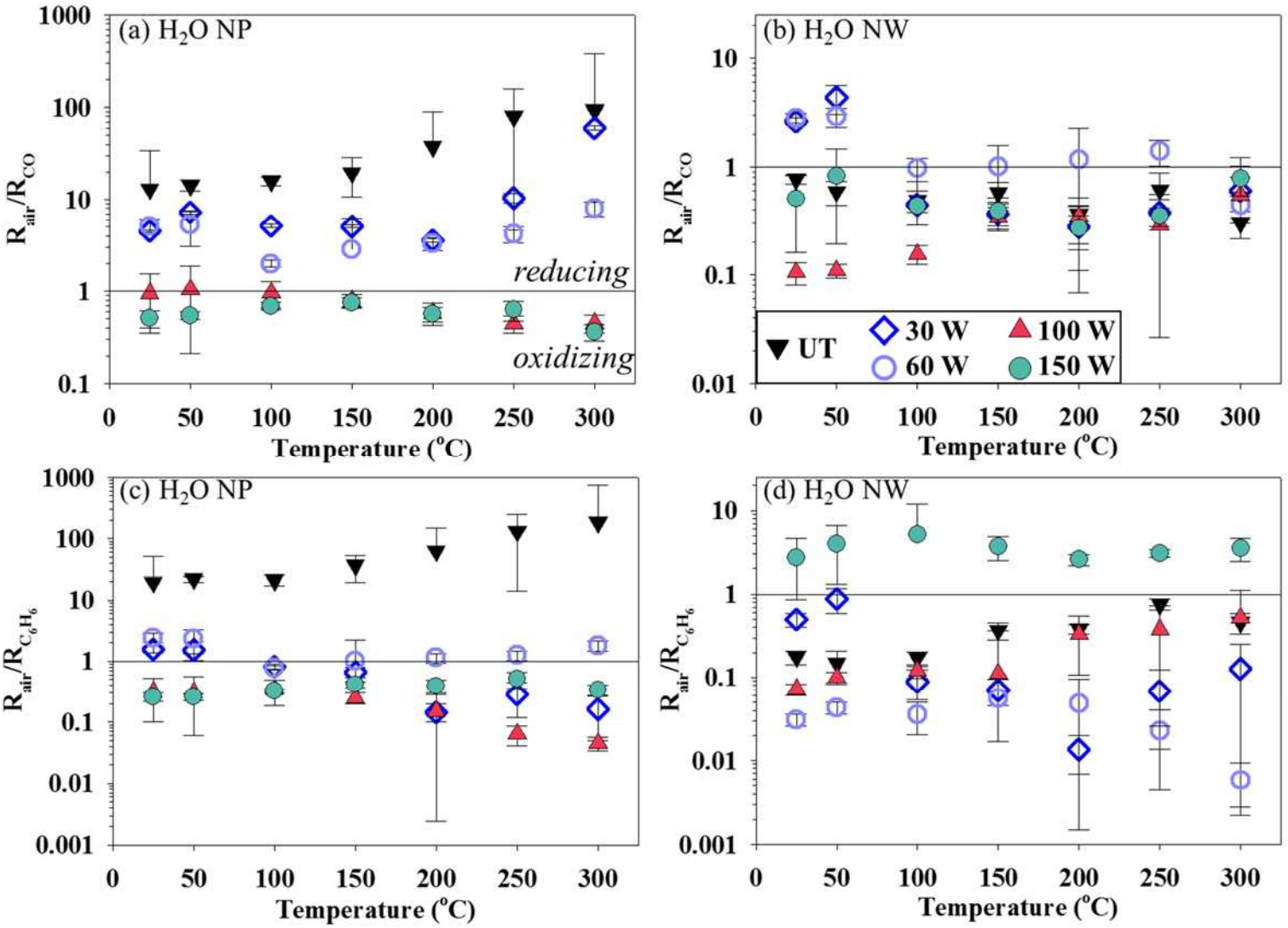

Figure 7.2. Gas sensor response R_{air}/R_{CO} for H_2O NP (a) and H_2O NW (b) and R_{air}/R_{C6H6} for H_2O NP (c) and H_2O NW (d) as a function of T_S and P. The horizontal line at 1 separates reducing interactions ($R_{air}/R_{gas} > 1$) from oxidizing interactions ($R_{air}/R_{gas} < 1$). Negative error not shown on plots are equivalent to positive error plotted.

7.2.2. Gas-surface redox interactions and plasma modification. It is also instructive to consider the nature of the gas-surface interaction in the sensing of the two target gases. UT NP have a reducing interaction ($R_{air}/R_{gas} > 1$) with both gases, whereas UT NW interact with the target gases in an oxidizing manner ($R_{air}/R_{gas} < 1$). CO and C_6H_6 interactions with Ar/O_2 NP remain reducing in nature under most plasma treatment and T_S conditions (Figure 7.1 (a, c)). Notably, with most Ar/O_2 NW, the carbon monoxide and benzene interactions with SnO_2 become reducing in nature (Figure 7.1 (b, d)). Target gas interactions with H_2O plasma-treated nanomaterials appear to be dependent on treatment conditions (i.e., P). Specifically, treating nanoparticles at lower applied power ($P \leq 60$ W) with H_2O plasma maintains the reducing nature of the interaction with both CO and C_6H_6 at most T_S conditions (Figure 7.2 (a, c)); however, with materials treated at higher applied power ($P \geq 100$ W), these become oxidizing gas-surface interactions. Under most plasma parameters and T_S, H_2O NW have oxidizing CO gas-surface interactions, as do H_2O NW ($P \leq 100$ W) when sensing benzene (Figure 7.2 (b, d)). When nanowires are treated in H_2O plasmas at the highest power examined ($P = 150$ W), their interactions with C_6H_6 become reducing in nature. The reasoning behind these changes in gas-surface interaction will be further explored in the discussion below.

7.2.3. Plasma modified materials and gas sensor sensitivity. As a result of these changes in redox interactions, the response (R_{air}/R_{gas}) data from Figures 7.1 and 7.2 were inverted to R_{gas}/R_{air}, where the larger of the two values is representative of the given material's sensitivity. For example, $R_{air}/R_{C6H6} = 0.10$ for 100 W Ar/O_2 NP at 250 °C and $R_{C6H6}/R_{air} = 9.89$; therefore 100 W Ar/O_2 NP have benzene sensitivity of 9.89 at 250 °C. Considering all of the data under these new conditions for sensitivity, the maximum sensitivity of UT and Ar/O_2 NW sensors across the studied temperature range is ~10 for both target gases. Furthermore, Ar/O_2 NP

displayed sensitivity similar to or decreased from that of UT NP, whereas Ar/O_2 treatment of nanowires resulted in sensitivity similar to or increased from that of UT NW. The sensitivity data also indicate that, on average, Ar/O_2 NP are more sensitive toward carbon monoxide and benzene than Ar/O_2 NW. Notably, the values of gas sensor sensitivity vary somewhat, with H_2O NW sensors yielding a maximum CO sensitivity of ~7, whereas H_2O NP have a maximum CO sensitivity of ~60. C_6H_6 sensitivity ranges from ~1 to ~15 for H_2O NP and from ~1 to ~70 for H_2O NW. In general, H_2O plasma modification of nanoparticles resulted in decreased sensitivity relative to that of UT nanoparticles, regardless of target gas. Unlike H_2O NP, H_2O NW displayed similar or increased CO and C_6H_6 sensitivity.

To further highlight the effects of different combinations of the parameters studied here (material morphology, plasma feed gas, P, and T_S), select carbon monoxide and benzene sensitivity data are shown in Figures 7.3-7.5. Figure 7.3 displays CO sensitivity as a function of P and T_S for H_2O NP, indicating a decrease in CO sensitivity as a function of P. Notably, only 30 W H_2O NP display a measurable difference in CO sensitivity as a function of T_S. Figure 7.4 highlights benzene sensitivity for Ar/O_2 NP and H_2O NW, revealing that although T_S does not affect sensitivity in most cases, plasma treatment conditions do affect these measurements. For example, C_6H_6 sensitivity of Ar/O_2 NP decreases with P, resulting in minimum sensitivity of ~1 at P = 60 and 100 W, whereas C_6H_6 sensitivity of H_2O NW increases with P, resulting in maximum sensitivity of ~175 at P = 60 W. Closer examination of the H_2O NW data reveals a T_S dependence, with the highest sensitivity at T_S = 25 and 50 °C, and the lowest at T_S = 300 °C for UT and 100 W H_2O NW, as indicated in the Figure 7.4 (b) inset. Figure 7.5 directly compares the effects of different plasma treatments on NW sensitivity toward CO and C_6H_6 as a function of P and T_S. With H_2O NW sensors (Figure 7.5 (a)), a maximum CO sensitivity of ~8 occurs

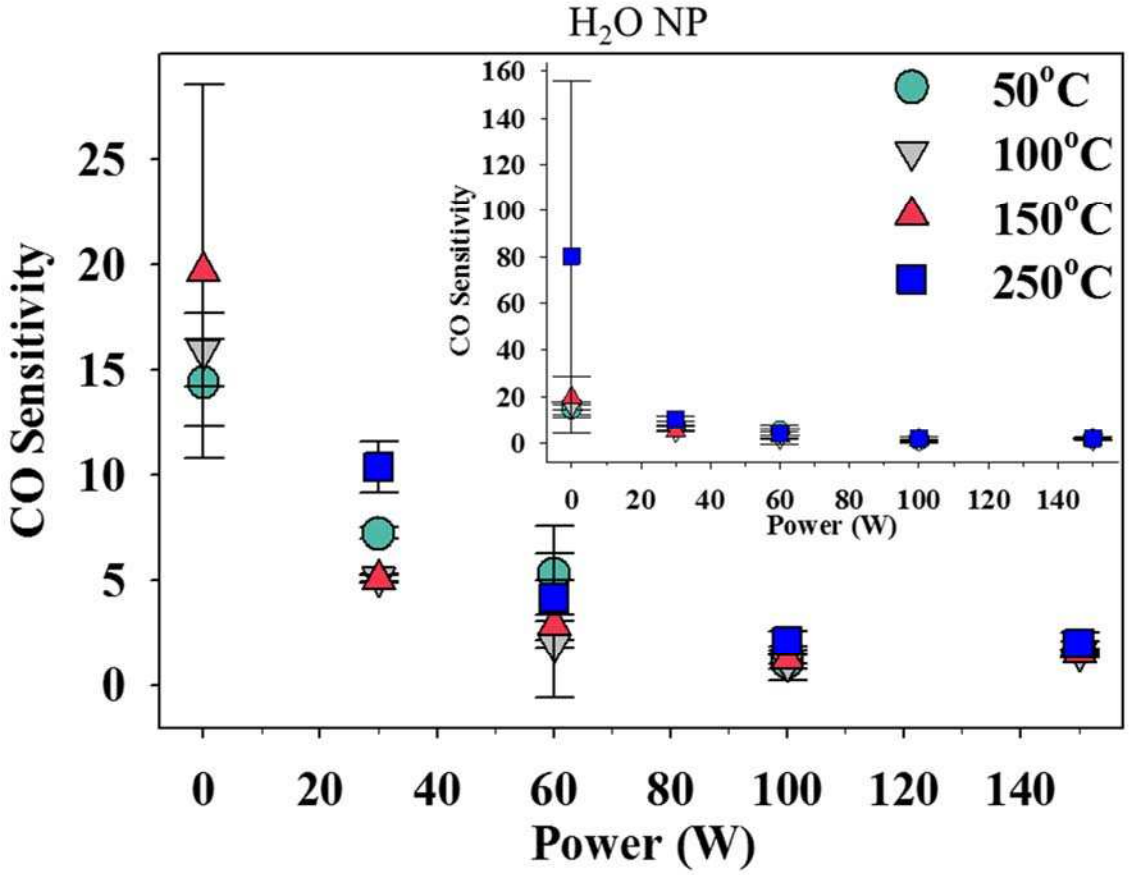

Figure 7.3. H_2O NP CO sensitivity as a function of *P* (0 W is equivalent to UT) and *Ts* for a subset of conditions. The inset plot shows additional data for UT NP at 250 °C.

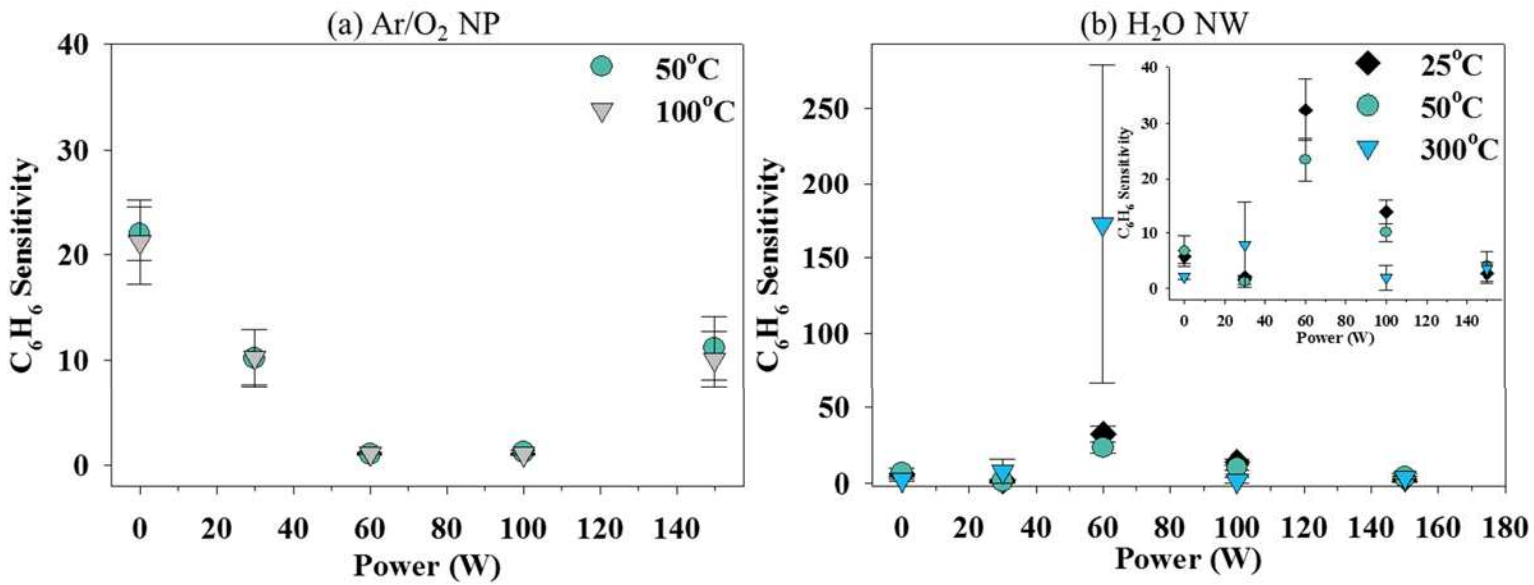

Figure 7.4. C_6H_6 sensitivity for Ar/O_2 NP (a) and H_2O NW (b) as a function of *P* (0 W is equivalent to UT) and T_S for a subset of conditions. The inset plot in (b) is absent the data for 60 W H_2O NW at 300 °C

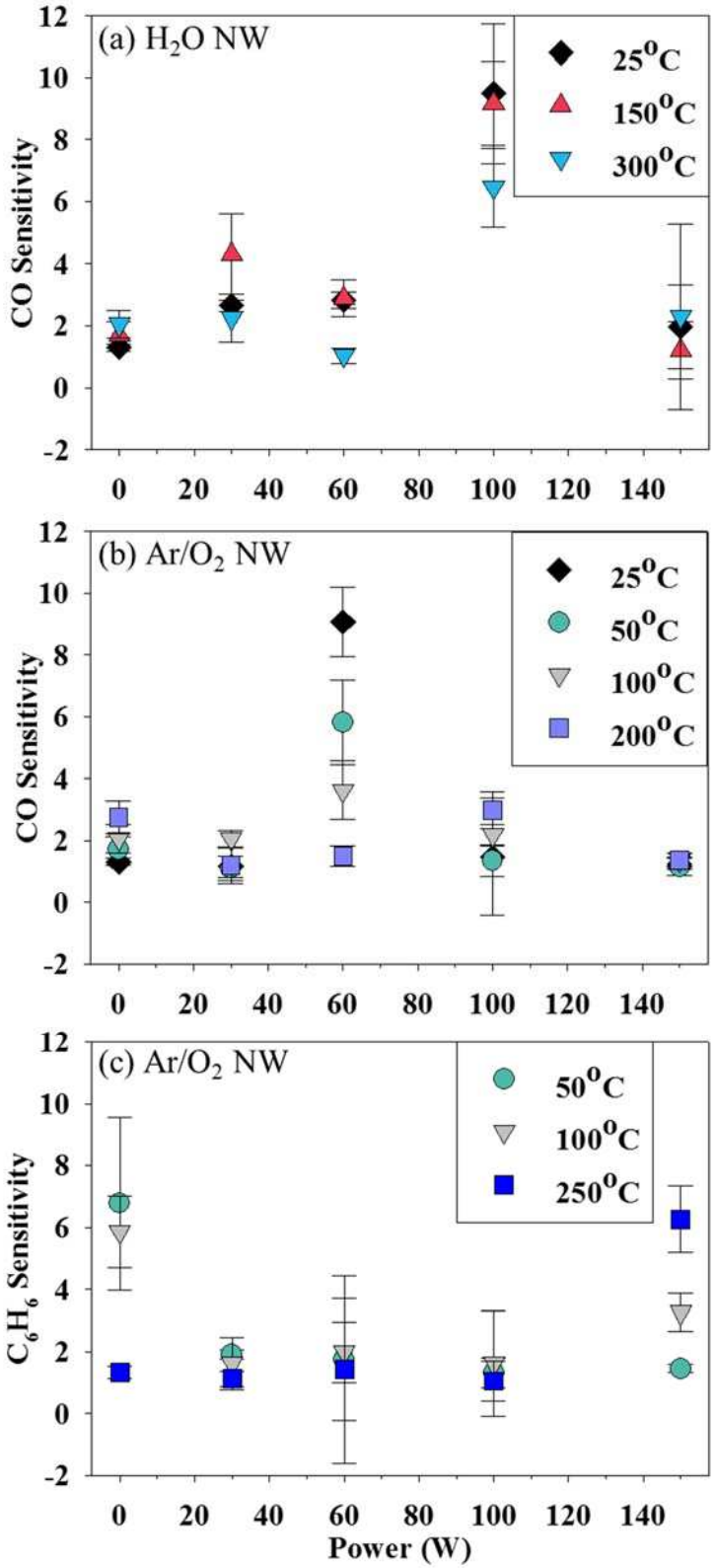

Figure 7.5. CO sensitivity for H_2O NW (a) and Ar/O_2 NW (b) as well as C_6H_6 sensitivity for Ar/O_2 NW (c) as a function of *P* (0 W is equivalent to UT) and T_S for a subset of conditions.

with 100 W treatment, at all T_S. In contrast, a maximum CO sensitivity for Ar/O_2 NW occurs at P = 60 W (Figure 7.5 (b)), but decreases from ~9 at T_S = 25 °C to ~1 at T_S = 200 °C. Figure 7.5 (c) demonstrates that Ar/O_2 NW generally display similar sensitivity toward C_6H_6 and CO. However, 150 W Ar/O_2 NW have greater C_6H_6 sensitivity (~6) than UT NW (~1) at T_S = 250 °C, but lower sensitivity at 50 °C (UT ~7; 150 W ~1).

7.3. Discussion

Much of the recent literature on SnO_2 gas sensors has focused on novel synthesis routes to a range of material morphologies, including electrospun fibers, nanoflowers, nanowires, and nanoparticles.[17, 47, 64] A few have further explored additional surface modification strategies to enhance sensor performance in detecting a range of atmospheric pollutants and other toxic gases.[28, 50-52] Here, we examined the effects of plasma surface modification on the ability of nanostructured SnO_2 sensors to detect carbon monoxide and benzene. More specifically, we correlated sensor performance with prior materials characterization results[1, 2] to elucidate structure-property-performance relationships.

7.3.1. Oxygen adsorption and metal oxide sensing mechanisms. To determine how carbon monoxide or benzene gas sensing properties of SnO_2 nanomaterials are affected by plasma modification or nanomaterial morphology/surface area, it is instructive to consider the mechanisms by which CO and C_6H_6 interact with adsorbed oxygen. The first step in the sensing mechanism is oxygen adsorbing to the UT SnO_2 surface, which is well known to selectively adsorb different oxygen species at different T_S, Figure 7.6 (a).[65-67] Specifically, Reactions 1-4 depict how adsorbed oxygen charge increases with temperature, often accompanied by higher sensitivity:

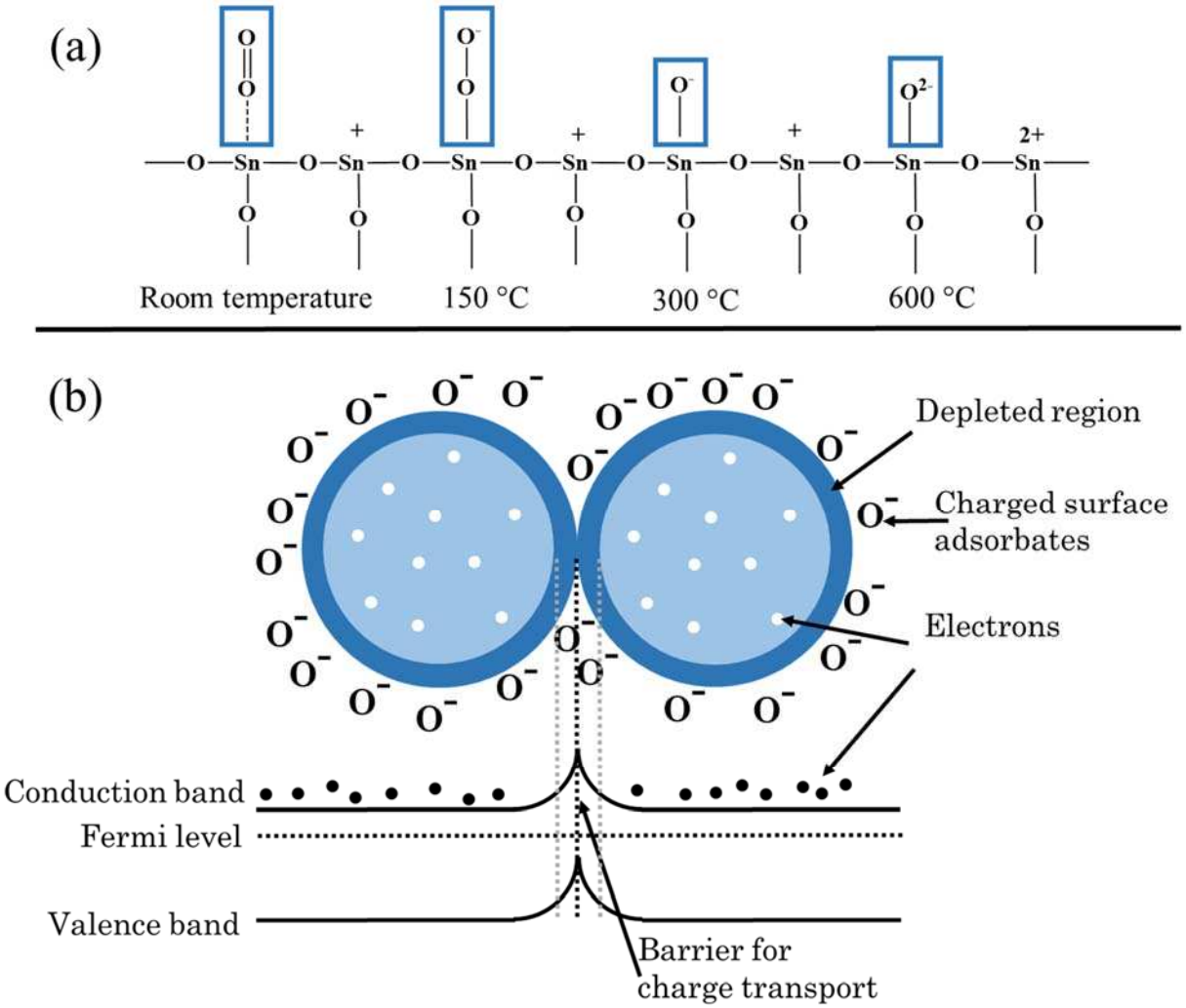

Figure 7.6. Adsorbed oxygen species on SnO_2 as a function of temperature (a) and the effect of adsorbed oxygen (at 300 °C) on SnO_2 conductivity (b).

$$O_{2(g)} \rightleftharpoons O_{2(ad)} \text{ at room temperature} \quad (1)$$

$$O_{2(ad)} + e^- \rightleftharpoons O_2^-{}_{(ad)} \text{ at 150 °C} \quad (2)$$

$$O_{2(ad)} + 2e^- \rightleftharpoons 2O^-_{(ad)} \text{ at 300 °C} \quad (3)$$

$$O_{2(ad)} + 4e^- \rightleftharpoons 2O^{2-}_{(ad)} \text{ at 600 °C} \quad (4)$$

As *Ts* increases, a more highly charged surface is created when oxygen adsorbs to UT SnO_2. Simultaneously, a region of electron depletion is formed between the bulk of UT SnO_2 and the surface adsorbed oxygen (Figure 7.6 (b)).[68-70] This shift in electrons results in band bending, creating a barrier to charge flow, and ultimately, increasing the initial resistance of the UT SnO_2 sensor in ambient air.

When CO reacts with adsorbed oxygen, CO_2 desorbs from the surface and releases electrons to the bulk material, decreasing resistance as indicated in Reactions 5-8.[68, 71, 72]

$$O_2^-{}_{(ad)} + e^- \longrightarrow 2O^-_{(ad)} \geq 150 \text{ °C} \quad (5)$$

$$CO + O_2^-{}_{(ad)} \longrightarrow CO_2 + O^-_{(ad)} \text{ at 150 °C} \quad (6)$$

$$CO + O^-_{(ad)} \longrightarrow CO_2 + e^- \text{ at 300 °C} \quad (7)$$

$$CO + O^{2-}_{(ad)} \longrightarrow CO_2 + 2e^- \text{ at 600 °C} \quad (8)$$

This type of interaction with the SnO_2 surface is often referred to as a reducing interaction because of the release of electrons back to the bulk SnO_2. Note that Reactions 5 and 6 are competitive reactions, often leading to decreased CO sensitivity and selectivity at 150 °C. Similarly, benzene also has a reducing interaction with SnO_2, which can occur through different pathways.[73] Here, resistance decreases upon addition of C_6H_6 to the ambient atmosphere via Reactions 9 and 10:[74]

$$C_6H_6 + {}^9/_2\, O_2 \longrightarrow C_4H_2O_3 + 2CO_2 + 2H_2O \quad (9a)$$

$$C_4H_2O_3 + 3O_2^-{}_{(ad)} \longrightarrow 4CO_2 + H_2O + 3e^- \text{ at 150 °C} \quad (9b)$$

$$C_6H_6 + 15O^-_{(ad)} \longrightarrow 6CO_2 + 3H_2O + 15e^- \text{ at } 300\ ^\circ C \quad (10)$$

At higher T_S, more electrons can be released back to the bulk than at lower T_S upon carbon monoxide or benzene interaction with surface adsorbed oxygen on an UT SnO_2 surface. This results in a greater decrease of the electron depleted region at higher T_S. Given this relatively simplistic interpretation of these gas-surface interactions, SnO_2 sensors operating at $T_S \geq 150\ ^\circ C$ should display a greater change in resistance with the addition of a target gas (i.e., $R_{air}/R_{gas} >> 1$), indicating a greater sensitivity than when operating at $T_S < 150\ ^\circ C$.

7.3.2. Nanomaterial structure and property effects on gas sensing mechanisms. CO and C_6H_6 response data (Figures 7.1 and 7.2) indicate that both gases interact with UT NP in a reducing manner and with UT NW in an oxidizing manner as described above. Because adsorbed oxygen species are controlled by T_S, as indicated by temperature programmed desorption (TPD) studies,[65, 66] similar oxygen species should be present on both materials. This suggests the sensing mechanism of UT SnO_2 nanomaterials is influenced by differences in morphology and accessible surface area. The larger the accessible surface area, the greater the expected relative amount of adsorbed oxygen. Thus, UT NW have the potential to adsorb more oxygen than UT NP. In addition, nanowires have fewer grain boundaries relative to the bulk SnO_2 because of substantial differences in dimensions, as previously indicated in SEM images and prior analyses.[1, 2] Given that UT NW have equivalent resistance in air relative to UT NP, it is likely that a combination of accessible surface area and grain boundary densities contribute to the sensing mechanism of UT SnO_2 nanomaterials. Moreover, the oxidizing interaction observed with UT NW reveals that CO and C_6H_6 may be less likely to desorb from UT NW than UT NP.

When Ar/O_2 plasma treating nanomaterials, morphology and bulk SnO_2 structure remain unchanged under all plasma parameters.[1] As such, morphology differences cannot be the source

of decreased sensitivity for Ar/O_2 NW and NP. Ar/O_2 NW and NP do, however, show increased oxygen adsorption as indicated in XPS spectra.[1] Furthermore, as nearly all Ar/O_2 NW and NP have reducing interactions with CO and C_6H_6 ($R_{air}/R_{gas} > 1$), these surface oxygen species must contribute to sensing as described above for UT nanomaterials. With increased surface oxygen and decreased sensitivity toward carbon monoxide and benzene, however, it appears that increasing oxygen adsorption alone is insufficient for enhancing CO and C_6H_6 sensitivity over UT nanomaterials under most plasma treatment conditions. Nevertheless, it is possible to somewhat control the sensitivity with Ar/O_2 plasma treatment as a function of P and T_S. Specifically, 60 W Ar/O_2 treatment of SnO_2 nanowires results in maximum CO sensitivity of ~9 over ~3 for UT NW (Figure 7.5 (b)). Not only are these plasma treatment and material parameters effective at enhancing CO sensitivity, but they do so at room temperature, indicating that such a sensor would have increased CO sensitivity and could last longer with less energy use than a sensor fabricated from UT NW.

To better understand why 60 W Ar/O_2 NW have higher sensitivity at lower temperatures than observed for the UT NW, it is necessary to consider our prior work on materials characterization and the likelihood of CO reacting with such a surface. Ar/O_2 NW treated at P = 60 W have increased oxygen adsorption observed via XPS while maintaining a tetragonal SnO_2 structure and the UT NW morphology.[2] Although other Ar/O_2 NW also have increased oxygen adsorption, the maximum CO sensitivity observed with 60 W Ar/O_2 NW suggests that a specific amount of adsorbed oxygen is more effective at enhancing CO sensitivity than maximizing oxygen adsorption. This hypothesis is somewhat at odds with what has been previously observed and claimed with other studies,[48-50] wherein sensitivity showed constant increase with plasma power. The observed variations from employing different plasma parameters and

different target gases, in conjunction with our CO sensitivity results, however, may simply suggest that although increasing oxygen adsorption is beneficial to enhanced sensitivity, the specific oxygen species adsorbed to the surface may drive gas-surface reactions. As such, additional studies on the nature of adsorbed oxygen species may provide greater detail on how certain plasma parameters affect adsorbed oxygen and surface charge. Such studies would allow us to determine whether the 60 W Ar/O_2 plasma treatment of nanowires not only increases oxygen adsorption, but if this particular treatment creates a surface that preferentially holds a negative surface charge, normally only observed at $T_S > 150$ °C, Figure 7.6 and Equations 1-4. Figure 7.7 (a, b) show how CO is less likely to react with an UT NW surface, relative to the surface of 60 W Ar/O_2 NW. Although 60 W Ar/O_2 NW have increased CO sensitivity, these materials do not display the same increase in C_6H_6 sensitivity; in particular, the materials formed under these parameters appear to have the same benzene sensitivity as UT NW. Benzene-SnO_2 surface reactions for UT NW and Ar/O_2 NW are shown in Figure 7.7 (d, e). These carbon monoxide and benzene performance results indicate that at room temperature, 60 W Ar/O_2 NW may be more selective toward CO than toward C_6H_6.

NW and NP, however, experience tin reduction and oxygen etching that effectively destroy the UT bulk SnO_2 structure and drastically alter morphology upon H_2O plasma treatment.[1, 3] Moreover, such changes in SnO_2 are enhanced at higher plasma power ($P \geq 100$ W). At lower powers ($P \leq 60$ W), some of the UT SnO_2 morphology and structure are maintained, but at $P \geq 150$ W none of the UT NW or NP morphology or structure remain. Thus, as the SnO_2 structure and morphology are lost, the oxygen adsorption and sensing mechanism observed for UT nanomaterials no longer holds true. Furthermore, increased tin reduction as a function of P leads to SnO_2 nanomaterials becoming Sn^0 aggregates, wherein the potential for

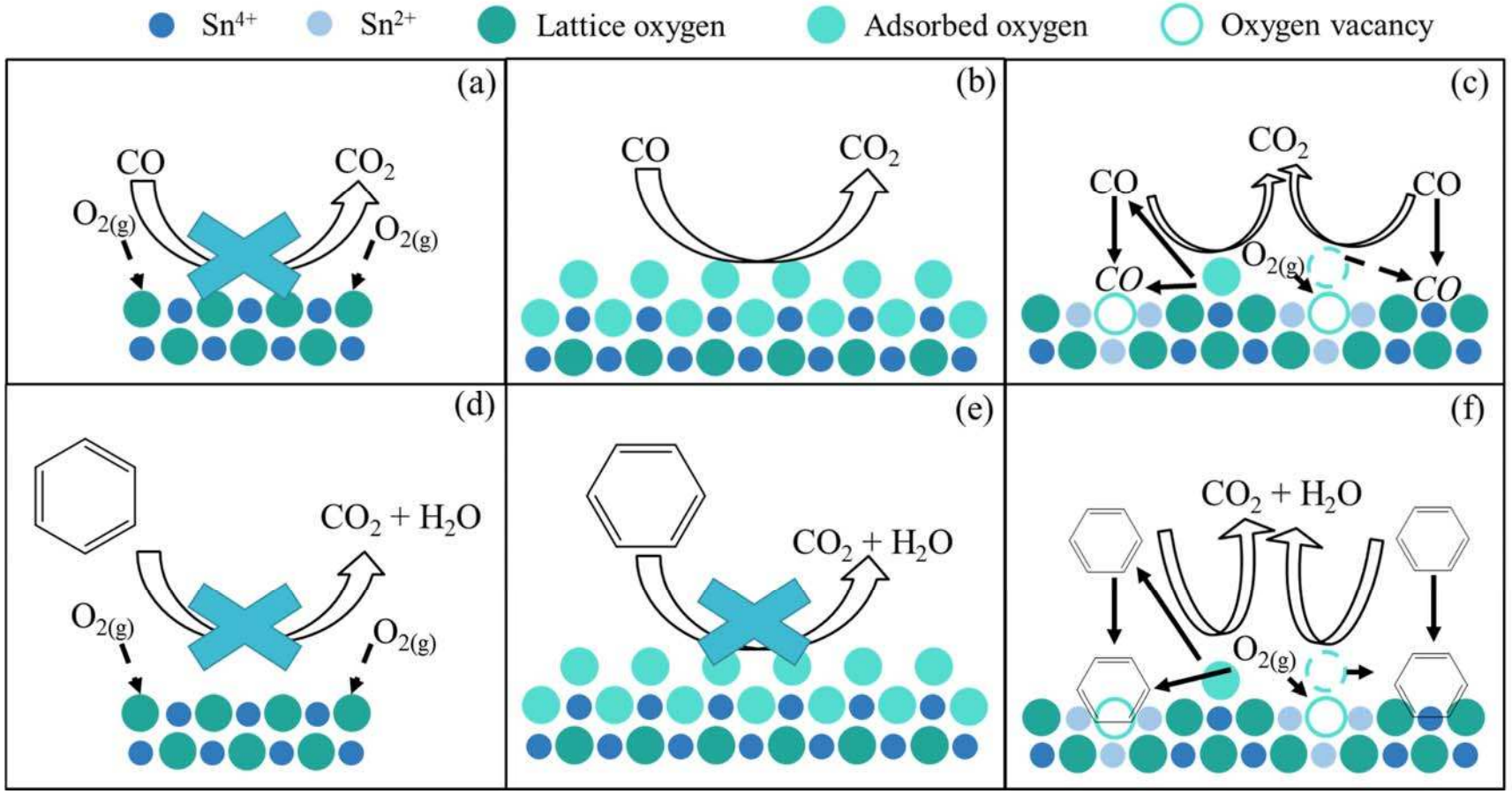

Figure 7.7. CO-SnO_2 surface reactions at room temperature for (a) untreated nanomaterials, (b) 60 W Ar/O_2 treated nanowires, and (c) 100 W H_2O treated nanowires. C_6H_6-SnO_2 surface reactions at room temperature for (d) untreated nanomaterials, (e) Ar/O_2 plasma treated nanomaterials, and (f) 60 W H_2O NW.

oxygen adsorption to occur decreases and any gas interactions result from CO or C_6H_6 reacting directly with Sn^0 aggregates. This ultimately increases the resistance over that measured in air ($R_{air}/R_{gas} < 1$), indicating a decreased sensitivity and change in redox interaction from UT nanomaterials under most H_2O plasma and T_S conditions. A similar phenomenon was observed by Tamaki *et al.*[65] in TPD studies of CO interactions with SnO_2 surfaces. They found there was less CO_2 desorption with a reduced SnO_2 surface than with an oxidized SnO_2 surface, potentially analogous to CO interactions with our H_2O NW and NP.

Furthermore, despite limited to no change in carbon monoxide or benzene sensitivity with H_2O plasma treatment, some specific conditions showed enhanced sensitivity over UT materials. Specifically, 100 W H_2O NW had increased CO sensitivity of ~10 over ~2 for UT NW where sensitivity was relatively independent of temperature (Figure 7.5 (a)). Therefore, a sensor designed from 100 W H_2O NW could operate with high sensitivity at room temperature to minimize energy requirements and extend sensor lifetime over a sensor designed from UT NW. Additionally, 60 W H_2O NW had maximum C_6H_6 sensitivity of ~175, relative to ~7 for UT NW (Figure 7.4 (b)). To have sensitivity of 175, the sensor had to operate at 300 °C and resulted in significant variation in sensitivity. The same sensor when operating at room temperature, however, still had increased benzene sensitivity of ~33. Thus, a 60 W H_2O NW sensor operating at room temperature would still have increased C_6H_6 sensitivity and would also benefit from lower energy costs and longer sensor lifetime. The increased sensor performance exhibited for these plasma treatments indicate that different combinations of oxygen adsorption and tin reduction are necessary to detect carbon monoxide versus benzene with maximum sensitivity. Potential reactions for CO with 100 W H_2O NW and C_6H_6 with 60 W H_2O NW are shown in Figure 7.7 (c, f), respectively, for comparison. Overall, the results reported here indicate that

plasma surface modification processes could be tuned to produce materials that have increased room temperature sensitivity to a range of potentially toxic gases. Moreover, the differences in response to the target gases utilized here suggest that we may also be able to increase selectivity of these materials with additional attention to optimizing plasma parameters.

7.4. Summary and Conclusions

Combining sensor performance of UT, Ar/O_2 and H_2O plasma treated nanomaterials with our prior materials characterization data allows for deeper understanding of structure-property-performance relationships necessary to create sensitive targeted SnO_2 gas sensors. Specifically, on average, all SnO_2 nanoparticles (UT, Ar/O_2 and H_2O plasma treated) were more sensitive toward carbon monoxide and benzene than SnO_2 nanowires. Furthermore, Ar/O_2 and H_2O NP displayed decreased sensitivity toward CO and C_6H_6 relative to UT NP (without changing redox interaction) under almost all plasma and T_S conditions. Alternatively, Ar/O_2 and H_2O NW, had much more varied sensitivity and redox interactions depending on plasma conditions and T_S, whereby some treatment conditions resulted in increased sensitivity toward CO and C_6H_6, especially H_2O NW. Specifically, sensor performance suggests a specific level of oxygen adsorption is necessary to enhance CO sensitivity. Enhanced C_6H_6 sensitivity, however, requires a combination of oxygen adsorption and Sn reduction. Moreover, some plasma modification conditions resulted in higher sensitivity at lower temperatures than measured for UT nanomaterials. Overall, H_2O plasma appears to be more effective than Ar/O_2 at altering SnO_2 nanomaterials (especially nanowires), to increase sensitivity toward carbon monoxide and benzene.

7.4.1. Project expansions for enhanced sensing capabilities. To determine if alternative plasma systems are more effective at increasing sensitivity toward CO or benzene we will be expanding our plasma reactor and sensing platform to include other plasma precursor systems (e.g., CO and aniline) as well as testing sensitivity of UT, Ar/O_2 and H_2O nanomaterials toward other gases (e.g., NO_x, formaldehyde) and utilizing other sensing materials. This will allow us to functionalize surfaces, vary morphology further, and create composite materials that may aid in creating more sensitive and selective sensing devices capable of operating at lower/room temperature.

REFERENCES

1. Stuckert, E. P.; Fisher, E. R. Ar/O_2 and H_2O Plasma Surface Modification of SnO_2 Nanomaterials to Increase Surface Oxidation. *Sens. Actuators B.* **2015**, *208* 379-388.
2. Stuckert, E. P.; Geiss, R. H.; Miller, C. J.; Fisher, E. R. In-depth View of the Structure and Formation of SnO_2 Nanowires and Nanobrushes. *ACS Appl. Mater. Interfaces.* **2016**, *8* 22345-22353.
3. Stuckert, E. P.; Miller, C. J.; Fisher, E. R. Gas-phase Diagnostics During H_2 and H_2O Plasma Treatment of SnO_2 Nanomaterials: Implications for Surface Modification. *J. Vac. Sci. Technol., B.* **2017**, submitted for publication.
4. Hodgkinson, J.; Tatam, R. P. Optical Gas Sensing: A Review. *Meas. Sci. Technol.* **2012**, *24* (1), 012004.
5. Liu, X.; Cheng, S.; Liu, H.; Hu, S.; Zhang, D.; Ning, H. A Survey on Gas Sensing Technology. *Sensors.* **2012**, *12* (7), 9635-9665.
6. Aleixandre, M.; Gerboles, M. Review of Small Commercial Sensors for Indicative Monitoring of Ambient Gas. *Chem. Eng. Trans.* **2012**, *30* 169-174.
7. Kumar, P.; Morawska, L.; Martani, C.; Biskos, G.; Neophytou, M.; Di Sabatino, S.; Bell, M.; Norford, L.; Britter, R. The Rise of Low-cost Sensing for Managing Air Pollution in Cities. *Environ. Intern.* **2015**, *75* 199-205.
8. Azad, A.; Akbar, S.; Mhaisalkar, S.; Birkefeld, L.; Goto, K. Solid-State Gas Sensors: A Review. *J. Electrochem. Soc.* **1992**, *139* (12), 3690-3704.
9. Batra, A. K.; Chilvery, A.; Guggilla, P.; Aggarwal, M.; Currie, J. R. Micro- and Nano-Structured Metal Oxides Based Chemical Sensors: An Overview. *J. Nanosci. Nanotechnol.* **2014**, *14* (2), 2065-2085.
10. Zhou, H.; Li, Z.; Niu, X.; Xia, X.; Wei, Q. The Enhanced Gas-Sensing and Photocatalytic Performance of Hollow and Hollow Core–Shell SnO_2-Based Nanofibers Induced by the Kirkendall Effect. *Ceram. Int.* **2016**, *42* (1), 1817-1826.
11. Eranna, G.; Joshi, B. C.; Runthala, D. P.; Gupta, R. P. Oxide Materials for Development of Integrated Gas Sensors - A Comprehensive Review. *Crit. Rev. Solid State Mater. Sci.* **2004**, *29* 111-188.
12. Fine, G. F.; Cavanagh, L. M.; Afonja, A.; Binions, R. Metal Oxide Semiconductor Gas Sensors in Environmental Monitoring. *Sensors.* **2010**, *10* (6), 5469-5502.
13. Zhang, J.; Hu, X.; Shi, J.; Lu, P.; Shen, X.; Xu, P.; Saito, N. Synthesis of SnO_2 Nanoparticles using a Solution Plasma and Their Gas-Sensing Properties. *Jpn. J. Appl. Phys., Part 1.* **2015**, *55* (1S), 01AE17.
14. Patil, S. J.; Patil, A. V.; Dighavkar, C. G.; Thakare, K. S.; Borase, R. Y.; Nandre, S. J.; Deshpande, N. G.; Ahire, R. R. Semiconductor Metal Oxide Compounds Based Gas Sensors: A Literature Review. *Front. Mater. Sci.* **2015**, *9* (1), 14-37.
15. Joulazadeh, M.; Navarchian, A. H. Ammonia Detection of One-dimensional Nano-structured Polypyrrole/Metal Oxide Nanocomposites Sensors. *Synth. Met.* **2015**, *210* 404-411.
16. Bing, Y.; Zeng, Y.; Liu, C.; Qiao, L.; Zheng, W. Synthesis of Double-shelled SnO_2 Nano-polyhedra and Their Improved Gas Sensing Properties. *Nanoscale.* **2015**, *7* (7), 3276-3284.
17. Miller, D. R.; Akbar, S. A.; Morris, P. A. Nanoscale Metal Oxide-Based Heterojunctions for Gas Sensing: A Review. *Sens. Actuators B.* **2014**, *204* 250-272.

18. Lee, J. S.; Jun, J.; Shin, D. H.; Jang, J. Urchin-like Polypyrrole Nanoparticles for Highly Sensitive and Selective Chemiresistive Sensor Application. *Nanoscale.* **2014**, *6* (8), 4188-4194.
19. Xiao, L.; Shu, S.; Liu, S. A Facile Synthesis of Pd-Doped SnO_2 Hollow Microcubes with Enhanced Sensing Performance. *Sens. Actuators B.* **2015**, *221* 120-126.
20. Labeau, M.; Gautheron, B.; Delabouglise, G.; Pena, J.; Ragel, V.; Varela, A.; Román, J.; Martinez, J.; González-Calbet, J.; Vallet-Regi, M. Synthesis, Structure and Gas Sensitivity Properties of Pure and Doped SnO_2. *Sens. Actuators B.* **1993**, *16* (1), 379-383.
21. Iizuka, K.; Kambara, M.; Yoshida, T. Highly Sensitive Formaldehyde Sensors Based on Catalyst Added Porous Films Fabricated by Plasma Spray Physical Vapor Deposition. *Sens. Actuators B.* **2013**, *182* 250-255.
22. Kannan, P. K.; Late, D. J.; Morgan, H.; Rout, C. S. Recent Developments in 2D Layered Inorganic Nanomaterials for Sensing. *Nanoscale.* **2015**, *7* (32), 13293-13312.
23. Wang, C.; Yin, L.; Zhang, L.; Xiang, D.; Gao, R. Metal Oxide Gas Sensors: Sensitivity and Influencing Factors. *Sensors.* **2010**, *10* (3), 2088-2106.
24. Korotcenkov, G. Metal Oxides for Solid-state Gas Sensors: What Determines Our Choice? *Mater. Sci. Eng., B.* **2007**, *139* (1), 1-23.
25. Moseley, P. Solid State Gas Sensors. *Meas. Sci. Technol.* **1997**, *8* (3), 223-237.
26. Zhang, C.; Wang, J.; Hu, R.; Qiao, Q.; Li, X. Synthesis and Gas Sensing Properties of Porous Hierarchical SnO_2 by Grapefruit Exocarp Biotemplate. *Sens. Actuators B.* **2016**, *222* 1134-1143.
27. Ruhland, B.; Becker, T.; Müller, G. Gas-Kinetic Interactions of Nitrous Oxides with SnO_2 Surfaces. *Sens. Actuators B.* **1998**, *50* (1), 85-94.
28. Chaturvedi, A.; Mishra, V. N.; Dwivedi, R.; Srivastava, S. K. Selectivity and Sensitivity Studies on Plasma Treated Thick Film Tin Oxide Gas Sensors. *Microelectron. J.* **2000**, *31* (4), 283-290.
29. Jeun, J.-H.; Kim, D.-H.; Hong, S.-H. Synthesis of Porous SnO_2 Foams on SiO_2/Si Substrate by Electrochemical Deposition and Their Gas Sensing Properties. *Sens. Actuators B.* **2012**, *161* (1), 784-790.
30. Sun, P.; Mei, X.; Cai, Y.; Ma, J.; Sun, Y.; Liang, X.; Liu, F.; Lu, G. Synthesis and Gas Sensing Properties of Hierarchical SnO_2 Nanostructures. *Sens. Actuators B.* **2013**, *187* 301-307.
31. Gu, C.; Xu, X.; Huang, J.; Wang, W.; Sun, Y.; Liu, J. Porous Flower-Like SnO_2 Nanostructures as Sensitive Gas Sensors for Volatile Organic Compounds Detection. *Sens. Actuators B.* **2012**, *174* 31-38.
32. Forleo, A.; Francioso, L.; Capone, S.; Casino, F.; Siciliano, P.; Tan, O.; Hui, H. Wafer-level Fabrication and Gas Sensing Properties of Miniaturized Gas Sensors Based on Inductively Coupled Plasma Deposited Tin Oxide Nanorods. *Procedia Chem.* **2009**, *1* (1), 196-199.
33. Singhal, A. V.; Chandra, K.; Agarwala, V. Doped Nano–Phase Tin Oxide Thin Films for Selective Gas Sensing. *Int. J. Nanotechnol.* **2015**, *12* (3-4), 248-262.
34. Gattu, K. P.; Ghule, K.; Kashale, A. A.; Patil, V.; Phase, D.; Mane, R.; Han, S.; Sharma, R.; Ghule, A. V. Bio-green Synthesis of Ni-doped Tin Oxide Nanoparticles and Its Influence on Gas Sensing Properties. *RSC Adv.* **2015**, *5* (89), 72849-72856.

35. Zhou, Q.; Chen, W.; Li, J.; Tang, C.; Zhang, H. Nanosheet-Assembled Flower-Like SnO_2 Hierarchical Structures with Enhanced Gas-Sensing Performance. *Mater. Lett.* **2015**, *161* 499-502.
36. Fan, X.-X.; He, X.-L.; Li, J.-P.; Gao, X.-G.; Jia, J. Ethanol Sensing Properties of Hierarchical SnO_2 Fibers Fabricated with Electrospun Polyvinylpyrrolidone Template. *Vacuum.* **2016**, *128* 112-117.
37. Filipovic, L.; Selberherr, S. In *Processing of Integrated Gas Sensor Devices*, TENCON 2015-2015 IEEE Region 10 Conference, IEEE: 2015; pp 1-6.
38. Kőrösi, L.; Papp, S.; Beke, S.; Oszkó, A.; Dékány, I. Effects of Phosphate Modification on the Structure and Surface Properties of Ordered Mesoporous SnO_2. *Microporous Mesoporous Mater.* **2010**, *134* (1), 79-86.
39. Huang, H.; Lee, Y.; Chow, C.; Tan, O.; Tse, M.; Guo, J.; White, T. Plasma Treatment of SnO_2 Nanocolumn Arrays Deposited by Liquid Injection Plasma-Enhanced Chemical Vapor Deposition for Gas Sensors. *Sens. Actuators B.* **2009**, *138* (1), 201-206.
40. Gasparotto, A.; Barreca, D.; Bekermann, D.; Devi, A.; Fischer, R. A.; Maccato, C.; Tondello, E. Plasma Processing of Nanomaterials: Emerging Technologies for Sensing and Energy Applications. *J. Nanosci. Nanotechnol.* **2011**, *11* (9), 8206-8213.
41. Seo, H.-K.; Ansari, S.; Al-Deyab, S. S.; Ansari, Z. Glucose Sensing Characteristics of Pd-doped Tin Oxide Thin Films Deposited by Plasma Enhanced CVD. *Sens. Actuators B.* **2012**, *168* 149-155.
42. Lee, D.-K.; Wan, Z.; Bae, J.-S.; Ahn, J.-H.; Kim, S.-D.; Kim, J.; Kwon, S.-H. Plasma-Enhanced Atomic Layer Deposition of SnO_2 Thin Films Using $SnCl_4$ and O_2 Plasma. *Mater. Lett.* **2016**, *166* 163-166.
43. Mitu, B.; Marotta, V.; Orlando, S. Multilayered Metal Oxide Thin Film Gas Sensors Obtained by Conventional and RF Plasma-assisted Laser Ablation. *Appl. Surf. Sci.* **2006**, *252* (13), 4637-4641.
44. Dai, Z.; Jia, L.; Duan, G.; Li, Y.; Zhang, H.; Wang, J.; Hu, J.; Cai, W. Crack-Free Periodic Porous Thin Films Assisted by Plasma Irradiation at Low Temperature and Their Enhanced Gas-Sensing Performance. *Chem. Eur. J.* **2013**, *19* (40), 13387-13395.
45. Dmitriev, S. V.; Brinzari, V. I.; Korotcenkov, G. S. In *Surface Plasma Treatment and Sensibilization of Tin Dioxide Films for Enhancement of Gas Sensitivity and Selectivity*, MRS Proceedings, Cambridge Univ Press: 2004; p A5.11.1.
46. Bierwagen, O.; White, M. E.; Tsai, M.-Y.; Nagata, T.; Speck, J. S. Non-alloyed Schottky and Ohmic Contacts to As-grown and Oxygen-plasma Treated n-Type SnO_2 (110) and (101) Thin Films. *Appl. Phys. Express.* **2009**, *2* (10), 106502.
47. Du, H.-Y.; Wang, J.; Yu, P.; Yu, N.-S.; Sun, Y.-H.; Tian, J.-L. Investigation of Gas Sensing Materials Tin Oxide Nanofibers Treated by Oxygen Plasma. *J. Nanopart. Res.* **2014**, *16* (2), 1-10.
48. Pan, J.; Ganesan, R.; Shen, H.; Mathur, S. Plasma-Modified SnO_2 Nanowires for Enhanced Gas Sensing. *J. Phys. Chem. C.* **2010**, *114* (18), 8245-8250.
49. Mathur, S.; Ganesan, R.; Grobelsek, I.; Shen, H.; Ruegamer, T.; Barth, S. Plasma-Assisted Modulation of Morphology and Composition in Tin Oxide Nanostructures for Sensing Applications. *Adv. Eng. Mater.* **2007**, *9* (8), 658-663.
50. Kim, H. W.; Choi, S.-W.; Katoch, A.; Kim, S. S. Enhanced Sensing Performances of Networked SnO_2 Nanowires by Surface Modification with Atmospheric Pressure Ar–O_2 Plasma. *Sens. Actuators B.* **2013**, *177* 654-658.

51. Karapatnitski, I. A.; Mit, K. A.; Mukhamedshina, D. M.; Baikov, G. G. In *Influence of Hydrogen Plasma Processing on Gas-sensitive Tin Dioxide Thin Film Properties*, 4th International Conference on Thin Film Physics and Applications, International Society for Optics and Photonics: 2000; pp 323-326.
52. Park, J. C.; Kim, J. K.; Kim, T. G.; Lee, D. W.; Cho, H.; Kim, H. S.; Yoon, S. J.; Jung, Y.-G. Dry Etching of SnO_2 and ZnO Films in Halogen-Based Inductively Coupled Plasmas. *Int. J. Mod Phys B.* **2011**, *25* (31), 4237-4240.
53. Tarlov, M. J.; Evans, J. F. Surface Characterization of Radio Frequency Water Plasma Treated and Annealed Polycrystalline Tin Oxide Thin Films. *Chem. Mater.* **1990**, *2* (1), 49-60.
54. Sabat, K.; Rajput, P.; Paramguru, R.; Bhoi, B.; Mishra, B. Reduction of Oxide Minerals by Hydrogen Plasma: An Overview. *Plasma Chem. Plasma Process.* **2014**, *34* (1), 1-23.
55. Chen, W.; Zhou, Q.; Wan, F.; Gao, T. Gas Sensing Properties and Mechanism of Nano-SnO_2-based Sensor for Hydrogen and Carbon Monoxide. *J. Nanomater.* **2012**, *2012* 1-9.
56. Vladimirova, S.; Rumyantseva, M.; Filatova, D.; Kozlovskii, V.; Chizhov, A.; Khmelevskii, N.; Marchevskii, A.; Li, X.; Gaskov, A. SnO_2 (Au0, CoII, III) Nanocomposites: A Synergistic Effect of the Modifiers in CO Detection. *Inorg. Mater.* **2016**, *52* (2), 94-100.
57. Marikutsa, A. V.; Rumyantseva, M. N.; Yashina, L. V.; Gaskov, A. M. Role of Surface Hydroxyl Groups in Promoting Room Temperature CO Sensing by Pd-Modified Nanocrystalline SnO_2. *J. Solid State Chem.* **2010**, *183* (10), 2389-2399.
58. Prades, J.; Hernández-Ramírez, F.; Fischer, T.; Hoffmann, M.; Müller, R.; López, N.; Mathur, S.; Morante, J. Quantitative Analysis of CO-humidity Gas Mixtures with Self-heated Nanowires Operated in Pulsed Mode. *Appl. Phys. Lett.* **2010**, *97* (24), 243105.
59. Hernandez-Ramirez, F.; Tarancon, A.; Casals, O.; Arbiol, J.; Romano-Rodriguez, A.; Morante, J. High Response and Stability in CO and Humidity Measures Using a Single SnO_2 Nanowire. *Sens. Actuators B.* **2007**, *121* (1), 3-17.
60. Ghaddab, B.; Berger, F.; Sanchez, J.-B.; Menini, P.; Mavon, C.; Yoboue, P.; Potin, V. Benzene Monitoring by Micro-Machined Sensors with SnO_2 Layer Obtained by Using Micro-Droplet Deposition Technique. *Sens. Actuators B.* **2011**, *152* (1), 68-72.
61. Wang, X.; Carey, W. P.; Yee, S. S. Monolithic Thin-Film Metal-Oxide Gas Sensor Arrays with Application to Monitoring of Organic Vapors. *Sens. Actuators B.* **1995**, *28* (1), 63-70.
62. Zhang, F.; Wang, X.; Dong, J.; Qin, N.; Xu, J. Selective BTEX Sensor Based on a SnO_2/V_2O_5 Composite. *Sens. Actuators B.* **2013**, *186* 126-131.
63. Kim, K.-M.; Choi, K.-I.; Jeong, H.-M.; Kim, H.-J.; Kim, H.-R.; Lee, J.-H. Highly Sensitive and Selective Trimethylamine Sensors Using Ru-Doped SnO_2 Hollow Spheres. *Sens. Actuators B.* **2012**, *166* 733-738.
64. Wang, L.; Wang, S.; Wang, Y.; Zhang, H.; Kang, Y.; Huang, W. Synthesis of Hierarchical SnO_2 Nanostructures Assembled with Nanosheets and Their Improved Gas Sensing Properties. *Sens. Actuators B.* **2013**, *188* 85-93.
65. Tamaki, J.; Nagaishi, M.; Teraoka, Y.; Miura, N.; Yamazoe, N.; Moriya, K.; Nakamura, Y. Adsorption Behavior of CO and Interfering Gases on SnO_2. *Surf. Sci.* **1989**, *221* (1), 183-196.
66. Yamazoe, N.; Fuchigami, J.; Kishikawa, M.; Seiyama, T. Interactions of Tin Oxide Surface with O_2, H_2O and H_2. *Surf. Sci.* **1979**, *86* 335-344.

67. Batzill, M. Surface Science Studies of Gas Sensing Materials: SnO_2. *Sensors.* **2006**, *6* (10), 1345-1366.
68. Kocemba, I.; Rynkowski, J. M. The Effect of Oxygen Adsorption on Catalytic Activity of SnO_2 in CO Oxidation. *Catal. Today.* **2011**, *169* (1), 192-199.
69. Bielański, A.; Najbar, M. Adsorption Species of Oxygen on the Surfaces of Transition Metal Oxides. *J. Catal.* **1972**, *25* (3), 398-406.
70. Suematsu, K.; Yuasa, M.; Kida, T.; Yamazoe, N.; Shimanoe, K. Determination of Oxygen Adsorption Species on SnO_2: Exact Analysis of Gas Sensing Properties Using a Sample Gas Pretreatment System. *J. Electrochem. Soc.* **2014**, *161* (6), B123-B128.
71. Fuller, M.; Warwick, M. The Catalytic Oxidation of Carbon Monoxide on Tin (IV) Oxide. *J. Catal.* **1973**, *29* (3), 441-450.
72. Nakata, S.; Kato, Y.; Kaneda, Y.; Yoshikawa, K. Rhythmic Chemical Reaction of CO on the Surface of a SnO_2 Gas Sensor. *Appl. Surf. Sci.* **1996**, *103* (4), 369-376.
73. Tang, W.; Wu, X.; Li, D.; Wang, Z.; Liu, G.; Liu, H.; Chen, Y. Oxalate Route for Promoting Activity of Manganese Oxide Catalysts in Total VOCs' Oxidation: Effect of Calcination Temperature and Preparation Method. *J. Mater. Chem. A.* **2014**, *2* (8), 2544-2554.
74. Vaishnav, V.; Patel, S.; Panchal, J. Development of ITO Thin Film Sensor for Detection of Benzene. *Sens. Actuators B.* **2015**, *206* 381-388.

CHAPTER 8

SUMMARY OF RESEARCH PERSPECTIVES AND FUTURE AVENUES OF EXPLORATION

This chapter summarizes the research presented in this dissertation, addressing global themes and broader impacts on gas detection technology research. Potential avenues for future research directions stemming from this project are also proposed.

8.1. Research Summary

8.1.1. A multi-faceted experimental approach. Gas sensors designed from several different materials and utilizing a variety of sensing mechanisms have been developed and used extensively in private homes and businesses. Although numerous detectors are commercially available, limitations persist for many types of sensors, including insufficient sensitivity and selectivity toward certain gases, and high operating temperatures that limit sensor lifetime. Although significant progress has been made to address some of these limitations, studies are often one-sided in their focus (e.g., materials analysis-focused versus performance-focused). For example, plasma modification of SnO_2 nanomaterials has gained interest in the past decade, but most studies focus on analysis of bulk and surface properties pre- and post-plasma treatment (e.g., PXRD, XPS, SEM). To more efficiently and effectively fabricate and modify materials for sensitive and targeted gas sensing at room temperature, it is necessary to create a holistic analysis approach. Specifically, it is essential to comprehensively characterize (1) materials structure and properties pre- and post-plasma modification, (2) plasma gas-phase species and energetics, and (3) gas sensor performance. By performing an array of complementary analyses, greater understanding can be gained on how materials are modified to result in specific sensing

properties. This knowledge aids in efficiently selecting appropriate base materials and plasma modification systems for a desired sensor application. The work presented in this dissertation is the compilation of these integral pieces of data that provide substantial new insight into the fabrication and plasma modification of gas sensor materials.

8.1.2. Emergent themes. This dissertation includes key studies for comprehensive understanding of all aspects of creating and testing gas sensors for understanding structure-property-performance relationships. Specifically, utilizing various complementary imaging and diffraction techniques (i.e., SEM, HRTEM, t-EBSD, STEM-DI) provides a more detailed view on the structure and morphology of nanomaterials than simply using a single technique. Moreover, structural detail may be lost in certain techniques, such as TEM, because of unintentional user bias when selecting materials to analyze. Combining high resolution analysis with t-EBSD data make it possible to analyze a larger number of wires/rods/etc. from a sample with minimal user bias. This allows for discerning potential structural variations within a sample of nanomaterials that may be lost when selecting specific wires or rods for analysis. Indeed, the structural study described in Chapter 3 indicates a similar tetragonal SnO_2 structure of SnO_2 nanowires and nanobrushes grown via CVD; however, through complementary diffraction analysis, slight variations in lattice spacing and growth face were measured.

Structure, surface chemistry, and morphology differences have the potential to result in different electrical properties, and thus, sensing capabilities for SnO_2 materials. Therefore, additional surface analysis of two different morphologies, nanoparticles and nanowires, were completed prior to and after plasma modification (Chapter 4). Plasma modification was employed because sensor sensitivity and selectivity are largely driven by surface properties (in conjunction with bulk structure). For this dissertation, the plasma precursors of interest were

Ar/O_2 and $H_2O_{(v)}$ as they are well known oxidizing plasma systems for enhancing nanomaterial surface oxidation to increase sensor sensitivity. After modifying SnO_2 nanoparticles and nanowires under different parameters with these systems, surface analysis showed clear distinctions between the two morphologies and plasma precursors. Prior to plasma treatment, nanoparticles and nanowires had tetragonal SnO_2 structures with similar ratios of adsorbed oxygen to lattice oxygen. After modification, however, nanoparticles and nanowires showed increased tin reduction as a function of increased *P* with H_2O plasma treatment while maintaining Sn^{4+} after Ar/O_2 plasma treatment at all *P*. Both plasma modification systems resulted in equivalent or greater ratios of adsorbed oxygen to lattice oxygen for nanowires than nanoparticles, indicating the two materials interact with plasma species in dissimilar ways.

Thus, to elucidate what plasma species alter surface chemistry, how nanomaterial morphology plays a role in surface modification, and therefore, if nanomaterials can alter plasma species, a complete plasma gas-phase diagnostics approach is key, as described in Chapter 5. This study explored nanomaterial interactions with H_2O and H_2 plasma systems given the unexpected reduction observed with H_2O plasma treatments—H_2 plasma was analyzed as a model reducing plasma containing similar reducing species (e.g., H*, H_2*). Gas-phase analysis also demonstrated that nanoparticles and nanowires interact with plasma species differently, as concentrations for excited state OH radical, H_α, and Sn varied, depending on plasma parameters and SnO_2 morphology. Specifically, it was determined that high-energy hydrogen species were responsible for tin reduction and SnO_2 etching in both plasmas. Furthermore, when these reducing species were in excess of the oxidizing species in H_2O plasmas, nanomaterial etching and tin reduction were observed. These gas-phase studies allowed us to better understand how

H_2 and H_2O plasmas interact with SnO_2 nanomaterials and vice versa, to aid in determining appropriate plasma parameters to achieve specific materials properties in the future.

The final step of the holistic approach to sensor design involves combining materials' structure and properties with sensor performance, linking the steps from material fabrication to modification and finally to sensor capabilities. Initial sensor performance studies focused on sensitivity of the different UT and plasma treated nanomaterials over a range of temperatures from 25-300 °C. These studies indicated that on average, Ar/O_2 plasma modification resulted in lower or equivalent sensitivity toward carbon monoxide and benzene under all plasma conditions and operating temperatures. Such changes, or lack thereof, suggest that increased adsorbed oxygen to lattice oxygen ratios alone are largely insufficient at increasing nanoparticle sensor sensitivity toward CO or C_6H_6. H_2O plasma treatment, on the other hand, resulted in increased sensitivity under more plasma parameters and operating temperatures than Ar/O_2 plasma modification. This likely is the result of both increased adsorbed oxygen as well as tin reduction leading to greater changes in material resistance in the presence of carbon monoxide or benzene. Furthermore, nanowire sensitivity was consistently less temperature dependent (in contrast with nanoparticle sensitivity), and led to increased sensitivity under more parameters than nanoparticles. Greater changes in nanowire sensitivity because of plasma treatment is likely the result of the greater surface area as well as the interconnected network of nanowires creating more potential for collective resistance change than possible with nanoparticles.

8.1.3. Broader impact and outlook. These studies emphasize the necessity of understanding structure-property-performance relationships of sensor materials to effectively choose materials and plasma systems for creating sensitive targeted gas sensors. As such, this dissertation demonstrates the need for comprehensive complementary analysis of materials and

plasmas from fabrication to modification to sensor performance when creating gas sensors. For research to address sensor limitations in an efficient manner, an active effort to follow a holistic approach to creating sensors must exist. Combining comprehensive analysis of sensor materials before and after modification in conjunction with sensor performance can allow for less uncertainty while fabricating gas sensors. Furthermore, this approach to sensor fabrication can be utilized for various different materials or morphologies, modification expansions, and additional performance tests which are discussed in greater detail below.

8.2. Future Directions

8.2.1. Completing the comparison of nanowire versus nanobrush modification and performance. Similar modification systems, materials analysis, and sensor performance tests presented in this dissertation can be utilized to complete analysis of SnO_2 nanobrushes.[1] These additional studies can aid in determining if this alternative nanomaterial morphology will interact with the plasma or target gas species in different ways to those observed here for SnO_2 nanowires and nanoparticles.[2] Such work will provide greater detail on structure-property-performance relationships of SnO_2 nanomaterials in gas sensing applications. Specifically, completing these modification and performance studies for nanobrushes will determine the effect of the different morphologies and structural variations from nanowires on sensor performance.

8.2.2. Using plasma surface functionalization to address sensor selectivity. To expand our studies and focus on addressing selectivity limitations, alternative plasma precursors can be utilized for surface functionalization. Some potential precursors include carbon monoxide for imparting –C=O and –C-O-R- functionality, ammonia for implanting $–NH_x$ functionality, and allyl alcohol for adding –OH functionality.[3-5] Because CO plasma can both increase surface

oxygen content and alter surface functionalization, this plasma system was chosen for further study. To determine the efficacy of CO plasma modification for enhanced gas sensing, preliminary surface and sensor performance analyses were performed. An example OES spectrum for 100 mTorr 150 W CO plasma shown in Figure 8.1 provides an overview of excited-state gaseous species present in the plasma. Initial XPS high resolution C_{1s}, O_{1s}, and Sn_{3d} spectra, Figure 8.2, reveal that CO plasma treatment (under a subset of plasma conditions) does not alter the tin oxidation state. High resolution O_{1s} and C_{1s} spectra, however, indicate the addition of carbonyl, ester, and aliphatic environments upon CO plasma treatment of SnO_2 nanoparticles not explainable solely as adventitious carbon. Additionally, initial CO sensitivity data for CO plasma treated SnO_2 nanoparticle gas sensors, Figure 8.3, indicate a switch from a reducing to an oxidizing gas-surface interaction, similar to what was observed with Ar/O_2 and H_2O plasma treated materials. Specifically, the change to an oxidizing interaction occurs at $T_S \geq 150$ °C, whereby CO sensitivity decreases with increasing temperature until $T_S = 200$ °C, where sensitivity begins to increase with increasing temperature. Although the CO sensitivity of CO plasma treated nanoparticles is substantially lower than that of UT nanoparticles, expanded studies are in progress by another Fisher group graduate student, Kim Hiyoto, for a wider range of plasma parameters, nanomaterial morphologies, and target gases to determine if any alternative CO plasma treatments or target gases may result in enhanced sensitivity over the UT nanoparticles.

8.2.3. Plasma deposition for creating polymeric nanocomposites. Another alternative form of plasma modification that moves beyond surface functionalization utilizes plasma polymerization[6-8] to conformally deposit a conductive polymer such as polyaniline (precursor aniline vapor) onto a SnO_2 nanomaterial.[9] Polymer nanocomposites are often fabricated from

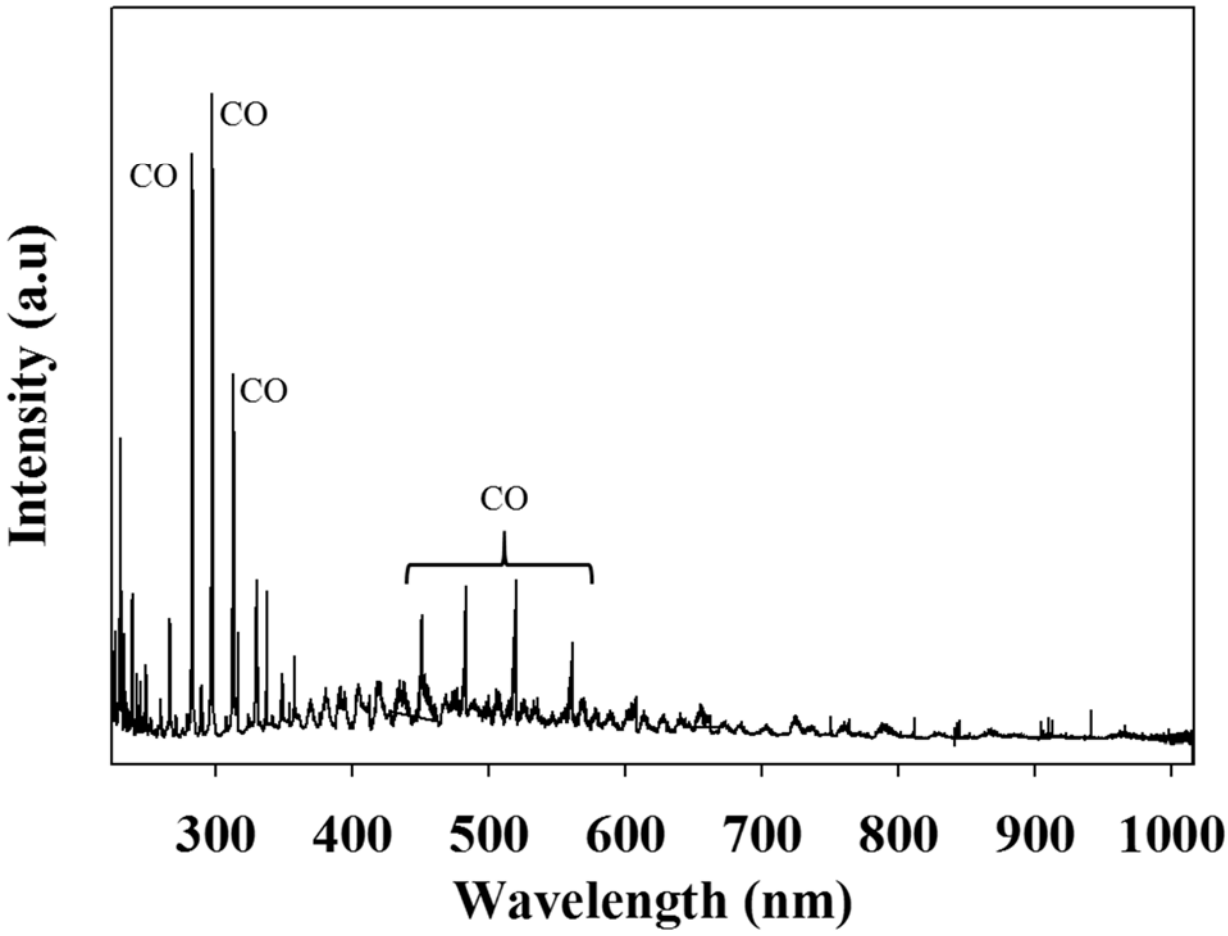

Figure 8.1. Raw OES spectrum for a 100 mTorr 150 W CO plasma.

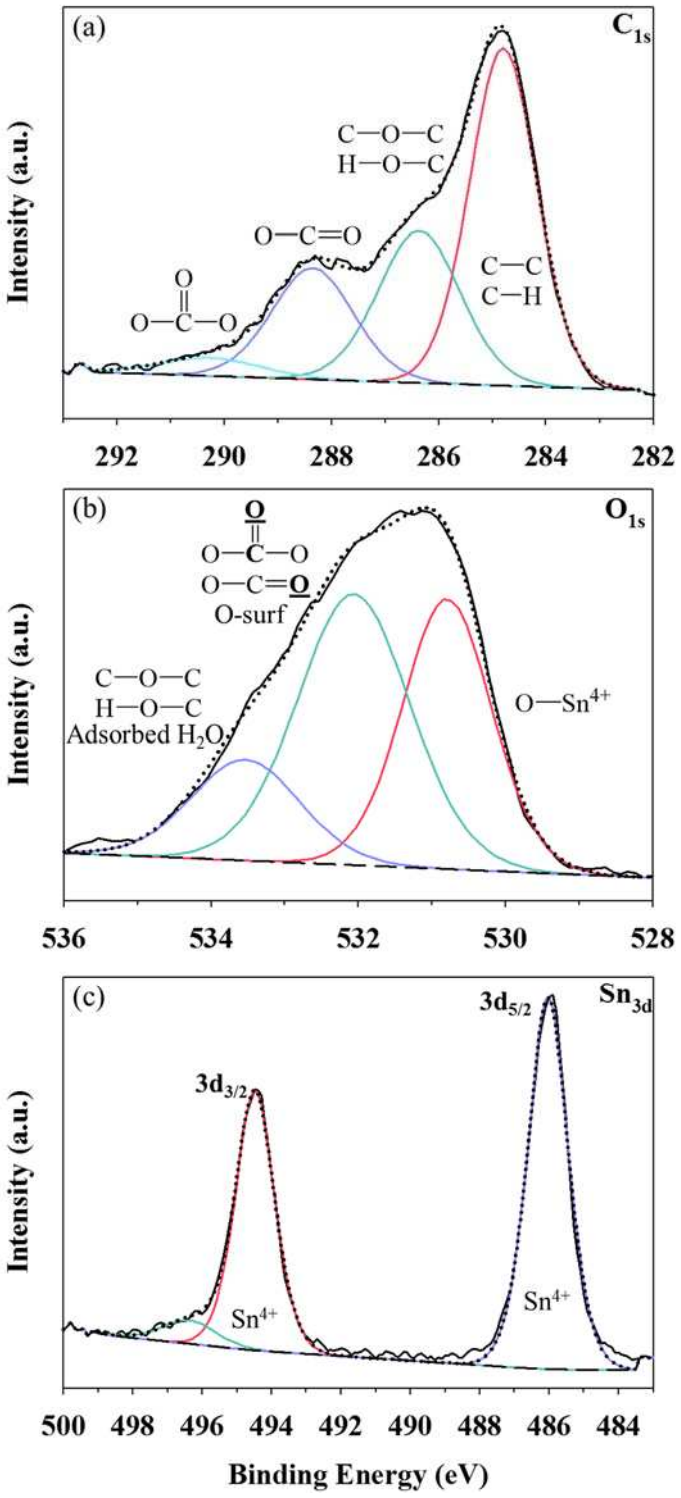

Figure 8.2. Representative high resolution (a) C_{1s}, (b) O_{1s}, and (c) Sn_{3d} XPS spectra for 145 mTorr 30 W CO plasma treated nanoparticles, with similar binding environments observed for materials treated at P = 10, 60, 80, and 100 W.

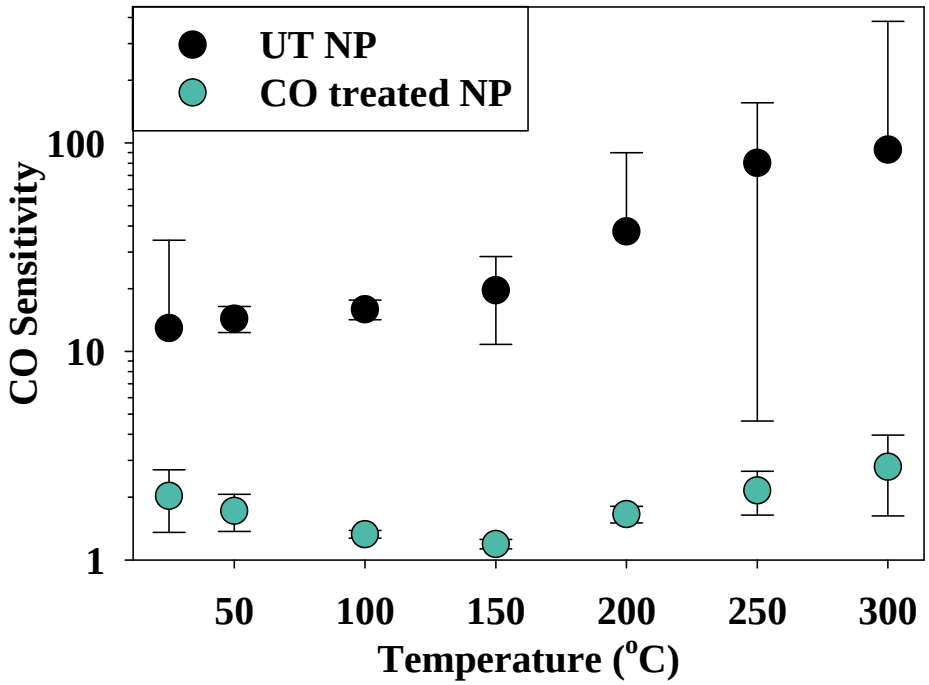

Figure 8.3. CO sensitivity for UT and 50 mTorr 50 W 5 min CO plasma treated nanoparticles.

mixtures cast into molds or various template processes whereby the polymer comprises the bulk material and limits morphology.[10-12] By conformally coating SnO_2 nanomaterials with a conductive polymer, the nanomaterial maintains bulk properties and the polymer surface coating can control gas-surface interactions. OES was initially used to evaluate if aniline could be successfully used to ignite a plasma within our systems because there are limited studies on aniline plasma polymerization in ICPs, especially for coating SnO_2 nanomaterials. Figure 8.4 shows OES spectra of an aniline plasma without a substrate, and with SnO_2 nanoparticle or nanowire substrates. The spectrum without a substrate displays emission from CH, CN, OH, NH, and N_2 gas-phase species, indicative of aniline in the gas phase, thereby maintaining monomer functionality. Given these results, an aniline plasma was used to deposit a polyaniline coating on SnO_2 nanowires. OES spectra collected during aniline plasma treatment of nanoparticles or nanowires show signals from the same gas-phase species as detected without a substrate but with different relative intensities. These data indicate that the gas-phase density of species such as NH and OH can be affected by the presence of different nanomaterial morphologies. Further optimization of plasma parameters with materials, gas-phase, and performance analyses are necessary to comprehensively understand the efficacy of utilizing a polyaniline film to enhance sensor sensitivity and/or selectivity.

8.2.4. Additional sensor substrates for cost-effective sensor fabrication. A promising area of research that requires significant development beyond plasma optimization and materials analysis lies in creating paper-based sensors with MO nanomaterials. Paper-based devices benefit from being robust, cheap, and easy to fabricate while incorporating rapid response and recovery with high sensitivity because of MO nanomaterial components.[13-15] Creating MO paper-based sensors, however, is difficult because of the high temperatures often required for

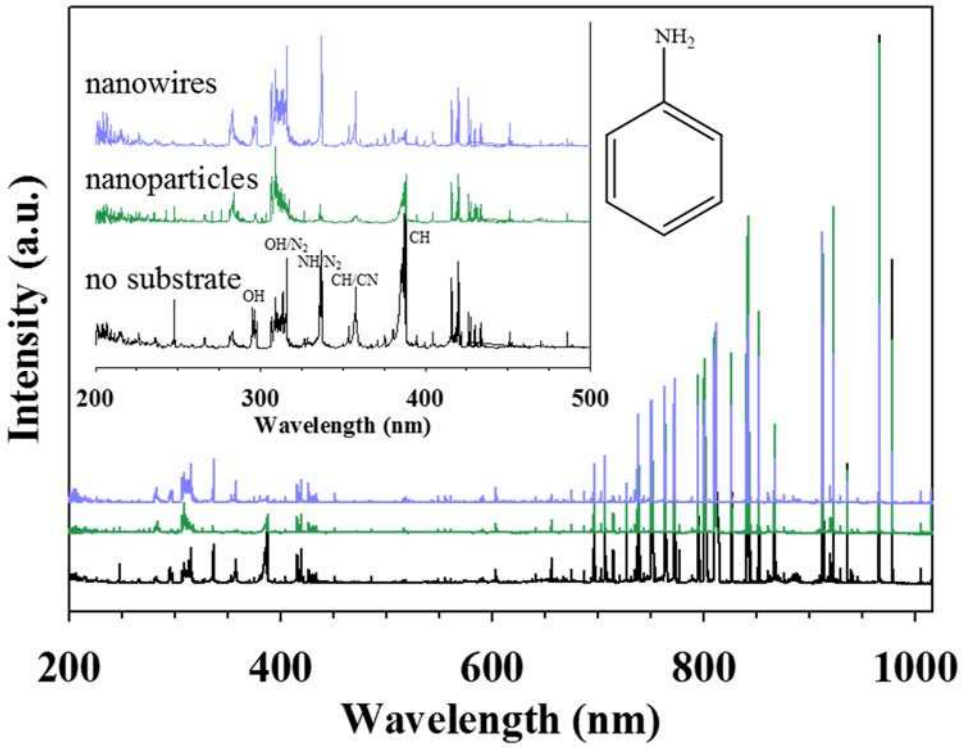

Figure 8.4. OES spectra for an 80 mTorr 100 W 5 min aniline plasma with no substrate, SnO_2 nanoparticles, and SnO_2 nanowires, with a magnified region from 200-500 nm and the aniline chemical structure inset.

growing nanomaterials and operating MO sensors.[1, 16, 17] Some methodologies show promise for creating such sensors but offer limited control over the fabrication process.[13, 18, 19] The nature of LTP deposition creates the potential for utilizing plasmas to directly deposit MO thin films/grow nanomaterials on paper.[20, 21] Similarly, regardless of fabrication process for MO paper-based sensors, there is ample utility in the expansive parameter space of plasma systems to modify the paper and/or the nanomaterial. A prime opportunity for utilizing plasmas lies with depositing conductive polymer films like polyaniline onto the paper, whereby the polyaniline can provide the necessary conductivity that a MO material would but may allow for more effective deposition given the similar organic composition of the paper and the polyaniline.

8.2.5. Expanding sensor performance repertoire. Alterations to our current sensing system and/or sensor fabrication methods should also be made to expand sensor performance studies. Specifically, these expansions include additional gas lines, flow controllers, and LabVIEW software which will allow for measuring sensor response and recovery, testing sensitivity as a function of gas concentration, and determining selectivity and sensitivity in mixed gas atmospheres. These complementary studies enhance understanding of structure-property-performance relationships of different materials for sensing applications. Additional details on these system modifications are provided in Chapter 6.

8.3. Project Overview

8.3.1. A multi-faceted approach to altering material capabilities. All of these continuing and future studies will benefit from our multi-faceted process to sensor fabrication, providing greater understanding of how fabrication and modification processes with their corresponding materials and gas-phase properties affect sensor performance. Thus, such project extensions

examine structure-property-performance relationships to enhance our knowledge of gas-surface interactions of different material structures and properties, plasma modification systems, and sensor designs. The work and future directions presented in this dissertation lay the foundation for a holistic approach to create sensitive targeted gas sensors in an efficient and definitive manner.

REFERENCES

1. Stuckert, E. P.; Geiss, R. H.; Miller, C. J.; Fisher, E. R. In-Depth View of the Structure and Growth of SnO_2 Nanowires and Nanobrushes. *ACS Appl. Mater. Interfaces.* **2016**, *8* (34), 22345-22353.
2. Stuckert, E. P.; Fisher, E. R. Ar/O_2 and H_2O Plasma Surface Modification of SnO_2 Nanomaterials to Increase Surface Oxidation. *Sens. Actuators B.* **2015**, *208* 379-388.
3. Shearer, J. C.; Fisher, E. R. Design and Operation of a Rotating Drum Radio Frequency Plasma Reactor for the Modification of Free Nanoparticles. *Rev. Sci. Instrum.* **2013**, *84* (6), 063904.
4. Vandencasteele, N.; Reniers, F. Surface Characterization of Plasma-Treated PTFE Surfaces: An OES, XPS and Contact Angle Study. *Surf. Interface Anal.* **2004**, *36* (8), 1027-1031.
5. Zaldivar, R.; Nokes, J.; Adams, P.; Hammoud, K.; Kim, H. Surface Functionalization Without Lattice Degradation of Highly Crystalline Nanoscaled Carbon Materials Using a Carbon Monoxide Atmospheric Plasma Treatment. *Carbon.* **2012**, *50* (8), 2966-2975.
6. Hawker, M. J.; Pegalajar-Jurado, A.; Hicks, K. I.; Shearer, J. C.; Fisher, E. R. Allylamine and Allyl Alcohol Plasma Copolymerization: Synthesis of Customizable Biologically-Reactive Three-Dimensional Scaffolds. *Plasma Process. Polym.* **2015**, *12* (12), 1435-1450.
7. Shearer, J. C.; Fisher, E. R. Enhancing Surface Functionality of Supported Fe_2O_3 Nanoparticles Using Pulsed Plasma Deposition of Allyl Alcohol. *Nanosci. Nanotechnol. Lett.* **2012**, *4* (3), 358-363.
8. Malkov, G. S.; Fisher, E. R. Pulsed Plasma Enhanced Chemical Vapor Deposition of Poly(allyl alcohol) onto Natural Fibers. *Plasma Process. Polym.* **2010**, *7* (8), 695-707.
9. Airoudj, A.; Debarnot, D.; Bêche, B.; Poncin-Epaillard, F. New Sensitive Layer Based on Pulsed Plasma-Polymerized Aniline for Integrated Optical Ammonia Sensor. *Anal. Chim. Acta.* **2008**, *626* (1), 44-52.
10. Joulazadeh, M.; Navarchian, A. H. Ammonia Detection of One-Dimensional Nano-Structured Polypyrrole/Metal Oxide Nanocomposites Sensors. *Synth. Met.* **2015**, *210* 404-411.
11. Rahman, M. M.; Khan, S. B.; Marwani, H. M.; Asiri, A. M. A SnO_2-Sb_2O_3 Nanocomposite for Selective Adsorption of Lead Ions from Water Samples Prior to Their Determination by ICP-OES. *Microchim. Acta.* **2015**, *182* (3-4), 579-588.
12. Lu, X.; Zhang, W.; Wang, C.; Wen, T.-C.; Wei, Y. One-Dimensional Conducting Polymer Nanocomposites: Synthesis, Properties and Applications. *Prog. Polym. Sci.* **2011**, *36* (5), 671-712.
13. Li, X.; Wang, Y.-H.; Lu, A.; Liu, X. Controllable Hydrothermal Growth of ZnO Nanowires on Cellulose Paper for Flexible Sensors and Electronics. *IEEE Sens. J.* **2015**, *15* (11), 6100-6107.
14. Katoch, A.; Abideen, Z. U.; Kim, J.-H.; Kim, S. S. Influence of Hollowness Variation on the Gas-Sensing Properties of ZnO Hollow Nanofibers. *Sens. Actuators B.* **2016**, *232* 698-704.
15. Korotcenkov, G. Metal Oxides for Solid-State Gas Sensors: What Determines Our Choice? *Mater. Sci. Eng., B.* **2007**, *139* (1), 1-23.

16. Chang, L.-W.; Huang, M.-W.; Li, C.-T.; Shih, H. C. Controllable Two-Step Growth and Photoluminescence of Waterweed-Like SnO_2 Nanowires. *Appl. Surf. Sci.* **2013**, *279* 167-170.
17. Thomson, M.; Hodgkinson, J.; Sheel, D. Control of Zinc Oxide Surface Structure Using Combined Atmospheric Pressure-Based CVD Growth and Plasma Etching. *Surf. Coat. Technol.* **2013**, *230* 190-195.
18. Gimenez, A. J.; Yáñez-Limón, J.; Seminario, J. M. ZnO−Paper Based Photoconductive UV Sensor. *J. Phys. Chem. C.* **2010**, *115* (1), 282-287.
19. Gimenez, A. J.; Luna-Bárcenas, G.; Sanchez, I. C.; Yánez-Limón, J. M. Paper-Based ZnO Oxygen Sensor. *IEEE Sens. J.* **2015**, *15* (2), 1246-1251.
20. Sahin, H.; Manolache, S.; Young, R.; Denes, F. Surface Fluorination of Paper in CF_4-RF Plasma Environments. *Cellulose.* **2002**, *9* (2), 171-181.
21. Şahin, H. Pyrrole Thin Films Deposited on Paper by Pulsed RF Plasma. *Open Chem.* **2007**, *5* (3), 824-834.

LIST OF ABBREVIATIONS

[X*]	relative concentration of excited state species X
Ar/O_2	argon and oxygen (1:1) mixed gas
B.E.	binding energy
C_6H_6	benzene
CBED	convergent beam electron diffraction
CO	carbon monoxide
CVD	chemical vapor deposition
CW	continuous wave
EDS	energy dispersive X-ray spectroscopy
H_2	hydrogen gas
$H_2O_{(v)}$	water vapor
HR	high resolution
I_X/I_{Ar}	relative concentration of species X
ICDD	International Centre for Diffraction Data
IPF	inverse pole figure
LT-ICP	low temperature-inductively coupled plasma
MOS	metal oxide semiconductor
NBED	nano-beam electron diffraction
NO_x	nitrogen oxides
NP	SnO_2 nanoparticles
NW	SnO_2 nanowires
OES	optical emission spectroscopy

OIM	Orientation Imaging Microscopy
P	applied rf power
PECVD	plasma enhanced chemical vapor deposition
PXRD	powder X-ray diffraction
R_{air}	resistance recorded in air
R_{gas}	resistance recorded in gas (i.e., carbon monoxide or benzene)
SnO_2	tin(IV) oxide
SAED	selective area electron diffraction
SEM	scanning electron microscopy
STEM-DI	scanning transmission electron microscopy-diffraction imaging
t-EBSD	transmission electron backscatter diffraction
T_R	rotational temperature
T_S	substrate temperature
T_V	vibrational temperature
UT	untreated or no plasma treatment
VLS	vapor liquid solid
XPS	X-ray photoelectron microscopy
X*	excited state gas species of interest X
XD	X dimensional, where X is the number of dimensions
ZrO_2	50 nm zirconium oxide on n-type 100 silicon wafer
ZA	zone axis